High Speed Switching in Magnetic Recording Thin-Film Heads

Submitted by

Gustavo Recio

to the University of Exeter as a thesis for the degree of Doctor of Philosophy in Engineering, July 2008

I certify that all the material in this thesis which is not my own work has been identified and that no material has previously been submitted and approved for the award of a degree by this or any other University.

.....

Abstract

There has always been an increasing demand for high density data storage. However, the increased areal storage densities of hard disk drives require a level of miniturisation of the recording heads where the micromagnetic details and switching mechanisms can no longer be ignored. Furthermore, theoretical and numerical studies on thin-film recording heads tend to separate the micromagnetics from the electromagnetic aspects of the head during switching and hence ignore the lossy nature of head materials.

This project was aimed to develop a numerical simulation approach that simultaneously incorporates the fundamental micromagnetic and electromagnetic details of magnetic materials to study the fast switching process in soft magnetic materials in general, and in thin-film inductive writers in particular. The project also was aimed at establishing an impedance measurement system to characterise losses in magnetic recording heads, and to allow comparison with the simulations.

This project successfully met all its original objectives. A numerical technique to simulate the dynamic behaviour of magnetic materials and devices has been developed, and applied to study the switching process in thin-film recording heads. Two-dimensional simulations of complete commercial head structures including the coils and pole regions were carried out and parameters such as gap field rise times, gap field distributions, and core inductances, which are important for head designers, were predicted. Moreover, the role of eddy currents delaying the magnetisation switching was elucidated. Furthermore, it was found that the gradient of the recording fields were sharper near the conrner regions of the poles when considering magnetic details. A high precision, high bandwidth impedance measurement system was established to characterise losses in magnetic heads. Fittings of measured core inductances to a proposed equivalent circuit model of the core's relaxation processes revealed the switching times of heads (of the order 0.1 to 1.0ns).

To the memory of

Mónica, Lola,
Mina and Julián.

Acknowledgments

I would like to thank my supervisors, Dr Mustafa M. Aziz and Professor C. David Wright. Thanks for your guidance, continuous supervision, support and encouragement. Without it, the progress which has been made through this work would not have been so.

I would also like to thank everybody from Engineering and Computer Science who has helped me over the past four years. Particularly to Colin Lovell who helped me with the SEM images of the heads; Keith Smith who helped me with the test fixture; and Dave Weightman for having everything you are looking for in the stores.

I must also thank to Dr Jim Miles from the University of Manchester and the people from Seagate in Northern Ireland for providing the whole lot of longitudinal heads I have been working with during these years.

Finally, I must not forget to thank my family and friends for their support, especially my parents for their moral and economic support when I most needed.

Contents

List of Figures

List of Tables

Chapter 1

Literature Review

1.1 Overview

Research on magnetic storage moves towards increasing the storage capacity of magnetic hard disks. This is achieved with developments of new thermally stable magnetic recording media having high energy with less magnetic noise that are capable of sustaining small recorded bits of information (Zhang et al., 2002); and with the improvement in efficiency of inductive thin-film magnetic recording heads and the reduction of their dimensions (Yuan et al., 2002). This overal miniaturisation enables the head to record shorter transition and narrower tracks thus increasing the areal storage density. Advances in recording speeds have reached a point where the micromagnetics of the heads have become a physical limit. Consequently, to continue with the rise in areal storage densities and to push towards higher recording speeds, research has been focused on understanding and improving flux propagation and reversal times in thin-films inductive recording heads (Hicken et al., 2002; Back et al., 1999). The flux reversal time is the time it takes for the magnetic flux in the head circuit to respond to changes in the write current waveform. Minimising this time in the head yoke reduces the rise time of the writing fields in the pole tip region and allows shorter and well defined magnetic

transitions to be written onto the storage medium (Middleton et al., 2001).

High-speed experimental studies using the time-resolved magneto-optical Kerr microscope on magnetic thin-films (Hicken et al., 2002) and on thin-film recording heads (Back et al., 1999) have contributed to furthering the understanding of the switching mechanisms in these magnetic structures. With the reduction of the size of the active regions in thin-film recording heads (Tagawa et al., 2000), the ability to obserrve the flux distribution during switching in the pole tip region of heads is becoming beyond the optical resolution of this technique. As a result, modelling and simulation are becoming increasingly important as alternative tools to understand the flux reversal process in these small head features and to enable the optimisation of write head designs.

Static models of characterising magnetic heads include equivalent circuit models, transmission line models and finite elements models (Engstrom, 1984; Paton, 1971; Jones, 1978; Arnoldussen, 1988; Yeh, 1982; Liu et al., 2001). These are either time independent or limited in the frequency domain to the fundamental response, and ignore the magnetic detail of the head material. Dynamic models, on the other hand, utilise full micromagnetic description of the magnetic material (Gao and Bertram, 2001), but the absence of electromagnetic formulation in these models neglects the eddy current effect coming from time varying fields in the finite resistivity thin-film materials. Therefore the need arises for a dynamic model that combines the solution to Maxwell's equations for the electromagnetic fields with micromagnetic models of the material to accurately simulate the reversal process in magnetic heads.

Modern computational methods such as the FDTD algorithm will play a key role in modelling magnetic heads in the future. The FDTD method solves the electromagnetic phenomena for a given geometry inside a computational space and, as a result, the magnitude and direction of the electromagnetic fields are given for the whole computational space. It is possible to extend the standard FDTD algorithm to model the

micromagnetics of materials together with the solution of Maxwell's equations having in this manner a better description of the reversal process. Studying and experimentally characterising the fast switching process (dynamics) in thin-film heads is the main aim of this research work and it is achieved through FDTD computations and impedance measurements of actual thin-film heads.

In the next four sections different approaches that have been taken to address the modelling and characterisation of thin films in general and thin film recording heads in particular will be presented. Starting with several experimental studies that have contributed to the understanding of the switching mechanisms in thin films and thin film recording heads. Continuing with a review of purely static and purely dynamic modelling methods in which the electromagnetic and micromagnetic phenomenon are addressed independently. And finishing with more complex models where both phenomena are combined.

This chapter concludes with a discussion on the merit of the papers referenced detailing the strength and limitations of the different methods. Leading, based on the above discussion, to the establishment of the research aim of this work.

1.2 Experimental Measurements

In Corb (1988) a scanning Kerr effect microscope (SKEM) was built that features 0.025μm step sizes and 5^o phase resolution over a 50MHz bandwidth. Scans were made on several NiFe and CoZr thin-film recording heads with different head geometries. The measured values of head saturation were in rough agreement with those calculated from a model for saturation near the back gap. The frequency response of the NiFe heads showed that the real component of the efficiency rolled off smoothly, and the imaginary component peaked between 15 and 40 MHz. The bandwidth increased with DC efficiency and was two to three times lower than computed values. The

frequency response of the CoZr head showed peaks and valleys that were attributed to a misoriented easy axis. The response of the heads studied was most likely determined by domain behavior.

With thin-film head/media systems, frequency-domain parametric measurements (SNR, resolution, decibel overwrite, etc.) often demonstrate poor correlation with actual disk-drive phase margin results. Superposition modelling and direct time-domain measurements are required to understand these systems better. In Brittenham (1988) several techniques were discussed: time-domain quantification of individual read and media noise, aggregate noise and offset deconvolution from phase margin graphs, and time-domain writeability measurements. Applications of these techniques include characterization of phenomena unique to thin-film systems, optimization of disk-drive electronics using these systems, and the creation of improved component and drive production tests.

A wide-field magnetooptic domain observation system with a time resolution of 10 ns was developed to study magnetization dynamics in thin-film heads (Liu et al., 1990). The instantaneous dynamic response on the top yoke of thin-film recording heads was examined at any chosen instant within the drive current cycle at frequencies up to 20 MHz. Different phase responses from different domain walls in the head were observed and interpreted in terms of hysteretic wall motion, effective field density variation in the head, and wall orientations relative to the flux conduction direction. Two different flux conduction mechanisms associated with two different domain structures in the central region of the head were observed and discussed. Flux conduction in the center of the head by motion of backgap walls and magnetization rotation for domain structures with and without the backgap walls was observed. The domain structure with the backgap walls is probably undesirable because the backgap wall motion may cause a decrease in head efficiency during high-frequency operation and could cause noise during read-back.

Magnetization response during high frequency and high amplitude write current excitations at the air-bearing surfaces (ABS) of thin film inductive and MR write heads have been observed by using a Scanning Kerr Effect Microscope (Liu et al., 1996). Under certain excitation conditions, bubble-like dynamic domain walls that separate the regions of 180 out-of-phase magnetization reversals were observed predominately at the ABS of trailing poles. This magnetization reversal mechanism is believed to be introduced by the combined effects of eddy current damping and local magnetization saturation, and is consistent with the model proposed by Wood et al. (1990).

Increasing data rates are requiring magnetic transducers to perform at higher frequencies. Core losses, which are the combined effect of eddy current losses, damped domain wall motion, and decreasing rotation susceptibility, act to reduce yoke permeance at high frequencies. In Payne et al. (1996), a technique for measuring core loss and demonstrate its application to a variety of heads was described. The method involves least-squares fitting of measured head impedance vs. frequency spectra to the response from an equivalent magnetic circuit having a complex and frequency-dependent inductance. The result is a description of how the complex inductance varies with frequency, thereby characterizing the core loss.

A thin-film write head model was described in Klaassen and Hirko (1996) which is based on electrical impedance versus frequency measurements. The model includes the effects of head saturation and eddy current damping making it useful for simulation of the electrical input port (head coil) and magnetic output port (pole tip) signals, which would be observed under actual write conditions.

Inductance-saturation characteristics in thin film heads are measurements of inductance as a function of write current. These measurements typically exhibit a series of step-like inductance discontinuities as various segments of the magnetic core saturate. In Payne et al. (1997), a framework for interpreting the location and magnitude of these

discontinuities was presented and the physical constitution of the core they reveal was discussed.

1.3 Static Models

Equations for the flux, magnetic field, and current distributions in a single-turn planar magnetic recording head were derived in Paton (1971) making the assumption that the magnetic material has constant permeability. These equations were solved in the frequency domain and an expression was given for the head efficiency in terms of the head dimensions, permeability, and frequency. Expressions for the flux in a multiturn thin film head were derived in Jones (1978) and used to obtain equations for the efficiency and inductance as a function of film structure and permeabilities.

It is assumed that fast and slow relaxation processes both occur in a thin film recording head. Linear response theory was applied in Engstrom (1984) to derive an equivalent circuit, which consisted of a resistor, describing the coil resistance, in series with an inductor, describing the fast relaxation process, in series with a parallel inductor - resistor combination whose time constant is that of the slow relaxation process. The complex impedance of a head was measured over a frequency range of 10 kHz to 12 MHz. An excellent fit to the experimental data was obtained by adjusting the values of the equivalent circuit elements.

The significance of head inductance and eddy currents in limiting field rise times was discussed in Wood et al. (1990). Poor rise times can cause severe distortion and loss of performance at high data rates. A simple reluctance model was developed to explore the relationship between the geometry of a head and its inductance. The model was extended to include the effects of eddy currents, and to allow the frequency-dependent efficiency (hence the field rise time) to be calculated. Based on this rise time, a geometric model was used to calculate the positions of the recorded transitions and the

resulting transition-shift distortion.

In Takano et al. (1995), the significance of suppressing eddy currents in recording heads as means of achieving recording channels with both higher recording densities and higher data rates was studied. The write characteristics of thin film heads using CoNiFe and CoTaZr films with different values of resistivity and saturation flux density was experimentally investigated. Write characteristics were analyzed by studying recorded patterns using sputtered magnetic particles and fringing field measurements using electron beam tomography. From the results of this study, it was found to be essential to increase the resistivity of the core itself for higher-density and higher-frequency recording. It was found that heads using low resistivity film not only suffer from the phase delay of the recording field relative to the write current, but also from a intensity drop which results in degraded rolloffs and write sensitivity. The phase shift could be compensated by shifting the transition during the writing process, but this does not improve the intensity drop. Reliable high density recording systems for frequencies of up to 100 MHz were developed for heads using CoTaZr amorphous poles.

A two-dimensional model of an MR write head was constructed using a finite element model in Torabi et al. (1998). The model includes the eddy currents as well as nonlinear saturation of recording head material. The recording head field (deep gap field) was calculated as a function of write-current frequency and amplitude for two recording-head materials, standard $Ni_{80}Fe_{20}$ and high saturation magnetization M_s material $Ni_{50}Fe_{50}$. The analysis was also done in the time domain and was compared with experimental data on field response, using both a microloop apparatus and impedance measurements. Fair agreement was obtained between the model and the data. It was observed that the deep gap field had a time delay relative to the write current, varying as a function of current frequency and amplitude.

A physical model for planar spiral inductors on silicon, which accounts for eddy current

effect in the conductor, crossover capacitance between the spiral and center-tap, capacitance between the spiral and substrate, substrate ohmic loss, and substrate capacitance was presented in Yue and Wong (2000). The model was verified with measured results of inductors having a wide range of layout and process parameters. This scalable inductor model enables the prediction and optimization of inductor performance.

Write fields and replay characteristics of gapped heads with magnetically recessed leading poles for high-frequency digital video were described in Shute et al. (2001). An investigation by finite-element analysis, a comparison of computed results for laminated Sendust and $Co_{91}Nb_6Zr_3$ heads and a discussion of the effects due to depositing a layer of copper inside the leading gap edge was given. It was observed that recessing the leading pole yielded an asymmetric field, while eddy currents in the copper layer caused an advantageous redistribution of flux in the head. Predicted increases in both maximum horizontal field and horizontal field gradient by at least 130% and 17% were predicted for Sendust and $Co_{91}Nb_6Zr_3$ heads, respectively, at 100 MHz. Hence, such a head can write on higher coercivity media than a conventional gapped head. The playback performance is also improved by an extension of the frequency response. The linear model proposed for the phase of the spectral response is valid over a wide range of frequencies, for each of two leading pole recessions.

In Kaya et al. (2005), an electrical circuit model of the impedance of an inductive write element that reproduces measured impedances to within 10% up to 9 GHz and allows interpretation in terms of the physical structure of the head was developed. The model was used to extract the complex inductance of the magnetic yoke region of the head as a function of frequency, which is assumed to be linearly proportional to the yoke material permeability (after subtraction of the coil inductance). A clear negative excursion of the real part of the permeability was seen in the analysis, indicating gyromagnetic damping as the dominant loss mechanism, since eddy currents cannot produce a negative real part of the permeability.

1.4 Dynamic Models

The switching dynamics in a thin-film head for both the writing and reading modes were studied in Soohoo (1982). To minimize magnetostatic energy, the film head was split up into multidomains subsequent to saturation writing in the hard (or track) direction. The domain structure was composed of elongated domains in the easy direction and closure domains at the edges. The results of the calculations showed that domain wall motion contributes increasingly to the effective head permeability as the track width is decreased. In the readback process, it was found that the switching time for wall motion τ_w (170 ns) in the edge domains was some two orders of magnitude larger than τ_r for rotation (1 ns) in the main domains. Since these motions are coupled due to the requirement of continuity of the perpendicular component of $\overrightarrow{M_s}$ at a 90^o wall, the switching dynamics are dominated by wall motion. A finite distribution of wall motion threshold field H_o can give rise to different time delays in the head response, leading to distortions in the readback signal, including the presence of wiggles at the trailing edge.

A transmission surface model (TSM) that analyzes the conduction of flux by rotation and wall motion was reported in Mallary et al. (1990). This model was used to quantitatively compare the predicted performance of thin-film heads with longitudinal and transverse magnetic anisotropy. The TSM analysis predicted that a transversely oriented type of thin-film head can be operated at much higher frequencies than a longitudinally oriented head. In addition, its group delay dispersion was much less. Finally, its susceptibility to wall pinning was an order of magnitude less. Therefore, the traditional adversion of head designers to the longitudinal orientation is justified for frequencies above several megahertz

In Jayasekara et al. (1998), the initial permeabilities of NiFe single layer films and single and multi-layer FeAlN films up to 500 MHz were presented. The permeability of

thin (<1500$\dot{A}$) NiFe and FeAlN films were fit with calculations based on the Landau-Lifshitz-Gilbert model for phenomenological damping, using damping factors of 0.016 and 0.026, respectively. Transverse bias permeability measurements identified larger ripple fields in FeAlN samples compared to those in thin NiFe samples. The permeability of 2μm thick NiFe and FeAlN films were well described by eddy current theory. The permeability roll off frequency of 2μm thick patterned FeAlN films increased from 20 to 200MHz when laminated into 32 layers separated by 25$\dot{A}$ thick SiN interlayers.

A scanning Kerr microscope set-up with picosecond time resolution and submicron spatial resolution was used to directly measure the flux response in magnetic recording heads in Back et al. (1999). The data rate limiting factor of a write head, which is the flux rise time at the gap, was measured for different geometries and head materials in polar Kerr mode. Flux propagation in the yoke, which is governed by a combination of wall displacement and magnetisation rotation, was studied by one dimensional and two dimensional time response measurements utilising the longitudinal Kerr effect. The local flux time response in the head was correlated to the respective micromagnetic structure as determined by static wide-field Kerr imaging. In addition to the intrinsic magnetic properties the flux time response was also studied by looking at the system properties of the head/write electronics and, by using a voltage source for excitation, information about classical eddy-current effects for different pole geometries were derived. Further, non-stationary effects in the flux reversal process were shown to produce non-linearities in the response at the write gap which contributed to non-linear transition shift in the write process.

A three-dimensional micromagnetic tip model was utilized to study magnetization switching dynamics and the external head fields of a write head in Gao and Bertram (2001). For a flux rise time of 0.1 ns, the head field followed the input flux up to about 60% of saturation, and slowly approached saturation. At a flux rise time of 0.5 ns, the head field followed the input flux closely. Calculated head held gradients agreed

well in the gap region with the theoretical Lindholm model. At the track edge, the perpendicular and crosstrack field components remained fairly constant.

In Wu et al. (2001), results of optical pump-probe measurements made on $Ni_{81}Fe_{19}$ films of thickness d = 50, 500 and 5000 $\dot{A}$ were presented. It was shown that the rise time of the pulsed field within the sample may be determined, and that when d is sufficiently small, the value of the Gilbert damping parameter may be obtained from the decay of the magneto-optical signal. The pulsed field was found to rise more slowly when applied perpendicular to the plane of the sample and as the thickness of the sample was increased. By changing the orientation of the pulsed field relative to the static magnetisation it is possible to alter the ellipticity of the trajectory of the precessing magnetisation and observe variations in the decay of the precession. These effects were discussed in terms of eddy current shielding of the rising field, eddy current damping of the motion of the magnetisation, and propagation of spin waves from the point at which the sample response is probed. For the thinnest sample studied (d = $50\dot{A}$) it was found that the value of the Gilbert damping parameter was strongly field dependent, so that, the calculated Ferromagnetic Resonance (FMR) line width increased as the field was reduced. Under certain circumstances a second mode of higher frequency was observed in the thickest film. It is believed that this is a magnetostatic surface mode that was not previously been observed by means of the optical pump-probe technique.

In Brown et al. (2002), the dynamic switching time in two classes of media by considering two different particle orientation distribution functions was studied . The switching constant was calculated directly from the Landau-Lifshitz-Gilbert equation of motion, which was chosen to simulate the dynamic properties of the media. A strong linear relation between the reciprocal of the switching time and the difference between the applied and anisotropy fields was illustrated.

A magneto-optical pump-probe spectroscopy used to study magnetisation dynamics with femtosecond temporal resolution was described in Hicken et al. (2002). Optically triggered magnetic field pulses were used to induce large amplitude picosecond precessional motion of the spontaneous magnetisation while direct optical stimulation was used to manipulate the magnitude of the spontaneous magnetisation on femtosecond time scales.

1.5 Combined Models

In Zheng and Chen (1992), the wide band transient signal propagation characteristics along microstrip lines with ferrite substrate were presented. In the analysis how the frequency dependent media such as ferrite may be genearally fomulated by FD-TD method was described. The distortions of transient signal in Gaussian shape propagating along uniform or step junction microstrip were simulated by the extended FD-TD method. Results showed the distinctive influence of applied DC magnetic field and magnetizaton on the dispersion of transient signal. In Reineix et al. (1992), a new method for analyzing ferrite structures was introduced.

A formulation for the FDTD treatment of partially magnetized ferrites was presented in Pereda et al. (1993). It was based on the derivation of a system of time-domain differential equations from an empirical expression of the permeability tensor, normally used for designing microwave devices. This approach was applied to the full-wave analysis of waveguides loaded with partially magnetized ferrites. A more efficient FDTD algorithm was introduced in Okoniewski and Okoniewska (1994) for the analysis of structures involving magnetized ferrites. The critical issue of time and space synchronism ensuring second order accuracy was discussed, and a method to provide it based on extrapolation rather than interpolation used by previous authors was presented. Numerical examples validating the method were given.

The design of high-speed recording heads requires one to consider the effect of eddy currents on performance. Experiments have shown that even for very thin laminations, there is an appreciable eddy current effect for high recording frequencies. In Torre and Eicke (1997) a technique was suggested for including these effects in a micromagnetic calculation. This technique was implemented in a finite difference calculation and some results were presented. The structure of the computational algorithm was considerably different from conventional eddy current calculations

A dynamic micromagnetic model which includes gyromagnetic effects (via the LandauLifshitz equation) and eddy currents was developed and applied to the rise time problem in thin film write heads (Sandler and Bertram, 1997). A cross-section of the part of the head covering the coils was simulated with this model, while the rest of the head was modeled as saturable reluctances. The reluctances did not include eddy currents, but they did include leakage, fringing and saturation, and allowed for computation of the deep gap field. This model was used to study the details of the dynamics of the magnetization in the yoke as well as the dependence of rise time on geometric and material parameters. It was found that switching starts at the surfaces of the pole and moves inward in "transition zones." Also, if rise time is defined as the time it takes the deep gap field to reach 7 kOe, the rise time increases with pole thickness but decreases with saturation magnetization and driving current.

A three-dimensional dynamic micromagnetic model including the effect of eddy currents was developed in Torres et al. (2003). Its application to magnetization reversal processes in permalloy nanocubes of 40nm side was presented for applied fields with rise times of 0.1ns. Under certain conditions, for damping parameters $\alpha = 0.01$ and $\alpha = 0.1$, the effect of the eddy currents triggered the precessional switching anticipating the reversal of the magnetization. For a damping constant $\alpha = 0.5$, the contribution of the eddy currents did not allow a full reversal of the magnetization.

A finite-element method (FEM) was developed in Takano (2004) to treat a whole write head structure as a micromagnetic model, and it was utilized to study the magnetization dynamics and head field of a planar writer. As the head had a domain structure, the leakage field differed from what was calculated by a conventional FEM except for the gap region, and it could induce some adjacent track erasure (ATE) problems in the case of high write currents. This leakage field comes from the shoulder of the bottom yoke pedestal and the sidewall of the upper pole. A conventional FEM for electromagnetic eddy-current field did not show much time delay of the head field rise in core sizes of 10μm or below. On the other hand, the head field could not follow the write current waveform perfectly, and showed time delay by the micromagnetic FEM analysis. This indicates that the delay mainly no longer comes from eddy-current effects but magnetization dynamics of the gyromagnetic precession, damping, and flux conduction. Furthermore, the head field rise time is affected by the damping constant, material, yoke length, and pole-tip dimension.

As data rates increase and the size of the disk write head decreases it is likely that a standard non-linear eddy-current simulation of a disk write head will not fully capture dynamic effects. In Sun et al. (2004) a coupled eddy-current and micromagnetics model for the disk write head was propossed. A simple finite difference formulation derived from a mass-lumped finite element method was presented. This derivation allowed to verify that, before time discretization, the semi-discrete scheme obeys the same energy decay equality as the partial differential equation model.

Dynamic modelling of thin ferromagnetic layers, based on the coupling of Maxwell's equations with the nonlinear Landau-Lifschitz-Gilbert law was discussed in Vacus and Vukadinovic (2005). A 2-D micromagnetic model was described which involved FDTD code to determine equilibrium configurations and finite element modelling to compute magnetostatic fields. Then, the susceptibility spectra of films supporting a weak-stripe-domain structure were computed and successfully compared to existing measurements

without introducing any fitting parameter.

In Takano et al. (2007), a micromagnetic modelling program for magnetic recording head analysis was developed, taking eddy current effects into account, and used to study the 1-GHz high-frequency response. When gyromagnetic precession is dominant with a small damping parameter of 0.01, the eddy current field caused the delay of the response, but the head field intensity increased a lot, compared to the no eddy current case, this is because the eddy current field cancels the precessional motion and improves the magnetization alignment. Since magnetic soft films have an intrinsic small damping, low-resistivity material is preferable for high-end magnetic recording heads.

1.6 Aim of Research

The main limitation of static models is that they ignore the magnetic detail of the material. By using dynamic models, the micromagnetic description of the material is accounted for, however, as these models do not include electromagnetic formulation the eddy current effect coming from time varying fields in the finite resistivity thin-film materials is not considered. The solution to the limitations of purely static and purely dynamic modelling methods is the combination of both techniques. So far, two different approaches have been adopted in developing combined methods. The first approach consists in using finite-element modelling (FEM) that include dynamic description of the micromagnetics of materials (Takano, 2004). The main limitation of using FEM is that it is limited in frequency to the fundamental response. On the other hand, the second approach consists in using the finite difference time domain method (FDTD) in combination with micromagnetic formulation (Vacus and Vukadinovic, 2005). The FDTD method is an explicit method for solving Maxwell's equations that through its structure and implementation provides a flexible platform for the electromagnetic

simulation of a wide range of applications, it also provides almost an infinite bandwidth due to its time domain nature and it is for these reasons that it was chosen to carry out dynamic simulations in this work.

Again, two approaches have been adopted to solve electromagnetic problems involving magnetic materials using the FDTD method. The first approach involved using a frequency dependent permeability tensor to relate the magnetic flux density to the field strangth in the simulated systems (Pereda et al., 1995). This is a frequency domain approach which requires transformation into the time domain before inclusion into the FDTD formulation, and does not yield information about the state of magnetisation of the material. It is also limited to static applied biasing fields and does not allow the inclusion of anisotropy and exchange fields. In the second approach Maxwell's equations are augmented with the Landau-Lifshitz-Gilbert (LLG) equation that describes the precessional motion of the magnetisation vectors in a magnetic material under the influence of an effective field. Hence, this formulation allows the inclusion of the anisotropy and exchange fields as effective fields in the model, and the electromagnetic fields due to magnetic and/or electric charges and currents are evaluated naturally through the solution of Maxwell's equations. Thus, this extension of the FDTD method allows the simulation of complete magnetic devices with dielectric and coducntive materials. Previous work using this approach were limited to small signal approximations (Pereda et al., 1993), or with no damping involved and limited to simple magnetic structures (Zheng and Chen, 1992; Reineix et al., 1992; Okoniewski and Okoniewska, 1994). The effects of anisotropy and exchange forces were not included in these treatments. Moreover, there were no analysis of the stability of the solution of the LLG equation and no treatments of boundary conditions.

The aim of this research is therefore to study and experimentally characterise the fast switching process (dynamics) in thin-film heads. This is achieved through FDTD computations and impedance measurements of actual thin-film heads. The FDTD

computations include micromagnetic description of materials in the form of the solution to the LLG equation and therefore the effects of anisotropy and exchange fields are considered in the model. The impedance measurements provide time constants closely related to the micromagnetic effect due to the magnetic nature of the head materials and thus allow comparison with the computation results.

Chapter 2

Introduction to Magnetic Recording

2.1 Introduction

Magnetic hard disk drives are the dominant mass storage devices used in modern computers. Figure 2.1 shows a picture of a typical magnetic hard disk drive. Every disk drive has an interface to a micropocessor located at the edge of the printed circuit board (PCB), which is hidden on the other side of the shown disk drive. The PCB also contains data detection and write current generation electronics. The mechanical servo and control system includes the spindle, actuators, suspension arms and control chips. The spindle holds one or more flat circular disks, onto which the data is recorded. The disks are made from a non-magnetic material and are coated with a thin layer of magnetic material. Each recording head is located at the trailing end of a slider which is mounted at the end of a stainless steel suspension arm. The arm is moved by a coil of wire mounted within a very strong magnetic field which is referred to as an actuator and allows positioning the head very quickly and accurately. The pair formed by the recording head and the recording disk surface is known as the head-disk assembly.

The operation of the head-disk assembly is based on a self-pressurized *air-bearing*

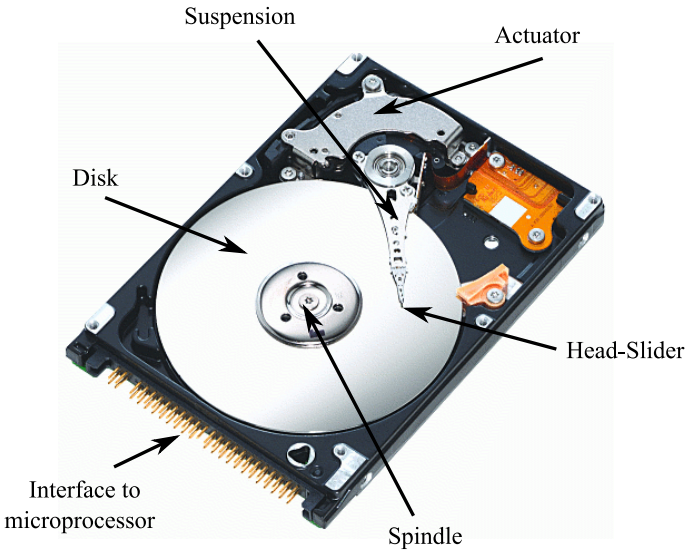

Figure 2.1: Inside of a magnetic hard disk drive showing main components.

between the slider and the spinning disk, which maintains a constant separation (called the *flying height*) between them, as shown in Figure 2.2. By positioning the head-slider along the radial direction, different data tracks can be written on the disk. Each data track is divided into many data sectors. Each sector stores a fixed amount of data. The typical formatting provides space for 512 bytes of user-accessible data per sector.

The read/write head is an essential component in all magnetic recording systems. An inductive head is basically a horseshoe-shaped soft magnet with an air gap and a coil. Ferrite ring heads consist of magnetically soft bulk ferrites machined into head structures where the coil is mechanically wounded around. Thin-film heads are manufactured using integrated circuit (IC) technology, therefore there is no machining involved. Using IC technology allows the miniaturisation of the head with its consequent advantages, e.g. higher track density. Ferrite ring heads were extensively used in hard disk drives in the beginning. However, nowadays thin-film heads have largely replaced ring heads in hard disk drives.

This chapter is intended as a general description of magnetic recording systems, in

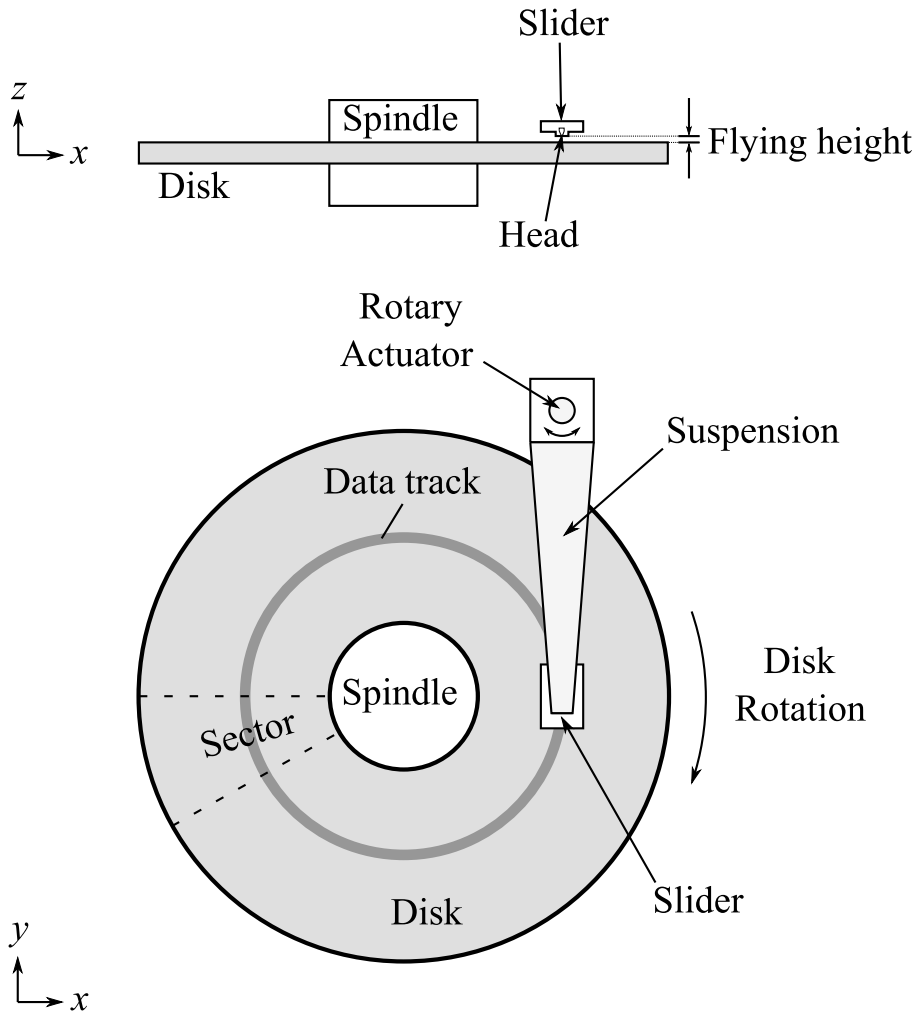

Figure 2.2: Schematic of a typical hard disk assembly.

particular those used in computer hard disk drives. Thus, the basic principles of operation of such a systems will be reviewed in detail in the next sections. Then, the chapter will continue focusing on thin-film heads for longitudinal recording, first on their fabrication process and materials and later on current methods to characterise the heads. This chapter provides the basis for the background and fundamental theories used throughout this thesis.

2.2 The Reading and Recording Processes

2.2.1 Overview

The magnetic recording process converts an electric current signal into an equivalent magnetisation in a magnetic disk. This is done with a transducer that transforms the electrical signal into a magnetic field through which the disk passes. As a final result the disk surface presents a magnetic remanence which is related to the magnitude of the field. This transducer is referred to as the head.

Figure 2.3 represents the write-read process in a magnetic recording system. The magnetic head consists of a magnetic yoke and a coil. When the coil is excited with a write current, a magnetic field is induced in the yoke. As a result of the material's high permeability (at least 300 times that of free space) and the small separation between the poles, the generated magnetic flux in the yoke is linked through the gap. Due to the separation between the poles, a small part of the field leaks from the generated flux and it is radiated outside the head. This portion of the field is used to store the binary information in the disk by means of magnetising its material in the appropriate direction at fixed intervals. The write field must be larger than the medium's coercivity to magnetise the medium along the field direction. By switching the direction of the write field or the write current, magnetisation transitions can be written in the

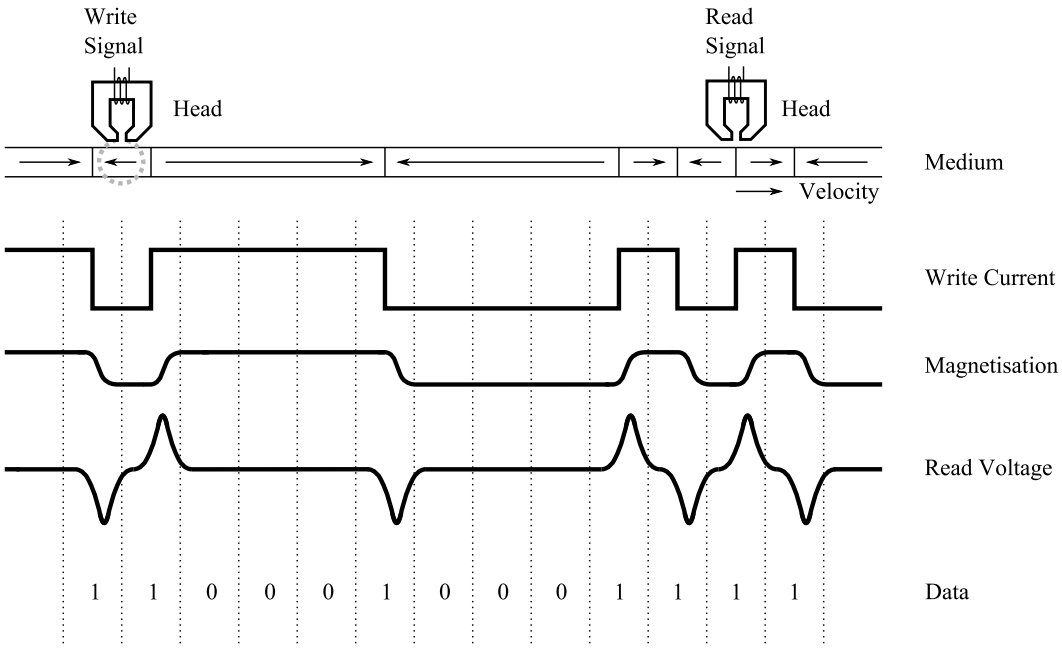

Figure 2.3: Writing and reading processes in a longitudinal magnetic storage system.

medium. In the reading process the sequence is just the opposite. The medium with transitions is passed underneath the gap. The relative motion between the head and the magnetostatic stray fields produced by the magnetic transitions generates induced voltage pulses in the coil due to the magnetic flux linked through the yoke.

When the magnetisation of the medium is parallel to the disk plane and the direction of travel the mode of recording is said to be *longitudinal*. On the contrary, in *perpendicular recording* the magnetisation of the medium is normal to the disk plane. Longitudinal recording has been used traditionally and it is still used, but perpendicular recording is gaining momentum due to its high density advantages. Note that this thesis focuses on thin-film heads used for longitudinal recording in magnetic hard drives but nevertheless the theory contents in this chapter also apply to perpendicular recording. Ideally, the pattern of magnetisation created by a recording signal would be like that shown in Figure 2.3. If the recording signal is a square wave with a fundamental frequency f

and the medium moves with a velocity v, the wavelength of the recorded pattern is

$$\lambda = \frac{v}{f} \tag{2.1}$$

and its bit length is defined as

$$b = \frac{\lambda}{2} \tag{2.2}$$

The linear density D_l is defined as the inverse of the bit length. The track density D_w is defined as the inverse of the track pitch or the distance between adjacent data track centres. The areal data density D_a is computed as the linear density times the track density and specifies the bits that can be recorded per unit area in the medium.

2.2.2 Reading Process

Before analysing in detail the readback signal, the reprocity principle will be introduced. The reciprocity principle is based on the fact that the mutual inductances M_{12} and M_{21} between two inductive circuits are the same when the medium surrounding the circuits is linear (i.e. in the absence of ferromagnetic material).

$$M_{12} = M_{21} = L_m \tag{2.3}$$

Consider two coils linked by a mutual inductance L_m as shown in Figure 2.4. A current i_1 in the left coil will cause a flux ϕ_{21} through the coil to the right given by

$$\phi_{21} = L_m i_1 \tag{2.4}$$

In a similar way, the flux ϕ_{12} through the left coil as a result of a current i_2 in the right coil is given by

$$\phi_{12} = L_m i_2 \tag{2.5}$$

Thus it is possible to write

$$\frac{\phi_{12}}{i_2} = \frac{\phi_{21}}{i_1} \tag{2.6}$$

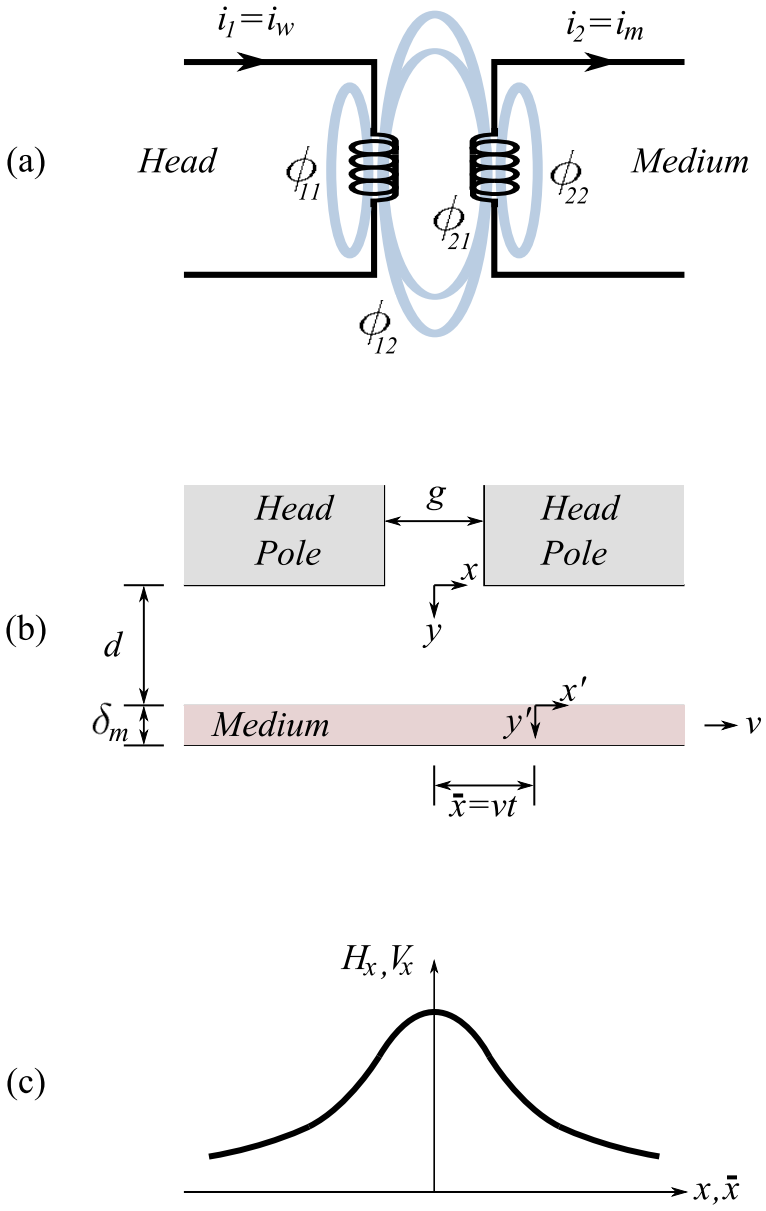

Figure 2.4: Reading process. (a)Magnetic interaction between two circuits, (b) recording medium with a relative speed $\boldsymbol{v}$ with respect to the head poles used to work out the readback signal and (c) readback signal.

Now take the left coil to represent the head's coil and the right coil to carry a current representing a magnetised element of the recording medium. Considering only x components, a write current i_w in the head's coil produces a head field $H_x(x, y)$. The flux through the coil representing the medium due to current i_w is related to the head field as

$$\phi_{21} = \mu_0 H_x(x, y) dydz \tag{2.7}$$

where $dydz$ is the area of the magnetised element through which the flux passes. The current i_m that represents the magnetisation at point x' in the medium can be expressed as

$$i_m = M_x(x')dx' \tag{2.8}$$

or

$$i_m = M_x(x - \overline{x})dx \tag{2.9}$$

where $\overline{x} = vt$ is the moving distance of the medium relative to the head as shown in Figure 2.4. Substituting (2.9) and (2.7) in (2.6) gives the flux in the head's coil as

$$\phi_{12} = \mu_0 M_x(x - \overline{x}) \frac{H_x(x, y)}{i_w} dxdydz \tag{2.10}$$

Integration over the total volume of the recording medium leads to the total flux in the coil

$$\phi_{12} = \mu_0 \int_{-\infty}^{+\infty} \int_{d}^{d+\delta_m} \int_{-\infty}^{+\infty} M_x(x - \overline{x}) \frac{H_x(x, y)}{i_w} dxdydz \tag{2.11}$$

Note that the head's coil current i_w is the write current rather than the readback current. The head field H_x is normally proportional to the write current i_w. Therefore, the magnetic flux ϕ_{12} is in general independent of the write current.

The readback voltage is related to the flux as

$$V(\overline{x}) = -\frac{\partial \phi}{\partial t} = -\frac{\partial \overline{x}}{\partial t} \frac{\partial \phi}{\partial \overline{x}} = v \frac{\partial \phi}{\partial \overline{x}} \tag{2.12}$$

which applied to (2.11) gives

$$V(\overline{x}) = -\mu_0 v \int_{-\infty}^{+\infty} \int_{d}^{d+\delta_m} \int_{-\infty}^{+\infty} \frac{\partial M_x(x-\overline{x})}{\partial \overline{x}} \frac{H_x(x,y)}{i_w} dxdydz \tag{2.13}$$

The derivative of the magnetisation represents the magnetic charge density. Expression (2.13) shows that a head senses the moving magnetic charge. If there is no charge density in the medium or the velocity is zero, then there is no readback signal.

A single step transition with a moving center $\overline{x} = vt$ is expressed as

$$M_x(x-\overline{x}) = \begin{cases} -M_r & \text{for } x < \overline{x} \\ M_r & \text{for } x > \overline{x} \end{cases} \tag{2.14}$$

where M_r is the remanence magnetisation of the medium. Then

$$\frac{\partial M_x(x-\overline{x})}{\partial \overline{x}} = -\frac{\partial M_x(x-\overline{x})}{\partial x} = -2M_r\delta(x-\overline{x}) \tag{2.15}$$

here, $\delta(x-\overline{x})$ refers to the δ-function. Substituting (2.15) into (2.13) after integration gives

$$V_x(\overline{x}) = 2\mu_0 v W M_r \delta_m \frac{H_x(\overline{x}, d)}{i_w} \tag{2.16}$$

This means that the readback signal of a thin magnetic medium with a single infinitesimal transition is in the shape of the head field profile at the medium. For this reason, the head field expression is often called head sensitivity function.

When considering multiple transitions, linear superposition applies as long as the transitions are not written too closely. Then, the readback voltage from a sequence of magnetic transitions is given by the sum of the single pulses corresponding to the individual magnetic trasitions. That is

$$V(x) = \sum_n (-1)^n V_{pulse}(x - x_n) \tag{2.17}$$

where x_n is the center of the nth individual magnetic transition, $(-1)^n$ represents the alternating polarity of the magnetic transitions, and V_{pulse} represents an individual single pulse.

The voltage waveform of a modified nonreturn-to-zero (NRZI) current pattern is shown in Figure 2.3. NRZI coding means that a bit "1" corresponds to a write current change, while a bit "0" corresponds to no change. The write current is either positive or negative but never zero. As seen in Figure 2.3, actual magnetisation transitions and voltage pulses are not ideal step functions. Quite the opposite, they are softened as a result of the finite time that takes for the magnetisation to reach its orientation.

It can be seen from equation (2.16) that the readout signal amplitude and resolution both depend on the head field distribution and transition length.

2.2.3 Writing Process

The writing process of a magnetic transition is shown in Figure 2.5. The DC erased magnetic medium is moving to the right relative to the recording head. The current initially magnetises the medium to the right. At the moment the current switches direction, the head field direction switches to the left. The head field rise time is actually finite but assumed to be zero here. The section of the magnetic medium enclosed by the write field is in this way magnetised to the left, a magnetic transition is formed at the right edge of the write bubble. As the medium moves to the right, the write field stays with the head gap, and the transition center moves out of the influence of the write field. On the contrary, the transition at the left edge of the write bubble gets erased as the medium moves to the right.

In digital magnetic writing the magnetisation of the medium is more or less saturated by the write field, i.e. any increase of the write current will not result in a proportional increase in the magnetisation. This is a basic characteristic of a nonlinear process, and thus the write process in digital magnetic recording is generally nonlinear as opposed to the readback process. In order to reproduce well defined voltage pulses from a magnetic medium, sharp magnetic transitions must be written.

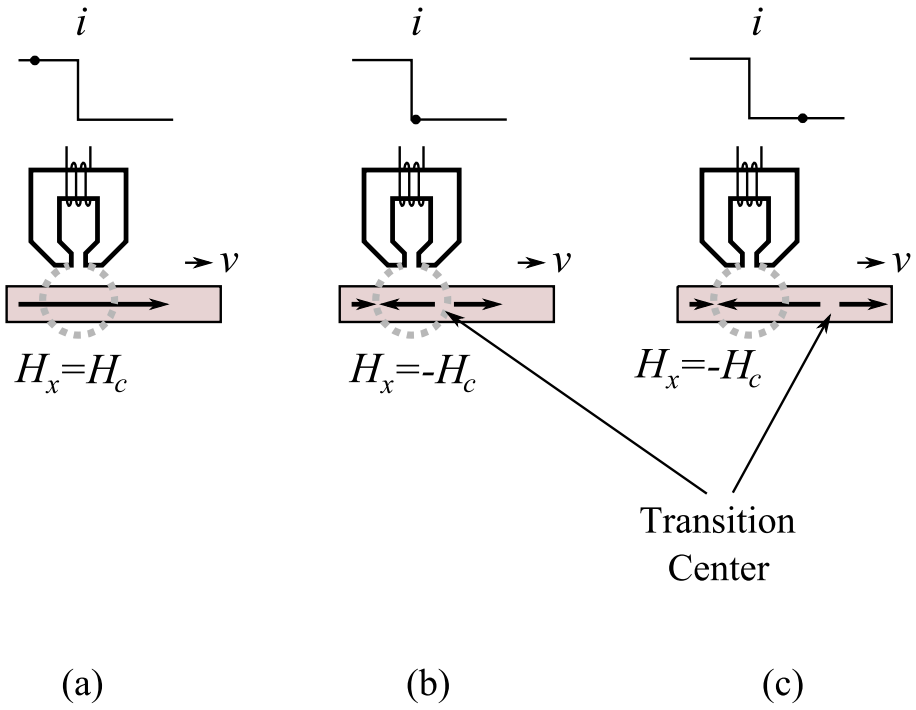

Figure 2.5: Formation of a magnetic transition.

The Williams-Comstock model (Williams and Comstock, 1971) provides an analytical expressions for the digital magnetic write process. In this model, magnetic transitions are presumed to be described by an arctangent function. The magnetisation distribution as a function of the applied field is assumed to be

$$M(H) = \frac{2M_s}{\pi} \arctan\left(\frac{H_{total} + H_c}{H_c} \tan\frac{\pi S}{2}\right) \tag{2.18}$$

where M_s is the saturation magnetisation, H_{total} is the total field, H_c is the coercive field of the medium and $S = M_r/M_s$ is the *remanence squareness*. When recording, the demagnetising field H_d due to the magnetisation of the medium and the applied field or head field H together determine the magnetisation, that is, $H_{total} = H_d + H$. The remanence squareness specifies the shape of the M-H loop, for the particular case of $S = 1$ the shape of the hysteresis loop is rectangular. On the other hand, the

magnetisation distribution as a function of space is assumed to be

$$M(x) = \frac{2M_r}{\pi} \arctan\left(\frac{x - x_0}{a_x}\right) \tag{2.19}$$

where M_r represents the remanence magnetisation, a_x the transition width and x_0 the transition center. The magnetisation gradient, which causes the reply pulse, is given by

$$\frac{\partial M}{\partial x} = \frac{\partial M(H_{total})}{\partial H_{total}} \frac{\partial H_{total}}{\partial x} \tag{2.20}$$

where

$$\frac{\partial H_{total}}{\partial x} = \frac{\partial H}{\partial x} + \frac{\partial H_d}{\partial x} \tag{2.21}$$

Equation (2.20) means that the magnetisation gradient is proportional to the product of the slope of the hysteresis loop and the total field gradient. Hence the requirements for short transition lengths are high total field gradients and rectangular hysteresis loops. At the time of switching the write current, the written transition is still under the influence of the head field. As the transition center moves away from the write bubble, the head field disminishes and only the demagnetising field remains. This results in a *relaxation* of the magnetisation. Figure 2.6 shows the shape of a typical M-H hysteresis loop, the demagnetisation curves after removal of the write field and the demagnetising field as a function of the magnetisation. Note the demagnetising field oposses the magnetisation as expected. In the relaxation process, every point in the magnetic transition moves along one of the dotted curves of Figure 2.6 to reach its final magnetic state. At the transition centre $x = x_0$, the magnetisation and demagnetising field should be both zero. Then, if $x = x_0$ position of the medium is to have zero remanence once the write field is removed, it must be subjected to a field $-H_1$ just slightly below the coercive point $-H_c$ on the hysteresis loop, so that the magnetisation will return to zero as the head field is removed (along the corresponding dotted curve). For very steep hysteresis loops $S \simeq 1$, H_1 is approximately H_c.

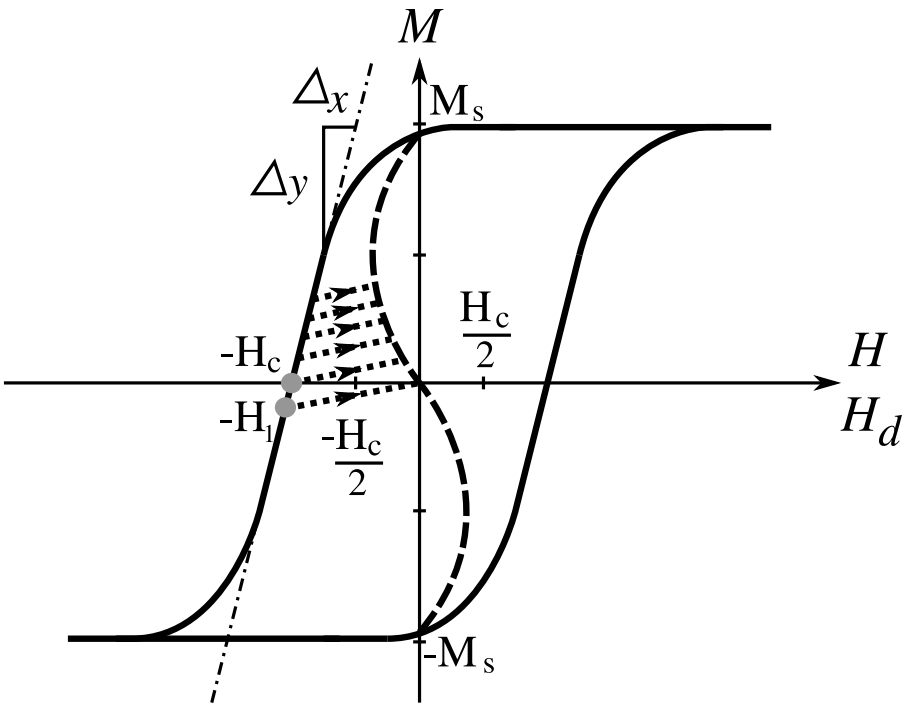

Figure 2.6: Magnetisation relaxation.

The transition length a_x in equation (2.19) can be determined by solving (2.20) at the transition center $x = x_0$. The aim is now to find an expression for each partial derivative in (2.20). As shown in Figure 2.6, the shape of the hysteresis loop near the coercivity can be aproximated by a straight line with slope

$$m = \frac{\Delta y}{\Delta x} = \frac{M_r}{H_c(1 - S^*)} \tag{2.22}$$

where S^* is the coercive squareness which is related to the slope at the coercive point and must not be confused with the remanence squareness S. Thus the slope of the hysteresis loop near the coercive point is

$$\frac{\partial M}{\partial H} = \frac{M_r}{H_c(1 - S^*)} \tag{2.23}$$

By taking the derivative of (2.19) with respect to x at the transition center, the mag-

netisation gradient is

$$\left.\frac{\partial M}{\partial x}\right|_{x=x_0} = \frac{2M_r}{\pi}\left.\frac{a_x}{a_x^2+(x-x_0)^2}\right|_{x=x_0} = \frac{2M_r}{\pi a_x} \tag{2.24}$$

The head field H can be described as the field generated in a Karlqvist head (see Section 2.4.2). Then its longitudinal component is determined by

$$H_x = \frac{H_g}{\pi}\left[\tan^{-1}\left(\frac{x+g/2}{y}\right) - \tan^{-1}\left(\frac{x-g/2}{y}\right)\right] \tag{2.25}$$

The head field must be evaluated at the centre of the magnetic medium, that means that y is the distance from the head pole tip to the center of the magnetic medium, $y = d + \delta_m/2$, where d is the flying height and δ_m is the thickness of the medium. The head field gradient at the transition centre $x = x_0$ is then

$$\left.\frac{\partial H_x}{\partial x}\right|_{x=x_0} = \frac{H_g}{\pi y}\left[\frac{1}{1+\left((x_0+g/2)/y\right)^2} - \frac{1}{1+\left((x_0-g/2)/y\right)^2}\right] \tag{2.26}$$

by defining Q as

$$Q = \frac{H_g}{\pi H_c}\left[\frac{y^2}{y^2+(x_0+g/2)^2} - \frac{y^2}{y^2+(x_0-g/2)^2}\right] \tag{2.27}$$

it is possible to rewrite (2.26) as

$$\left.\frac{\partial H_x}{\partial x}\right|_{x=x_0} = \frac{H_c Q}{y} \tag{2.28}$$

The demagnetising field along the center of the medium is (see Appendix A)

$$H_d(x) = -\frac{2M_r}{\pi}\left[\tan^{-1}\left(\frac{x-x_0}{a_x}\right) - \tan^{-1}\left(\frac{x-x_0}{a_x+\delta_m/2}\right)\right] \tag{2.29}$$

Therefore, the demagnetising field gradient at the transition center is

$$\left.\frac{\partial H_d}{\partial x}\right|_{x=x_0} = -\frac{2Mr}{\pi}\left[\frac{1}{a_x} - \frac{1}{a_x+\delta_m/2}\right] = -\frac{M_r\delta_m}{\pi}\frac{1}{a_x\left(a_x+\delta_m/2\right)} \tag{2.30}$$

Note that at the transition centre, the demagnetising field is zero, but its gradient is nonzero.

Now, substitution of (2.23), (2.24), (2.28) and (2.30) into (2.20) and (2.21) and asuming a thin medium, $\delta_m << a_x$, gives

$$\frac{2M_r}{\pi a_x} = \frac{M_r}{H_c(1-S^*)}\left[\frac{H_cQ}{y} - \frac{M_r\delta_m}{\pi a_x^2}\right] \tag{2.31}$$

Multiplying both sides by a_x^2 and rearranging the equation, it is possible to write

$$a_x^2 - \frac{2(1-S^*)y}{\pi Q}a_x - \frac{M_r\delta_m y}{\pi H_c Q} = 0 \tag{2.32}$$

which is a quadratic equation of a_x with positive solution

$$a_x = \frac{(1-S^*)y}{\pi Q} + \sqrt{\left[\frac{(1-S^*)y}{\pi Q}\right]^2 + \frac{M_r\delta_m y}{\pi H_c Q}} \tag{2.33}$$

where $y = d + \delta_m/2$. In the special case of a square M-H hysteresis loop, $S^* = 1$, equation (2.33) becomes

$$a_x = \sqrt{\frac{M_r\delta_m y}{\pi H_c Q}} \tag{2.34}$$

In general, $S^* \simeq 1$ thus a_x can be approximated to (2.34). To achieve high linear density, the transition length parameter a_x must be reduced as much as possible. This implies large medium coercivity H_c, small $M_r\delta_m$ product, small flying height d such that $y = d + \delta_m/2$ is small, and large coercive squareness S^*.

From equations (2.20) and (2.34), the final length of the recorded transition is determined by the recording head field gradient. Therefore higher field gradients are needed to record shorter transitions and therefore increase the linear density of the system.

2.3 Thin-Film Recording Heads

Figure 2.7 shows the typical internal configuration of a thin-film head. The drawing to the left represents the cross section through the center of the head (i.e. x-y plane or side view). This section is expanded to show detail from the poles to the center

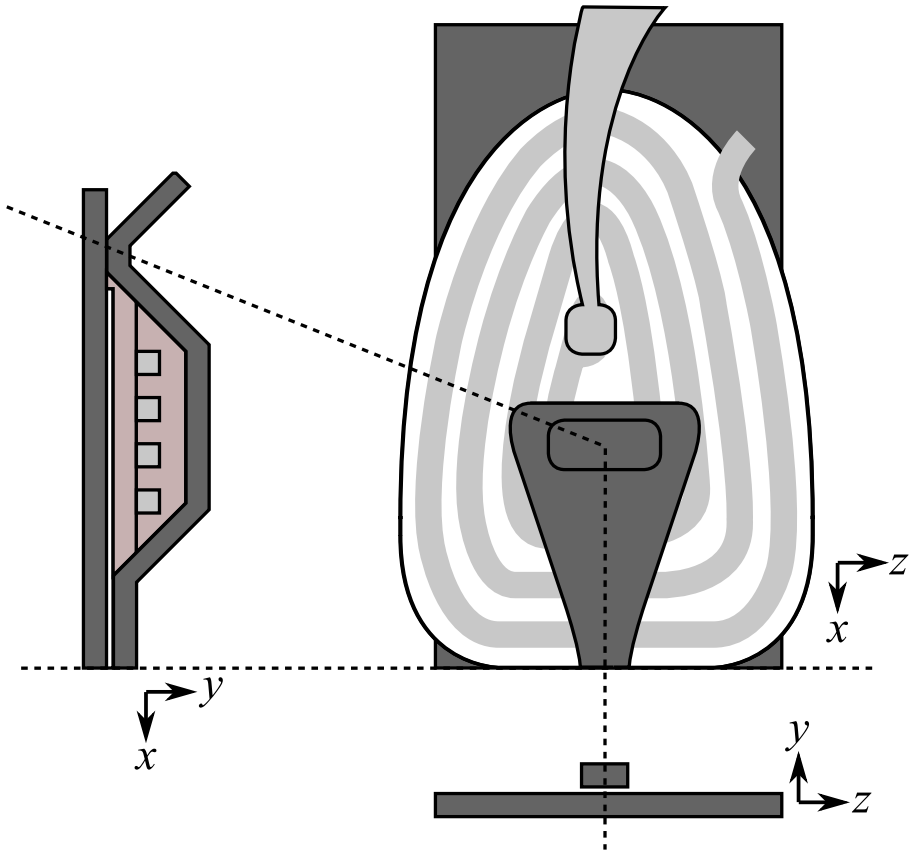

Figure 2.7: Top view of a typical thin-film head. The diagram to the left shows the cross section through the dashed line. The diagram to the bottom represents the front view of the head poles.

of the coils as shown by the dashed lines. In the top view of the head (x-z plane) it is possible to observe complete coil turns whereas the end view (y-z plane) shows the pole tip detail. The heads are fabricated in consecutive steps in which thin layers of material are deposited over a base or substrate. These steps will be briefly discussed next.

2.3.1 Fabrication

The substrate is the material where the different head material layers are deposited. It is typically a disk wafer aproximately 2.5mm thick and 12cm in diameter (R. E. Jones, 1980). The different layers are built up one at a time on the surface of this wafer as shown in Figure 1.8 from top to bottom. After all film depositions, the wafer is sliced up into many heads. On a single wafer, between 3000 and 6000 heads can be produced.

Each head is mounted to a special device called a head slider or just slider. The function of the slider is to physically support the head and hold it in the correct position as the recording medium moves underneath the head. The slider is suspended over the surface of the disk at the end of the head suspension arm. The head arm is mechanically fused into a single structure that is moved around the surface of the disk by the actuator (see Figure 2.1).

The first film to be deposited on the substrate is a thin film of alumina to provide a smooth surface for further processing and insulation of the heads from the conductive slider body. The next layer to be deposited is the lower film which forms one of the two pole tips at the air bearing surface. The inslulating gap layer is deposited on top of the lower film. A hole in this insulation layer is made near the coil center to allow physical contact between the lower and upper films and make a complete yoke. Subsequent layers of insulation must also provide a hole for this purpose. Another insulation layer is deposited on top of the gap layer prior to the coil deposition. Then

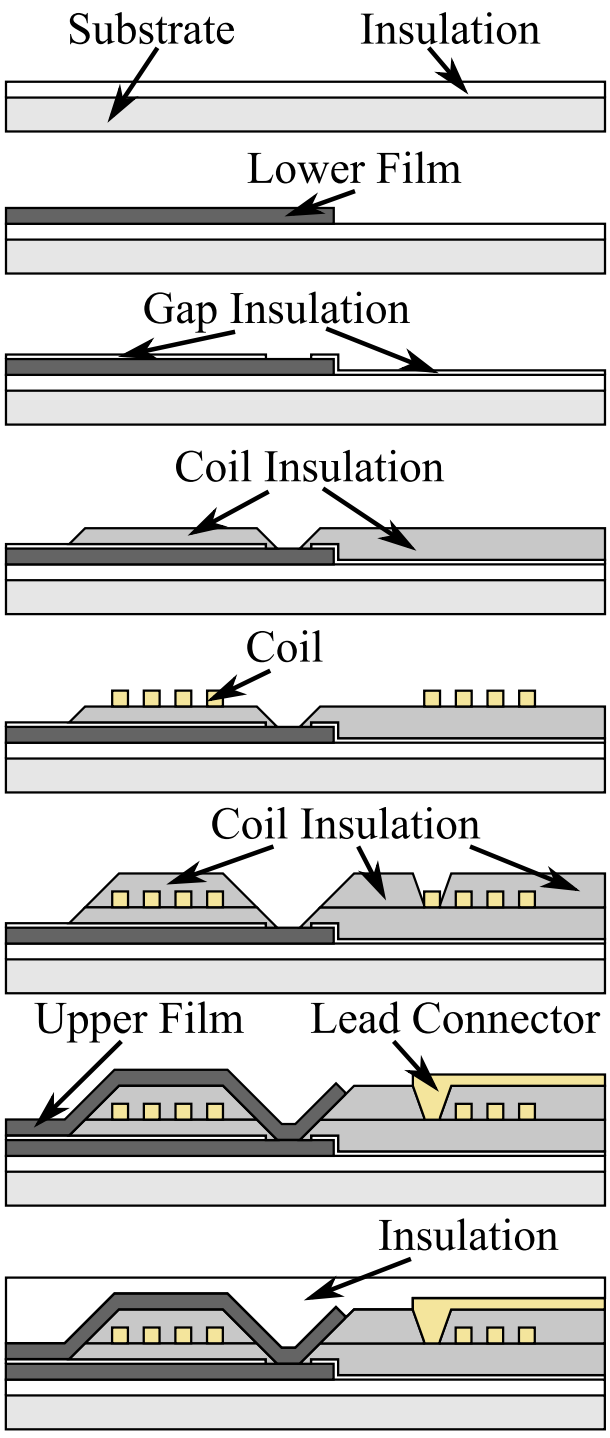

Figure 2.8: Thin-film head's fabrication process.

the coil is lithographically patterned. A second insulating layer is deposited to provide insulation between the coil and the upper thin film. A hole in this second insu- lating layer allows connection of the center of the coil to the coil lead. The deposition of the upper thin film is next. The second pole tip at the air bearing surface is formed by this layer. The overpass lead that provides electrical connection to the coil fol- lows. And finally, a covering layer of alumina is deposited to provide protection to the sensitive film layer from chemical or mechanical attack during further processing (e.g. slicing to separate individual sliders, soldering of leads, mounting on the suspension arm, etc.).

2.3.2 Head Materials

Different head materials are classified according to their magnetic, electrical and mechanical properties. Table 2.1 sumarises the definition of magnetic, electrical and mechanical properties generally used to characterise the materials of thin-film heads.

The magnetic layers of thin-film heads are generally made of a Ni-Fe alloy with approximately 80% Ni and 20% Fe. The typical parameters of a $Ni_{80}Fe_{20}$ alloy are shown in Table 2.2.

In fabricating the conductor sections of the heads the most commonly used material is Copper, characterised by a relative permittivity ϵ_r of 4.8 and a conductivity σ of 5.8×10^7 $1/\Omega$m.

The most frequently used insulation and gap materials in film heads are SiO_2, SiO and Al_2O_3. Although all three show non-magnetic behavior, Al_2O_3 may be preferred because it has the highest thermal expansion coefficient of the three, hence will have smaller thermally induced stresses (Wang and Taratorin, 1999).

Finally, film heads must be deposited on a substrate which must exhibit good wear characteristics. Ferrite materials have been typically used as substrate materials due

Table 2.1: List of notation for different mateial properties. A complete review of materials used in thin films can be found on Chapter 4, Mee and Daniel (1990).

Symbol	*Name*	*Definition*
ϵ	*Permittivity*	*Phisical quantity that describes how an electric field affects and is affected by a dielectric medium*
μ	*Permeability*	*Ratio of the magnetic induction B to the field H*
B_s	*Saturation induction*	*Indicates the maximum flux density which can be obtained in the head poles*
H_c	*Coercivity*	*Field necessary to reverse the magnetisation and decrease the magnetisation induction to zero*
B_r	*Remanent magnetic induction*	*Magnetic induction with zero applied field it controls the residual field when writing has ceased*
σ	*Electrical conductivity*	*It influences the high frequency performance of the heads due to the existence of eddy currents (shielding)*
α	*Damping coefficient*	*Describes a phenomenon associated with spin resonance which dictates the ability of magnetic materials to follow applied fields*
H_k	*Anisotropy field*	*Gives a natural measure of the strength of the anisotropy effect and the torque necessary to take the magnetisation away from the easy axis*
T_{Curie}	*Curie temperature*	*Because of the head heating it is desirable to have materials with high Curie temperature*
	hardness	*characteristic of a solid material expressing its resistance to permanent deformation*
	wear	*erosion of material from a solid surface by the action of another substance*

Table 2.2: Typical parameters of a $Ni_{80}Fe_{20}$ alloy (Wang and Taratorin, 1999).

Anisotropy field	H_k	200 to 400 A/m
Saturation induction	B_s	$\simeq$ 10 Tesla
Low frequency permeability	μ_r	2000 to 4000
Electrical conductivity	σ	5.6×10^6 $1/\Omega$m
Damping constant	α	0.01 to 0.1

to its characteristic hardness and durability.

2.4 Characterisation of Recording Heads

2.4.1 Losses in Magnetic Materials

Understanding the loss mechanisms in magnetic materials is of practical importance in order to characterise the heads. The losses in magnetic materials can be divided in three main categories: hysteresis loss, dielectric loss and relaxation loss. These three types of losses will be discussed next.

Hysteresis Loss

Figure 2.9 represent the relationship between the applied magnetic field strength H and the magnetisation M in a magnetic material. This is an example of non-linear response, when plotting the relationship for increasing levels of field strength, the magnetisation will follow a curve up to a point where further increases in magnetic field strength will result in no further change in the magnetisation. This condition is called magnetic saturation M_s. If the magnetic field is now reduced linearly, the magnetisation will follow a different curve back towards zero field strength at which point it will be offset from the initial magnetisation curve by an amount called the remanent

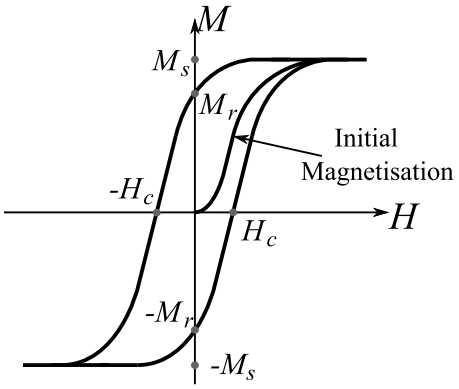

Figure 2.9: Typical hysteresis loop.

magnetisation M_r. If this relationship is plotted for all strengths of applied magnetic field the hysteresis loop of Figure 2.9 results where the points of zero magnetisation occur at the coercive field of the material H_c and points with zero applied field are offset $2M_r$. The coercivity is defined as the intensity of the applied magnetic field required to reduce the magnetisation of a given magnetic material to zero after the magnetisation of the sample has been driven to saturation.

Every change in the magnetisation involves an energy transfer which can be defined as

$$\Delta\mathcal{E} = W - Q \tag{2.35}$$

where W represents the work of magnetic force on realignment of the magnetisation with the applied field strength, and Q represents the dissipated heat in the material. The work in a magnetic material whose magnetisation changes from M_1 to M_2 under the effect of an external field $\mathbf{H}$ is defined as

$$W = \int_{M_1}^{M_2} \mathbf{H} d\mathbf{M} \tag{2.36}$$

In going around the hysteresis loop of Figure 2.9 the total work is

$$W = \int_{-M_s}^{-M_r} \mathbf{H_1} d\mathbf{M} + \int_{-M_r}^{M_s} \mathbf{H_1} d\mathbf{M} + \int_{M_s}^{M_r} \mathbf{H_2} d\mathbf{M} + \int_{M_r}^{-M_s} \mathbf{H_2} d\mathbf{M} \tag{2.37}$$

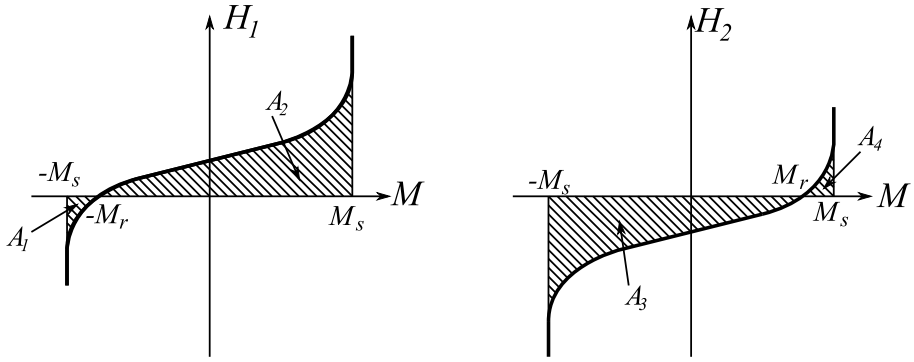

Figure 2.10: Rearrangement of the hysteresis loop in order to compute the hysteresis loss.

where $\mathbf{H_1}$ represent the right curve of the hysteresis loop and $\mathbf{H_2}$ represents the left curve of the hysteresis loop. In order to compute the integrals of the right hand side of (2.37), the hysteresis loop has been redrawn in Figure 2.10. Equation (2.37) can be rewritten as

$$W = \int_{-M_s}^{-M_r} \mathbf{H_1} d\mathbf{M} + \int_{-M_r}^{M_s} \mathbf{H_1} d\mathbf{M} - \int_{-M_s}^{M_r} \mathbf{H_2} d\mathbf{M} - \int_{M_r}^{M_s} \mathbf{H_2} d\mathbf{M} \tag{2.38}$$

The integrals in (2.38) correspond to the areas A_1, A_2, A_3 and A_4 of Figure 2.10 respectively. Thus, the total work equals the equivalent area of the hysteresis loop. Now, by applying the conservation of energy principle $\Delta\mathcal{E} = 0$ to (2.35) results in a dissipated heat in the material equal to the area of the hysteresis loop. This energy dissipation is known as hysteresis loss.

Dielectric Loss

The second kind of loss comes from the shielding effect due to eddy currents in lossy materials. A time varying magnetic field $\mathbf{H}$ produces an electric field $\mathbf{E}$. According to Maxwell's curl equation for the electric field this is

$$\nabla \times \mathbf{E} = -\mu \frac{\partial \mathbf{H}}{\partial t} \tag{2.39}$$

This field results in a current density **J** given by Ohm's law

$$\mathbf{J} = \sigma \mathbf{E} \tag{2.40}$$

These eddy currents must be taken into account in Maxwell's curl equation for the magnetic field as

$$\nabla \times \mathbf{H} = \sigma \mathbf{E} + \epsilon \frac{\partial \mathbf{E}}{\partial t} \tag{2.41}$$

Equations (2.39) and (2.41) are first order, coupled differential equations. That is, both the unknown fields **E** and **H** appear in each equation. Uncoupling these equations to obtain the wave equation gives

$$\nabla^2 \breve{\mathbf{E}} = j\omega\mu\sigma\breve{\mathbf{E}} - \omega^2\mu\epsilon\breve{\mathbf{E}} = \gamma^2\breve{\mathbf{E}} \tag{2.42}$$

$$\nabla^2 \breve{\mathbf{H}} = j\omega\mu\sigma\breve{\mathbf{H}} - \omega^2\mu\epsilon\breve{\mathbf{H}} = \gamma^2\breve{\mathbf{H}} \tag{2.43}$$

Where $\breve{\mathbf{E}}$ and $\breve{\mathbf{H}}$ represent the electric and magnetic fields in the frequency domain. Equations (2.42) and (2.43) are the wave equations for the electric and magnetic fields in a source-free lossy material. The propagation constant γ is a parameter of the traveling wave defined as

$$\gamma = \alpha + j\beta = \sqrt{j\omega\mu\sigma - \omega^2\mu\epsilon} = \sqrt{j\omega\mu(\sigma + j\omega\epsilon)} \tag{2.44}$$

Here, the propagation and atenuation constants are represented as γ and α respectively in agreement with the general convention. It must be said that throughout this thesis while not talking about propagation of electromagnetic waves α represents the damping coefficient of the rotational motion of the magnetisation and γ represents the gyromagnetic ratio.

Taking the square of (2.44) gives

$$\alpha^2 - \beta^2 = -\omega^2\mu\epsilon \tag{2.45}$$

$$2\alpha\beta = \omega\mu\sigma \tag{2.46}$$

Substituting the value of α from (2.46) into (2.45) gives

$$\alpha^2 - \left(\frac{\omega\mu\sigma}{2\alpha}\right)^2 = -\omega^2\mu\epsilon \tag{2.47}$$

or

$$4\left(\alpha^2\right)^2 + 4\omega^2\mu\epsilon\alpha^2 - (\omega\mu\sigma)^2 = 0 \tag{2.48}$$

which is a quadratic equation for α^2. The attenuation constant α is then given by

$$\alpha = \omega\sqrt{\mu\epsilon}\left(\frac{1}{2}\left[\sqrt{1+\left(\frac{\sigma}{\omega\epsilon}\right)^2} - 1\right]\right)^{\frac{1}{2}} \tag{2.49}$$

where the signs of the square roots have been chosen to describe a traveling wave in the z direction that concurrently decays.

Similarly, it is possible to obtain an expression for the phase constant β as

$$\beta = \omega\sqrt{\mu\epsilon}\left(\frac{1}{2}\left[\sqrt{1+\left(\frac{\sigma}{\omega\epsilon}\right)^2} + 1\right]\right)^{\frac{1}{2}} \tag{2.50}$$

Assuming a uniform plane wave traveling in a lossy medium across the z direction, its electric and magnetic field take the form

$$E_z = E_0 e^{-\gamma z} = E_0 e^{-\alpha z} e^{-j\beta z} \tag{2.51}$$

$$H_y = H_0 e^{-\gamma z} = H_0 e^{-\alpha z} e^{-j\beta z} \tag{2.52}$$

Equations (2.51) and (2.52) show that the magnitudes of the electric and magnetic fields decay exponentially with the traveled distance. At a particular distance, denoted as the skin depth δ, the traveling wave reduces its value to $e^{-1} = 0.37$, as shown in Figure 2.11. That is

$$\delta = \frac{1}{\alpha} = \frac{1}{\omega\sqrt{\mu\epsilon}\left(1/2\left[\sqrt{1+(\sigma/\omega\epsilon)^2} - 1\right]\right)^{\frac{1}{2}}} \tag{2.53}$$

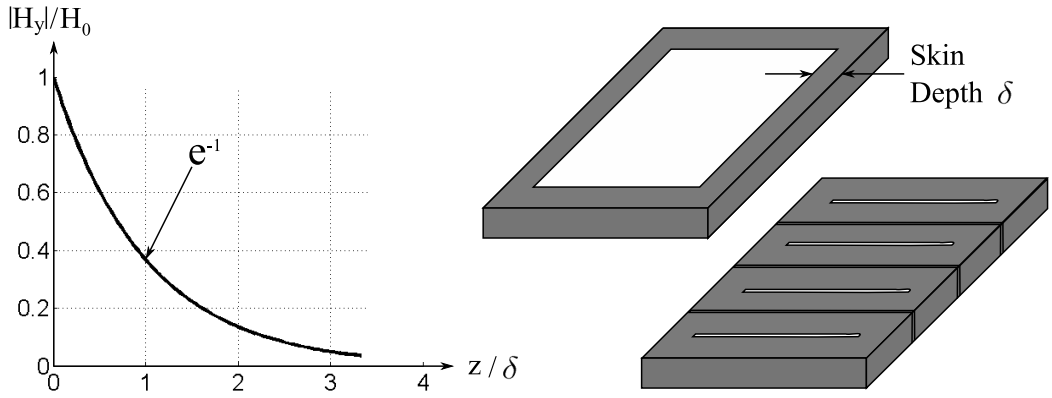

Figure 2.11: Shielding effect due to eddy currents.

When the lossy material considered is a good conductor, $(\sigma/\omega\epsilon)^2 >> 1$, the skin depth reduces to

$$\delta = \sqrt{\frac{2}{\omega\mu\sigma}} \tag{2.54}$$

The appearance of eddy currents in magnetic heads implies a reduction in the flux-carrying capacity of the core. When the eddy currents are strong enough, that is from the time derivative of (2.39) with increasing frequency, no magnetic field penetrates to the center section of the material. Then, the flux will be concentrated in the edges of the core as shown in Figure 2.11 affecting the performance of the head. The effective area through which the flux passes may be increased by dividing the core into laminations of thicknesses equal to twice the skin depth at the frequency of interest as shown in Figure 2.11. Another effect of eddy currents is that the rate of change of $\mathbf{B}$ (hence $\mathbf{H}$ and $\mathbf{M}$) produces a circulating eletric field or currents inside the yoke. These currents produce an opposing field which dampens the switching of fields iside the head.

If an electric current, such as an eddy current, passes through a resistive material, electrical energy is converted to heat. The amount of electrical energy due to an

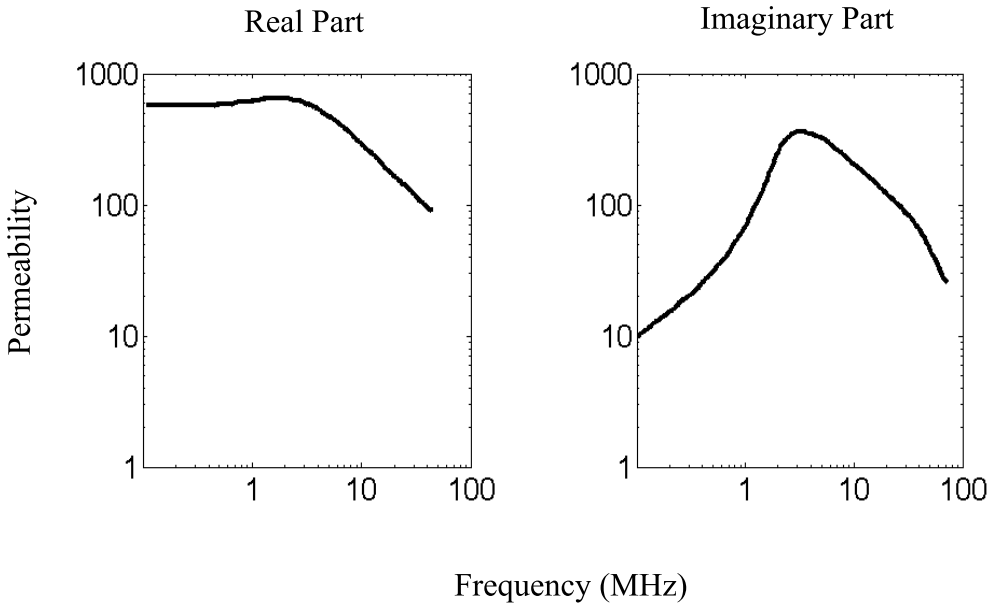

Figure 2.12: Complex permeability of a typical permalloy (White, 1984).

electrical current can be expressed as

$$\mathcal{E} = Pt \tag{2.55}$$

where P is the power in watts and t is the time in seconds. The power dissipated by the eddy currents can be calculated as the integral of the power over the volume of the core

$$P = \int_{V_{core}} \mathbf{JE} dV_{core} \tag{2.56}$$

where $\mathbf{J}$ and $\mathbf{E}$ are calculated using (2.39) and (2.40) respectively.

The effects of eddy currents may be described by a complex permeability with a frequency dependence similar to that shown in Figure 2.12. At low frequencies, the real part of the permeability μ' is constant and much bigger than the imaginary part μ'' so the permeability $\mu = \mu' - j\mu''$ is mostly real. At a certain frequency f_{max}, at which the skin depth equals the lamination thickness, the real part μ' falls with increases in frequency making the imaginary part μ'' become more important. For frequencies below

f_{max}, the skin depth is greater than the lamination thickness so the total core area is available for the flux. At higher frequencies, the flux is carried by a smaller equivalent area which is equivalent to having the total core area with a smaller permeability. The complex nature of the permeability allows to account for the losses.

Relaxation Loss

The third type of loss is related to the precessional motion of the magnetisation. When a field is applied to a magnetic material, the magnetisation precesses until it is aligned with the direction of the field. This precession is described by the equation of motion (Gilbert, 1955)

$$\frac{\partial \mathbf{M}}{\partial t} = -\gamma(\mathbf{M} \times \mathbf{H}) + \frac{\alpha}{M_s}\left(\mathbf{M} \times \frac{\partial \mathbf{M}}{\partial t}\right) \tag{2.57}$$

As will be seen in section 3.3.2, in solving the equation of motion, a characteristic time τ, known as the relaxation time, is involved, and hence, the name relaxation loss.

It has been observed that magnetic materials are divided into magnetic domains where the orientation of the magnetisation is practically uniform. In between adjacent domains the magnetisation rotates from one orientation to the other forming domain boundaries or domain walls as shown in Figure 2.13. When a magnetic field is applied, the alignment of the magnetisation happens in two different ways: domain wall motion and domain rotation. When an external field is applied to antiparallel domains, like domains A and B in Figure 2.13, if the direction of the field is parallel to the magnetisation of the domains, the domains with favorable orientation will grow, by displacement of the wall, at the expense of other domains unfavorably oriented. The orientation of the magnetisation near the favorable domain aligns with the field first, that is, the arrows denoted m_1, m_2 and m_3 will be the first to orientate themselves with the applied field, with a precessional motion ruled by (2.57) and shown in Figure 2.13 by m_4. As soon as one arrow moves, all other arrows in the wall must rearrange themselves to

maintain the wall condition. This corresponds to a movement of the wall as a whole, in a direction perpendicular to the field, such as to increase the volume of the favorable domain. Domain rotation happens when there is no reason for one domain to grow at expenses of other with antiparallel magnetisation, it is the case of domains C and D with respect to A. Here, the magnetisation has to proceed by rotation only, ruled again by (2.57) and shown in Figure 2.13 by m_4, gradually coming into alignment with the applied field until the domain wall disappears.

It has been observed experimentally that both these processes occur. In fact, domain wall motion is the process which requires least magnetic energy and is the first to occur as the applied field is increased from zero (Anderson, 1968). At small applied fields the domain walls move through small distances and return to their original positions on removal of the field, this is known as reversible domain wall motion. For larger applied fields, the domain walls are found to jump discontinuously through larger distances and do not return to their original position on removal of the field, that is irreversible domain wall motion. When all the unfavorable domains have disappeared, the remaining non aligned domains orient themselves by domain rotation only until saturation is reached.

It has been shown experimentally that domain wall motion and domain rotation correspond to slow and fast processes respectively, (Jorgersen, 1995). For an isotropic material whose properties are independent of direction, the typical domain configuration of the pole tip of a magnetic thin-film head is that shown in Figure 2.14(a) where the central wall will move from one side to the other during flux reversals, these flux reversals are dominated by a slow process, domain wall motion. If an anisotropic material is considered, the typical domain configuration is shown in Figure 2.14(b) and the magnetisation reversals take place through domain rotation, which is a fast process. The research carried out in this thesis is to study these processes along with their time scales, and their influence on the switching speed of magnetic heads.

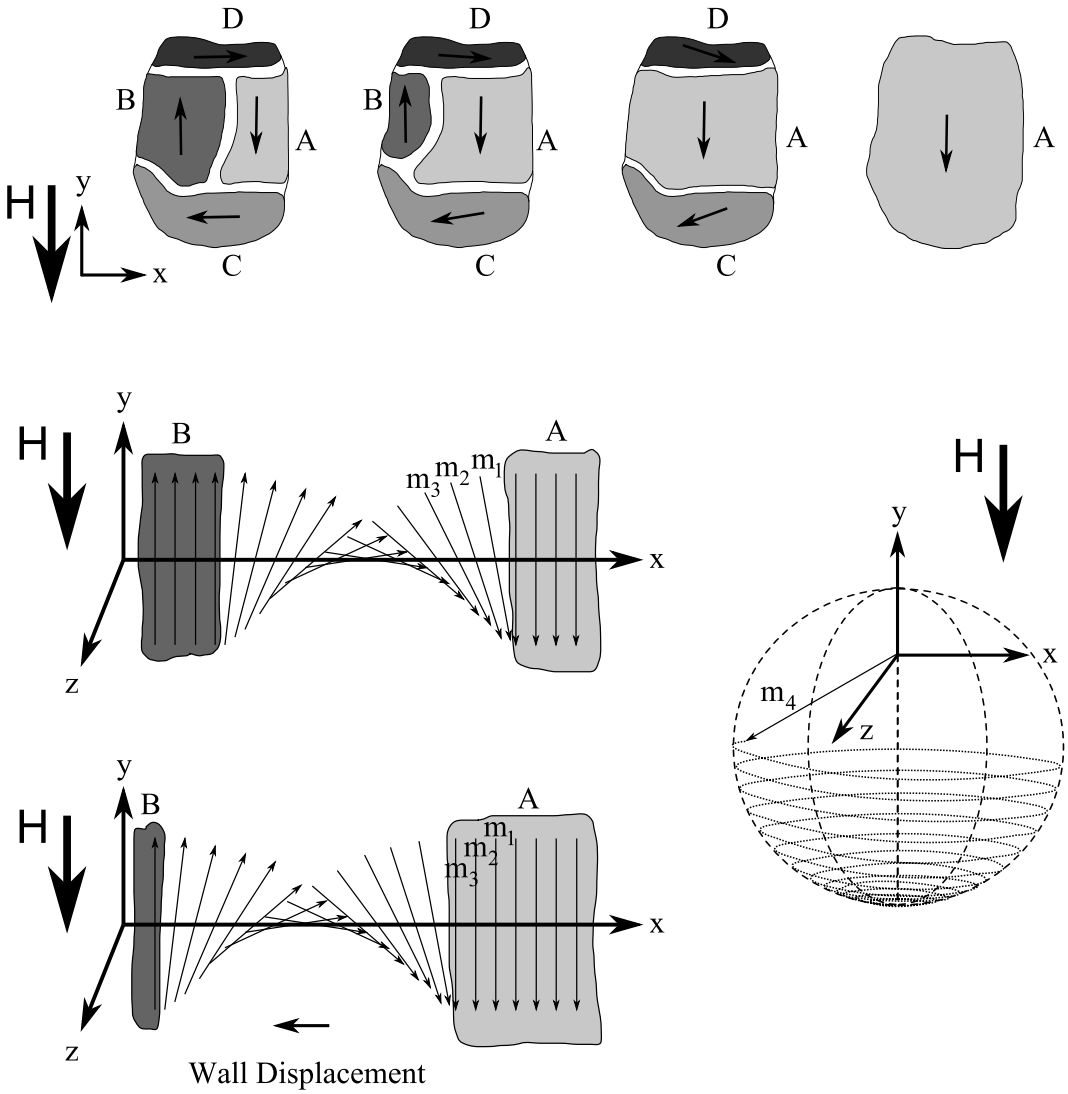

Figure 2.13: Saturation of a magnetic material by domain wall motion and domain rotation.

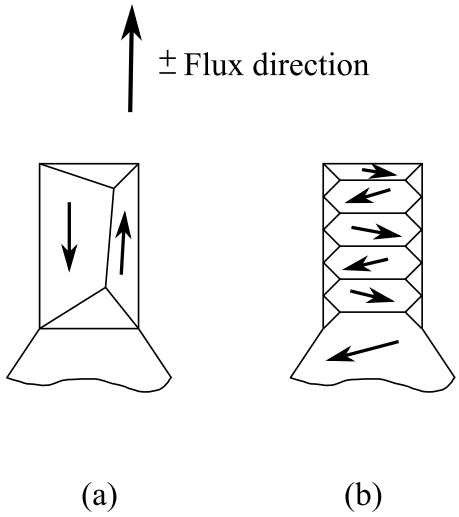

Figure 2.14: Domain configuration for isotropic and anisotropic materials.

From the equation of motion (2.57), the power dissipated by the orientation of the magnetisation is

$$P = \int_V \mathbf{H} \left(\frac{\partial \mathbf{M}}{\partial t} \right) dV \tag{2.58}$$

which applies for both domain wall motion and domain rotation.

2.4.2 Head Models

The purpose of this section is to review several methods for characterising magnetic heads. The inductance and efficiency of the heads are directly related to the permability of the magnetic film that the head is made of and therefore they reflect any magnetic losses in the core material. The methods studied here to characterise the head's inductance and efficiency will be used in Chapter 6.

Solving magnetic field problems is in general a difficult task that involves solving differential equations with their respective initial conditions. The application of circuit theory to solving magnetic field problems simplifies the complexity of the calculations.

Magnetic devices may be considered as magnetic circuits. The magnetomotive force (mmf) is the work that would be required to carry a hypothetical isolated magnetic pole of unit strength completely around a magnetic circuit. It can also be seen as the force associated with a magnetic field and that produces magnetic flux. The standard definition of magnetomotive force involves current passing through an electrical conductor. The unit of magnetomotive force is the ampere-turn. Figure 2.15 represents an coil wound around a head core material. When the coil is excited by an electric current magnetic flux is generated through the closed path of the core. By applying Ampere's law, the mmf in the coil is mathematically expressed as the line integral of the field around the closed path

$$\oint \mathbf{H} d\mathbf{l} = H_{core} l_c + H_g l_g = NI \tag{2.59}$$

and therefore it is possible to separate the mmf in the coil and the mmf in the gap regions of a ferrite head.

Magnetic reluctance is defined by analogy to the concept of resistance in an electrical circuit as the ratio of the magnetomotive force (mmf) in a passive magnetic circuit and the magnetic flux in this circuit. In terms of material properties, the reluctance of a magnetic circuit can be expressed as

$$\mathcal{R} = \frac{l}{\mu_0 \mu_r A} \tag{2.60}$$

where l is the length of the circuit in metres, μ_0 is the permeability of free space, μ_r is the relative magnetic permeability of the material and A is the cross-sectional area of the circuit in square metres.

Thanks to the analogy between electric and magnetic circuits, electric circuit laws can be applied to solve magnetic circuits. In the electric domain, a circuit is defined by an electric voltage source, a current and a resistance whereas in the magnetic domain a circuit is defined by a magnetic source, a magnetic flux and a reluctance. In this

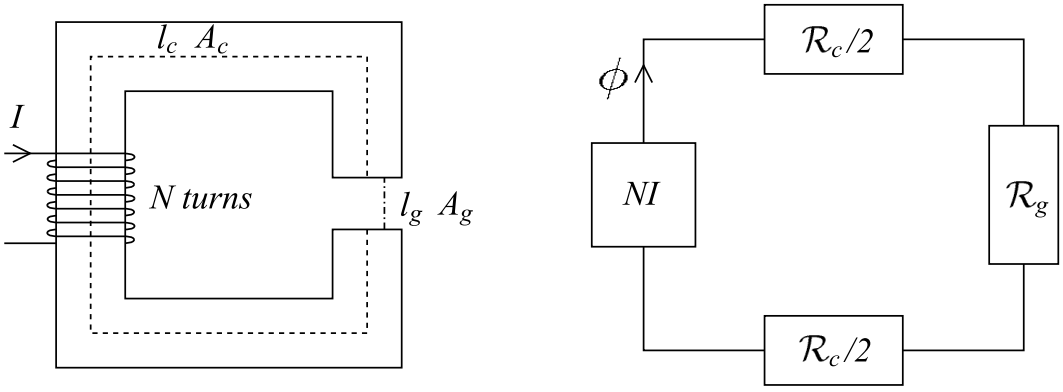

Figure 2.15: Equivalent magnetic circuit of a ferrite head. The subscripts c and g refer to head core and the head gap respectively.

manner, for example, it is possible to define the equivalent magnetic circuit of a ferrite head as the sum of reluctances $\mathcal{R}_c/2$, $\mathcal{R}_c/2$ and $\mathcal{R}_g$ in Figure 2.15 connected to the magnetic source NI which links a magnetic flux ϕ through the circuit.

The flux flowing through the magnetic circuit is given by

$$\phi = \frac{NI}{\mathcal{R}_c/2 + \mathcal{R}_g + \mathcal{R}_c/2} = \frac{NI}{\mathcal{R}_c + \mathcal{R}_g} \tag{2.61}$$

where the reluctances $\mathcal{R}_c$ and $\mathcal{R}_g$ are given by

$$\mathcal{R}_c = \frac{l_c}{\mu_0 \mu_r A_c} \tag{2.62}$$

and

$$\mathcal{R}_g = \frac{l_g}{\mu_0 A_g} \tag{2.63}$$

here, l_c, l_g, A_c and A_g represent the core and gap lengths and the core and gap cross sectional areas respectively.

Due to magnetic losses, the magnetomotive force (mmf) in the gap is less than the magnetomotive force applied in the coil. The ratio of the mmf in the gap to that in coil is a quantity η known as the head efficiency. That is

$$\eta = \frac{H_g l_g}{NI} \tag{2.64}$$

Considering the cross section of the core and the gap to be uniform and of values A_c and A_g, the flux through the magnetic circuit can be expressed as

$$\phi = \mu_0 \mu_r H_{core} A_c = \mu_0 H_g A_g \tag{2.65}$$

then, solving (2.65) for H_{core} and H_g and substituting in (2.59) and (2.64) gives

$$\eta = \frac{l_g/\mu_0 A_g}{l_g/\mu_0 A_g + l_c/\mu_r \mu_0 A_c} \tag{2.66}$$

or in terms of the core and gap reluctances (2.62) and (2.63)

$$\eta = \frac{\mathcal{R}_g}{\mathcal{R}_g + \mathcal{R}_c} \tag{2.67}$$

Clearly, the reluctance of the core effectively divides the magnetomotive force created by the current in the turns, so only a fraction η of the magneto motive force appears between the pole tips of the head. This fraction can approach unity only as the product of permeability and magnetic cross section approaches infinity, or as the magnetic path length approaches zero.

The head inductance, which is important in characterising the head frequency response, can also be derived from magnetic circuit models. The inductance is defined as the ratio of the magnetic flux linkage to the current through the coil, that is

$$L = \frac{N\phi}{I} \tag{2.68}$$

Again, substituting the values of H_{core} and H_g from (2.65) in (2.59) and solving for ϕ gives

$$\phi = \frac{NI}{l_g/\mu_0 A_g + l_c/\mu_r \mu_0 A_c} \tag{2.69}$$

Now substituting (2.68) in (2.69) leads to

$$L = \frac{N^2}{l_g/\mu_0 A_g + l_c/\mu_r \mu_0 A_c} = \frac{N^2}{\mathcal{R}_g + \mathcal{R}_c} \tag{2.70}$$

Equations (2.66) and (2.70) show that the efficiency and inductance of a magnetic head are functions of the permeability of the magnetic material and therefore they reflect the magnetic losses that occur in the head core.

2.5 Organisation of Thesis

A comprehensive introductory chapter to discuss possible approaches to the problem set was given in Chapter 1. This is supported by a comprehensive literature survey of alternative approaches that details the strengths and limitations of different methods and arguments the final choice followed.

A general introduction to magnetic recording focused on hard disk drives and their basic performance was given in this chapter. The reading and recording processes were described first. Then, the fabrication process of thin-film heads was explained. This introduction chapter concluded with the characterisation of recording heads including a study of the losses and several methods for magnetic head modelling.

Chapter 3 will focus on the general electromagnetic theory and the micromagnetic models which form the basis behind the numerical work in this research. The former is centered around Maxwell's equations and the electric and magnetic properties of matter whereas the latter is a general description of the micromagnetic model from its atomic origins to the actual equation of motion that was used to model magnetic materials in Chapter 5.

The FDTD algorithm is described in detail in Chapter 4, from its basic formulation to numerical dispersion and the stablishment of stability conditions. Reflections into the main computational space are then studied to develop a perfectly matched layer boundary condition to absorb outgoing waves for the experiments in Chapter 5 with satisfactory results. This chapter also analyses in detail the extension of the classical FDTD method to model magnetic materials. This includes important implementation issues and studies of the stability requirement of the extended scheme.

Code has been written in Matlab to fully implement both the standard and the extended FDTD algorithms. The preformance of the developed code has been tested

over a number of test cases in Chapter 5. Then linear and non-linear simulations of an actual head structure are demonstrated.

The experiments in Chapter 6 start with a study of the physical dimensions of two commercial thin-film heads using the SEM. The chapter continues with derivations of equivalent circuit models that best describe the impedance of thin-film heads including the relaxation effects of the domain wall motion and the rotational magnetisation. By fitting these models to measured impedance spectra, information about the time scales of these relaxation processes will be presented.

The main text of this thesis concludes with a discussion in Chapter 7 where the background theory is summarised and the research aims are reviewed. The limitations of the numerical simulations leave open future lines of research which are described at the end of this chapter.

Chapter 3

Theory

3.1 Introduction

Prior to analysing magnetic recording in depth heads it is necessary to review the theory involved in the performance of such devices. In particular the electromagnetic theroy of Maxwell's equations which provide the relationship between the electric and magnetic fields in a medium; and the theory of micromagnetics which gives an explanation of the magnetic behaviour of matter in the presence of fields. These theories will be used in the numerical implementation and experimental work carried out in this thesis.

The organisation of this chapter is as follows. First the basic concepts of the electrical and magnetic properties of matter will be reviewed in detail. Dielectric, magnetic and conducting materials will be studied with the corresponding definition of polarisation, permittivity, magnetisation, permeability, currents and conductivity. Maxwell's equations and the corresponding electromagnetic wave propagation will be described. Then the micromagnetic model will be analysed, from its origin in the atomic model and the angular momentum of the electrons to the actual equation of motion of the magnetisation and the effective field that generates its rotation.

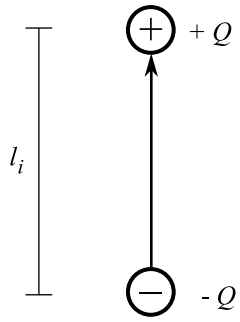

Figure 3.1: Formation of a dipole between two opposite charges of equal magnitude Q

3.2 General Electromagnetic Theory

3.2.1 Electrical Properties of Matter

Dielectric Materials, Polarisation and Permittivity

Dielectrics or *insulators* are materials whose dominant charges in atoms and molecules are held in place by atomic and molecular forces, and they are not free to travel. Thus ideal dielectrics do not contain any free charges (such as in conductors).

For dielectrics, the formation of electric dipoles is usually referred to as *orientational polarisation*. The effect of this polarisation can be represented by a dipole (see Figure 3.1) with a dipole moment $d\mathbf{p}_i$ given by

$$d\mathbf{p}_i = Ql_i \tag{3.1}$$

where Q is the magnitude of each of the negative and positive charges whose centers are displaced by distance l_i.

The total electric dipole moment of a given material is obtained by summing the dipole moments for all the orientational polarisation dipoles represented by the Bohr atomic model. For a volume ΔV where there are N_e electric dipoles per unit volume, or a

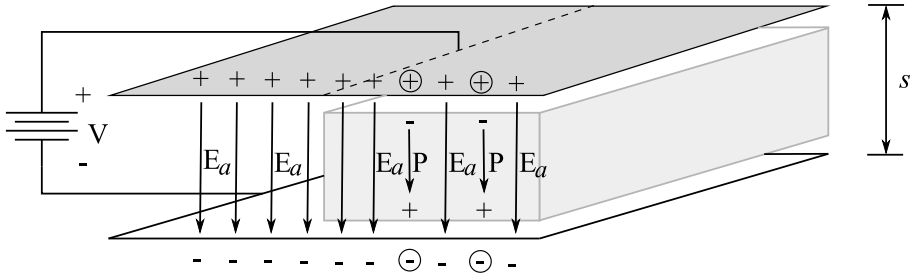

Figure 3.2: Dielectric salb connected to an applied electric field **E**

total of $N_e \Delta V$ electric dipoles, the total electric dipole moment is

$$\mathbf{p}_t = \sum_{i=1}^{N_e \Delta V} d\mathbf{p}i \tag{3.2}$$

The *electric polarisation vector* **P** can then be defined as the *dipole moment per unit volume*, or

$$\mathbf{P} = \lim_{\Delta V \to 0} \left[\frac{1}{\Delta V} \mathbf{p}_t \right] \tag{3.3}$$

The units of **P** are coulombs per square meter (C/m^2) which is representative of a surface charge density.

For dielectrics, the interaction between the polarisation dipoles and an applied electromagnetic field provides the material with the ability to store electric energy. Figure 3.2 shows a DC voltage source connected across two parallel plates separated by distance *s*. The charges on the dielectric material align themselves with the applied field forming electric dipoles. The polarisation vector **P** gives rise to the surface charge density found on the upper and lower surface of the dielectric slab as shown in Figure 3.2.

Whereas the applied electric field **E** maintains its value, the electric flux density **D** inside the dielectric material differs from what would exist where the dielectric material is replaced by free space. The electric flux density **D** inside the dielectric material can

be expressed as

$$\mathbf{D} = \epsilon_0 \mathbf{E} + \mathbf{P} \tag{3.4}$$

where ϵ_0 is a constant known as the *permittivity of free space*, $\mathbf{E}$ is the applied electric field, and $\mathbf{P}$ is polarisation vector given by equation (3.3).

The electric flux denstity $\mathbf{D}$ of (3.4) can also be related to the applied electric field intensity $\mathbf{E}$ by a parameter designated as ϵ, with units of farads per meter (F/m), such that

$$\mathbf{D} = \epsilon \mathbf{E} \tag{3.5}$$

As the polarisation vector $\mathbf{P}$ is in the same direction as the applied field $\mathbf{E}$, it can be expressed in terms of $\mathbf{E}$ as

$$\mathbf{P} = P \frac{\mathbf{E}}{E} \tag{3.6}$$

or

$$\mathbf{P} = \epsilon_0 \chi_e \mathbf{E} \tag{3.7}$$

where

$$\chi_e = \frac{P}{\epsilon_0 E} \tag{3.8}$$

The parameter χ is known as the dimensionless quantity *electric susceptibility*.

Substituting (3.7) into (3.4) and using (3.5) it is possible to write

$$\mathbf{D} = \epsilon_0 \mathbf{E} + \epsilon_0 \chi_e \mathbf{E} = \epsilon_0 (1 + \chi_e) \mathbf{E} = \epsilon \mathbf{E} \tag{3.9}$$

Therefore

$$\epsilon = \epsilon_0 (1 + \chi_e) \tag{3.10}$$

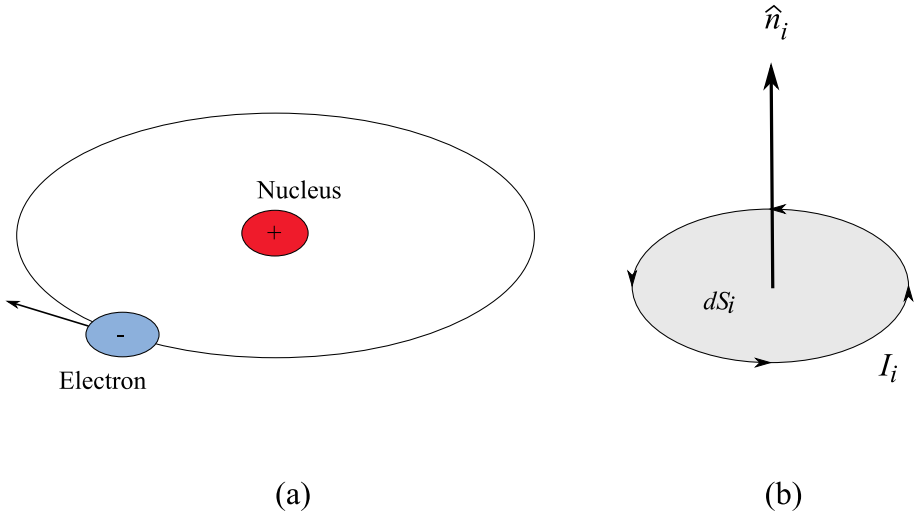

Figure 3.3: Atomic model to represent magnetic materials (a) orbiting electron and (b) equivalent electric loop

The parameter ϵ is called the *static permittivity* of the medium. It is common to express the permittivity of a medium in terms of its relative value to that of free space as

$$\epsilon_r = \frac{\epsilon}{\epsilon_0} = 1 + \chi_e \tag{3.11}$$

which is refered to as the *relative permittivity*.

Magnetic Materials, Magnetisation and Permeability

Magnetic materials are those that exhibit magnetic polarisation when they are subjected to an applied magnetic field. The magnetisation phenomenon is represented by the alignment of the magnetic dipoles of the material with the applied magnetic field and is similar to the alignment of the electric dipoles of the dielectric material with the applied electric field.

The behaviour of a magnetic material can be predicted by using simple atomic models to represent the atomic lattice structure of the material like the one shown in Figure 3.3(a). Each orbiting electron can be modeled by an equivalent small electric current

loop of area ds whose current flows in the direction oppostite to the electron orbit, as shown in Figure 3.3(b). The fields produced by a small loop of electric current at large distances are the same as those produced by a linear bar magnet (magnetic dipole) of length d.

By referring to the equivalent loop model of Figure 3.3(b), the angular momentum associated with an orbiting electron can be represented by a magnetic dipole moment $d\mathbf{m}_i$ such that

$$d\mathbf{m}_i = I_i d\mathbf{S}_i = \hat{\mathbf{n}}_i I_i dS_i \tag{3.12}$$

For atoms that possess many orbiting electrons, the total magnetic dipole moment $\mathbf{m}_t$ is equal to the sum of all the individual magnetic dipole moments $d\mathbf{m}_i$ represented by (3.12). For a volume ΔV where there are N_m obiting electrons (equivalent loops) per unit volume, the total magnetic dipole moment is

$$\mathbf{m}_t = \sum_{i=1}^{N_m \Delta V} d\mathbf{m}_i \tag{3.13}$$

A magnetic polarisation (magnetisation) vector $\mathbf{M}$ is then defined as

$$\mathbf{M} = \lim_{\Delta V \to 0} \left[\frac{1}{\Delta V} \mathbf{m}_t \right] \tag{3.14}$$

The magnetisation vector $\mathbf{M}$ resulting from the realignment of the magnetic dipoles is better illustrated by considering a slab of magnetic material with a magnetic field $\mathbf{B}_a$ applied across it, as shown in Figure 3.4. Ideally, on a microscopic scale, for most magnetic material all the magnetic dipoles will align themselves so that their individual magnetic moments point in the direction of the applied field. However, this depends on the magnitude of the field for each application. Taking as an example the storage layer of a magnetic disk the magnetic dipoles would not align with the field unless the applied field was very large. In the limit, as the number of magnetic dipoles and

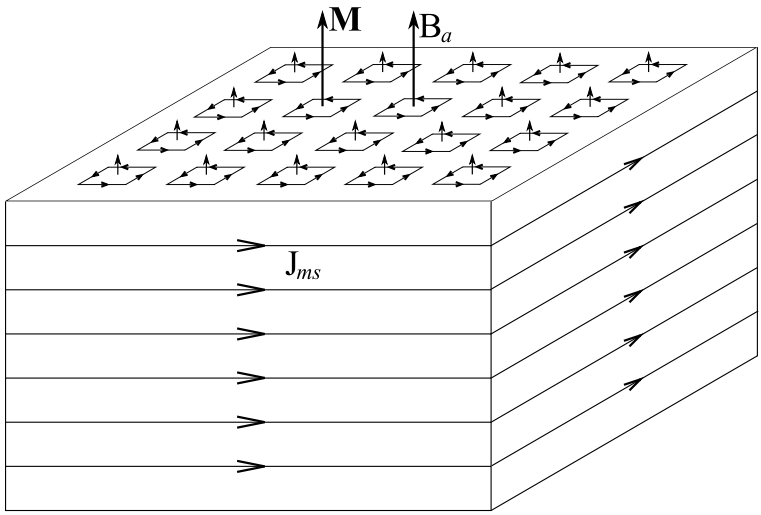

Figure 3.4: Magnetic slab subjected to an applied magnetic field

their corresponding equivalent electric loops become very large, the currents of the loops found in the interior parts of the slab are cancelled by those of the neighboring loops (opposite circled current arrows shown on Figure 3.4). On a macroscopic scale a net nonzero equivalent magnetic current, resulting in an equivalent magnetic current surface density, is found on the exterior surface of the slab. This equivalent magneitc current density $\mathbf{J}_{ms}$ is responsible for the introduction of the magnetisation vector in the direction of $\mathbf{B}$.

The magnetic flux density across the slab is increased by the presence of $\mathbf{M}$ so that the net magnetic flux density at any interior point of the slab is given by

$$\mathbf{B} = \mu_0(\mathbf{H} + \mathbf{M}) \tag{3.15}$$

where μ_0 is a constant known as the *permeability of free space*, $\mathbf{H}$ is the applied magnetic field, and $\mathbf{M}$ is given by equation (3.14).

The magnetic flux denstity $\mathbf{B}$ can also be related to the applied magnetic field intensity $\mathbf{H}$ by a parameter designated as μ, with units Henries per meter (H/m), such that

$$\mathbf{B} = \mu\mathbf{H} \tag{3.16}$$

Comparing (3.15) and (3.16) indicates that $\mathbf{M}$ is also related to $\mathbf{H}$ by

$$\mathbf{M} = \chi_m \mathbf{H} \tag{3.17}$$

where χ_m is a dimensionless quantity called the *magnetic susceptibility*.

Substituting (3.17) into (3.15) and using (3.16) it is possible to write

$$\mathbf{B} = \mu_0(\mathbf{H} + \chi_m \mathbf{H}) = \mu_0(1 + \chi_m)\mathbf{H} = \mu \mathbf{H} \tag{3.18}$$

Therefore

$$\mu = \mu_0(1 + \chi_m) \tag{3.19}$$

The parameter μ is called the *static permeability* of the medium. It is common to express the permability of a medium in terms of its relative value to that of free space as

$$\mu_r = \frac{\mu}{\mu_0} = 1 + \chi_m \tag{3.20}$$

which is refered to as the *relative permeability*.

Conductive Materials, Currents and Conductivity

The current through a given cross sectional area is defined as the electric charge passing through the area per unit time, that is

$$\Delta I = \lim_{\Delta t \to 0} \left[\frac{\Delta Q}{\Delta t} \right] \tag{3.21}$$

It is useful to define the current density J as the current per unit area such that

$$J = \frac{\Delta I}{\Delta S} \tag{3.22}$$

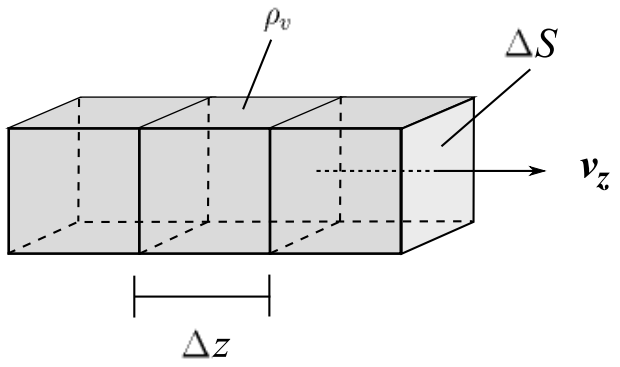

Figure 3.5: Current in a filament

Now consider the filament of Figure 3.5. If there is a flow of charge, of volume density ρ_v, at a velocity $\mathbf{v} = v_z\hat{\mathbf{z}}$, from (3.21), the current through the filament is

$$\Delta I = \lim_{\Delta t \to 0}\left[\frac{\Delta Q}{\Delta t}\right] = \lim_{\Delta t \to 0}\left[\rho_v \Delta S \frac{\Delta z}{\Delta t}\right] = \rho_v \Delta S v_z \tag{3.23}$$

Hence in general using (3.22) for every J component it can be said that

$$\mathbf{J} = \rho_v \mathbf{v} \tag{3.24}$$

In (3.24) $\mathbf{J}$ is defined as *convection current density* in Amperes per square meter (A/m^2). Convection current, as distinct from conduction current, does not involve conductors and consequently does not satisfy Ohm's law (3.30). It occurs when a current flows through an insulating medium such as liquid, rarefied gas, or vacumm.

Conduction currents require a conductor. A conductor is characterised by a large amount of free electrons that provide conduction current as consequence of an applied electric field. When an electric field $\mathbf{E}$ is applied, the force on an electron with charge $-e$ is

$$\mathbf{F} = -e\mathbf{E} \tag{3.25}$$

Since the electron is not in free space, it suffers constant collision with the atomic lattice and drifts from one atom to another. If the electron with mass m is moving in an electric field $\mathbf{E}$ with an average drift velocity $\mathbf{v}$, according to Newton's law, the average change in momentum of the free electron must match the applied force. Thus

$$\frac{m\mathbf{v}}{\tau} = -e\mathbf{E} \tag{3.26}$$

or

$$\mathbf{v} = -\frac{e\tau}{m}\mathbf{E} \tag{3.27}$$

where τ is the average time interval between collisions. This indicates that the drift velocity of the electron is directly proportional to the applied field. If there are n electrons per unit volume, the electronic charge density is given by

$$\rho_v = -ne \tag{3.28}$$

Thus the *conduction current density* is

$$\mathbf{J} = \rho_v\mathbf{v} = \frac{ne^2\tau}{m}\mathbf{E} \tag{3.29}$$

or

$$\mathbf{J} = \sigma\mathbf{E} \tag{3.30}$$

where $\sigma = ne^2\tau/m$ is known as the *conductivity* of the conductor. The relationship in (3.30) is known as the Ohm's law for conductor materials.

The third type of current denoted as *displacement current* will be explained in detail in section 3.2.2 when talking about Maxwell's equations.

A conductor has abundance of charge that is free to move. Consider an isolated conductor, such as shown in Figure 3.6(a). When an external electric field $\mathbf{E}_e$ is applied, the positive free charges are pushed along the same direction as the applied field, while

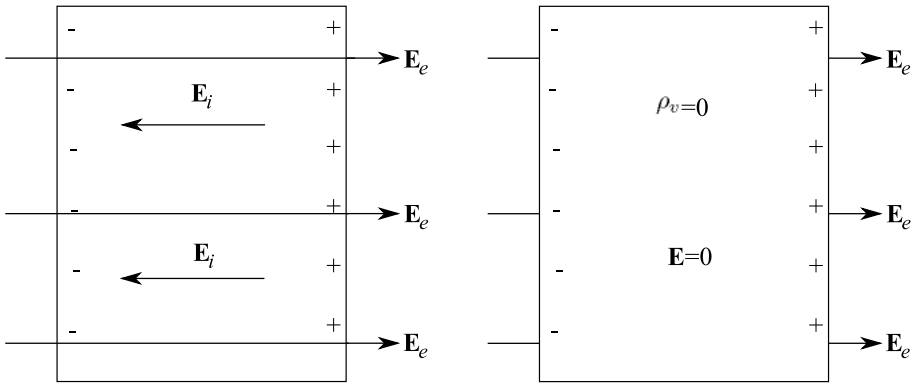

Figure 3.6: (a)An isolated conductor under the influence of an applied field and (b) a conductor has zero electric field under static conditions

the negative free charges move in the opposite direction. This charge migration takes place very quickly. The free charges do two things. First, they accumulate on the surface of the conductor and form an *induced surface charge*. Second, the induced charges set up an internal induced field $\mathbf{E}_i$, which cancels the externally applied field $\mathbf{E}_e$ inside the conductor. The result is illustrated in Figure 3.6(b). This leads to an important property of a conductor, a perfect conductor cannot contain an electrostatic field within it.

Linear, Homogeneous, Isotropic and Non-dispersive Media

The electrical behaviour of materials when they are subjected to electromagnetic fields is characterised by their constitutive parameters (ϵ, μ and σ).

Materials whose constitutive parameters are not functions of the applied field are usually known as *linear*, otherwise they are considered as *nonlinear*. In practise, many material exhibit almost linear characteristics as long as the applied fields are within certain ranges. Beyond those points, the material may exhibit a high degree of nonlinearity.

When the constitutive parameters of media are not functions of position, the materials are called *homogeneous*, otherwise they are *nonhomogeneous*. Almost all materials exhibit some degree of nonhomogeneity. However for most materials used in practise the nonhomogeneity is so small that the materials are threated as being purely homogeneous.

Anisotropic materials are those whose constitutive parameters are a function of the direction of the applied field, otherwise they are known as *Isotropic*. Many materials, especially crystals, exhibit a rather high degree of anisotropy. For such materials, the permittivities and susceptibilities can not be represented as a single value. Instead, they have to be represented as 3×3 tensor matrices.

If the constitutive parameters of a material vary as a function of frequency, they are denoted as being *dispersive*, otherwise they are *nondispersive*. All materials used in practise display some form of dispersion. The permittivities and conductivities, especially of dielectric materials, and the permeabilities of ferromagnetic materials and ferrites exhibit rather pronounced dispersive characteristics.

3.2.2 Maxwell's Equations

Gauss's Law

Gauss's law states that the total electric flux through any closed surface is equal to the total charge enclosed by that surface as shown in Figure 3.7(a).

$$\oint_S \mathbf{D} \cdot d\mathbf{S} = \int_v \rho_v dv = Q_{enc} \tag{3.31}$$

By applying the divergence theorem (Sadiku, 2001) to the left hand side of equation (3.31) yields

$$\oint_S \mathbf{D} \cdot d\mathbf{S} = Q_{enc} = \int_v \nabla \cdot \mathbf{D} dv \tag{3.32}$$

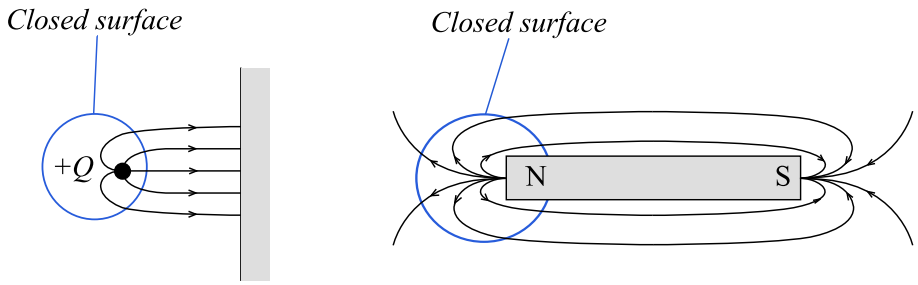

(a) (b)

Figure 3.7: Flux lines due to: (a) isolated electric charge and (b)magnetic charge

comparing the two volume integrals in equations (3.31) and (3.32) results in

$$\rho_v = \nabla \cdot \mathbf{D} \tag{3.33}$$

which is the differential form of Gauss's law.

Conservation of Magnetic Flux

The magnetic flux through a surface S is given by

$$\Psi = \int_S \mathbf{B} d\mathbf{S} \tag{3.34}$$

The magnetic flux line is the path to which $\mathbf{B}$ is tangential at every point. Magnetic flux lines always close upong themselves as in figure 3.7(b). This is due to the fact that it is not possible to have isolated magnetic poles (or magnetic charges). Therefore the total flux through a closed surface in a magnetic field must be zero.

$$\oint \mathbf{B} \cdot d\mathbf{S} = 0 \tag{3.35}$$

This equation is refered to as the law of conservation of magnetic flux. Again, by applying the divergence theorem to equation (3.35) gives

$$\oint_S \mathbf{B} \cdot d\mathbf{S} = \int_v \nabla \cdot \mathbf{B} dv = 0 \tag{3.36}$$

therefore

$$\nabla \cdot \mathbf{B} = 0 \tag{3.37}$$

which is the differential form of (3.35).

Faraday's Law

The induced electromotive force in any closed circuit is equal to the time rate of change of the magnetic flux linked by the circuit. Expressed mathematically as

$$\oint_L \mathbf{E} \cdot d\mathbf{l} = -\frac{d}{dt} \int_S \mathbf{B} \cdot d\mathbf{S} \tag{3.38}$$

where the negative sign shows that the induced voltage acts in such a way as to create a current in the closed path opposing the flux producing it. Applying Stoke's theorem to equation (3.38) gives

$$\int_S (\nabla \times \mathbf{E}) \cdot d\mathbf{S} = -\int_S \frac{\partial \mathbf{B}}{\partial t} \cdot d\mathbf{S} \tag{3.39}$$

Then

$$\nabla \times \mathbf{E} = -\frac{\partial \mathbf{B}}{\partial t} \tag{3.40}$$

Equation (3.40) shows that the time varying $\mathbf{E}$ field is not conservative ($\nabla \times \mathbf{E} \neq 0$).

Displacement Current

Ampere's circuit law states that the line integral of the tangential component of $\mathbf{H}$ around a closed path is the same as the net current I_{enc} enclosed by the path.

$$\oint \mathbf{H} \cdot d\mathbf{l} = I_{enc} \tag{3.41}$$

By applying Stoke's theorem to the left hand side of equation (3.41)

$$\int_S (\nabla \times \mathbf{H}) \cdot d\mathbf{S} = I_{enc} \tag{3.42}$$

where

$$I_{enc} = \int_S \mathbf{J} \cdot d\mathbf{S} \tag{3.43}$$

Comparing the surface integrals in equations (3.41) and (3.43) clearly reveals that

$$\nabla \times \mathbf{H} = \mathbf{J} \tag{3.44}$$

However the divergence of the curl of any vector field is equal to zero. Hence,

$$\nabla \cdot (\nabla \times \mathbf{H}) = 0 = \nabla \cdot \mathbf{J} \tag{3.45}$$

The continuity of current equation is given by

$$\nabla \cdot \mathbf{J} = -\frac{\partial \rho_v}{\partial t} \tag{3.46}$$

which differs from zero when varying currents are considered. Thus equation (3.44) must be modified to agree with (3.46). A new term must be added so that it becomes

$$\nabla \times \mathbf{H} = \mathbf{J} + \mathbf{J_d} \tag{3.47}$$

where $\mathbf{J_d}$ is defined such that

$$\nabla \cdot \mathbf{J} + \nabla \cdot \mathbf{J_d} = 0 \tag{3.48}$$

thus,

$$\nabla \cdot \mathbf{J_d} = -\nabla \cdot \mathbf{J} = \frac{\partial \rho_v}{\partial t} = \frac{\partial}{\partial t}(\nabla \cdot \mathbf{D}) = \nabla \cdot \frac{\partial \mathbf{D}}{\partial t} \tag{3.49}$$

or

$$\mathbf{J_d} = \frac{\partial \mathbf{D}}{\partial t} \tag{3.50}$$

rewriting (3.44)

$$\nabla \times \mathbf{H} = \mathbf{J} + \frac{\partial \mathbf{D}}{\partial t} \tag{3.51}$$

The term $\mathbf{J_d}$ is known as the displacement current density and $\mathbf{J}$ represents the conduction current. The insertion of $\mathbf{J_d}$ into (3.44) was one of the major contributions of Maxwell. Without the term $\mathbf{J_d}$, electromagnetic wave propagation would be impossible.

Final Form of Maxwell's Equations

James Clerk Maxwell is regarded as the founder of electromagnetic theory in its present form. Maxwell's work led to the discovery of electromagnetic waves. Maxwell published the first unified theory of electricity and magnetism (Maxwell, 1873). The theory comprised all previously known results plus the introduction of the displacement current with the prediction of existence of electromagnetic waves. The laws of electromagnetism that Maxwell put together in the form of four equations are shown in the more generalised form, when time varying conditions are considered, in equations (3.52) to (3.55) in their differential and integral forms.

$$\nabla \cdot \mathbf{D} = \rho_v \qquad \oint_S \mathbf{D} \cdot d\mathbf{S} = \int_v \rho_v dv \tag{3.52}$$

$$\nabla \cdot \mathbf{B} = 0 \qquad \oint_S \mathbf{B} \cdot d\mathbf{S} = 0 \tag{3.53}$$

$$\nabla \times \mathbf{E} = -\frac{\partial \mathbf{B}}{\partial t} \qquad \oint_L \mathbf{E} \cdot d\mathbf{L} = -\frac{\partial}{\partial t} \int_S \mathbf{B} \cdot d\mathbf{S} \tag{3.54}$$

$$\nabla \times \mathbf{H} = \mathbf{J} + \frac{\partial \mathbf{D}}{\partial t} \qquad \oint_L \mathbf{H} \cdot d\mathbf{L} = \int_S \left(\mathbf{J} + \frac{\partial \mathbf{D}}{\partial t} \right) \cdot d\mathbf{S} \tag{3.55}$$

Maxwell's equations are complemented by the equation of continuity (3.56) and the constitutive relations (3.57) to (3.59).

$$\nabla \cdot \mathbf{J} = -\frac{\partial \rho_v}{\partial t} \tag{3.56}$$

In a linear, homogeneous, and isotropic medium characterised by σ, ϵ, and μ, the constitutive relations

$$\mathbf{D} = \epsilon \mathbf{E} = \epsilon_0 \mathbf{E} + \mathbf{P} \tag{3.57}$$

$$\mathbf{B} = \mu \mathbf{H} = \mu_0 (\mathbf{H} + \mathbf{M}) \tag{3.58}$$

$$\mathbf{J} = \sigma \mathbf{E} + \frac{\partial \mathbf{D}}{\partial t} \tag{3.59}$$

hold for time varying fields.

The Wave Equation

The two curl equations (3.54) and (3.55) of Maxwell's equations in differential form are first order coupled differential equations. That is, both the unknown fileds **E** and **H** appear in each equation. Usually it is desirable, for convenience in solving for **E** and **H**, to uncouple these equations. This can be accomplished at the expense of increasing the order of the differential equations to second order.

Taking the curl of both sides of equations (3.54) and (3.55) and assuming a homogeneous and source free medium, it can be written

$$\nabla \times \nabla \times \mathbf{E} = -\mu \nabla \times \left(\frac{\partial \mathbf{H}}{\partial t} \right) = -\mu \frac{\partial}{\partial t} (\nabla \times \mathbf{H}) \tag{3.60}$$

$$\nabla \times \nabla \times \mathbf{H} = \nabla \times \left(\mathbf{J} + \frac{\partial \mathbf{D}}{\partial t} \right) = \sigma \nabla \times \mathbf{E} + \epsilon \frac{\partial}{\partial t} (\nabla \times \mathbf{E}) \tag{3.61}$$

Substituting (3.55) into the right hand side of (3.60) and applying the vector identity

$$\nabla \times \nabla \times \mathbf{A} = \nabla (\nabla \cdot \mathbf{A}) - \nabla^2 \mathbf{A} \tag{3.62}$$

to the left hand side, it is possible to rewrite (3.60) as

$$\nabla (\nabla \cdot \mathbf{E}) - \nabla^2 \mathbf{E} = -\mu \sigma \frac{\partial \mathbf{E}}{\partial t} - \mu \epsilon \frac{\partial^2 \mathbf{E}}{\partial t^2} \tag{3.63}$$

For a source free region (ρ_v in (3.52) equals 0)

$$\nabla \cdot \mathbf{D} = \epsilon \nabla \cdot \mathbf{E} = 0 \tag{3.64}$$

consequently the wave equation for the electric field in a source free region reduces to

$$\nabla^2 \mathbf{E} = \mu \sigma \frac{\partial \mathbf{E}}{\partial t} + \mu \epsilon \frac{\partial^2 \mathbf{E}}{\partial t^2} \tag{3.65}$$

In a similar way it is possible to obtain the wave equation for the magnetic field leading to

$$\nabla^2 \mathbf{H} = \mu \sigma \frac{\partial \mathbf{H}}{\partial t} + \mu \epsilon \frac{\partial^2 \mathbf{H}}{\partial t^2} \tag{3.66}$$

For a source free and lossless medium ($\rho_v = 0$ and $\sigma = 0$), the wave equations (3.65) and (3.66) reduce to

$$\nabla^2 \mathbf{E} = \mu\epsilon \frac{\partial^2 \mathbf{E}}{\partial t^2} \tag{3.67}$$

$$\nabla^2 \mathbf{H} = \mu\epsilon \frac{\partial^2 \mathbf{H}}{\partial t^2} \tag{3.68}$$

Asuming time variations of the form $e^{j\omega t}$ and taking Fourier transforms

$$\nabla^2 \breve{\mathbf{E}} = -\omega^2 \mu\epsilon \breve{\mathbf{E}} \tag{3.69}$$

$$\nabla^2 \breve{\mathbf{H}} = -\omega^2 \mu\epsilon \breve{\mathbf{H}} \tag{3.70}$$

Using the expansion of the laplacian ∇^2 in a cartesian coordinate system, (3.69) becomes

$$\frac{\partial^2 \breve{\mathbf{E}}}{\partial x^2} + \frac{\partial^2 \breve{\mathbf{E}}}{\partial y^2} + \frac{\partial^2 \breve{\mathbf{E}}}{\partial z^2} = -\omega^2 \mu\epsilon \breve{\mathbf{E}} \tag{3.71}$$

Since the cartesian coordinate system is orthogonal, (3.71) is separable into its individual component parts so that there is an equivalent differential equation for each of the components of the vector.

$$\frac{\partial^2 E_x}{\partial x^2} + \frac{\partial^2 E_x}{\partial y^2} + \frac{\partial^2 E_x}{\partial z^2} = -\omega^2 \mu\epsilon E_x \tag{3.72}$$

$$\frac{\partial^2 E_y}{\partial x^2} + \frac{\partial^2 E_y}{\partial y^2} + \frac{\partial^2 E_y}{\partial z^2} = -\omega^2 \mu\epsilon E_y \tag{3.73}$$

$$\frac{\partial^2 E_z}{\partial x^2} + \frac{\partial^2 E_z}{\partial y^2} + \frac{\partial^2 E_z}{\partial z^2} = -\omega^2 \mu\epsilon E_z \tag{3.74}$$

Where there is a variation of the field quantities in only one direction, z, then

$$\frac{\partial}{\partial x} = \frac{\partial}{\partial y} = 0 \tag{3.75}$$

and equation (3.71) becomes

$$\frac{\partial^2 \breve{\mathbf{E}}}{\partial z^2} = -\omega^2 \mu\epsilon \breve{\mathbf{E}} \tag{3.76}$$

Equation (3.76) may now be separated into three similar equations involving the three component parts of the electric field. They are

$$\frac{\partial^2 E_x}{\partial z^2} = -\omega^2 \mu \epsilon E_x \tag{3.77}$$

$$\frac{\partial^2 E_y}{\partial z^2} = -\omega^2 \mu \epsilon E_y \tag{3.78}$$

$$\frac{\partial^2 E_z}{\partial z^2} = -\omega^2 \mu \epsilon E_z \tag{3.79}$$

Equation (3.77) is a differential equation which will have a solution of the form

$$E_x = Ae^{-\gamma z} + Be^{\gamma z} \tag{3.80}$$

where

$$\gamma^2 = -\omega^2 \mu \epsilon \tag{3.81}$$

In (3.80), γ is a parameter of the travelling plane wave called the *propagating constant* which in general has real and imaginary parts of the form

$$\gamma = \alpha + j\beta \tag{3.82}$$

where α is called the *attenuation constant* and β the *phase constant*. Here α and γ must not be confused with the damping coefficient and gyromagnetic ratio. Provided that μ and ϵ are both real, the propagation constant has no real part therefore no losses are incurred in the propagating wave

$$\gamma = j\beta \tag{3.83}$$

where

$$\beta = \omega\sqrt{\mu\epsilon} \tag{3.84}$$

However, if there are any losses incurred by the wave as it propagates through the medium, the wave will be attenuated and the propagation constant γ will have real and imaginary parts.

Inspection of equation (3.80) shows that it represents two traveling waves. The first term represents a wave travelling in the positive z direction and the second represents a wave travelling in the opposite direction.

The electromagnetic wave described above is denoted as a plane wave due to the fact that the fields described by it are constant in a plane (in this case, xy) at an instant in time for a wave propagating along an axis normal to the plane (in this case, z).

The above analysis forms the fundamental basis of wave propagation which describes how the electromagnetic fields behave inside magnetic recording heads. This analysis will be used in later chapters when understanding the propagation of electromagnetic waves inside thin-film recording heads, when studying the eddy current shielding effects, when developing absorbing boundary conditions, etc.

3.3 The Micromagnetic Model

3.3.1 Atomic Theory of Magnetism

In the simple picture of an atom the electron is taken to move in a closed orbit about the central nucleus. Since it carries a charge, the electron represents current circulating in a closed loop and it has already been seen that this produces a magnetic dipole moment. Incidentally, such a picture also accounts for the non-existence of a free magnetic pole, since only dipoles are produced even on the atomic scale.

$$m = \int i dS \tag{3.85}$$

The moment of the electron in orbit will be given by equation (3.85) where i is the current equivalent to the circulating electron and the integration gives the total orbital area, (Anderson, 1968). For the simple case of a circular orbit of radius r in which the electron, of charge -e, rotates at a constant angular velocity ω, since the electron

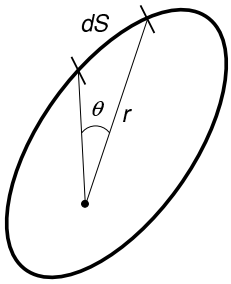

Figure 3.8: Evaluation of the momentum for the general non-circular electron orbit

makes $\omega/2\pi$ revolutions per second the equivalent current $i = -e\omega/2\pi$. The magnetic moment is then given by

$$m = -\frac{e\omega}{2\pi}\pi r^2 = -\frac{1}{2}e\omega r^2 \tag{3.86}$$

The angular momentum of the electron, G, is given by $m_e\omega r^2$, where m_e is the mass of the electron, so that

$$m = -\frac{e}{2m_e}G \tag{3.87}$$

For the more general case of a non-circular orbit the vector d$\mathbf{S}$ must be evaluated which is equal in magnitude to the area it represents and has the direction of the normal to the surface. Considering an orbit as in Figure 3.8, let the area d$\mathbf{S}$ be described by the triangle of which d$\mathbf{S}$ is the base and $\mathbf{r}$ the distance from the reference point. The area of this triangle is $(dS\sin\theta)r/2$ and $(d\mathbf{S}\times\mathbf{r})/2$ represents a vector of magnitude equal to the area in the direction normal to the plane in which it lies. Thus the expression for the magnetic moment can be written as

$$\mathbf{m} = \int \frac{1}{2}i(d\mathbf{S}\times\mathbf{r}) \tag{3.88}$$

The magnitude of the current will be given by $i = dq/dt$ where q is charge, and if it moves with a linear velocity $\mathbf{v}$ then $id\mathbf{S} = (dq/dt)\mathbf{v}dt = dq\mathbf{v}$, thus

$$\mathbf{m} = \frac{1}{2}\int dq(\mathbf{v}\times\mathbf{r}) \tag{3.89}$$

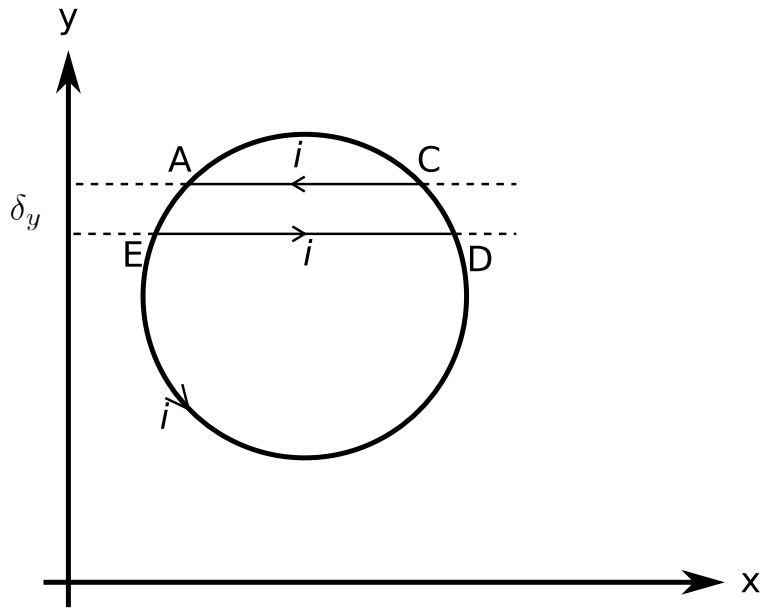

Figure 3.9: Plane coil carrying a current i for illustration of magnetic torque.

But angular momentum of a particle of mass m_e in a orbit is, by definition

$$\mathbf{G} = m_e(\mathbf{v} \times \mathbf{r}) \tag{3.90}$$

and, in the absence of external forces, this is a constant. Thus

$$\mathbf{m} = \frac{\mathbf{G}}{2m_e} \int dq \tag{3.91}$$

i.e.

$$\mathbf{m} = -\frac{e\mathbf{G}}{2m_e} = -\gamma\mathbf{G} \tag{3.92}$$

where $-e$ is the total electronic charge, m_e is the rest mass of the electron and $\gamma = \mu_o e/2m_e$ is known as the *gyromagnetic ratio*.

If a plane coil, carrying a current i, is placed in a region of uniform magnetic flux, $\mathbf{B}$, it will experience a torque whose magnitude depends on the area of the coil, the current, and the component of $\mathbf{B}$ in the plane of the coil. This may be seen by reference to Figure 3.9. Considering the coil to be divided up into strips, parallel to the x-axis,

such as ACDE. The y-axis is taken perpendicular to the direction of $B\sin\theta$, which is in the plane of the coil. The flux density $\mathbf{B}$, itself, comes out of the paper at an angle θ to the normal and its other component is $B\cos\theta$ perpendicular to the plane of the coil. The elements of the coil AE and DC are assumed to be connected by wires CA and ED which carry the current i. The whole coil may be made up from such strips and the wires such as CA and ED may then be eliminated, since they carry equal and opposite current, leaving only the coil carrying the current i.

Due to $B\cos\theta$, there will be a force on each section of the strip. These forces will be in the plane of the coil, each perpendicular to one of the wires AE, DC, CA, and ED. They will be in equilibrium, producing no net force on the strips. The $B\sin\theta$ component will generate no forces on ED and CA, since they are parallel to it. There will, however, be equal and opposite forces, perpendicular to the plane of the coil, on each of AE and DC, producing a torque on the strip. The forces, and hence the torque, will be proportional to the projection of AE and DC on the y-axis, these being the elements of ds (in this case δ_y) perpendicular to $B\sin\theta$. Thus, the torque on the strip will be given by one of the forces times the distance between them, i.e. $(i\delta_y B\sin\theta)$ED, and will tend to turn the strip about the y-axis. Now δ_yED is the area of the strip and can be represented by a vector $\mathbf{ds}$ having a magnitude equal to the area and direction normal to the strip. The torque can then be written

$$\mathbf{L} = i\mathbf{ds}\times\mathbf{B} \tag{3.93}$$

since the vectors $\mathbf{ds}$ and $\mathbf{B}$ have the angle θ between them and assuming the coil is in free space, equation (3.93) becomes

$$\mathbf{L} = i\mu_0\mathbf{ds}\times\mathbf{H} = \mathbf{m}\times\mathbf{H} \tag{3.94}$$

Thus, when a field is applied to the atom a torque is exerted on the dipole moment, and, since torque is rate of change of angular momentum, it can be written

$$\mathbf{L} = \dot{\mathbf{G}} = \mathbf{m}\times\mathbf{H} \tag{3.95}$$

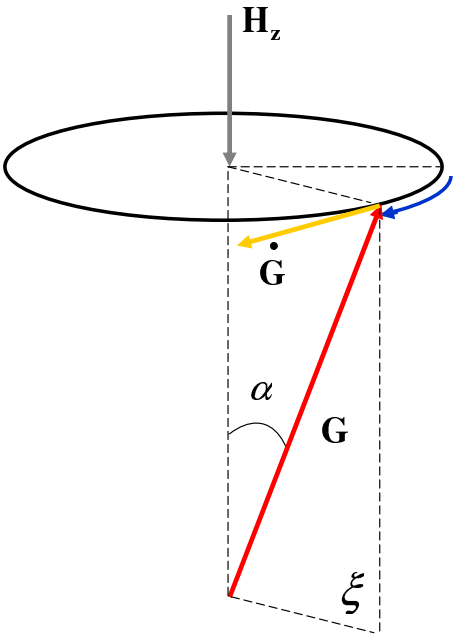

Figure 3.10: Precessional motion without damping factor

Now **m** and **G** are proportional and collinear from equation (3.92) since γ is a scalar so that

$$\dot{\mathbf{G}} = -\gamma \mathbf{G} \times \mathbf{H} \tag{3.96}$$

Since the product of two vectors is another vector perpendicular to both, $\dot{\mathbf{G}}$ must always be normal to **G** and **H**. Thus, referring to Figure 3.10, if **G** and **H** are in the plane ξ at any instant, $\dot{\mathbf{G}}$ is perpendicular to the plane, i.e. if **G** is drawn from a fixed point, its tip must move in a circle, so that **G** precesses about **H**. Expanding (3.96), the following expression is obtained

$$\dot{\mathbf{G}} = -\gamma[\hat{\mathbf{i}}(G_y H_z - G_z H_y) + \hat{\mathbf{j}}(G_z H_x - G_x H_z) + \hat{\mathbf{k}}(G_x H_y - G_y H_x)] \tag{3.97}$$

If the field, **H** is applied in the -z direction as in Figure (3.10) then

$$\left.\begin{aligned} \dot{G}_x &= \gamma H G_y \\ \dot{G}_y &= -\gamma H G_x \\ \dot{G}_z &= 0 \end{aligned}\right\} \tag{3.98}$$

Since dG_z/dt is zero, G_z itself must evidently be a constant. Referring to Figure 3.10, $G_z = G\cos\alpha$, and so the angle α must be constant. Thus the effect of the field is to cause **G** (and hence **m**) to precess about the field direction at a constant angle.

Differentiating (3.98) yields

$$\ddot{G_x} = \gamma H\dot{G_y} = \gamma H(-\gamma H G_x) = -\gamma^2 H^2 G_x \tag{3.99}$$

Equation (3.99) is the well-known second-order differential equation with solution

$$G_x = A\cos(-\gamma Ht + \phi) \tag{3.100}$$

where A is the peak amplitude in the x-y plane and ϕ a constant phase angle; similarly $G_y = A\sin(-\gamma Ht + \phi)$

The peak amplitude of G in the x-y plane is constant and of value $G\sin\alpha$ so that the full solution of equation (3.98) is

$$\left.\begin{array}{l} G_x = G\sin\alpha\cos(\omega_p t + \phi) \\ G_x = G\sin\alpha\sin(\omega_p t + \phi) \\ G_z = G\cos\alpha \end{array}\right\} \tag{3.101}$$

where $\omega_p = -\gamma H$ is the angular precession frequency depending only on the value of the field and the gyromagnetic ratio. The negative sign indicates the direction of the precession, which is that of a right-handed screw along the direction of **H**. Were $-\gamma H$ positive the opposite would apply. The value α is simply the angle between the direction of the dipole moment and the axis along which the field is applied at the moment of switching it on.

The above theory is, of course, over-simplified as may be seen by means of a simple experiment. If a gyroscope is set spinning and hung from a suitable stand on the end of a long thread, it can be made to precess by setting its axis at an angle to the vertical and releasing it. The gyroscope will precess about the vertical, the direction of the gravitational force, which is the analogue of the magnetic field in the case of the

atomic gyroscope. However, the precessional motion will be observed to be a spiral with the precessional angle (α in Figure 3.10) gradually decreasing until the gyroscope hangs vertically. This is due to the frictional damping forces on the gyroscope due to air; if a pointer attached to the lower end of its axis is allowed to dip into a bowl of water, increasing the damping, it spirals in to the vertical position more quickly. Equation 3.96 contains no damping term and is therefore incomplete.

3.3.2 The Equation of Motion

Since the magnetisation vector is always oppositely directed to the angular momentum vector, equation (3.96) gives the basic equation of motion of the magnetisation as

$$\frac{\partial \mathbf{M}}{\partial t} = -\gamma[\mathbf{M} \times \mathbf{H}] \tag{3.102}$$

where $\mathbf{H}$ is the effective field acting on $\mathbf{M}$ and γ is the gyromagnetic ratio (Tan et al., 2005). The magnetisation is assumed to have a spatial as well as a time-dependence, so the time derivative is written as a partial derivative. According to equation (3.102) the magnetisation will precess about the direction of $\mathbf{H}$ at a constant angle so long as $\mathbf{H}$ is a uniform, constant field. In practice, the magnetisation spirals into parallelism with the applied field due to damping effects. This is described by the Landau and Lifshitz damping effect (Landau and Lifshitz, 1935) expressed in equation 3.103 where the damping factor λ is a constant, (Bertotti, 1998).

$$\frac{\partial \mathbf{M}}{\partial t} = -\gamma[\mathbf{M} \times \mathbf{H}] + \lambda[\mathbf{M} \times (\mathbf{M} \times \mathbf{H})] \tag{3.103}$$

An alternative damping term has been proposed by Gilbert (1955) of the form

$$\frac{\alpha}{M_s}\left[\mathbf{M} \times \frac{\partial \mathbf{M}}{\partial t}\right] \tag{3.104}$$

and this reduces to the Landau-Lifshitz term, for small values of α if $\lambda = \gamma\alpha/M_s$. For a number of applications in ferromagnetic resonance the Gilbert term gives a better

description of the loss mechanisms. The full equation of motion of magnetisation used in this work is therefore

$$\frac{\partial \mathbf{M}}{\partial t} = -\gamma(\mathbf{M} \times \mathbf{H}) + \frac{\alpha}{M_s}\left(\mathbf{M} \times \frac{\partial \mathbf{M}}{\partial t}\right) \tag{3.105}$$

Above equation is known as Gilbert's equation (Gilbert, 1955). A full comparison of the original Landau-Lifshitz form and Gilbert's modification is given in Mallinson (1987).

If damping is neglected ($\alpha = 0$), the solution of equation (3.105) will be given by equation (3.98), where the field $H = H_z$, is in the z-direction only. Thus

$$\left.\begin{aligned} \frac{dM_x}{dt} &= \gamma M_y H \\ \frac{dM_y}{dt} &= -\gamma M_x H \\ \frac{dM_z}{dt} &= 0 \end{aligned}\right\} \tag{3.106}$$

which corresponds to precession of the magnetisation at a constant angle and angular frequency given by

$$\omega_0 = -\gamma H \tag{3.107}$$

If the damping term α is now included, expanding the vector product gives

$$\begin{aligned} \frac{\partial M_x}{\partial t} &= \omega_0 M_y + \frac{\alpha}{M_s}\left(M_y \frac{\partial M_z}{\partial t} - M_z \frac{\partial M_y}{\partial t}\right) \\ \frac{\partial M_y}{\partial t} &= -\omega_0 M_x + \frac{\alpha}{M_s}\left(M_z \frac{\partial M_x}{\partial t} - M_x \frac{\partial M_z}{\partial t}\right) \\ \frac{\partial M_z}{\partial t} &= \frac{\alpha}{M_s}\left(M_x \frac{\partial M_y}{\partial t} - M_z \frac{\partial M_x}{\partial t}\right) \end{aligned} \tag{3.108}$$

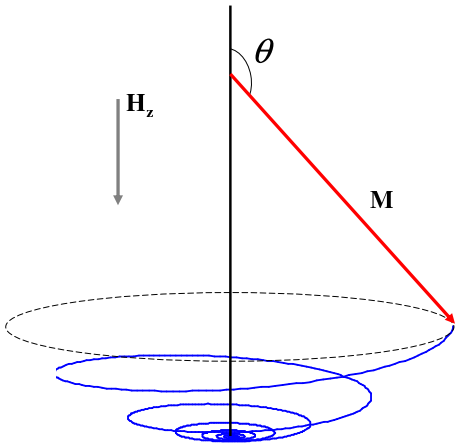

Figure 3.11: Rotation of the magnetisation vector with damping effect (continuous line) and without damping (doted line)

These equations may be solved simultaneously to give

$$\begin{aligned}
\frac{\partial M_x}{\partial t} &= \frac{\omega_0}{1+\alpha^2} M_y + \frac{\omega_0 \alpha}{1+\alpha^2} \frac{M_x M_z}{M_s} \\
\frac{\partial M_y}{\partial t} &= -\frac{\omega_0}{1+\alpha^2} M_x + \frac{\omega_0 \alpha}{1+\alpha^2} \frac{M_y M_z}{M_s} \\
\frac{\partial M_z}{\partial t} &= -\frac{\omega_0 \alpha}{1+\alpha^2} M_s + \frac{\omega_0 \alpha}{1+\alpha^2} \frac{M_z^2}{M_s}
\end{aligned} \tag{3.109}$$

When $\alpha \ll 1$ equations (3.109) have the same form as the solution of the Landau-Lifshitz equation with $\lambda = \gamma\alpha/M_s$.

Considering the case of a z directed field the solution of the system of equations (3.109) for an initial angle θ_0 between the applied field and the magnetisation is:

$$\begin{aligned}
M_x &= M_s \sin[\theta(t)] \cos[\phi(t)] \\
M_y &= M_s \sin[\theta(t)] \sin[\phi(t)] \\
M_z &= M_s \cos[\theta(t)]
\end{aligned} \tag{3.110}$$

where

$$\theta(t) = 2 \tan^{-1} \left[\tan \left(\frac{\theta_0}{2} \right) e^{\frac{-t}{\tau}} \right] \tag{3.111}$$

$$\phi(t) = \left(\omega_0 - \frac{\phi_0}{2} \right) t \tag{3.112}$$

and

$$\tau = \frac{\alpha\omega_0}{1 + alpha^2} \tag{3.113}$$

Thus as $t \to \infty$, θ tends to zero or 180° and the magnetisation tends to alignment with the applied field as shown in Figure 3.11. τ is clearly a characteristic time, known as the relaxation time, for this process.

3.3.3 The Effective Field

The free energy of a ferromagnetic body is composed of several energy contributions; accordingly, several field contributions add up to the effective magnetic field $\mathbf{H_{eff}}$. An equilibrium configuration of $\mathbf{M}$ can be found by locally minimising the free energy, (Brown, 1978). Therefore, the free energy of a ferromagnetic specimen can be written as

$$\mathcal{E} = \mathcal{E}_{ext} + \mathcal{E}_{exch} + \mathcal{E}_{anis} + \mathcal{E}_{demag} \tag{3.114}$$

Where $\mathcal{E}_{ext}$ is the energy due to the interaction between an applied field and magnetic moments, $\mathcal{E}_{exch}$ is the energy due to quantum mechanical exchange effects between nearest neighbors, $\mathcal{E}_{anis}$ is the energy due to the crystalline anisotropy and $\mathcal{E}_{demag}$ is the demagnetising energy arising from the interactions of magnetic moments.

Assuming the magnetic material considered occupies a volume V, then the energy due to the interaction between the external applied field $\mathbf{H_{ext}}$ and the magnetic moments can be expressed as (Tan et al., 2005)

$$\mathcal{E}_{ext} = -\mu_0 \int_V \mathbf{M} \cdot \mathbf{H_{ext}} dv \tag{3.115}$$

In the same manner, the demagnetising energy can be expresed in terms of the demagnetising field $\mathbf{H_{demag}}$ as (see Appendix A)

$$\mathcal{E}_{demag} = -\frac{1}{2}\mu_0 \int_V \mathbf{M} \cdot \mathbf{H_{demag}} dv \tag{3.116}$$

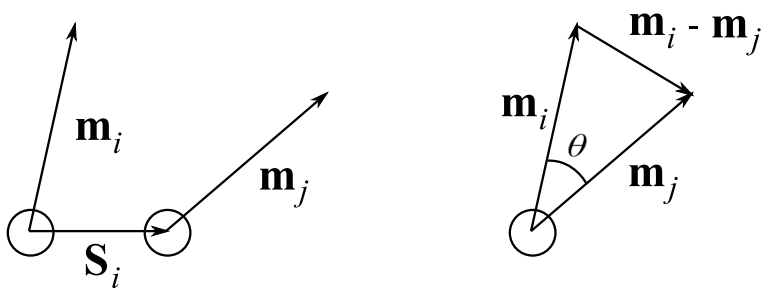

Figure 3.12: Schematic representation of the change in the angle between neighbouring spins i and j.

Equation (3.116) represents the interaction of each dipole with the demagnetising field $\mathbf{H_{demag}}$ created by the other dipoles, the factor $\frac{1}{2}$ is needed in order to avoid counting twice the interaction of the dipoles.

In ferromagnetic materials the atomic spins interact with each other, each of them trying to align the others in its own direction. This interaction between them originates from the quantum mechanical properties of spins (Aharoni, 2000). The force that tries to align spins is known as exchange interaction and it is normally expressed as the exchange energy between the spins. The exchange force has very short range, it affects nearest neighbours only. It is a very strong force between such neighbours, but it does not extend to spins which are farther away. With small angles between neighbouring spins, large changes of the angle over a distance of many atoms do not involve a large exchange energy. Therefore domain wall formation is the natural way of reducing the exchange energy in a magnetic material.

The interaction between adjacent spins can be represented as in Figure 3.12 where $\mathbf{m}_i$ and $\mathbf{m}_j$ are unit vectors parallel to the local spin direction, therefore parallel to the local direction of the magnetisation vector. $\mathbf{S}_i$ represents the position vector between them. From quantum mechanics, the exchange energy among spins can be written in

terms of the angle $\phi_{i,j}$ between spin i and j as

$$\mathcal{E} = JS^2 \sum_{neighbours} \phi_{i,j}^2 \tag{3.117}$$

Where J is a parameter of the material known as exchange integral, the convention is that a positive J means a ferromagnetic coupling that tends to align spins parallel to each other, while a negative J means an antiferromagnetic coupling. For small angles $|\phi_{i,j}| \simeq |\mathbf{m}_i - \mathbf{m}_j|$, then taking the first-order expansion in a Taylor series gives

$$|\mathbf{m}_i - \mathbf{m}_j| = |(\mathbf{S}_i \cdot \nabla)\mathbf{m}| \tag{3.118}$$

Substitution of (3.118) into (3.117) and integranting over the ferromagnetic body yields

$$\mathcal{E}_{exch} = \int_V \frac{A_x}{\mu_0 M_s^2} \left((\nabla M_x)^2 + (\nabla M_y)^2 + (\nabla M_z)^2 \right) dv \tag{3.119}$$

where A_x is the exchange stifness constant of the ferromagnetic material, M_s is the saturation magnetisation and M_x, M_y and M_z are the x, y and z components of the magnetisation.

The anisotropy or magnetocrystalline energy of a ferromagnetic crystal acts in such a way that the magnetisation tends to be directed along certain crystallographic axes which, accordingly, are called directions of easy magnetisation, while the directions along which it is most difficult to magnetise the crystal are called hard directions. It is found experimentally to require the expenditure of a certain, and often considerable, amount of energy to magnetise a crystal to saturation in a hard direction, referred to the lower energy required to saturate along a direction of easy magnetisation. The excess energy required in the hard direction is known as anisotropy energy. If there is only one easy direction in the material, then it is refered to as uniaxial anisotropy.

The uniaxial anisotropy energy is a function of only one parameter, the angle θ between the easy axis and the direction of the magnetisation. It is often expressed in terms of the anisotropy energy density function $w_{uniaxial}$ as

$$w_{unixial} = -K_1 \cos^2\theta + K_2 \cos^4\theta = -K_1 m_z^2 + K_2 m_z^4 \tag{3.120}$$

where it is assumed that z is parallel to the easy crystallographic axis and $\mathbf{m}$ is a unit vector parallel to the magnetisation $\mathbf{M}$ and the parameters K_1 and K_2 are the anisotropy constants for which values are taken from experiments (Aharoni, 2000). The right hand side of (3.120) is the power series expansion of the central term. This expansion may be carried to higher orders, but none of the known ferromagnetic materials seem to require it. In all known cases even the term $K_2 << K_1$ or negligible which justifies the use of the power series expansion (Aharoni, 2000).

The anisotropy energy is then obtained by integrating the anisotropy density function over the ferromagnetic body

$$\mathcal{E}_{anis} = \int_V \left(-K_1 m_z^2 + K_2 m_z^4\right) dv \tag{3.121}$$

A deep insight into the nature of the exchange and anisotropy energy terms is stated in (Kittel, 1949; Brown, 1978).

The effective field is defined via the variational derivative of $\mathcal{E}$ with respect to $\mathbf{M}$

$$\mathbf{H_{eff}} = -\frac{\partial \mathcal{E}}{\partial \mathbf{M}} \tag{3.122}$$

Accordingly, it can be written as

$$\mathbf{H_{eff}} = \mathbf{H_{ext}} + \mathbf{H_{exch}} + \mathbf{H_{anis}} + \mathbf{H_{demag}} \tag{3.123}$$

where $\mathbf{H_{ext}}$, $\mathbf{H_{exch}}$, $\mathbf{H_{anis}}$ and$\mathbf{H_{demag}}$ are the external field, exchange field, anisotropy field and demagnetising fields respectively. The externally applied field $\mathbf{H_{ext}}$ is known in general, the demagnetising field $\mathbf{H_{demag}}$ is dependant on the geometry and magnetic state of the sample. $\mathbf{H_{exch}}$ and $\mathbf{H_{anis}}$ can be obtained from (3.119) and (3.119) using (3.122).

$$\mathbf{H_{exch}} = -\frac{\partial \mathcal{E}_{exch}}{\partial \mathbf{M}} = \frac{2A_x \nabla^2 \mathbf{M}}{\mu_0 M_s^2} \tag{3.124}$$

$$\mathbf{H_{anis}} = -\frac{\partial \mathcal{E}_{anis}}{\partial \mathbf{M}} = \frac{2M_z}{\mu_0 M_s^2}\left(K_1 - 2K_2 \frac{M_z^2}{M_s^2}\right)\mathbf{k} \tag{3.125}$$

where ∇^2 denotes the Laplacian and $\mathbf{k}$ represents a unit vector in the z direction.

All the above theory will be used later in the implementation of the extended FDTD algorithm to simulate magnetic materials.

3.4 Summary

The general electromagnetic theory and the micromagnetic model which form the basic theory behind this research have been studied in detail. In the general electromagnetic theory section electrical properties of matter such as permittivity, permeability and conductivity, and the formulation of Maxwell's equations and the concept of wave propagation were introduced. The origin of micromagnetism, the formulation of the equation of motion and the individual contributions to the effective field which rules the equation of motion were also described.

Chapter 4

The Finite Difference Time Domain Method

4.1 Introduction

The FDTD method is a numerical approximation to the time dependant form of Maxwell's equations. Maxwell's partial differential equations of electrodynamics represent a fundamental unification of electric and magnetic fields predicting electromagnetic wave phenomena (Hagness and Taflove, 2000).

The FDTD method treats impulsive behaviour naturally; being a time domain technique, it directly calculates the impulse response of an electromagnetic system. Therefore, a single FDTD simulation can provide either ultrawideband temporal waveforms or the sinusoidal steady state response at any frequency within the excitation spectrum. FDTD treats nonlinear behavior naturally. Being a time domain technique; the algorithm directly calculates the nonlinear response of an electromagnetic system.

The FDTD algorithm is a systematic approach. With it, specifying a new structure to be modelled is reduced to a problem of mesh generation rather than the potentially complex reformulation of an integral equation.

Computer memory capacities are increasing rapidly. While this trend positively influences all numerical techniques, it is of particular advantage to the FDTD method which is founded on discretizing space over a volume, and therefore inherently requires a large random access memory.

The FDTD algorithm can be extended to model non-linear, dispersive and therefore magnetic materials. This is, in adition to all above reasons, why the FDTD algorithm was chosen to solve Maxwell's equations in this thesis.

4.2 Maxwell's Equations Rearrangement for the FDTD method

Maxwell's curl equations in linear, isotropic, nondispersive, lossy materials are:

$$\frac{\partial \mathbf{H}}{\partial t} = -\frac{1}{\mu}\nabla \times \mathbf{E} - \frac{1}{\mu}(\mathbf{M}_{source} + \sigma^* \mathbf{H}) \tag{4.1}$$

$$\frac{\partial \mathbf{E}}{\partial t} = -\frac{1}{\varepsilon}\nabla \times \mathbf{H} - \frac{1}{\varepsilon}(\mathbf{J}_{source} + \sigma \mathbf{E}) \tag{4.2}$$

The vector components of the curl operators of (4.1) and (4.2) written in Cartesian coordinates yield the following system of six coupled scalar equations for **H** and **E**:

$$\frac{\partial H_x}{\partial t} = \frac{1}{\mu}\left[\frac{\partial E_y}{\partial z} - \frac{\partial E_z}{\partial y} - (M_{source_x} + \sigma^* H_x)\right] \tag{4.3}$$

$$\frac{\partial H_y}{\partial t} = \frac{1}{\mu}\left[\frac{\partial E_z}{\partial x} - \frac{\partial E_x}{\partial z} - (M_{source_y} + \sigma^* H_y)\right] \tag{4.4}$$

$$\frac{\partial H_z}{\partial t} = \frac{1}{\mu}\left[\frac{\partial E_x}{\partial y} - \frac{\partial E_y}{\partial x} - (M_{source_z} + \sigma^* H_z)\right] \tag{4.5}$$

$$\frac{\partial E_x}{\partial t} = \frac{1}{\varepsilon}\left[\frac{\partial H_z}{\partial y} - \frac{\partial H_y}{\partial z} - (J_{source_x} + \sigma E_x)\right] \tag{4.6}$$

$$\frac{\partial E_y}{\partial t} = \frac{1}{\varepsilon}\left[\frac{\partial H_x}{\partial z} - \frac{\partial H_z}{\partial x} - (J_{source_y} + \sigma E_y)\right] \tag{4.7}$$

$$\frac{\partial E_z}{\partial t} = \frac{1}{\varepsilon}\left[\frac{\partial H_y}{\partial x} - \frac{\partial H_x}{\partial y} - (J_{source_z} + \sigma E_z)\right] \tag{4.8}$$

Where σ and σ^* are electric and magnetic conductivities respectively, μ is the permeability, ε represents the permittivity and J_{source} and M_{source} are the electric and magnetic sources.

The system of six coupled partial differential equations of (4.3) to (4.5) and (4.6) to (4.8) forms the basis of the FDTD numerical algorithm for electromagnetic wave interactions with general three dimensional objects.

To obtain a two dimensional model, it is assumed that the structure being modelled extends to infinity in the z direction with no change in the shape or position of its transverse cross section. If the incident wave is also uniform in the z direction, then all partial derivatives of the fields with respect to z must equal zero. Under these conditions, the full set of Maxwell's curl equations given by (4.3) to (4.8) reduces to

$$\frac{\partial H_x}{\partial t} = \frac{1}{\mu}\left[-\frac{\partial E_z}{\partial y} - (M_{source_x} + \sigma^* H_x)\right] \tag{4.9}$$

$$\frac{\partial H_y}{\partial t} = \frac{1}{\mu}\left[\frac{\partial E_z}{\partial x} - (M_{source_y} + \sigma^* H_y)\right] \tag{4.10}$$

$$\frac{\partial H_z}{\partial t} = \frac{1}{\mu}\left[\frac{\partial E_x}{\partial y} - \frac{\partial E_y}{\partial x} - (M_{source_z} + \sigma^* H_z)\right] \tag{4.11}$$

$$\frac{\partial E_x}{\partial t} = \frac{1}{\varepsilon}\left[\frac{\partial H_z}{\partial y} - (J_{source_x} + \sigma E_x)\right] \tag{4.12}$$

$$\frac{\partial E_y}{\partial t} = \frac{1}{\varepsilon}\left[-\frac{\partial H_z}{\partial x} - (J_{source_y} + \sigma E_y)\right] \tag{4.13}$$

$$\frac{\partial E_z}{\partial t} = \frac{1}{\varepsilon}\left[\frac{\partial H_y}{\partial x} - \frac{\partial H_x}{\partial y} - (J_{source_z} + \sigma E_z)\right] \tag{4.14}$$

Consider grouping equations (4.9) to (4.14) according to the field vector components. The group formed by (4.9), (4.10) and (4.14) involves only H_x, H_y and E_z. This set of components is denoted as the transverse magnetic mode with respect to z (TM_z) in two dimensions:

$$\frac{\partial H_x}{\partial t} = \frac{1}{\mu}\left[-\frac{\partial E_z}{\partial y} - (M_{source_x} + \sigma^* H_x)\right] \tag{4.15}$$

$$\frac{\partial H_y}{\partial t} = \frac{1}{\mu}\left[\frac{\partial E_z}{\partial x} - (M_{source_y} + \sigma^* H_y)\right] \tag{4.16}$$

$$\frac{\partial E_z}{\partial t} = \frac{1}{\varepsilon}\left[\frac{\partial H_y}{\partial x} - \frac{\partial H_x}{\partial y} - (J_{source_z} + \sigma E_z)\right] \tag{4.17}$$

In a similar way it is possible to obtain the equations for the transverse electric mode TE_z by grouping (4.11), (4.12) and (4.13).

4.3 The Yee Algorithm

In 1966 Yee originated a set of finite difference equations for the time dependent Maxwell's curl equations system of (4.3) to (4.8) for the lossless materials case $\sigma^* = 0$ and $\sigma = 0$ (Yee, 1966). Yee's algorithm persists in having great usefulness, since its fundamental basis is very robust.

The Yee algorithm solves for both electric and magnetic fields in time and space using the coupled Maxwell's curl equations rather than solving for the electric field alone (or

the magnetic field alone) with a wave equation. Using both **E** and **H** information, the solution is more robust than using either alone (i.e. it is accurate for a wider class of structures). Both electric and magnetic material properties can be modelled in a straightforward manner. Features unique to each field such as tangential **H** singularities near edges and corners, azimuthal (looping) **H** singularities near thin wires, and radial **E** singularities near points, edges, and thin wires can be individually modelled if both electric and magnetic fields are available.

As illustrated in Figure 4.1, the Yee algorithm centers its **E** and **H** components in three dimensional space so that every **E** component is surrounded by four circulating **H** components, and every **H** component is surrounded by four circulating **E** components. This provides a simple picture of three dimensional space being filled by an interlinked array of Faraday's Law and Ampere's Law contours. For example, it is possible to identify Yee **E** components associated with displacement current flux linking **H** loops, as well as **H** components associated with magnetic flux linking **E** loops. In effect, the Yee algorithm simultaneously simulates the pointwise differential form and the macroscopic integral form of Maxwell's equations. The latter is extremely useful in specifying field boundary conditions and singularities.

In addition, the Yee space lattice has the following attributes: The finite difference expressions for the space derivatives used in the curl operators are central difference in nature and second order accurate; continuity of tangential **E** and **H** is naturally maintained across an interface of dissimilar materials if the interface is parallel to one of the lattice coordinate axes. For this case, there is no need to specially enforce field boundary conditions at the interface. At the beginning of the problem, the material permittivity and permeability at each field component location are specified. This leads to a stepped or "staircase" approximation of the surface and internal geometry of the structure, with a space resolution set by the size of the lattice unit cell. The location of the **E** and **H** components in the Yee space lattice and the central difference

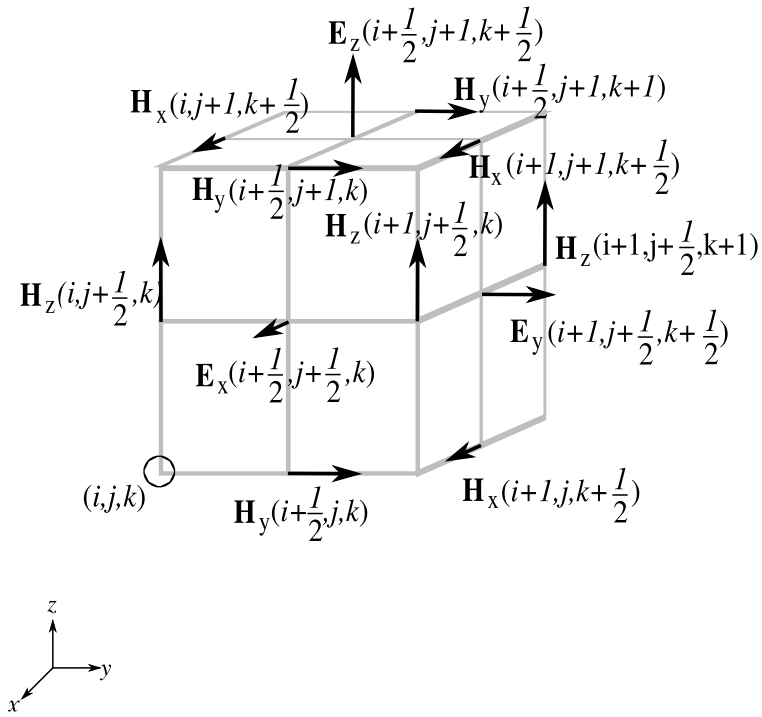

Figure 4.1: Position of the electric and magnetic field vector components about a cubic unit cell of the Yee space lattice.

operations on these components implicitly enforce Gauss' Law. Thus, the Yee mesh is divergence free with respect to its E and H fields in the absence of free electric and magnetic charges.

As illustrated in Figure 4.2, the Yee algorithm also centers its **E** and **H** components in time in what is termed a leapfrog arrangement. All of the **E** computations in the modelled space are completed and stored in memory for a particular time point using previously stored **H** data. Then all of the **H** computations in the space are completed and stored in memory using the **E** data just computed. The cycle begins again with the recomputation of the **E** components based on the newly obtained **H**. This process continues until time stepping is concluded. Leapfrog time stepping is fully explicit, thereby avoiding problems involved with simultaneous equations and matrix inversion. The finite difference expression for the time derivatives are central difference in nature and second order accurate. The time stepping algorithm is nondissipative. That is, numerical wave modes propagating in the mesh do not spuriously decay due to a nonphysical artifact of the time stepping algorithm.

4.4 Finite Differences Notation

A space point in a uniform, rectangular lattice is denoted as

$$(x, y, z) = (i\Delta x, j\Delta y, k\Delta z) \tag{4.18}$$

Here Δx, Δy, and Δz are, respectively, the lattice space increments in the x, y, and z coordinate directions, and i, j, and k are integers. Further, any function u of space and time evaluated at a discrete point in the grid and at a discrete point in time is expressed as

$$u(i\Delta x, j\Delta y, k\Delta z, n\Delta t) = u^n_{i,j,k} \tag{4.19}$$

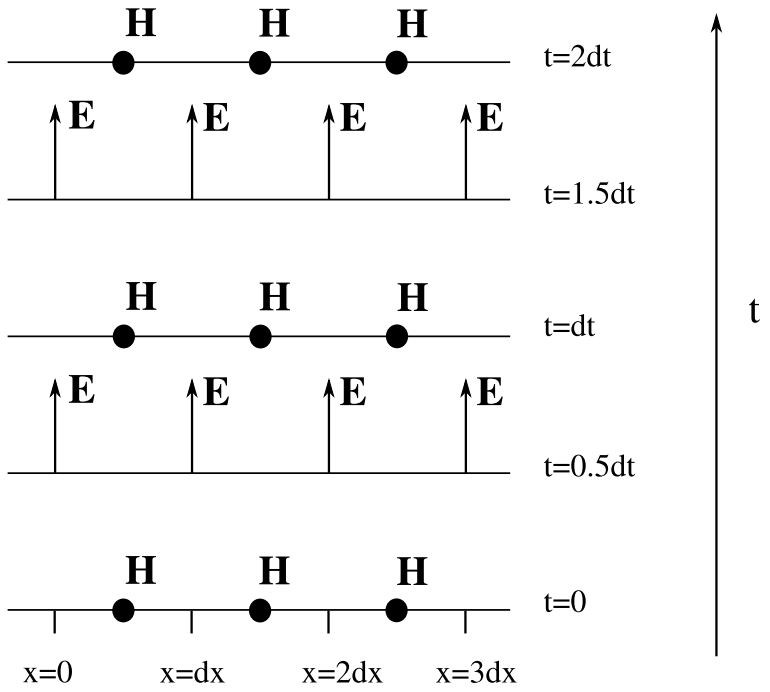

Figure 4.2: Space time chart of the Yee algorithm for a one dimensional wave showing the use of central differences for the space derivatives and leapfrog for the time derivatives. Initial conditions for both electric and magnetic fields are zero everywhere in the grid.

where Δt is the time increment, assumed uniform over the observation interval, and n is an integer.

Yee used centred finite difference or central difference expressions for the space and time derivatives that are both simply programmed and second order accurate in the space and time increments. Consider his expression for the first partial space derivative of u in the x-direction, evaluated at the fixed time $t_n = n\Delta t$:

$$\frac{\partial u}{\partial x}(i\Delta x, j\Delta y, k\Delta z, n\Delta t) = \frac{u^n_{i+\frac{1}{2},j,k} - u^n_{i-\frac{1}{2},j,k}}{\Delta x} + O[(\Delta x)^2] \tag{4.20}$$

Where $O[(\Delta x)^2]$ is the approximation error due to the discretization of the computation space. Note the $\pm 1/2$ increment in the i subscript (x-coordinate) of u, meaning a space finite difference over $\pm\Delta x/2$. Yee chose this notation because he wished to interleave his **E** and **H** components in the space lattice at intervals of $\Delta/2$. For example the difference of two adjacent **E** components, separated by Δx and located $\pm\Delta/2$ on either side of an **H** component, would be used to provide a numerical approximation for $\partial E/\partial x$ to permit stepping the component in t time. For completeness, the numerical approximations for $\partial u/\partial y$ and $\partial u/\partial z$ can be written by incrementing the j or k subscript of u by $\pm\Delta y/2$ or $\pm\Delta z/2$, respectively.

By analogy, Yee's expression for the first time partial derivative of u, evaluated at the fixed space point (i , j, k) is:

$$\frac{\partial u}{\partial t}(i\Delta x, j\Delta y, k\Delta z, n\Delta t) = \frac{u^{n+\frac{1}{2}}_{i,j,k} - u^{n-\frac{1}{2}}_{i,j,k}}{\Delta t} + O[(\Delta t)^2] \tag{4.21}$$

Now the $\pm\Delta/2$ increment is in the n superscript (time coordinate) of u, denoting a time finite-difference over $\pm\Delta t/2$. Yee chose this notation because he wished to interleave his **E** and **H** field components in time at intervals of $\Delta t/2$ for purposes of implementing a leapfrog algorithm.

4.5 Finite Difference Expression for the Two-Dimensional TM_z Mode

Two dimensional implementations of the TM_z mode will be used in Chapter 5 to simulate magnetic head stuctures. The TM_z mode was chosen to carry out simulations where the source is an electric current flowing in the z direction because it gives a better description of the propagation of magnetic fields around the current, that is H_x and H_y.

Previous ideas and notation are now applied to achieve a numerical approximation of Maxwell's curl equations in two dimensions given by the system of equations of (4.15) to (4.17). Considering first the E_z field component in equation (4.17) and applying the central difference expressions (4.20) and (4.21) for the time and space derivatives following Figure 4.1, at for example $E_z(i+\frac{1}{2}, j+\frac{1}{2}, n)$ yields

$$\begin{aligned}
&(E_z|^{n+\frac{1}{2}}_{i+\frac{1}{2},j+\frac{1}{2}} - E_z|^{n-\frac{1}{2}}_{i+\frac{1}{2},j+\frac{1}{2}})/\Delta t = \\
&= 1/\varepsilon_{i+\frac{1}{2},j+\frac{1}{2}} \Big((H_y|^n_{i+1,j+\frac{1}{2}} - H_y|^n_{i,j+\frac{1}{2}})/\Delta x - (H_x|^n_{i+\frac{1}{2},j+1} - H_x|^n_{i+\frac{1}{2},j})/\Delta y \\
&- J_{source_z}|^n_{i+\frac{1}{2},j+\frac{1}{2}} + \sigma_{i+\frac{1}{2},j+\frac{1}{2}} E_z|^n_{i+\frac{1}{2},j+\frac{1}{2}} \Big)
\end{aligned} \tag{4.22}$$

Note that all field quantities on the right-hand side are evaluated at time step n, including the electric field E_z appearing due to the material conductivity σ. Since E_z values at time step n are not assumed to be stored in the computer's memory (only the previous values of E_z at time step $n-1/2$ are assumed to be in memory), some way to estimate such terms is needed. A very good way forward is to use the semi-implicit approximation (or interpolation):

$$E_z|^n_{i+\frac{1}{2},j+\frac{1}{2}} = (E_z|^{n+\frac{1}{2}}_{i+\frac{1}{2},j+\frac{1}{2}} + E_z|^{n-\frac{1}{2}}_{i+\frac{1}{2},j+\frac{1}{2}})/2 \tag{4.23}$$

Here E_z values at time-step n are assumed to be simply the arithmetic average of the stored values of E_z at time-step $n-1/2$ and the yet to be computed new values of E_z

at time-step $n + 1/2$. Substituting (4.23) into (4.22) after multiplying both sides by Δt and rearranging yields the desired explicit time step relation for $E_z|_{i+\frac{1}{2},j+\frac{1}{2}}^{n+\frac{1}{2}}$

$$\begin{aligned} E_z|_{i+\frac{1}{2},j+\frac{1}{2}}^{n+\frac{1}{2}} &= \left(1 - \frac{\sigma_{i+\frac{1}{2},j+\frac{1}{2}}\Delta t}{2\varepsilon_{i+\frac{1}{2},j+\frac{1}{2}}}\right) \Bigg/ \left(1 + \frac{\sigma_{i+\frac{1}{2},j+\frac{1}{2}}\Delta t}{2\varepsilon_{i+\frac{1}{2},j+\frac{1}{2}}}\right) E_z|_{i+\frac{1}{2},j+\frac{1}{2}}^{n-\frac{1}{2}} \\ &+ \left(\frac{\Delta t}{\varepsilon_{i+\frac{1}{2},j+\frac{1}{2}}}\right) \Bigg/ \left(1 + \frac{\sigma_{i+\frac{1}{2},j+\frac{1}{2}}\Delta t}{2\varepsilon_{i+\frac{1}{2},j+\frac{1}{2}}}\right) \left(\left(H_y|_{i+1,j+\frac{1}{2}}^{n} - H_y|_{i,j+\frac{1}{2}}^{n}\right)/\Delta x\right. \\ &\left. - \left(H_x|_{i+\frac{1}{2},j+1}^{n} - H_x|_{i+\frac{1}{2},j}^{n}\right)/\Delta y - J_{source_z}|_{i+\frac{1}{2},j+\frac{1}{2}}^{n}\right) \end{aligned} \tag{4.24}$$

The semi implicit assumption of (4.23) has been found to yield numerically stable and accurate results for values of σ from zero to infinity, (Hagness and Taflove, 2000). As seen above, this assumption avoids simultaneous equations for $E_z|^{n+\frac{1}{2}}$.

Similarly, it is possible to derive finite-difference expressions based on Yee's algorithm for the H_x and H_y field components given by Maxwell's equations in (4.15) to (4.17). In addition, a set of updating coefficients for the electric and magnetic fields components at a general location (i,j) can be defined as follows

$$C_a|_{i,j} = \left(1 - \frac{\sigma_{i,j}\Delta t}{2\varepsilon_{i,j}}\right) \Bigg/ \left(1 + \frac{\sigma_{i,j}\Delta t}{2\varepsilon_{i,j}}\right) \tag{4.25}$$

$$C_b|_{i,j} = \left(\frac{\Delta t}{\varepsilon_{i,j}}\Delta\right) \Bigg/ \left(1 + \frac{\sigma_{i,j}\Delta t}{2\varepsilon_{i,j}}\right) \tag{4.26}$$

$$D_a|_{i,j} = \left(1 - \frac{\sigma^*_{i,j}\Delta t}{2\mu_{i,j}}\right) \Bigg/ \left(1 + \frac{\sigma^*_{i,j}\Delta t}{2\mu_{i,j}}\right) \tag{4.27}$$

$$D_b|_{i,j} = \left(\frac{\Delta t}{\mu_{i,j}\Delta}\right) \Bigg/ \left(1 + \frac{\sigma^*_{i,j}\Delta t}{2\mu_{i,j}}\right) \tag{4.28}$$

where $\Delta x = \Delta y = \Delta$ is assumed. Now the final equations for the TM_z mode can be written as

$$\begin{aligned} E_z|_{i+\frac{1}{2},j+\frac{1}{2}}^{n+\frac{1}{2}} &= C_a|_{i+\frac{1}{2},j+\frac{1}{2}} E_z|_{i+\frac{1}{2},j+\frac{1}{2}}^{n-\frac{1}{2}} \\ &+ C_b|_{i+\frac{1}{2},j+\frac{1}{2}} \begin{pmatrix} H_y|_{i+1,j+\frac{1}{2}}^{n} - H_y|_{i,j+\frac{1}{2}}^{n} \\ + H_x|_{i+\frac{1}{2},j}^{n} - H_x|_{i+\frac{1}{2},j+1}^{n} \\ - J_{source_z}|_{i+\frac{1}{2},j+\frac{1}{2}}^{n}\Delta \end{pmatrix} \end{aligned} \tag{4.29}$$

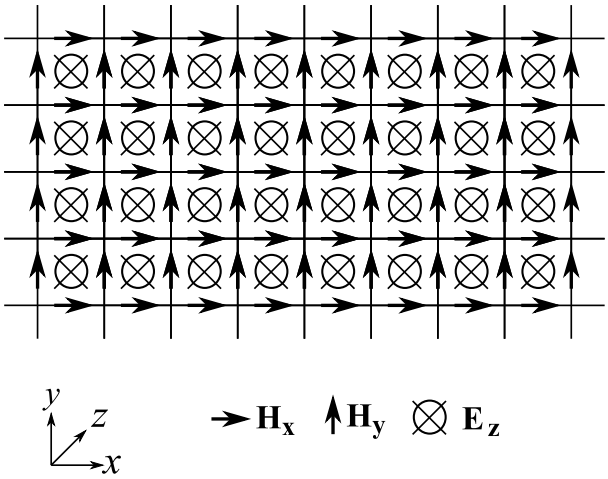

Figure 4.3: Two dimensional Yee cell field components distribution for the TM_z mode.

$$
\begin{aligned}
H_x|^{n+1}_{i+\frac{1}{2},j+1} &= D_a|_{i+\frac{1}{2},j+1} H_x|^{n}_{i+\frac{1}{2},j+1} \\
&+ D_b|_{i+\frac{1}{2},j+1} \left(\begin{array}{l} E_z|^{n+\frac{1}{2}}_{i+\frac{1}{2},j+\frac{1}{2}} - E_z|^{n+\frac{1}{2}}_{i+\frac{1}{2},j+\frac{3}{2}} \\ -M_{source_x}|^{n+\frac{1}{2}}_{i+\frac{1}{2},j+1} \Delta \end{array} \right)
\end{aligned} \tag{4.30}
$$

$$
\begin{aligned}
H_y|^{n+1}_{i+1,j+\frac{1}{2}} &= D_a|_{i+1,j+\frac{1}{2}} H_y|^{n}_{i+1,j+\frac{1}{2}} \\
&+ D_b|_{i+1,j+\frac{1}{2}} \left(\begin{array}{l} E_z|^{n+\frac{1}{2}}_{i+\frac{3}{2},j+\frac{1}{2}} - E_z|^{n+\frac{1}{2}}_{i+\frac{1}{2},j+\frac{1}{2}} \\ -M_{source_y}|^{n+\frac{1}{2}}_{i+1,j+\frac{1}{2}} \Delta \end{array} \right)
\end{aligned} \tag{4.31}
$$

With the system of finite-difference expressions of (4.29) to (4.31), the new value of an electromagnetic field vector component at any lattice point depends only on its previous value, the previous values of the components of the other field vector at adjacent points (see Figure 4.3), and the known electric and magnetic current sources.

4.6 Finite Difference Expression for the Two-Dimensional TE_z Mode

In a similar manner to the above procedure it is possible to obtain the finite difference expression for the two-dimensional TE_z mode. Here only the final form of the expres-

sion is stated. It will be use in next chapter to carry out simulation of an actual head pole tip.

$$
\begin{aligned}
H_z|^{n+\frac{1}{2}}_{i+\frac{1}{2},j+\frac{1}{2}} &= D_a|_{i+\frac{1}{2},j+\frac{1}{2}} H_z|^{n-\frac{1}{2}}_{i+\frac{1}{2},j+\frac{1}{2}} \\
&+D_b|_{i+\frac{1}{2},j+\frac{1}{2}} \begin{pmatrix} E_y|^n_{i+1,j+\frac{1}{2}} - E_y|^n_{i,j+\frac{1}{2}} \\ +E_x|^n_{i+\frac{1}{2},j} - E_x|^n_{i+\frac{1}{2},j+1} \\ -M_{source_z}|^n_{i+\frac{1}{2},j+\frac{1}{2}} \Delta \end{pmatrix}
\end{aligned} \tag{4.32}
$$

$$
\begin{aligned}
E_x|^{n+1}_{i+\frac{1}{2},j+1} &= C_a|_{i+\frac{1}{2},j+1} E_x|^n_{i+\frac{1}{2},j+1} \\
&+C_b|_{i+\frac{1}{2},j+1} \begin{pmatrix} H_z|^{n+\frac{1}{2}}_{i+\frac{1}{2},j+\frac{1}{2}} - H_z|^{n+\frac{1}{2}}_{i+\frac{1}{2},j+\frac{3}{2}} \\ -J_{source_x}|^{n+\frac{1}{2}}_{i+\frac{1}{2},j+1} \Delta \end{pmatrix}
\end{aligned} \tag{4.33}
$$

$$
\begin{aligned}
E_y|^{n+1}_{i+1,j+\frac{1}{2}} &= C_a|_{i+1,j+\frac{1}{2}} E_y|^n_{i+1,j+\frac{1}{2}} \\
&+C_b|_{i+1,j+\frac{1}{2}} \begin{pmatrix} H_z|^{n+\frac{1}{2}}_{i+\frac{3}{2},j+\frac{1}{2}} - H_z|^{n+\frac{1}{2}}_{i+\frac{1}{2},j+\frac{1}{2}} \\ -J_{source_y}|^{n+\frac{1}{2}}_{i+1,j+\frac{1}{2}} \Delta \end{pmatrix}
\end{aligned} \tag{4.34}
$$

Considering the TE_z mode as completely independent from the TM_z, the above formulation is correct for a two-dimensional Yee's grid centered around H_z. It is important that the electric and magnetic field are staggered in time. However, if a full three-dimensional model is being considered, the time and space index in equations (4.32) to (4.34) must be rewritten accordingly to a three dimensional Yee's cell containing all field components, see Figure 4.1.

4.7 Numerical Dispersion

The FDTD algorithm for Maxwell's curl equations causes nonphysical dispersion of the simulated waves in a free-space computational lattice. That is, the phase velocity of numerical wave modes can differ from the velocity of light c by an amount varying with the wavelength, direction of propagation in the grid, and grid discretisation.

An intuitive way to view this phenomenon is that the FDTD algorithm embeds the electromagnetic wave interaction with the structure of interest in a tenuous *numerical aether* having properties very close to vacuum, but not quite. This *aether* causes propagating numerical waves to accumulate delay or phase errors that can lead to nonphysical results such as broadening and ringing of pulsed waveforms, imprecise cancelation of multiple scattered waves, anisotropy, and pseudorefraction, (Hagness and Taflove, 2000). Numerical dispersion is a factor in FDTD modelling that must be accounted for to understand its operation and its accuracy limits.

The basic procedure for the numerical dispersion analysis involves substitution of a plane, monochromatic, traveling-wave trial solution into the finite-difference system that describes Maxwell's equations, (Hagness and Taflove, 2000). After algebraic manipulation, an equation is derived that relates the numerical wavevector components, the wave frequency, the time-step, and the grid space increments.

The finite-difference expressions for the two-dimensional TM_z mode are

$$\frac{H_x|_{i,j+\frac{1}{2}}^{n+\frac{1}{2}} - H_x|_{i,j+\frac{1}{2}}^{n-\frac{1}{2}}}{\Delta t} = -\frac{1}{\mu}\left(\frac{E_z|_{i,j+1}^{n} - E_z|_{i,j}^{n}}{\Delta y}\right) \tag{4.35}$$

$$\frac{H_y|_{i+\frac{1}{2},j}^{n+\frac{1}{2}} - H_y|_{i+\frac{1}{2},j}^{n-\frac{1}{2}}}{\Delta t} = \frac{1}{\mu}\left(\frac{E_z|_{i+1,j}^{n} - E_z|_{i,j}^{n}}{\Delta x}\right) \tag{4.36}$$

$$\frac{E_z|_{i,j}^{n+1} - E_z|_{i,j}^{n}}{\Delta t} = \frac{1}{\epsilon}\left(\frac{H_y|_{i+\frac{1}{2},j}^{n+\frac{1}{2}} - H_y|_{i-\frac{1}{2},j}^{n+\frac{1}{2}}}{\Delta x} - \frac{H_x|_{i,j+\frac{1}{2}}^{n+\frac{1}{2}} - H_x|_{i,j-\frac{1}{2}}^{n+\frac{1}{2}}}{\Delta y}\right) \tag{4.37}$$

The plane wave solution that will be introduced in (4.35) to (4.37) is defined as

$$E_z|_{i,j}^{n} = E_{z_o} e^{j(\omega n\Delta t - \tilde{k}_x i\Delta x - \tilde{k}_y j\Delta y)} \tag{4.38}$$

$$H_x|_{i,j}^{n} = H_{x_o} e^{j(\omega n\Delta t - \tilde{k}_x i\Delta x - \tilde{k}_y j\Delta y)} \tag{4.39}$$

$$H_y|_{i,j}^n = H_{y_o} e^{j(\omega n\Delta t - \tilde{k}_x i\Delta x - \tilde{k}_y j\Delta y)} \tag{4.40}$$

where $\tilde{k}_x$ and $\tilde{k}_y$ are the x and y components of the numerical wavevector, ω is the wave angular frequency and the first j to the left of the exponential represents the complex number $\sqrt{-1}$.

After substituting (4.38) to (4.40) into (4.35) to (4.37) and some simplifications yields

$$H_{x_o} = \frac{\Delta t E_{z_o}}{\mu \Delta y} \frac{\sin\left(\tilde{k}_y \Delta y/2\right)}{\sin\left(\omega\Delta t/2\right)} \tag{4.41}$$

$$H_{y_o} = \frac{\Delta t E_{z_o}}{\mu \Delta x} \frac{\sin\left(\tilde{k}_x \Delta x/2\right)}{\sin\left(\omega\Delta t/2\right)} \tag{4.42}$$

$$E_{z_o} \sin\left(\frac{\omega\Delta t}{2}\right) = \frac{\Delta t}{\epsilon}\left[\frac{H_{x_o}}{\Delta y}\sin\left(\frac{\tilde{k}_y\Delta y}{2}\right) - \frac{H_{y_o}}{\Delta x}\sin\left(\frac{\tilde{k}_x\Delta x}{2}\right)\right] \tag{4.43}$$

Upon substituting H_{x_o} of (4.41) and H_{y_o} of (4.42) into (4.43), leads to

$$\left[\frac{1}{c\Delta t}\sin\left(\frac{\omega\Delta t}{2}\right)\right]^2 = \left[\frac{1}{\Delta x}\sin\left(\frac{\tilde{k}_x\Delta x}{2}\right)\right]^2 + \left[\frac{1}{\Delta y}\sin\left(\frac{\tilde{k}_y\Delta y}{2}\right)\right]^2 \tag{4.44}$$

where $c = 1/\sqrt{\mu\epsilon}$ is the speed of light in the material being modeled. Equation (4.44) is the general numerical dispersion relation of the Yee algorithm for the two-dimensional TM_z mode which will be used in next section to establish a stability condition for the two-dimensional FDTD algorithm.

4.8 Stability

The FDTD algorithm requires that the time step Δt has a specific bound relative to the lattice space increments Δx and Δy. This bound is necessary to avoid numerical instability, an undesirable possibility with explicit differential equation solvers that

can cause the computed results to spuriously increase without limit as time-marching continues.

If a complex-valued numerical angular frequency $\tilde{\omega} = \tilde{\omega}_{real} + j\tilde{\omega}_{imag}$ is allowed, with an imaginary part which is responsible for instability, (4.44) can be rewritten as

$$\left[\frac{1}{c\Delta t}\sin\left(\frac{\tilde{\omega}\Delta t}{2}\right)\right]^2 = \left[\frac{1}{\Delta x}\sin\left(\frac{\tilde{k}_x\Delta x}{2}\right)\right]^2 + \left[\frac{1}{\Delta y}\sin\left(\frac{\tilde{k}_y\Delta y}{2}\right)\right]^2 \tag{4.45}$$

solving (4.45) for $\tilde{\omega}$ yields

$$\tilde{\omega} = \frac{2}{\Delta t}\sin^{-1}(\xi) \tag{4.46}$$

where

$$\xi = c\Delta t\sqrt{\frac{1}{(\Delta x)^2}\sin^2\left(\frac{\tilde{k}_x\Delta x}{2}\right) + \frac{1}{(\Delta y)^2}\sin^2\left(\frac{\tilde{k}_y\Delta y}{2}\right)} \tag{4.47}$$

From (4.47) it is noticed that

$$0 \le \xi \le c\Delta t\sqrt{\frac{1}{(\Delta x)^2} + \frac{1}{(\Delta y)^2}} \equiv \xi_{upper\ bound} \tag{4.48}$$

for all possible real values of $\tilde{k}$, that is, those numerical waves having zero exponential attenuation per grid space cell. $\xi_{upper\ bound}$ is obtained when each $\sin^2$ term under the square root of (4.47) simultaneously reaches a value of 1. This occurs for the propagating numerical wave having the wavevector components

$$\tilde{k}_x = \pm\frac{\pi}{\Delta x}; \qquad \tilde{k}_y = \pm\frac{\pi}{\Delta y} \tag{4.49}$$

It is clear that $\xi_{upper\ bound}$ can exceed 1 depending upon the choice of Δt. This can yield complex values of $\sin^{-1}(\xi)$ in (4.46), and therefore complex values for $\tilde{\omega}$ which give rise to numerical instability. To investigate further, the range of ξ given in (4.48) is divided in two subranges

Stable Range: $0 < \xi < 1$

Here, $\sin^{-1}(\xi)$ is real-valued and hence, real values of $\tilde{\omega}$ are obtained in (4.46). With $\tilde{\omega}_{imag} = 0$, a constant wave amplitude with time is obtained.

Unstable Range: $1 < \xi < \xi_{upper\ bound}$

This subrange exists only if

$$\xi_{upper\ bound} = c\Delta t\sqrt{\frac{1}{(\Delta x)^2} + \frac{1}{(\Delta y)^2}} > 1 \tag{4.50}$$

The unstable range is defined in an equivalent manner by

$$\Delta t > 1 \Big/ c\sqrt{\frac{1}{(\Delta x)^2} + \frac{1}{(\Delta y)^2}} \equiv \Delta t_{stable\ limit_{2D}} \tag{4.51}$$

Now, $\tilde{\omega}_{imag} \neq 0$ therefore the numerical wave exponentially grows with time hence the stability requirement for the FDTD method is for $\Delta x = \Delta y$

$$\Delta t < \frac{\Delta x}{\sqrt{2}c} \tag{4.52}$$

The above criterion will be used throughout this work and in subsequent chapters for the choice of Δt in order have a stable solution.

The spatial increment Δx is chosen to provide sufficient points to sample the shortest wavelength in the simulation (normally determined by the bandwidth of the wavesource) and/or the smallest feature in the simulated geometry. Δx will be chosen first such as it covers the smallest region of the implemented geometry with enough resolution, at least 5 cells, then condition (4.52) will be satisfied by choosing the apropriate Δt.

4.9 Perfectly Matched Layer (PML)

Since the initial work of Yee (Yee, 1966), the finite-difference time-domain technique has been widely used in electromagnetic computations. One of the inconveniences of this technique lies in the fact that the Maxwell equations have to be solved in a discretized domain whose sizes need to be restrained. Nevertheless, open problems involving theoretically boundless space extension can be solved when applying special conditions on the boundaries of the computational domain, in order to absorb the outgoing waves, otherwise, these waves would be reflected into the computational domain and result in incorrect computations.

To absorb the outgoing waves, the outer boundary of the space lattice must be terminated in an absorbing material medium (Hagness and Taflove, 2000). Ideally, the absorbing medium is only a few lattice cells thick, reflectionless to all impinging waves over their full frequency spectrum, highly absorbing, and effective in the near field of a source or a scatterer.

In 1994 Berenger introduced a highly effective absorbing material designated the perfectly matched layer, or PML (Berenger, 1994). The innovation of Berenger's PML is that plane waves of arbitrary incidence, polarization, and frequency are matched at the boundary while in early attempts the absorbing boundary was matched only to normally incident plane waves. To achieve this, Berenger derived a novel split-field formulation of Maxwell's equations where each vector field component is split into two orthogonal components. The principles of this technique and field splitting modifications will be described in the next section.

Numerical experiments comparing Berenger's PML with previous standard second order Mur absorbing boundary condition (Mur, 1981) show that the PML global error is in between 10^{-7} and 10^{-12} times that of the Mur ABC (Katz et al., 1994).

4.9.1 Reflectionless matching condition

Considering a plane wave incident normally at the interface between two materials, the reflection coefficient is:

$$\Gamma = \frac{Z_1 - Z_2}{Z_1 + Z_2} \tag{4.53}$$

where the wave impedances in region 1 (free space), Z_1, and region 2 (lossy material), Z_2, are given by

$$Z_1 = \sqrt{\frac{\mu_1}{\varepsilon_1}} \qquad ; \qquad Z_2 = \sqrt{\frac{\mu_2 \left(1 + \sigma^*/j\omega\mu_2\right)}{\varepsilon_2 \left(1 + \sigma/j\omega\varepsilon_2\right)}} \tag{4.54}$$

Where the subscript 1 or 2 refers to the free space or lossy material region respectively. Then, by setting $\varepsilon_1 = \varepsilon_2$ and $\mu_1 = \mu_2$ and further enforcing the condition

$$\frac{\sigma}{\varepsilon} = \frac{\sigma^*}{\mu} \tag{4.55}$$

yields $\Gamma = 0$, a reflectionless region 1 / region 2 interface for the normally impinging wave. These conditions form the bases of the PML and will be implemented next in the TM_z mode formulation.

4.9.2 Field splitting modification of Maxwell's equations in TM_z mode

Maxwell's curl equations (4.15) to (4.17) as modified by Berenger for a TE_z plane wave impining in the lossy materal region 2 are

$$\mu_2 \frac{\partial H_x}{\partial t} + \sigma_y^* H_x = -\frac{\partial E_z}{\partial y} \tag{4.56}$$

$$\mu_2 \frac{\partial H_y}{\partial t} + \sigma_x^* H_y = -\frac{\partial E_z}{\partial x} \tag{4.57}$$

$$\varepsilon_2 \frac{\partial E_{zx}}{\partial t} + \sigma_x E_{zx} = \frac{\partial H_y}{\partial x} \tag{4.58}$$

$$\varepsilon_2 \frac{\partial E_{zy}}{\partial t} + \sigma_y E_{zy} = \frac{\partial H_x}{\partial y} \tag{4.59}$$

Here the subscript 2 refers to the lossy material region and E_z is assumed to be split into two additive subcomponets

$$E_z = E_{zx} + E_{zy} \tag{4.60}$$

Further, the parameters σ_x and σ_y denote electric conductivities and the parameters σ_x^* and σ_y^* denote magnetic losses.

Berenger's formulation represents a generalization of normally modelled physical media. If $\sigma_x = \sigma_y = 0$ and $\sigma_x^* = \sigma_y^* = 0$, the system (4.56) to (4.59) reduces to Maxwell's equations in a lossless medium. If $\sigma_x = \sigma_y = \sigma$ and $\sigma_x^* = \sigma_y^* = 0$, (4.56) to (4.59) describes an electrically conductive medium. And if $\varepsilon_2 = \varepsilon_1$, $\mu_2 = \mu_1$, $\sigma_x = \sigma_y = \sigma$, $\sigma_x^* = \sigma_y^* = \sigma^*$ and (4.55) is satisfied, then (4.56) to (4.59) describe an absorbing medium that is impedance-matched to region 1 for normally incident plane waves as discussed in section 4.9.1.

4.9.3 Structure of an FDTD grid employing Brenger's PML

From Berenger's field formulation it is possoble to observe that if $\sigma_y = \sigma_y^* = 0$, the medium can absorb a plane wave having field components (H_y, E_{zx}) propagating along x, but does not absorb a wave having field components (H_x, E_{zy}) propagating along y, since in the first case propagation is governed by (4.57)and (4.58), and in the second case by (4.56)and (4.59). The converse situation is true for waves (H_y, E_{zx}) and (H_x, Ezy) if $\sigma_x = \sigma_x^* = 0$. These properties of particular Berenger media characterized by the pairwise parameters sets $(\sigma_x, \sigma_x^*, 0, 0)$ and $(0, 0, \sigma_y, \sigma_y^*)$ are the fundamental premise of this absorbing boundary condition. That is, if the pairwise electric and magnetic losses satisfy (4.55), then at interfaces normal to x and y, respectively, the Berenger media has zero reflection of electromagnetic waves.

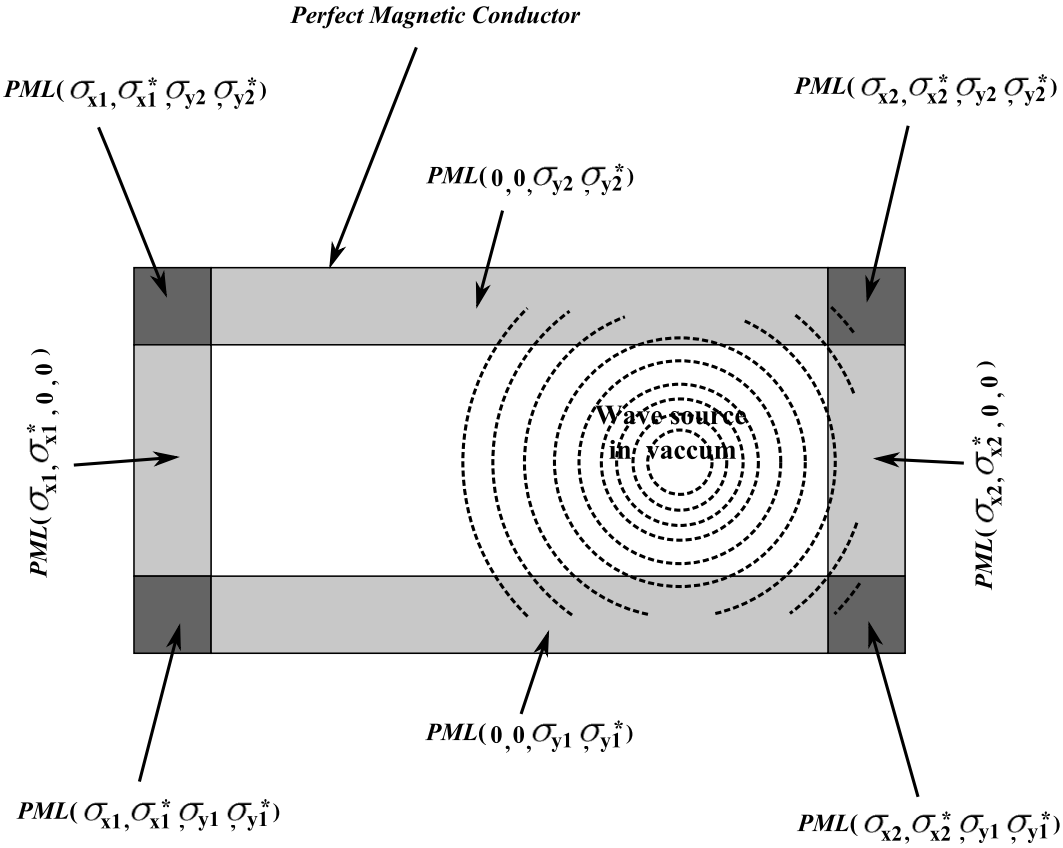

Figure 4.4: Structure of a two dimensional FDTD grid employing the Berenger's PML.

The above analysis permitted Berenger to propose the two dimensional FDTD grid scheme shown in Figure 4.4 which uses PMLs to greatly reduce outer-boundary reflections. Here, a free-space computation zone is surrounded by PML backed by a perfect magnetic conductor, i.e. $H_x = H_y = 0$. At the left and right sides of the grid (x_1 and x_2), each PML has σ_x and σ_x^* matched according to (4.55) along with $\sigma_y = \sigma_y^* = 0$ to permit reflectionless transmission across the vacuum-PML interface. At the lower and upper sides of the grid (y_1 and y_2), each PML has σ_y and σ_y^* matched according to (4.55) along with $\sigma_x = \sigma_x^* = 0$. At the four corners of the grid where there is overlap of two PMLs, all four losses $(\sigma_x, \sigma_x^*, \sigma_y, \sigma_y^*)$ are present and set equal to those of the adjacent PMLs. These boundary conditions will be used in the split field formulae of the FDTD TM_z mode implementation in Chapter 5.

4.9.4 PML performance

The continuous space

When used to truncate an FDTD lattice, the PML has a thickness d and is terminated by the outer boundary of the lattice. If the outer boundary is assumed to be a perfect magnetic conductor wall, as shown in Figure 4.4, finite power reflects back into the primary computation zone. For a wave impinging upon the PML at angle θ relative to the w-directed surface normal (where w means x or y), this reflection can be computed using transmission line analysis, yielding (Hagness and Taflove, 2000)

$$R(\theta) = e^{-2\sigma_w Z d \cos(\theta)} \tag{4.61}$$

Here, Z and σ_w are,respectively, the PML's characteristic wave impedance and its conductivity, referred to propagation in the w-direction. In the context of an FDTD simulation, $R(\theta)$ is referred to as the "reflection error" since it is a non-physical reflection due to the perfect magnetic conductor wall that backs the PML. This error decreases exponentially with σ_w and d. However, the reflection error increases as $\exp(\cos(\theta))$, reaching the worst case for $\theta = 90°$. At this grazing angle of incidence, $R = 1$ and the PML is completely ineffective. To be useful within an FDTD simulation, $R(\theta)$ must be as small as possible. Clearly, for a thin PML, σ_w must be as large as possible to reduce $R(\theta)$ to acceptably small levels, especially for θ approaching 90°.

The discrete space

Theoretically, reflectionless wave transmission can take place across a PML interface regardless of the local step-discontinuity in σ and σ^* presented to the continuous impinging electromagnetic field. However, in FDTD or any discrete representation of Maxwell's equations, numerical artifacts arise due to the finite spatial sampling. Con-

sequently, implementing a PML as a single step-discontinuity of σ and σ^* in the FDTD lattice leads to significant spurious wave reflection at the PML surface.

To reduce this reflection error, Berenger proposed that the PML losses along the direction normal to the interface gradually rise from zero (Berenger, 1994). Assuming such a grading, the PML remains matched. Pursuing this idea, consider as an example an x-directed plane wave impinging at angle θ upon a perfect magnetic conductor backed PML slab of thickness d, with the front planar interface located in the $x = 0$ plane. Assuming the graded PML conductivity profile $\sigma_x(x)$, then the reflection factor is

$$R(\theta) = e^{-2Z\cos(\theta)\int_0^d \sigma_x(x)dx} \tag{4.62}$$

Several profiles have been suggested for grading $\sigma_x(x)$. The most successful use a polynomial variation of the PML loss with depth x (Berenger, 1996). Polynomial grading is simply

$$\sigma_x(x) = \left(\frac{x}{d}\right)^m \sigma_{x,max} \tag{4.63}$$

This increases the value of the PML σ_x from zero at $x = 0$, the surface of the PML, to $\sigma_{x,max}$ at $x = d$ controlled by the degree of polynomial through m, the perfect magnetic conductor outer boundary. Substituting (4.63) into (4.62) yields

$$R(\theta) = e^{-2Z\sigma_{x,max}d\cos(\theta)/(m+1)} \tag{4.64}$$

For a fixed d, polynomial grading provides two parameters: $\sigma_{x,max}$ and m. A large m yields a $\sigma_x(x)$ distribution that is relatively flat near the PML surface. However, deeper within the PML, σ_x increases more rapidly than for small m. In this region, the field amplitudes are substantially decayed and reflections due to the discretisation error contribute less. Typically, $3 \leq m \leq 4$ has been found to be nearly optimal for many FDTD simulations (Berenger, 1996; 1997; Gedney, 1996).

For polynomial grading, the PML parameters can be readily determined for a given error estimate. For example, let m, d, and the desired reflection error $R(0)$ be known, then, from (4.64), $\sigma_{x,max}$ is computed as

$$\sigma_{x,max} = -\frac{(m+1)\ln[R(0)]}{2Zd} \tag{4.65}$$

Discretisation error

The design of an effective PML requires balancing the theoretical reflection error, $R(0)$, and the numerical discretization error. For example, (4.65) provides $\sigma_{x,max}$ for a polynomial-graded conductivity given a predetermined $R(0)$ and m. If $\sigma_{x,max}$ is small, the primary reflection from the PML is due to its perfect magnetic conductor backing. Equation (4.62) provides a fairly accurate approximation of the reflection error for this case. However, $\sigma_{x,max}$ is normally chosen to be as large as possible to minimize $R(0)$. Unfortunately, if $\sigma_{x,max}$ is too large, the discretization error due to the FDTD approximation dominates, and the actual reflection error is potentially orders of magnitude higher than that predicted by (4.62). Consequently, there is an optimal choice for $\sigma_{x,max}$ that balances reflection from the perfect magnetic conductor outer boundary and discretization error.

It was postulated by Berenger (Berenger, 1996; 1997) that the largest discretization error manifested as reflection occurs at $x = 0$, the PML surface. Any wave energy that penetrates further into the PML and then is reflected undergoes attenuation both before and after its point of reflection, and typically is not as large a contribution. Thus, it is desirable to minimize the discontinuity at $x = 0$. As discussed earlier, one way to achieve this is by flattening the PML loss profile near $x = 0$. However, if the subsequent rise of loss with depth is too rapid, reflections from deeper within the PML can dominate.

Through an extensive series of numerical experiments, it was demonstrated in (Gedney,

1996; He, 1997) that, for a broad range of applications, an optimal choice for a 10-cell thick, polynomial graded PML is $R(0) \approx e^{-16}$. For a 5-cell thick PML, $R(0) \approx e^{-8}$ is optimal. From (4.65), this leads to an optimal choice for $\sigma_{x,max}$ for polynomial grading in a 10 cell thick PML:

$$\sigma_{x,max} = -\frac{(m+1)(-16)}{(2Z)(10\Delta)} = \frac{0.8(m+1)}{Z\Delta} \tag{4.66}$$

The simulations of head structures carried out in Chapter 6 will use a 10 cell thick PML with polynomial grading as in (4.66) to avoid reflections in the computational space.

4.10 Maxwell Equations for Non-linear Magnetic Materials

When a linear magnetic material is considered, the magnetic flux density $\mathbf{B}$ is proportional to the magnetic field $\mathbf{H}$ by a constant called the permeability of the material as in equation (3.16). If a non-linear magnetic material is considered, equation (3.16) does not apply and the more fundamental equation (3.15) is needed where the magnetisation vector is taken into account to calculate the magnetic flux density, repeated here for convenience.

$$\mathbf{B} = \mu_o(\mathbf{H} + \mathbf{M})$$

To extend the FDTD method to non-linear magnetic materials, first consider Maxwell's curl equations for a general medium.

$$\frac{\partial \mathbf{B}}{\partial t} = -\nabla \times \mathbf{E} \tag{4.67}$$

$$\frac{\partial \mathbf{D}}{\partial t} = \nabla \times \mathbf{H} \tag{4.68}$$

where $\mathbf{B}$ is as above and

$$\mathbf{D} = \epsilon \mathbf{E} \tag{4.69}$$

Substituting $\mathbf{B}$ and $\mathbf{D}$ into (4.67) and (4.68) yields

$$\frac{\partial \mathbf{H}}{\partial t} = -\frac{1}{\mu_o} \nabla \times \mathbf{E} - \frac{\partial \mathbf{M}}{\partial t} \tag{4.70}$$

$$\frac{\partial \mathbf{E}}{\partial t} = \frac{1}{\epsilon} \nabla \times \mathbf{H} \tag{4.71}$$

The nonlinearity introduced by the term $\partial \mathbf{M}/\partial t$ is described by Gilbert's equation (3.105) repeated here for convenience.

$$\frac{\partial \mathbf{M}}{\partial t} = -\gamma(\mathbf{M} \times \mathbf{H}) + \frac{\alpha}{M_s} \left(\mathbf{M} \times \frac{\partial \mathbf{M}}{\partial t} \right)$$

4.11 Discretisation of the Equation of Motion

To discretise all of above equations, central finite difference expressions for the space and time derivatives described in equations (4.20) and (4.21) are used. These expressions are easy to program and also provide second order accuracy.

Equation (4.71) follows the same expression as in the normal FDTD method therefore no changes are needed for the E_z component in the 2D TM_z mode.

$$\begin{array}{l} E_z|^{n+\frac{1}{2}}_{i+\frac{1}{2},j+\frac{1}{2}} = C_a|_{i+\frac{1}{2},j+\frac{1}{2}} E_z|^{n-\frac{1}{2}}_{i+\frac{1}{2},j+\frac{1}{2}} \\ +C_b|_{i+\frac{1}{2},j+\frac{1}{2}} \left(\begin{array}{l} H_y|^n_{i+1,j+\frac{1}{2}} - H_y|^n_{i,j+\frac{1}{2}} \\ +H_x|^n_{i+\frac{1}{2},j} - H_x|^n_{i+\frac{1}{2},j+1} \end{array} \right) \end{array} \tag{4.72}$$

Equation (4.70) has a new term $\partial M/\partial t$, which is discretised using central differences in time, and it must be included in the final expressions for H_x and H_y.

$$\begin{array}{l} H_x|^{n+1}_{i+\frac{1}{2},j+1} = D_a|_{i+\frac{1}{2},j+1} H_x|^n_{i+\frac{1}{2},j+1} \\ +D_b|_{i+\frac{1}{2},j+1} \left(E_z|^{n+\frac{1}{2}}_{i+\frac{1}{2},j+\frac{1}{2}} - E_z|^{n+\frac{1}{2}}_{i+\frac{1}{2},j+\frac{3}{2}} \right) \\ -M_x|^{n+1}_{i+\frac{1}{2},j+1} + M_x|^n_{i+\frac{1}{2},j+1} \end{array} \tag{4.73}$$

$$\begin{aligned} H_y|^{n+1}_{i+1,j+\frac{1}{2}} &= D_a|_{i+1,j+\frac{1}{2}} H_y|^{n}_{i+1,j+\frac{1}{2}} \\ &+D_b|_{i+1,j+\frac{1}{2}} \left(\; E_z|^{n+\frac{1}{2}}_{i+\frac{3}{2},j+\frac{1}{2}} - E_z|^{n+\frac{1}{2}}_{i+\frac{1}{2},j+\frac{1}{2}} \; \right) \\ &-M_y|^{n+1}_{i+\frac{1}{2},j+1} + M_y|^{n}_{i+\frac{1}{2},j+1} \end{aligned} \tag{4.74}$$

Where the coefficients C and D are as described previously in section 4.5.

An expression for the magnetisation vector components can be obtained by expanding the vector product in Gilbert's equation (3.105) and solving for $\partial M_x/\partial t$, $\partial M_y/\partial t$ and $\partial M_z/\partial t$; this yields

$$\begin{aligned} \frac{\partial M_x}{\partial t} = \; & \frac{\gamma}{M_s(1+\alpha^2)}[M_s(H_z M_y - H_y M_z) + \alpha M_x(H_y M_y + H_z M_z) \\ & -\alpha H_x(M_s^2 - M_x^2)] \end{aligned} \tag{4.75}$$

$$\begin{aligned} \frac{\partial M_y}{\partial t} = \; & \frac{\gamma}{M_s(1+\alpha^2)}[M_s(H_x M_z - H_z M_x) + \alpha M_y(H_x M_x + H_z M_z) \\ & -\alpha H_y(M_s^2 - M_y^2)] \end{aligned} \tag{4.76}$$

$$\begin{aligned} \frac{\partial M_z}{\partial t} = \; & \frac{\gamma}{M_s(1+\alpha^2)}[M_s(H_y M_x - H_x M_y) + \alpha M_z(H_x M_x + H_y M_y) \\ & -\alpha H_z(M_s^2 - M_z^2)] \end{aligned} \tag{4.77}$$

Now applying central time differences to (4.75) to evaluate M_x at time step $n + 1/2$:

$$\frac{M_x|^{n+1} - M_x|^{n}}{\Delta t} = f(H_x, H_y, H_z, M_x, M_y, M_z)|^{n+\frac{1}{2}} \tag{4.78}$$

and rearranging terms gives the time marching scheme for M_x

$$M_x|^{n+1} = M_x|^{n} + f(H_x, H_y, H_z, M_x, M_y, M_z)|^{n+\frac{1}{2}} \Delta t \tag{4.79}$$

where $f(H_x, H_y, H_z, M_x, M_y, M_z)$ is a function of the magnetic field and the magnetisation vector components coming from (4.75) and has the form

$$\begin{aligned} f(H_x, H_y, H_z, M_x, M_y, M_z) = \; & \frac{\gamma}{M_s(1+\alpha^2)} \Bigg[M_s(H_z M_y - H_y M_z) \\ & +\alpha M_x(H_y M_y + H_z M_z) \\ & -\alpha H_x \frac{M_s^2 - M_x^2}{M_y^2 + M_z^2} \Bigg] \end{aligned} \tag{4.80}$$

The magnetisation components are evaluated at the same spatial location as the magnetic field components in the Yee's cell. Time marching expressions for M_y and M_z are derived in the same manner. From equation (4.79) it is noticed that M_y, M_z, H_y and H_z are used to compute the new value of M_x, however, these are placed at different locations than M_x within the Yee's cell, therefore spacial interpolation is needed. It is also noticed that equation (4.79) uses M_x, M_y, M_z, H_x, H_y and H_z evaluated at time step $n + 1/2$ while their values are only known at time step n, with n being an integer, thus time extrapolation is required. The proper space and time discretisation of Gilbert's equation to maintain second order accuracy are addressed in detail next.

4.12 Space and Time Syncronism

Here two different problems are addressed to maintain second order accuracy of the central difference scheme. First, H_x, H_y, H_z, M_x, M_y and M_z are not known at time step $n + 1/2$ in (4.79) or any other M (the same applies for the time marching expressions for M_y and M_z). A simple approach to solve this problem is to use an extrapolation scheme (Okoniewski and Okoniewska, 1994) in which the current value of a variable depends on the previous values using the backward differencing approximation

$$u|^{n+\frac{1}{2}} \simeq u|^{n-\frac{1}{2}} + \left.\frac{\partial u}{\partial t}\right|^{n-\frac{1}{2}} \Delta t \tag{4.81}$$

The unknown value of $u|^{n-\frac{1}{2}}$ on the right side of the equation can be expressed as the average of $u|^{n-1}$ and $u|^n$ and the derivative can be estimated using the standard central differences in (4.21). These operations lead to the second order accurate time marching formalism for correct integration into the FDTD scheme.

$$u|^{n+\frac{1}{2}} \simeq \frac{u|^{n-1} + u|^n}{2} + u|^n - u|^{n-1} = \frac{1}{2}(3u|^n - u|^{n-1}) \tag{4.82}$$

To illustrate the time synchronism, M_x will be computed for time step $n + 1$. From

(4.79), H_x, H_y, H_z, M_x, M_y and M_z must be known at time step $n + 1/2$ in order to evaluate $M_x|^{n+1}$. This is done by applying the time synchronism equation (4.82) to all vector components of $\mathbf{H}$ and $\mathbf{M}$ using previous values at time steps n and $n - 1$.

$$H_x|^{n+\frac{1}{2}} = \frac{1}{2}(3H_x|^n - H_x|^{n-1}) \tag{4.83}$$

$$H_y|^{n+\frac{1}{2}} = \frac{1}{2}(3H_y|^n - H_y|^{n-1}) \tag{4.84}$$

$$H_z|^{n+\frac{1}{2}} = \frac{1}{2}(3H_z|^n - H_z|^{n-1}) \tag{4.85}$$

$$M_x|^{n+\frac{1}{2}} = \frac{1}{2}(3M_x|^n - M_x|^{n-1}) \tag{4.86}$$

$$M_y|^{n+\frac{1}{2}} = \frac{1}{2}(3M_y|^n - M_y|^{n-1}) \tag{4.87}$$

$$M_z|^{n+\frac{1}{2}} = \frac{1}{2}(3M_z|^n - M_z|^{n-1}) \tag{4.88}$$

Now, all components on the right side of equations (4.83) to (4.88) are known, however, it is not yet possible to compute the magnetisation vector at time step $n + 1$ in the time marching scheme because space syncronism has not been applied.

In the Yee's cell, the $\mathbf{M}$ components are evaluated at the same spatial location as the $\mathbf{H}$ components. Therefore when any component of the magnetisation vector say M_x is being computed at a given point, say $(i + \frac{1}{2}, j)$, the y and z components of $\mathbf{H}$ and $\mathbf{M}$ used to compute $\mathbf{M_x}$ are located at different space locations as shown in Figure 4.5.

Thus, all the components in equations (4.83) to (4.88) must be reallocated to M_x position. This is done by interpolation of all components surrounding M_x in the Yee's cell (Okoniewski and Okoniewska, 1994). This can be easy understood by a graphical example. Figure 4.5 represents the space synchronism operations needed to compute

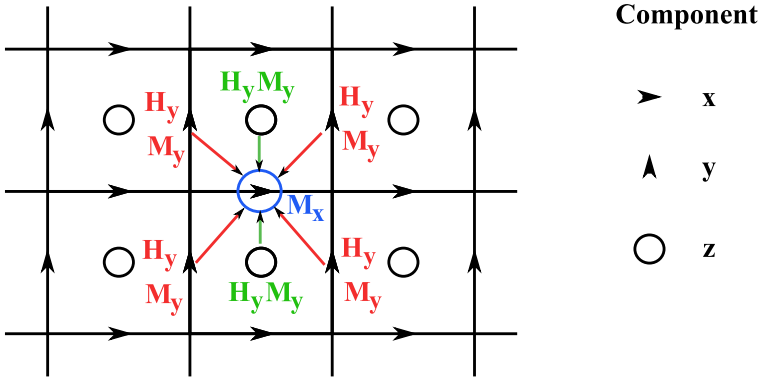

Figure 4.5: Reallocation of components in a 2D Yee's cell for space synchronisation

M_x (blue circle) where M_y at spatial point $(i+\frac{1}{2}, j)$ will be the average of the four M_y components surrounding Mx in Figure 4.5. This is the operation represented by the red arrows denoted below as $M_y\_M_x$.

$$M_y\_M_x\big|_{i+\frac{1}{2},j}^{n+\frac{1}{2}} = \frac{M_y\big|_{i,j-\frac{1}{2}}^{n+\frac{1}{2}} + M_y\big|_{i,j+\frac{1}{2}}^{n+\frac{1}{2}} + M_y\big|_{i+1,j-\frac{1}{2}}^{n+\frac{1}{2}} + M_y\big|_{i+1,j+\frac{1}{2}}^{n+\frac{1}{2}}}{4} \tag{4.89}$$

The same must be done with $H_y\_M_x$ (red arrows operation)

$$H_y\_M_x\big|_{i+\frac{1}{2},j}^{n+\frac{1}{2}} = \frac{H_y\big|_{i,j-\frac{1}{2}}^{n+\frac{1}{2}} + H_y\big|_{i,j+\frac{1}{2}}^{n+\frac{1}{2}} + H_y\big|_{i+1,j-\frac{1}{2}}^{n+\frac{1}{2}} + H_y\big|_{i+1,j+\frac{1}{2}}^{n+\frac{1}{2}}}{4} \tag{4.90}$$

In a similar way $M_z\_M_x$ (M_z to compute M_x) is described by the operation represented by green arrows.

$$M_z\_M_x\big|_{i+\frac{1}{2},j}^{n+\frac{1}{2}} = \frac{M_z\big|_{i+\frac{1}{2},j-\frac{1}{2}}^{n+\frac{1}{2}} + M_z\big|_{i+\frac{1}{2},j-\frac{1}{2}}^{n+\frac{1}{2}}}{2} \tag{4.91}$$

The same must be done with $H_z\_M_x$ if any (green arrows operation).

$$H_z\_M_x\big|_{i+\frac{1}{2},j}^{n+\frac{1}{2}} = \frac{H_z\big|_{i+\frac{1}{2},j-\frac{1}{2}}^{n+\frac{1}{2}} + H_z\big|_{i+\frac{1}{2},j-\frac{1}{2}}^{n+\frac{1}{2}}}{2} \tag{4.92}$$

H_x and M_x to compute M_x will remain the same as they are already in the same spatial position as M_x.

$$M_x\_M_x\big|_{i+\frac{1}{2},j}^{n+\frac{1}{2}} = M_x\big|_{i+\frac{1}{2},j}^{n+\frac{1}{2}} \tag{4.93}$$

$$H_x\_M_x|_{i+\frac{1}{2},j}^{n+\frac{1}{2}} = H_x|_{i+\frac{1}{2},j}^{n+\frac{1}{2}} \tag{4.94}$$

Then the values obtained from (4.89) to (4.94) are used in (4.80) to calculate $f(H_x, H_y, H_z, M_x, M_y, M_z)$ at time step $n+1/2$. To finish the computation of $M_x|^{n+1}$ the previous result and the known value of M_x at time n are introduced in (4.79).

The purpose of all these operations refered here as space and time synchronism is to maintain the second order accuracy in the differentiating scheme.

4.13 Boundary Conditions

From the minimisation of the total energy in a magnetic material, the following boundary condition is derived (Brown, 1978; Aharoni, 2000):

$$\frac{\partial \mathbf{M}}{\partial \mathbf{n}} = 0 \tag{4.95}$$

where $\mathbf{n}$ is the direction normal to the material surface. For example, solving (4.95) at the left boundary of the material ($n = -x$) involves the following operations

$$M_x|_{i+\frac{1}{2}} = M_x|_{i+\frac{3}{2}} \tag{4.96}$$

$$M_y|_i = M_y|_{i+1} \tag{4.97}$$

$$M_z|_{i+\frac{1}{2}} = M_z|_{i+\frac{3}{2}} \tag{4.98}$$

and similar equations would apply for other directions of $\mathbf{n}$.

The perfectly matched layer (PML) around the computational space used in normal FDTD to absorb the outgoing waves can be used for the extended method as far as the magnetic material is surrounded by the computational space and not in contact with the PML areas. This is based on the fact that the magnetisation vector has zero value outside the material (it doesn't exist) therefore the extended equations without the magnetisation are the same as in the normal FDTD method.

4.14 Stability of the Extended Method

Due to the rotation of the magnetisation in a magnetic material another upper limit in Δt must be considered to make a stable solution for Gilbert's equation. The worst case happens when damping is neglected and a strong field is applied in one direction, therefore the magnetisation describes a circular movement perpendicular to the applied field with a precession angular frequency $\omega_0 = \gamma H$ which in this particular case will be equal to the maximum rotational angular frequency of the magnetisation. Then, the equation of motion can be written as:

$$\left.\begin{aligned} \frac{dM_x}{dt} &= \omega_0 M_y \\ \frac{dM_y}{dt} &= -\omega_0 M_x \\ \frac{dM_z}{dt} &= 0 \end{aligned}\right\} \tag{4.99}$$

In order to obtain an equation explicitly for, say M_x, expression (4.99) must be differentiated to give:

$$\frac{d^2 M_x}{dt^2} = \omega_0 \frac{dM_y}{dt} \tag{4.100}$$

Substituting dM_y/dt from (4.99) into (4.100) yields the ordinary differential equation for M_x:

$$\frac{d^2 M_x}{dt^2} = -\omega_0^2 M_x \tag{4.101}$$

Now, applying central finite differences to this equation:

$$\frac{M_x^{n+1} - 2M_x^n + M_x^{n-1}}{(\Delta t)^2} = -\omega_0^2 M_x^n \tag{4.102}$$

and solving for M_x^{n+1} yields the explicit time marching scheme for M_x

$$\begin{aligned} M_x^{n+1} &= 2M_x^n - M_x^{n-1} - \omega_0^2 \Delta t^2 M_x^n \\ &= M_x^n (2 - \omega_0^2 \Delta t^2) - M_x^{n-1} \end{aligned} \tag{4.103}$$

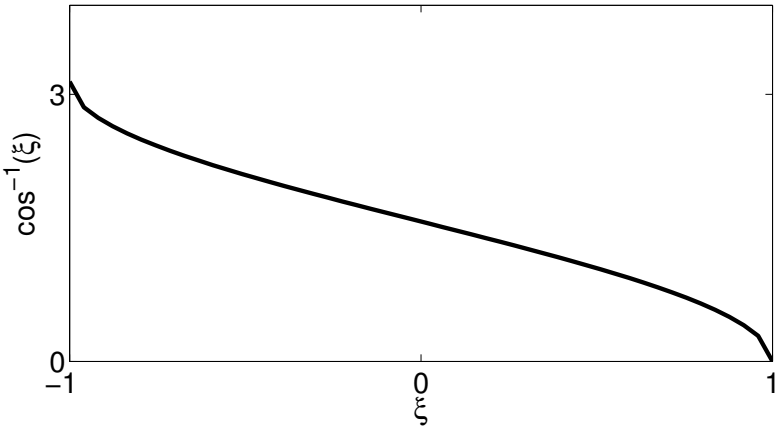

Figure 4.6: Region where $\cos^{-1}\xi$ is real valued

Using a complex exponential solution $M_x = M_s e^{j\omega_0 t}$ and substituting in (4.103) gives

$$e^{j\omega_0(n+1)\Delta t} = e^{j\omega_0 n\Delta t}(2 - \omega_0^2\Delta t^2) - e^{j\omega_0(n-1)\Delta t} \tag{4.104}$$

Expanding the exponential terms and applying Euler's relation to the exponential terms gives

$$2\cos(\omega_0\Delta t) = 2 - \omega_0^2\Delta t^2 \tag{4.105}$$

Equation (4.105) is similar to (4.45) in the fact that it relates the angular frequency of the system to the time increment. Furthermore

$$\omega_0\Delta t = \cos^{-1}\left(1 - \frac{\omega_0^2\Delta t^2}{2}\right) = \cos^{-1}\xi \tag{4.106}$$

As in the general case, stability is found for the values of ξ that make $\omega_0\Delta t$ in equation (4.106) real.

Figure 4.6 represents the region where the function $\cos^{-1}\xi$ has real values (and therefore expression (4.106) has only real values). To have a real valued expression ξ must be between -1 and 1. For any other value of ξ the function $\cos^{-1}\xi$ will be complex valued

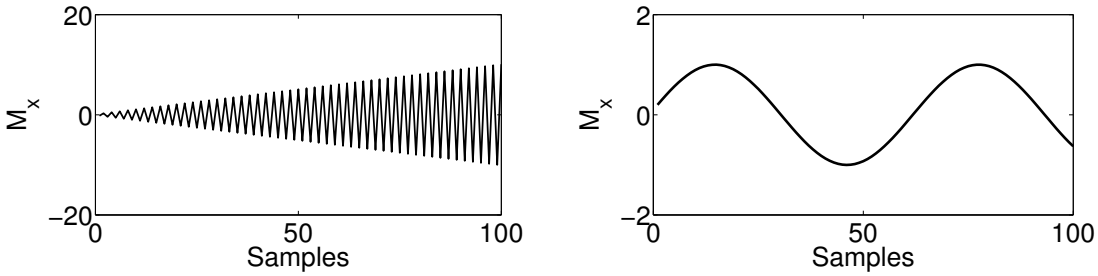

(a) (b)

Figure 4.7: Solution of (4.101) sampled with (a) $\Delta t = 2/\omega_0$ which makes the system unstable and (b) $\Delta t = 0.1/\omega_0$ which makes the system stable.

and therefore the rotation of magnetisation will produce an unstable solution. At the limits of ξ shown in Figure 4.6

$$\xi = 1 - \frac{\omega_0^2 \Delta t^2}{2} = 1 \qquad \rightarrow \qquad \Delta t = 0 \tag{4.107}$$

$$\xi = 1 - \frac{\omega_0^2 \Delta t^2}{2} = -1 \qquad \rightarrow \qquad \Delta t = \frac{2}{\omega_0} \tag{4.108}$$

Therefore defining the range of Δt for the stable solution of the oscillator equation (4.101)

$$0 < \Delta t < \frac{2}{\omega_0} = UpperBound \tag{4.109}$$

This is clearly understood by an example. Figure 4.7(a) represents a sampled solution of (4.101) with a sampling rate of $\Delta t = 2/\omega_0$ which is just over the limit in (4.109) therefore the system is unstable and the solution grows to infinity as time goes on. Figure 4.7(b) is an example of a stable solution where $\Delta t = 0.1/\omega_0$ implies a stable solution.

Although equation (4.109) defines the stable range when the magnetisation is introduced, equation (4.51) still needs to be considered as it rules the stability of the differencing algorithm. Therefore the time increment of the system Δt must be bounded in such a way that satisfies both (4.109) and (4.51) to avoid instability.

To finalise with the stability section, the solution to Gilbert's equation is convergent when the magnetisation is aligned with the applied filed or expressed mathematically as:

$$\frac{|\mathbf{M} \times \mathbf{H}|}{|\mathbf{M}| \cdot |\mathbf{H}|} \approx 1 \tag{4.110}$$

This then provides a test of convergence in the numerical implementation.

4.15 Extended FDTD Routine

To summarise, the flowchart of the main loop of the extended algorithm is shown in Figure 4.8. First, the general initialisation where the constants and variables are declared and the stability condition is satisfied through the apropriate choice of the time and space intervals Δt and Δx. Next, the z component of the electric field is computed as in the normal FDTD method (4.72). Then, the magnetisation vector $\mathbf{M}$ is calculated (the fields that $\mathbf{M}$ depends on are extrapolated, time synchronisation, and interpolated, space synchronisation, in order to be used to calculate the new $\mathbf{M}$ values). After that, the appropriate magnetic boundary condition is enforced. Once the magnetisation vector has been calculated, the new magnetic field components H_x and H_y can be calculated using (4.73) to (4.74). At the end of the process, the current sources if any are updated. This completes a cycle of the main loop, the new field values are delayed Δt seconds in time with respect to their previous values. The cycle is then repeated until the total simulation time is reached.

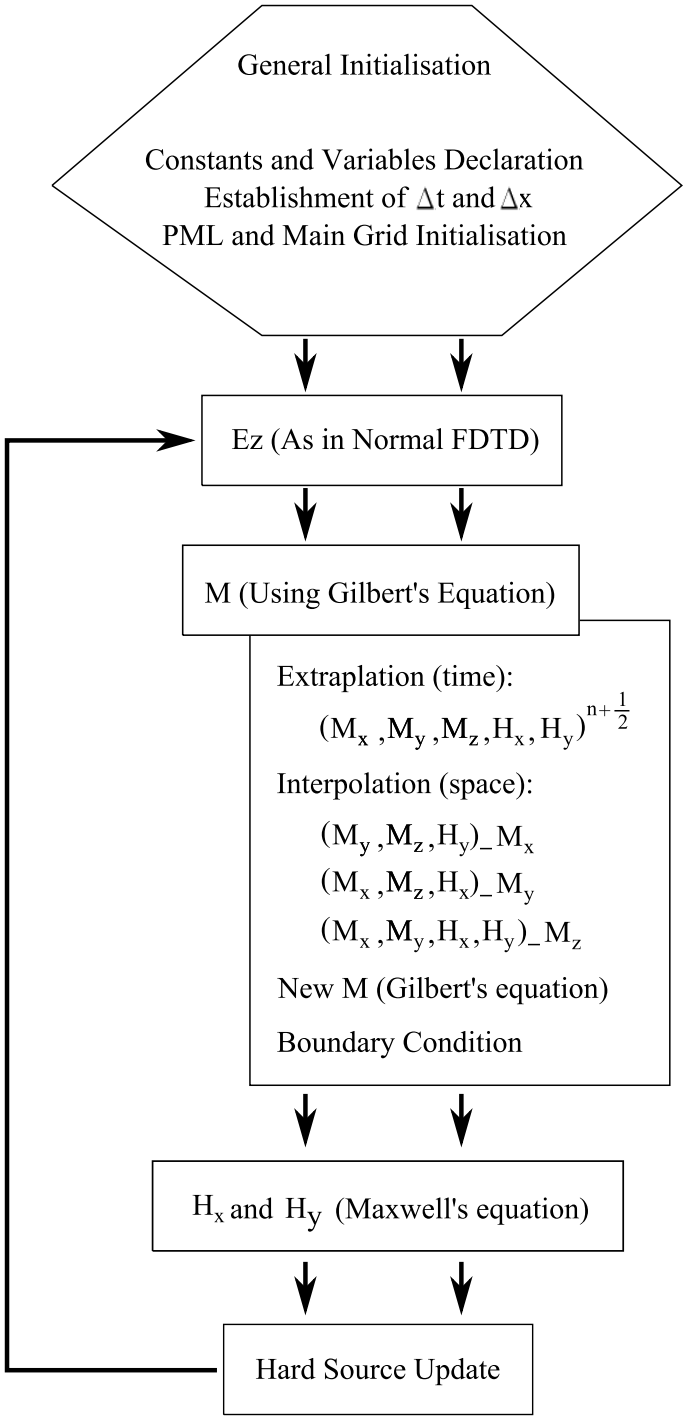

Figure 4.8: Flowchart of the main loop of the FDTD algorithm for non-linear magnetic materials

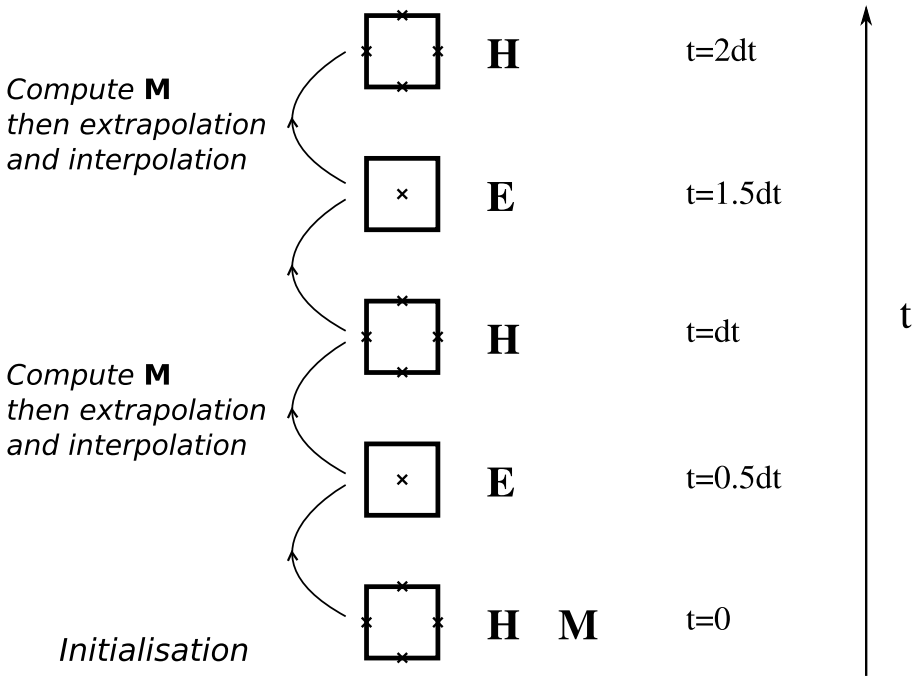

Figure 4.9: Time chart of the extended algorithm showing the leapfrog due to the time derivatives.

4.16 Summary

The FDTD algorithm has been explained and general expressions have been given to allow its implementation. Dificulties in implementing the FDTD algorithm such as stability and reflections into the computational space have been stated and studied. To avoid instability a stability condition has been obtained. To avoid reflections into the computational space a perfectly matched layer boundary condition has been considered. An extended FDTD method for modelling of non-linear magnetic materials has been proposed. General expressions relating field propagation to the rotational magnetisation have been given to allow the implementation of the extended method. Difficulties in implementing the extended method such as the reallocation of the fields and the enforced boundary condition on the material surfaces have been analysed. Finally, the stability of the extended method has been studied and an expression has been given to assure the stability of the method.

Chapter 5

Modelling and Simulation of Thin-Film Heads Using the FDTD Method

5.1 Introduction

The finite difference time domain (FDTD) technique is an explicit and versatile time domain method for solving Maxwell's equations. It provides spatial and temporal representation of electric and magnetic fields within the simulation space and offers an infinite bandwidth for fields and sources due to its time domain nature (Hagness and Taflove, 2000). Thus it provides the ideal platform for studying the high frequency dynamics in magnetic recording heads.

Previous extensions to the FDTD method to model Ferrites were limited to including a frequency dependant permeability tensor (Pereda et al., 1995), or a linearised form of the equation of motion of the magnetisation (Okoniewski and Okoniewska, 1994) without detailed treatment of anisotropy and exchange forces. They also lacked treatment of boundaries and numerical stability. A full treatment of the damped, precessional motion of the magnetisation in a magnetic material, as described by the LLG equa-

tion (Brown, 1978), has been implemented and tested in the following sections for the purpose of this thesis. The effective field in this implementation includes magnetocrystalline anisotropy fields, exchange fields, applied fields, and the magnetostatic and eddy current fields (both computed naturally by the FDTD method). Implementation of this new approach requires resolution of a number of issues. First, the conflict between the local nature of fields and magnetisation components in space in the equation of motion, and the uncolocated nature of the FDTD cell where fields are displaced by half-cells in space.

One of the main aims of this research is to perform numerical simulations of actual thin-film heads that include a micromagnetic description of the material and therefore this chapter covers the essence behind this work. In the following sections the extended FDTD method described in Chapter 4 will be built up from the initial FDTD model for linear materials and tested for a number of structures before attempting to simulate the head structures obtained by experimentation in Chapter 6. First, the standard FDTD algorithm will be implemented and surrounded by an absorbing PML boundary, as described in Chapter 4. Then the correct implementation of current sources and the propagation of electromagnetic waves within the computational space will be studied. The chapter will continue with the implementation of materials having linear properties inside the computational space to observe reflections and the penetration of the waves as related to the concept of skin depth studied in Chapter 2. Implementation of magnetic materials having non-linear properties will follow and magnetic fields and magnetisation distributions will be analysed using the micromagnetic theory explained in section 3.3. Finally, the purpose of this chapter, to compute numerical simulation of practical and/or realistic head structures, will be dealt with. The head geometry and materials were obtained by experimentation in Chapter 6. The results of the simulations will be analysed in detail to observe the effects introduced by the micromagnetic formulation into the FDTD method.

5.2 The Computational Space and PML Absorbing Boundary Condition

The computational space is defined as the region where the electric and magnetic fields **E** and **H** are being computed. Considering the two-dimensional TM_z mode, the computational space consists of three field matrices, E_z, H_x and H_y. Due to the characteristic positioning of electric and magnetic fields in a Yee's cell the three field matrices have different dimensions. In a TM_z mode two-dimensional Yee's cell at a given position, every E_z component of the electric field is surrounded by four magnetic field components as shown in Figure 5.1.

The mathematical representation of an $i_m \times j_m$ dimensional computational space consists of a matrix with dimensions $[i_m \times j_m]$ representing the z component of the electric field E_z, and another two matrices with dimensions $[i_m \times (j_m + 1)]$ and $[(i_m + 1) \times j_m]$ representing the x and y components of the magnetic field, H_x and H_y. In this manner each field component at a given position (i, j) in the Yee's cell diagram of Figure 5.1 can be easily addressed, the E_z component in the diagram corresponds with the row j, column i element of the electric field matrix $E_z|_{i,j}$, H_{y1} and H_{y2} are addressed as $H_y|_{i,j}$ and $H_y|_{i+1,j}$ respectively and H_{x1} and H_{x2} as $H_x|_{i,j}$ and $H_x|_{i,j+1}$. At a given iteration n, the updated E_z matrix represents the electric field at time $(n+\frac{1}{2})\Delta t$ whereas the updated H_x and H_y matrices represent the magnetic field components at time $(n+1)\Delta t$. That is $E_z|^{n+\frac{1}{2}}$, $H_x|^{n+1}$ and $H_y|^{n+1}$. Δt is the time step of the FDTD algorithm that, in combination with the grid size Δx, ensures that the stability condition (4.52) is satisfied.

The computational space will be initially filled with air and later on with dielectric, conductor and magnetic materials to observe the propagation of electromagnetic waves through them. Linear materials can be defined by specifying their electrical and magnetic parameters, i.e. relative permeability (μ_r) and permittivity (ϵ_r), and electrical

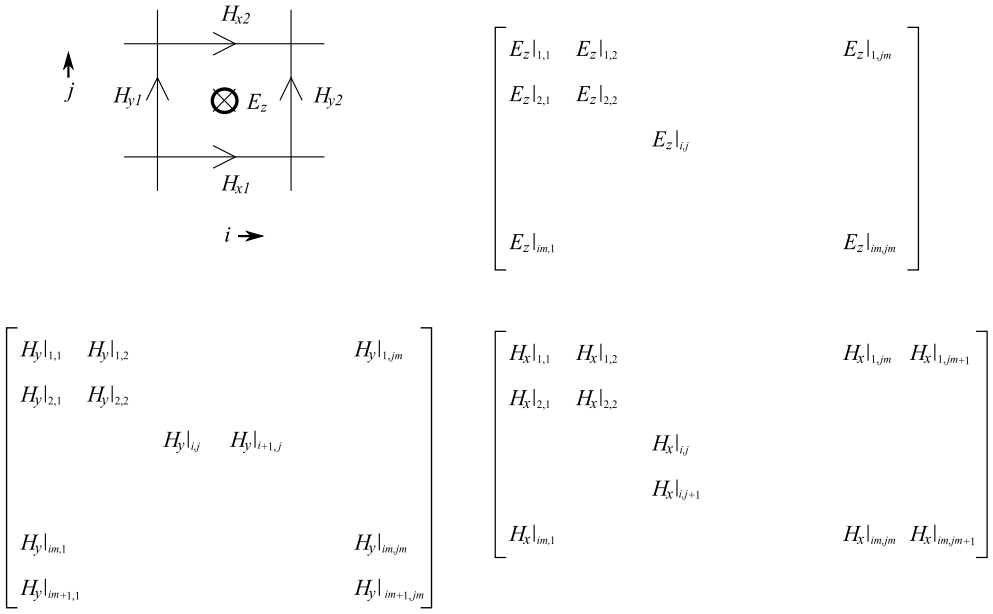

Figure 5.1: Two-dimensional TM_z mode Yee's cell at position (i, j) and mathematical representation of the computational space.

(σ) and magnetic (σ^*) conductivities, over the region of the computational space they occupy. Note that the magnetic conductivity σ^* is only used in the implementation of the PML boundary which is needed to simulate an infinite computational space (i.e. to absorb outgoing waves). Non-linear materials will be studied in detail in section 5.5. In every iteration of the FDTD algorithm, these material parameters will have an effect on the electromagnetic fields through the updating coefficients defined in equations (4.25) to (4.28). For simplicity when doing matrix operations the following matrices are used in the implementation: C_a and C_b with same dimensions as the Ez field matrix, D_{ax} and D_{bx} with same dimensions as the H_x field matrix and D_{ay} and D_{by} with same dimensions as the H_y field matrix. The matrices defined in Table 5.1 together with the updating coefficients equations (4.25) to (4.28) and the finite difference expressions of (4.29) to (4.31) form the basic two-dimensional TM_z mode FDTD algorithm. However, with this simple implementation the computational space is surrounded by a perfect magnetic conductor which reflects all the outgoing waves back into the computational

Table 5.1: Summary of matrices and dimensions in main computational space of the standard FDTD algorithm.

Field Matrices	Updating Coefficients	
	ϵ_r and σ	μ_r and σ^*
$E_z[i_m \times j_m]$	$C_a[i_m \times j_m]$	$D_{ax}[i_m \times (j_m + 1)]$
$H_x[i_m \times (j_m + 1)]$	$C_b[i_m \times j_m]$	$D_{bx}[i_m \times (j_m + 1)]$
$H_y[(i_m + 1) \times j_m]$		$D_{ay}[(i_m + 1) \times j_m]$
		$D_{by}[(i_m + 1) \times j_m]$

space.

As seen in section 4.9, in order to implement an infinitely large theoretical space extension the computational space must be surrounded by an absorbing boundary material or perfectly matched layer (PML). If this is not implemented the propagating electromagnetic waves would be reflected into the computational space and result in incorrect computations. For the purpose of this work a 10-cell thick PML boundary with polynomial grading was implemented around the computational space.

An efficient implementation of a 10-cell thick PML requires some modification of the matrices in Table 5.1. The PML region must surround the main computational space as in Figure 4.4, thus, all matrices must be increased in size each one having twenty more rows and twenty more columns. The field splitting modification studied in section 4.9.2 lead to the following finite difference expressions for the PML regions of the FDTD algorithm

$$\begin{aligned} E_{zx}|^{n+\frac{1}{2}}_{i+\frac{1}{2},j+\frac{1}{2}} &= C_{ax}|_{i+\frac{1}{2},j+\frac{1}{2}} E_{zx}|^{n-\frac{1}{2}}_{i+\frac{1}{2},j+\frac{1}{2}} \\ &+C_{bx}|_{i+\frac{1}{2},j+\frac{1}{2}} \left(H_y|^{n}_{i+1,j+\frac{1}{2}} - H_y|^{n}_{i,j+\frac{1}{2}} \right) \end{aligned} \tag{5.1}$$

$$\begin{aligned} E_{zy}|^{n+\frac{1}{2}}_{i+\frac{1}{2},j+\frac{1}{2}} &= C_{ay}|_{i+\frac{1}{2},j+\frac{1}{2}} E_{zy}|^{n-\frac{1}{2}}_{i+\frac{1}{2},j+\frac{1}{2}} \\ &+C_{by}|_{i+\frac{1}{2},j+\frac{1}{2}} \left(+H_x|^{n}_{i+\frac{1}{2},j} - H_x|^{n}_{i+\frac{1}{2},j+1} \right) \end{aligned} \tag{5.2}$$

$$E_z|^{n+\frac{1}{2}}_{i+\frac{1}{2},j+\frac{1}{2}} = E_{zx}|^{n+\frac{1}{2}}_{i+\frac{1}{2},j+\frac{1}{2}} + E_{zy}|^{n+\frac{1}{2}}_{i+\frac{1}{2},j+\frac{1}{2}} \tag{5.3}$$

$$\begin{aligned} H_x|^{n+1}_{i+\frac{1}{2},j+1} &= D_{ax}|_{i+\frac{1}{2},j+1} H_x|^{n}_{i+\frac{1}{2},j+1} \\ &+ D_{bx}|_{i+\frac{1}{2},j+1} \left(E_z|^{n+\frac{1}{2}}_{i+\frac{1}{2},j+\frac{1}{2}} - E_z|^{n+\frac{1}{2}}_{i+\frac{1}{2},j+\frac{3}{2}} \right) \end{aligned} \tag{5.4}$$

$$\begin{aligned} H_y|^{n+1}_{i+1,j+\frac{1}{2}} &= D_{ay}|_{i+1,j+\frac{1}{2}} H_y|^{n}_{i+1,j+\frac{1}{2}} \\ &+ D_{by}|_{i+1,j+\frac{1}{2}} \left(E_z|^{n+\frac{1}{2}}_{i+\frac{3}{2},j+\frac{1}{2}} - E_z|^{n+\frac{1}{2}}_{i+\frac{1}{2},j+\frac{1}{2}} \right) \end{aligned} \tag{5.5}$$

Where the updating coefficients C_{ax}, C_{ay}, C_{bx}, C_{by}, D_{ax}, D_{ay}, D_{bx} and D_{by} are calculated using the PML material conductivities σ_x, σ_y, σ_x^* and σ_y^* as follows

$$C_{ax}|_{i,j} = \left(1 - \frac{\sigma_x|_{i,j}\Delta t}{2\varepsilon_{i,j}}\right) \Big/ \left(1 + \frac{\sigma_x|_{i,j}\Delta t}{2\varepsilon_{i,j}}\right) \tag{5.6}$$

$$C_{ay}|_{i,j} = \left(1 - \frac{\sigma_y|_{i,j}\Delta t}{2\varepsilon_{i,j}}\right) \Big/ \left(1 + \frac{\sigma_y|_{i,j}\Delta t}{2\varepsilon_{i,j}}\right) \tag{5.7}$$

$$C_{bx}|_{i,j} = \left(\frac{\Delta t}{\varepsilon_{i,j}\Delta}\right) \Big/ \left(1 + \frac{\sigma_x|_{i,j}\Delta t}{2\varepsilon_{i,j}}\right) \tag{5.8}$$

$$C_{by}|_{i,j} = \left(\frac{\Delta t}{\varepsilon_{i,j}\Delta}\right) \Big/ \left(1 + \frac{\sigma_y|_{i,j}\Delta t}{2\varepsilon_{i,j}}\right) \tag{5.9}$$

$$D_{ax}|_{i,j} = \left(1 - \frac{\sigma_x^*|_{i,j}\Delta t}{2\mu_{i,j}}\right) \Big/ \left(1 + \frac{\sigma_x^*|_{i,j}\Delta t}{2\mu_{i,j}}\right) \tag{5.10}$$

$$D_{ay}|_{i,j} = \left(1 - \frac{\sigma_y^*|_{i,j}\Delta t}{2\mu_{i,j}}\right) \Big/ \left(1 + \frac{\sigma_y^*|_{i,j}\Delta t}{2\mu_{i,j}}\right) \tag{5.11}$$

$$D_{bx}|_{i,j} = \left(\frac{\Delta t}{\mu_{i,j}\Delta}\right) \Big/ \left(1 + \frac{\sigma_x^*|_{i,j}\Delta t}{2\mu_{i,j}}\right) \tag{5.12}$$

$$D_{by}|_{i,j} = \left(\frac{\Delta t}{\mu_{i,j}\Delta}\right) \Big/ \left(1 + \frac{\sigma_y^*|_{i,j}\Delta t}{2\mu_{i,j}}\right) \tag{5.13}$$

The main computational space parameters are initially set up to be free space, therefore $\sigma_x = \sigma_y = \sigma_x^* = \sigma_y^* = 0$ applies. Furthermore, if any material region is to be defined

in the main computational space its parameters must be defined such as $\sigma_x = \sigma_y = \sigma_{material}$ and $\sigma_x^* = \sigma_y^* = \sigma_{material}^*$. In this manner, the above equations in the main computational space reduce to the system of equations in (4.29) to (4.31) and the set of updating coefficients (4.25) to (4.28) studied in section 4.5. In the PML regions the electrical and magnetic conductivities have finite values according to Figure 4.4 but changing their values gradually within the thickness of the PML boundary. The optimal value of the electrical conductivity σ_{max} is expressed in equation (4.66). Then the magnetic conductivity σ^* can be computed as

$$\sigma^* = \sigma \frac{\mu_0 \mu_r}{\epsilon_0 \epsilon_r} \tag{5.14}$$

The grading of the PML is done by increasing the conductivity values from zero in the inner boundary to σ_{max} and σ_{max}^* at the outer boundary. These gradually increasing values of the electrical and magnetic conductivities are taken into account in the algorithm through the updating coefficient matrices and therefore all outgoing traveling waves will be absorbed at the PML boundary.

With this implementation of the PML each iteration of the main loop of the FDTD algorithm will only require to traverse the matrices at once without the need of special intervals especially dedicated to the wave absorbing functions of the PML boundary.

5.3 Sources and Propagation

Sources of electromagnetic waves can be classified in two different categories, they can be soft or hard sources. The difference between them lies in the way they are implemented. Soft sources are updated to the current value of the field whereas hard sources take the place of the current value of the field. For instance, to generate a point source at position (i_s, j_s) inside of a TM_z mode computational space the electric

field E_z matrix should be excited at the source position as

$$E_z|_{i_s,j_s} = E_z|_{i_s,j_s} + Source \tag{5.15}$$

in order to implement a soft source. On the other hand, if the excitation takes the form

$$E_z|_{i_s,j_s} = Source \tag{5.16}$$

a hard source is implemented. The sources of electromagnetic waves are in general time dependant functions and the waveforms to be used in this work are summarised in Figure 5.2. They are the Gaussian pulse of amplitude A and decay rate τ centered around t_0 and mathematically expressed as

$$S_1 = Ae^{-\left(\frac{t-t_0}{\tau}\right)^2} \tag{5.17}$$

and the step function of amplitude A and rise time τ is given by

$$S_2 = A\left(1 - e^{\frac{-t}{\tau}}\right) \tag{5.18}$$

A point source located at the center of a two-dimensional FDTD computational space generates a radially propagating cylindrical wave centered on the source point which eventually, assuming that the appropriate absorbing boundary has been implemented, exits the computational space. For the purpose of this work, as the excitations on magnetic heads take the form of electric currents through a coil, electromagnetic waves coming from electric current excitations will be studied. The soft source in equation (5.15) is equivalent to applying a current source J_{source_z} directly in the E_z field equation (4.29) of the two-dimensional FDTD algorithm for the TM_z mode.

In addition to radiating fields to infinity, soft sources implemented as in (5.15) can deposit charge and generate charge-associated fields. Such charge can exist even though there is no explicit storage location for it. Indeed, the charge exists only insofar as

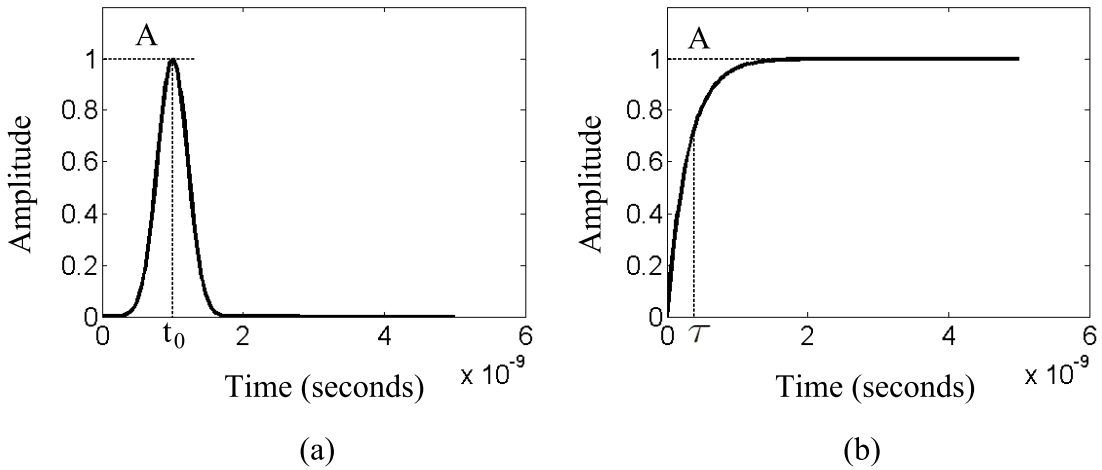

Figure 5.2: Typical time dependant source amplitude waveform over a 5ms time interval (a) Gaussian pulse centered at $t_0 = 1$ns, unitarian amplitude and decay rate $\tau = 0.3$ns. (b) Step function of unitarian amplitude and rise time $\tau = 0.3$ns.

diverging fields exist. These diverging fields can persist indefinitely and hence, remain in the computational domain even after all of the radiated fields have exited.

To understand this, consider the relation between the electric field $\mathbf{E}$ and the electric charge density ρ in free space given by Gauss' law

$$\epsilon_0 \nabla \cdot \mathbf{E} = \rho \tag{5.19}$$

Thus, when the electric field diverges from a point, (5.19) states that the charge density is nonzero. The relation between the electric current density $\mathbf{J}$ and the electric charge density ρ is then given by the continuity equation

$$\nabla \cdot \mathbf{J} = -\frac{\partial \rho}{\partial t} \tag{5.20}$$

Figure 5.3 shows the magnitude of the electric and magnetic fields for three consecutive time steps in a two-dimensional FDTD lattice which was excited at the center with a soft Gaussian pulse current point source, equation (5.17). In this visualisation it is possible to observe the propagation of the electromagnetic fields and the electric

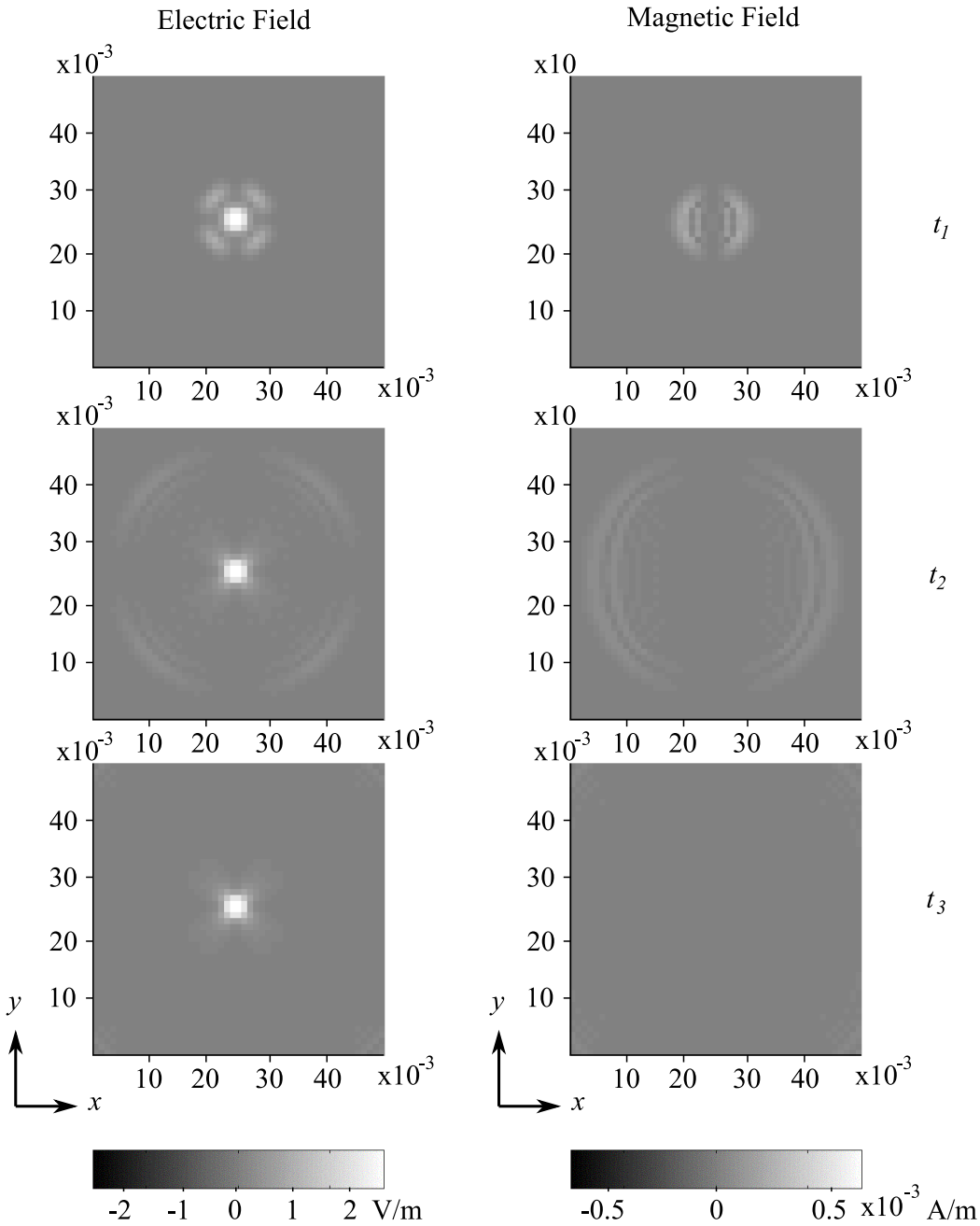

Figure 5.3: Soft current source at the center of an FDTD lattice and the electric field associate to the charge. Simulation parameters: $\Delta x = 1$mm, $\Delta t = 1.6$ps, $t_1 = 49.6$ps, $t_1 = 99.2$ps, $t_1 = 148.8$ps. Soft source parameters: Gaussian point source current characterised by an amplitude of 40mA, decay rate $\tau = 5$ps and delay $t_0 = 33$ps. Computational space properties set up to free space.

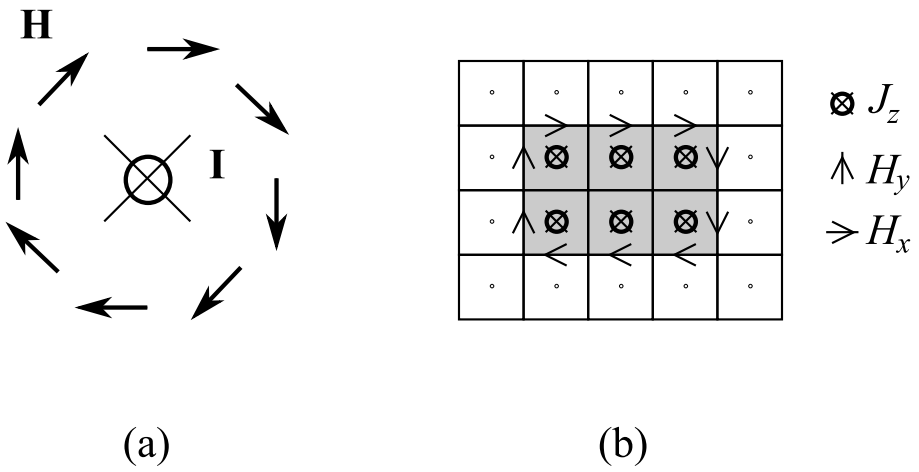

Figure 5.4: Current in a filament. (a) cross section of the filament showing the direction of the current and the distribution of the generated magnetic fields. (b) FDTD implementation of current sources, note the direction of the magnetic field components. The gray region represents the filament therefore the appropriate electrical conductivity and permittivity must be set to those of the actual filament.

field associated with the charge due to the divergence of the electric fields which still remains after all the fields have disappeared. This field magnitude associated with the electric charge may cause incorrect computations, therefore an alternative implementation using magnetic field excitation hard sources will be considered next.

Figure 5.4(a) shows the magnetic field generated around a filament carrying a current. Assuming that the current is the z direction, it can be implemented in a TM_z mode FDTD lattice by setting up the x and y component of the magnetic field, H_x and H_y, around the filament as in Figure 5.4(b) to a certain value which will be calculated according to Ampere's law (3.41). That is

$$H_x = H_{x(source)} \tag{5.21}$$

$$H_y = H_{y(source)} \tag{5.22}$$

such as that $H_{x(source)}$ and $H_{y(source)}$ represent the electric current density J_z through the filament. When implementing sources, the electrical properties of the coil material (e.g. copper) must be set up and taken into account by the algorithm through the

updating coefficients. Assuming as an example a grid cell size of 1μm for the diagram in Figure 5.4(b), a 10mA current would be implemented by setting up the value of the magnetic field component around the filament to 1000A/m, which comes from solving Gauss' law for $\mathbf{H}$, 10mA = $\mathbf{H}[10 \times 1\mu]$m. The magnetic field components inside the cross section of the source have zero value because the contribution due to adjacent current densities J_z located at the center of every individual cell cancel each other. Note that arrows pointing upwards and downwards in the diagram correspond to positive and negative values of the vertical component H_y and arrows pointing rightwards and leftwards correspond to positive and negative values of the horizontal component H_x. This is the way in which electric currents are implemented through this work, rather than applying a soft source (J_z), to avoid the problem of charges. In order to prove the above statement, the same FDTD lattice used in Figure 5.3 was excited now with a hard Gaussian current point source and the results are shown in Figure 5.5 where no charge-associated electric field remains as the time goes on and the propagating electromagnetic field leave the computational space.

Besides enforcing the source fields on the computational lattice, the electrical and magnetic properties of the source material must be defined inside the computational space in order to fully simulate electric currents in a filament. If this is not implemented there would be fields inside the filament which is not in agreement with reality. The typical parameters of a perfect electric conductor (e.g. copper) are conductivity $\sigma = 5.8 \times 10^7$ [$1/\Omega$m] and relative permittivity $\epsilon_r = 4.8$. Material structures inside the computational domain are considered next.

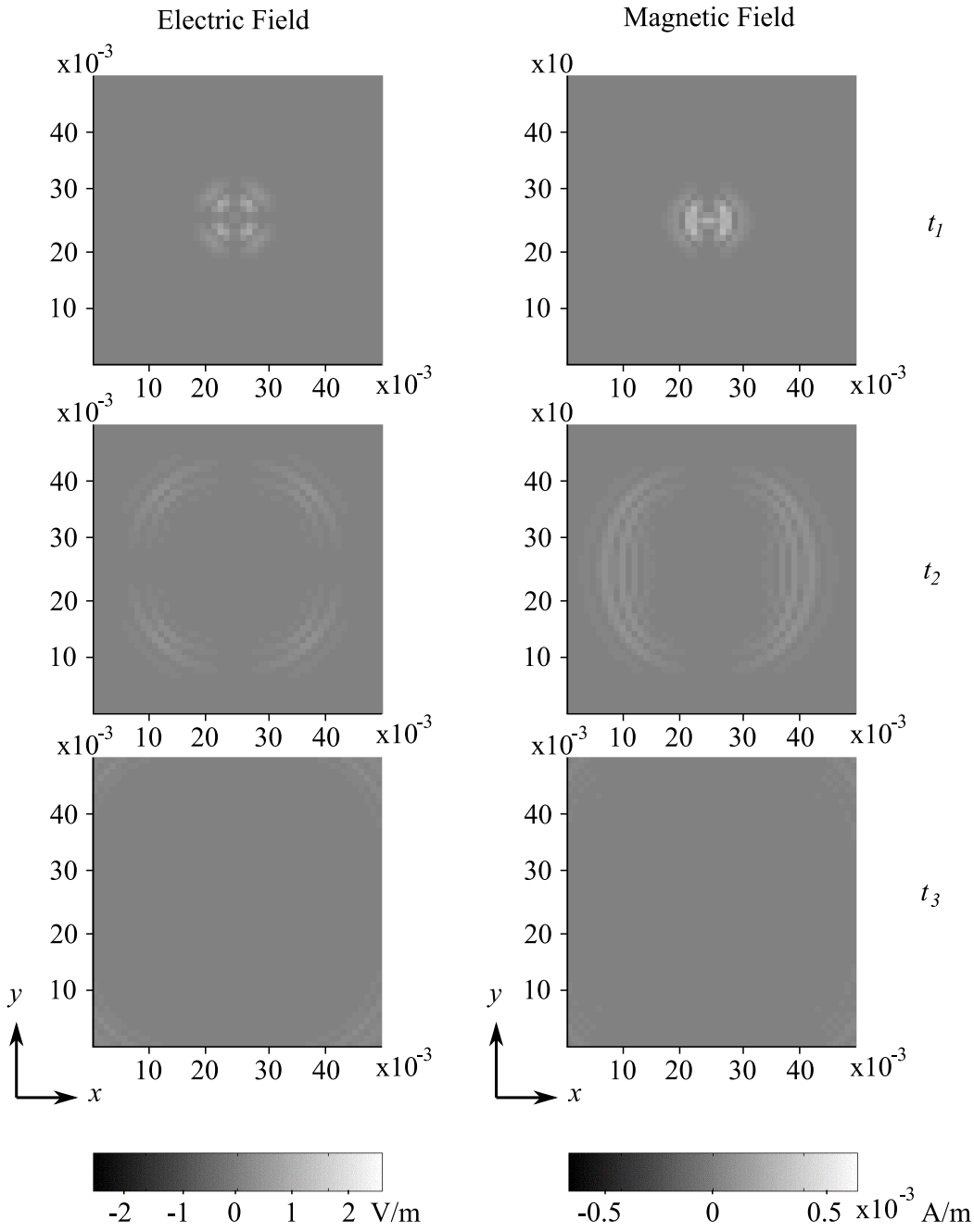

Figure 5.5: Hard current source excitation with no remanent charge effect. Simulation parameters: $\Delta x = 1$mm, $\Delta t = 1.6$ps, $t_1 = 49.6$ps, $t_1 = 99.2$ps, $t_1 = 148.8$ps. Hard source parameters: Gaussian point source current characterised by an amplitude of 40mA, decay rate $\tau = 5$ps and delay $t_0 = 33$ps. Computational space properties set up to free space.

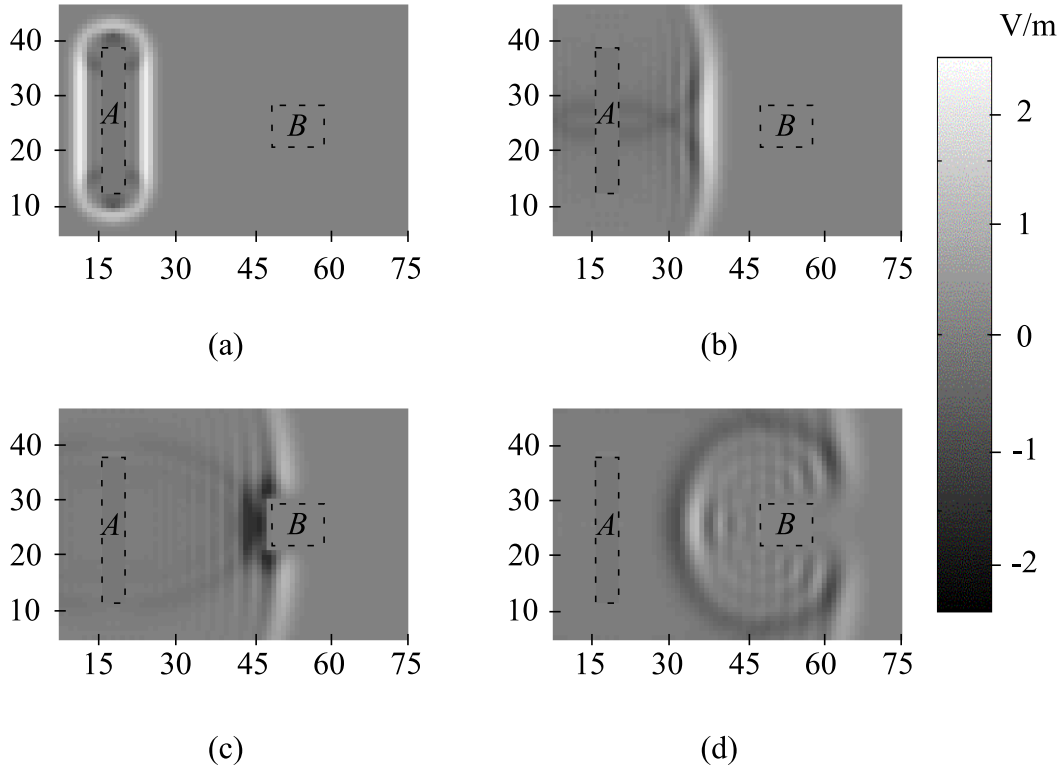

Figure 5.6: Propagation of the electric field E_z arising from an electric current on a TM_z mode FDTD lattice containing a region of conductive material at four consecutive time instants. (a)$t = 50$ps, (b)$t = 100$ps, (c)$t = 150$ps and (d)$t = 200$ps.

5.4 Computational Space Containing Linear Materials

Materials are defined by setting up their electrical and magnetic parameters, ϵ, σ, μ and σ^* over a region of the space. These parameters are taken into account when computing the electric and magnetic fields through the updating coefficients (4.25) to (4.28).

Consider a TM_z computational domain with dimensions 75×50mm where a rectangular hard current source of dimensions 5×30mm (A in Figure 5.6) and a 10×10mm region

made of conductive material (B in Figure 5.6). The space increment of the main grid is $\Delta x = 1 \times 10^{-3}$m and the corresponding time increment for stability is $\Delta t = 1.67$ps. The source region A is made of a good conductor material, characterised by $\sigma = 5.8 \times 10^{+7}$ $1/\Omega$m and $\epsilon_r = 4.8$. The permeable material region B has properties $\sigma = 5 \times 10^{+6}$ $1/\Omega$m and $\mu_r = 2000$. The excitation is a Gaussian current source with an amplitude of 14mA, time delay $t_0 = 30$ps and decay rate $\tau = 5$ps. Figure 5.6 shows the propagation of the generated electric field E_z by the excitation source at four consecutive time instants at a sampling rate of 50ps where reflections from the material structure B can be observed. In this example the propagation of electric field was chosen for ilustration. However, similar plots can be obtained to ilustrate the propagation of magnetic fields. The rise time of the source excitation is very small which in turn forces a very large frequency range. The Fourier transform of the source pulse allows the estimation of the cut off frequency or -3dB point, which, for this particular waveform, is about 100GHz. The skin depth of material B at the maximum frequency of operation computed using equation (2.54) is $\delta = 1.59 \times 10^{-12}$mm, which is in agreement with Figure 5.6(d) where no field can be observed inside the material region.

Figure 5.7 shows the propagation of a Gaussian pulse with decay time $\tau = 100\mu$s through a one-dimensional medium containing a section of linear material with relative permeability $\mu_r = 200$ and electrical conductivity $\sigma = 4.5 \times 10^2 1/\Omega$m. For this particular example, the material region skin depth at the cut off frequency is $\delta = 18.8\mu$m. Therefore, the field penetrating the material is subjected to an exponential decay where its amplitude has been decreased to e^{-1} when the skin depth is reached.

Materials defined with the method described in this section are considered linear as it is assumed that the magnetic field density $\mathbf{B}$ is a linear function of the magnetic field $\mathbf{H}$. Non-linear materials, where the relation between $\mathbf{B}$ and $\mathbf{H}$ is not linear, are addressed in the next section.

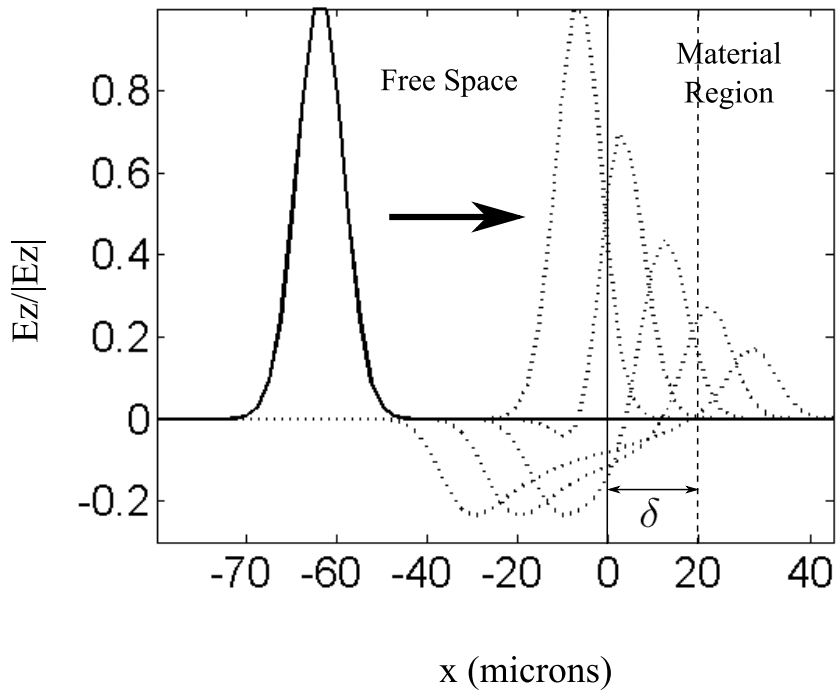

Figure 5.7: Propagation of a Gaussian pulse on a computational space containing a linear material. The skin depth of the material region at the frequency of the pulse is $\delta = 20\mu$m

5.5 Computational Space Containing Non-Linear Materials

The purpose of this section is to implement and test the extended FDTD algorithm described in Chapter 4. This method combines the micromagnetic description of materials with the field solution of Maxwell's equations and therefore would be used to characterise non-linear magnetic behaviour of materials.

The main repercussion of a non-linear magnetic behaviour is that the magnetic flux density **B** can no longer be expressed as a linear function of the magnetic field **H**, instead, it must be expressed as a function of the sum of the applied magnetic field **H** and the magnetisation **M** of the material as stated in equation (3.15).

As seen in section 3.3.2 the magnetisation of a non-linear magnetic material is described by a differential equation called the equation of motion (3.105) which analytical solution for the particular case of a z directed magnetic field was given in (3.110). Thus, the first problem to overcome in describing non-linear materials is to obtain an accurate solution for M_x, M_y and M_z in the equation of motion for any given effective field **H**. A finite difference method for solving the equation of motion was given in section 4.11 which will be now tested and compared with the analytical solution.

Figure 5.8 compares the solution of the equation of motion using the method described in section 3.3.2 with the analytical solution given in (3.110) for two different values of the damping coefficient α and a z directed effective field. To obtain these results a very strong applied field of 20kOe was applied to a material having a saturation magnetisation of 100A/m for a period of time of 100ps. As expected, the response of the material with greater damping factor is quicker. It is also observed that the results obtained using the discretisation of the equation of motion are in agreement with the analytical solution.

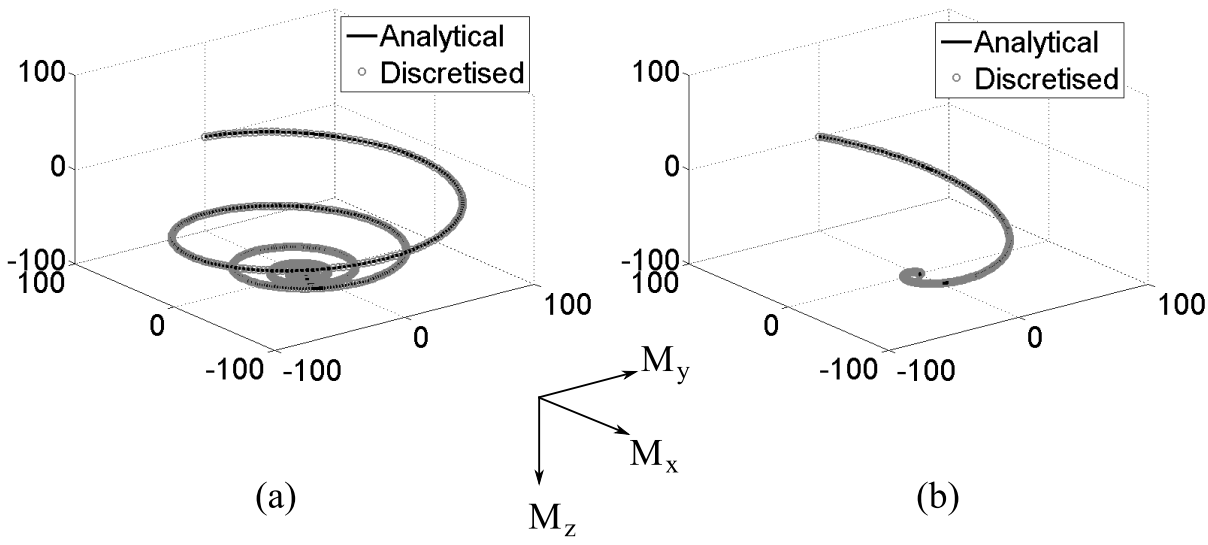

Figure 5.8: Solution of the equation of motion for a z directed effective field using the analytical solution and the method explained in section 4.11 for two different values of the damping coefficient (a) $\alpha = 0.1$ and (b) $\alpha = 0.6$.

The next step in describing non-linear materials is to implement the modified FDTD algorithm described in section 4.15 where magnetic materials are characterised by their conductivity σ and magnetisation $\mathbf{M}$, i.e. no relative permeability μ_r is defined. The material's conductivity affects the electromagnetic fields of the calculations as before through the updating coefficients (4.25) to (4.28). The magnetisation vector is now taken into account directly in the algorithm's equations through the time derivative (time difference of M_x and M_y components) as shown in (4.73) and (4.74). In order to compute the new values of the magnetisation at each iteration, syncronisation in time and in space are required (section 4.12). Enforcing synchronism yields to the definition of a new set of auxiliary matrices that must be added to the computational space. These are listed in Table 5.1, section 5.2.

From equations (4.73) and (4.74), four new matrices are needed which represent the x and y components of the magnetisation at time instants n and $n+1$. That is, $M_x|^n$, $M_x|^{n+1}$, $M_y|^n$ and $M_y|^{n+1}$. The magnetisation components at time instant $n+1$ are

obtained using the system of equations (4.75) to (4.77). Hence, as M_z is used in all three equations, matrices for the z component of the magnetisation at time n and $n+1$ are also needed, that is $M_z|^n$ and $M_z|^{n+1}$. M_x, M_y and M_z matrices are the same size as H_x, H_y and E_z respectively. Here the magnetic field components represent the effective field (section 3.3.3).

As described in section 4.12, equation (4.82) must be applied to every component that appears on the right hand side of equations (4.75) to (4.77) in order to solve the problem of time synchronism. This leads to the definition of matrices $H_x|^{n+\frac{1}{2}}$, $H_y|^{n+\frac{1}{2}}$, $H_z|^{n+\frac{1}{2}}$, $M_x|^{n+\frac{1}{2}}$, $M_y|^{n+\frac{1}{2}}$ and $M_z|^{n+\frac{1}{2}}$. However, in order to compute the above matrices at time instant $n+\frac{1}{2}$, their values at time $n-1$ need to be stored in memory hence the need for $H_x|^{n-1}$, $H_y|^{n-1}$, $H_z|^{n-1}$, $M_x|^{n-1}$, $M_y|^{n-1}$ and $M_z|^{n-1}$.

The contributions to the effective field from the demagnetising field $\mathbf{H_{demag}}$ is taken into account inherently by the nature of the FDTD algorithm in the computed magnetic field. If the externally applied field $\mathbf{H_{ext}}$ takes the form of a radiating hard source, the propagating fields are computed inherently by the algorithm from a propagating hard source. On the other hand, this external field can be obtained separately, as the case of uniformly distributed applied fields from current sources, and then added to the FDTD computed field. The anisotropy and exchange fields ($\mathbf{H_{anis}}$, $\mathbf{H_{exch}}$) need to be obtained separately and added to the magnetic field resulting from the FDTD computations before synchronism. The anisotropy field $\mathbf{H_{anis}}$ depends on the z component of the magnetisation and was given in (3.125). An expression for the exchange field was given in (3.124). The Laplacian ∇^2 of each vector component of $\mathbf{M}$ can be evaluated using second order accurate finite differencing. Considering the x component and assuming $\Delta x = \Delta y = \Delta z = \Delta h$, the Laplacian yields

$$\nabla^2 M_x = \frac{\partial^2 M_x}{\partial x^2} + \frac{\partial^2 M_x}{\partial y^2} + \frac{\partial^2 M_x}{\partial z^2} \tag{5.23}$$

In two dimensions there is no variation in the z direction, thus $\partial^2/\partial z^2 = 0$. Then by

taking finite central differences

$$\begin{aligned}\nabla^2 M_x = \; & [M_x(x+\Delta h, y) + M_x(x-\Delta h, y) \\ & M_x(x, y+\Delta h) + M_x(x, y-\Delta h) \\ & -4M_x(x,y)]\,/(\Delta h)^2\end{aligned} \tag{5.24}$$

Expressions for $\nabla^2 M_y$ and $\nabla^2 M_z$ can be derived in a similar way.

Figure 5.9(a) represents the left hand boundary ($-x$ directed) of a magnetic material where the M_x component at the boundary ($x = i$) is highlighted in gray for illustration. If $\nabla^2 M_x$ is computed using equation (5.24), at the air/magnetic material boundary there is a mismatch between the magnetisation values at $(i-1)$ and $(i+1)$ resulting in an incorrect exchange field even if the magnetisation is uniform inside the magnetic material. To overcome this incorrect computation an extrapolation approximation is used. Considering the x component, the exchange field at position $(i+1)$ can be expressed as

$$H_{x\ exch}|_{i+1} = \frac{H_{x\ exch}|_i + H_{x\ exch}|_{i+2}}{2} \tag{5.25}$$

Then

$$H_{x\ exch}|_i = 2H_{x\ exch}|_{i+1} - H_{x\ exch}|_{i+2} \tag{5.26}$$

The same problem appears when considering other boundaries and expressions similar to (5.26) must be applied. The final result is the modification of the exchange field component at the outer boundary of the material as a function of the two immediate inner boundaries shown in figure 5.9(b). This boundary modification applies to the three components of the exchange field.

The space synchronism or reallocation of magnetisation and effective magnetic field components to M_x position, described in equations (4.89) to (4.92), requires the definition of four new matrices $M_y\_M_x|^{n+\frac{1}{2}}$,$M_z\_M_x|^{n+\frac{1}{2}}$, $H_y\_M_x|^{n+\frac{1}{2}}$ and $H_z\_M_x|^{n+\frac{1}{2}}$. Note that M_x and H_x are already collocated. In a similar manner, the reallocation of components to M_y and M_z positions requires the definition of the following matrices:

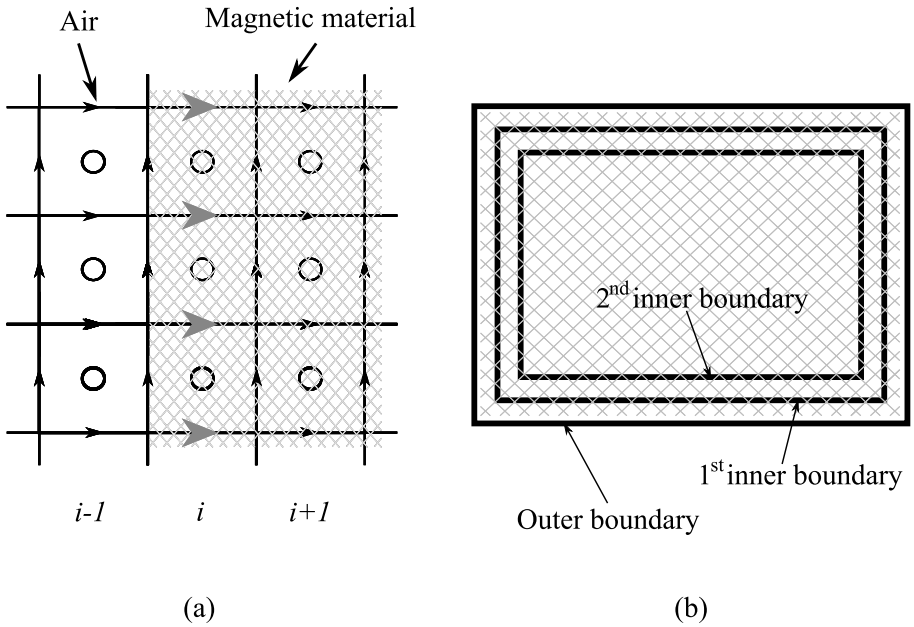

Figure 5.9: Computation of the x component of the exchange field $H_{x\ exch}$ in a magnetic material (a) $-x$ directed boundary showing M_x component of the magnetisation (b) the outer boundary of the exchange field has to be modified as a function of the two inner boundaries to obtain an accurate result.

$M_x\_M_y|^{n+\frac{1}{2}}$, $M_z\_M_y|^{n+\frac{1}{2}}$, $H_x\_M_y|^{n+\frac{1}{2}}$, $H_z\_M_y|^{n+\frac{1}{2}}$, $M_x\_M_z|^{n+\frac{1}{2}}$, $M_y\_M_z|^{n+\frac{1}{2}}$, $H_x\_M_z|^{n+\frac{1}{2}}$ and $H_y\_M_z|^{n+\frac{1}{2}}$.

To complete the discussion of the extended algorithm, the magnetic boundary conditions are described next. The magnetic material boundary condition described in section 4.13 must be applied at every iteration of the main FDTD algorithm. In order to satisfy equation (4.95) for the magnetisation $\mathbf{M}$, a similar procedure to that in Figure 5.9(b) is applied. In this particular case, the magnetisation components at the outer boundary of the material are set equal to the values at the first inner boundary following the condition $\partial\mathbf{M}/\partial\mathbf{n} = 0$. The same 10-cell thick PML absorbing material boundary that was used in the standard FDTD implementation is used in the extended algorithm. Table 5.2 with their associate dimensions summarises the definition of matrices in the extended FDTD computational space.

In order to test the algorithm, the magnetisation of a $400 \times 70\mu$m block of magnetic material has been switched from its original orientation in the y direction towards the direction of an external applied field in the x direction as shown in Figure 5.10. This external field was implemented in two different ways, that is, as an applied field inside the LLG equation with magnitude 8.5×10^6A/m (represented in the diagram of Figure 5.10(a)) and as the result of a current excitation around the material (Figure 5.10(b)). The magnetic block is defined by a low electrical conductivity $\sigma = 5000$ $1/\Omega$m, which allows deeper penetration of the fields inside the block, a saturation magnetisation of 8×10^5A/m initially oriented in the y direction and a damping coefficient of $\alpha = 0.1$. The space increment of the main grid is $\Delta x = 0.1\mu$m and the corresponding time increment for stability is $\Delta t = 0.0167$ps. Uniaxial anisotropy was considered for this experiment, with $K_1 >> K_2$, then, expression (3.125) reduces to

$$H_k = \frac{2K_u}{\mu_0 M_s} \tag{5.27}$$

The typical values of saturation magnetisation and anisotropy field for a $Ni_{80}Fe_{20}$ material are $M_s = 800$kA/m and $H_k = 400$A/m (Wang and Taratorin, 1999). Then the

Table 5.2: Summary of matrices and dimensions in the main computational space of the extended FDTD algorithm.

Essential Matrices	Updating Coefficients	Auxiliary Matrices
$E_z\|^n[i_m \times j_m]$	$C_a[i_m \times j_m]$	$M_z\|^n[i_m \times j_m]$
$H_x\|^n[i_m \times (j_m+1)]$	$C_b[i_m \times j_m]$	$M_z\|^{n+1}[i_m \times j_m]$
$H_y\|^n[(i_m+1) \times j_m]$	$D_{ax}[i_m \times (j_m+1)]$	$H_x\|^{n-1}[i_m \times (j_m+1)]$
$M_x\|^n[i_m \times (j_m+1)]$	$D_{bx}[i_m \times (j_m+1)]$	$H_y\|^{n-1}[(i_m+1) \times j_m]$
$M_x\|^{n+1}[i_m \times (j_m+1)]$	$D_{ay}[(i_m+1) \times j_m]$	$H_z\|^{n-1}[i_m \times j_m]$
$M_y\|^n[(i_m+1) \times j_m]$	$D_{by}[(i_m+1) \times j_m]$	$M_x\|^{n-1}[i_m \times (j_m+1)]$
$M_y\|^{n+1}[(i_m+1) \times j_m]$		$M_y\|^{n-1}[(i_m+1) \times j_m]$
		$M_z\|^{n-1}[i_m \times j_m]$
		$H_x\|^{n+\frac{1}{2}}[i_m \times (j_m+1)]$
		$H_y\|^{n+\frac{1}{2}}[(i_m+1) \times j_m]$
		$H_z\|^{n+\frac{1}{2}}[i_m \times j_m]$
		$M_x\|^{n+\frac{1}{2}}[i_m \times (j_m+1)]$
		$M_y\|^{n+\frac{1}{2}}[(i_m+1) \times j_m]$
		$M_z\|^{n+\frac{1}{2}}[i_m \times j_m]$
		$H_{anis}[i_m \times j_m]$
		$H_{x\ exch}[i_m \times (j_m+1)]$
		$H_{y\ exch}[(i_m+1) \times j_m]$
		$H_{z\ exch}[i_m \times j_m]$
		$M_y\_M_x\|^{n+\frac{1}{2}}[i_m \times (j_m+1)]$
		$M_z\_M_x\|^{n+\frac{1}{2}}[i_m \times (j_m+1)]$
		$H_y\_M_x\|^{n+\frac{1}{2}}[i_m \times (j_m+1)]$
		$H_z\_M_x\|^{n+\frac{1}{2}}[i_m \times (j_m+1)]$
		$M_x\_M_y\|^{n+\frac{1}{2}}[(i_m+1) \times j_m]$
		$M_z\_M_y\|^{n+\frac{1}{2}}[(i_m+1) \times j_m]$
		$H_x\_M_y\|^{n+\frac{1}{2}}[(i_m+1) \times j_m]$
		$H_z\_M_y\|^{n+\frac{1}{2}}[(i_m+1) \times j_m]$
		$M_x\_M_z\|^{n+\frac{1}{2}}[i_m \times j_m]$
		$M_y\_M_z\|^{n+\frac{1}{2}}[i_m \times j_m]$
		$H_x\_M_z\|^{n+\frac{1}{2}}[i_m \times j_m]$
		$H_y\_M_z\|^{n+\frac{1}{2}}[i_m \times j_m]$

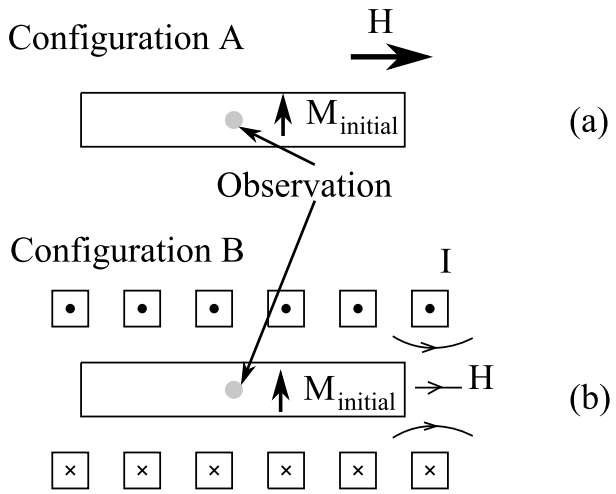

Figure 5.10: Magnetic material bar under the effect of a magnetic field. The magnetic field is applied in LLG equation in configuration A and by an external current in configuration B.

anisotropy constant, K_u, was chosen to be $K_u = 200\text{J}/m^3$ to fit the above values. Exchange interaction was also considered using equation (3.124). The magnetic field magnitude at the observation point in the center of the material is shown in Figure 5.11(b), the applied field in configurations A and B has a rise time of 1ps, the difference between the rise time of both plots in Figure 5.11(b), corresponding to configurations A and B, is due to the penetration of the fields inside the material. Figure 5.11(a) shows the magnitudes of each magnetisation component, M_x, M_y and M_z, at the observation point in the center of the material. The final magnetisation points towards x for both experiments as expected. Figure 5.11(c) shows the convergence check of the magnetisation orientation given by

$$\frac{|\mathbf{M} \times \mathbf{H}|}{|\mathbf{M}||\mathbf{H}|} \tag{5.28}$$

which clearly tends to zero meaning the vectors $\mathbf{M}$ and $\mathbf{H}$ are parallel.

Figure 5.12(a) shows the configuration of another simulation used to test the extended algorithm. It consists of a block of magnetic material with the same dimensions as before having two external coils underneath that generate a magnetic field pointing

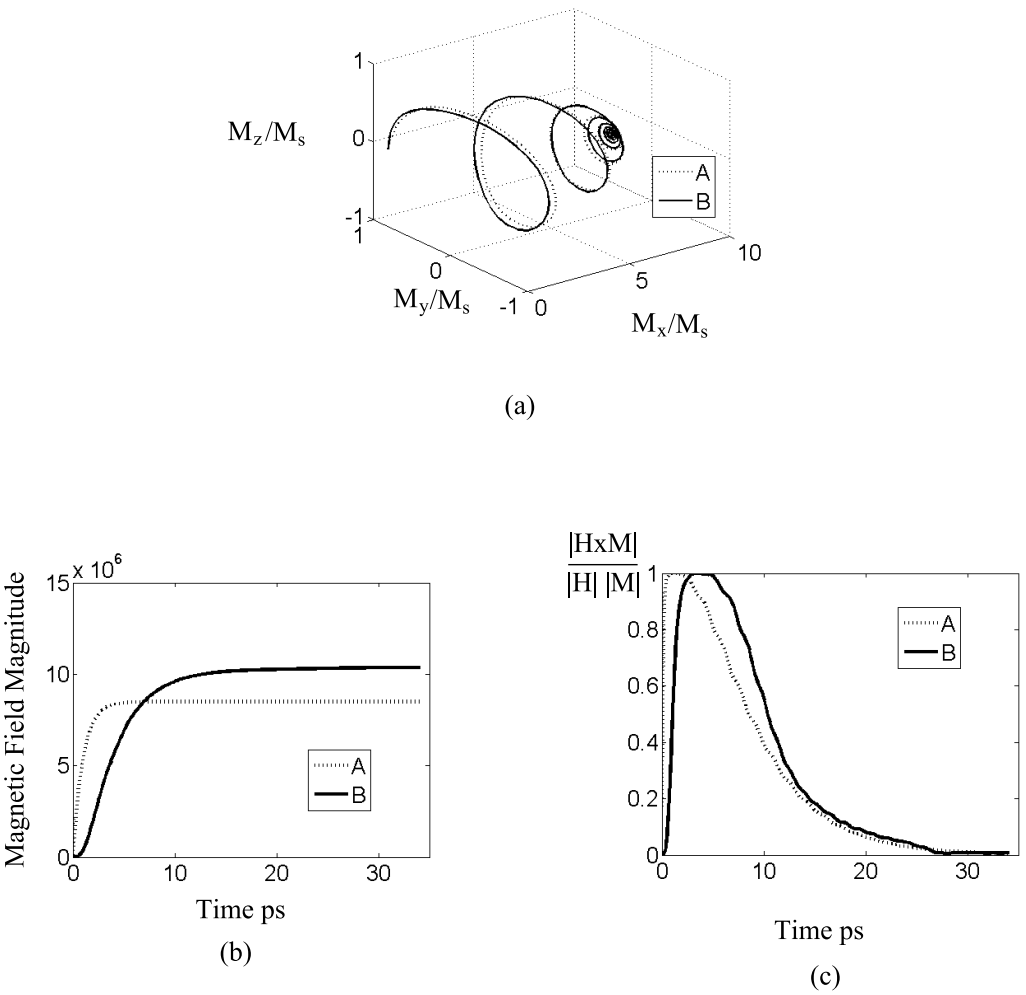

Figure 5.11: (a) Rotational magnetisation due to an applied field for configurations A and B. (b) Magnetic field magnitude at observation point. (c) Convergence check of the magnetisation orientation.

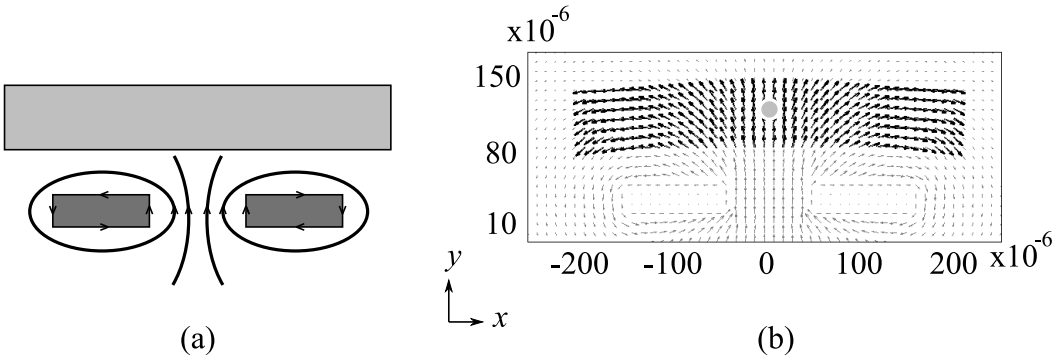

Figure 5.12: Magnetisation distribution. (a) Diagram of the excitation configuration using an external field generated by a current. (b) Final distribution of the magnetisation. The black and grey arrows represent the magnetisation and the magnetic field respectively.

towards the y direction at the center of the slab. The initial magnetisation was pointing in the z direction and, as previously indicated, the current forces a field in the y direction at the center of the material. The magnetic field excitation and the material and simulation parameters are the same as in the previous simulation. The orientation of the magnetisation in the whole material block at time 25ps is shown in Figure 5.12(b). It can be clearly seen that the magnetisation (dark arrows) orientates everywhere in the same direction of the magnetic field (light arrows).

5.6 FDTD Simulation of Thin-Film Heads

The standard and extended FDTD algorithms have been implemented and tested over a block of material in the previous sections. The results of different simulations have shown the FDTD modelling as a powerful technique that includes both dynamic calculations of the micromagnetics of the head material and the description of the electromagnetic fenomena. Next, the standard and extended FDTD algorithms will be tested

using the geometry and parameters of an actual commercial thin-film head.

5.6.1 Thin-film Head Geometry and Parameters

The detailed method of obtaining the physical dimensions of two commercial thin-film heads and their material characterisation is described in Section 6.2 of this thesis. This provided the physical dimensions and material composition of the two different thin-film heads. In order to run an FDTD simulation, these material compositions and geometry must be specified within the computational space of both the standard and the extended FDTD algorithm. It is observed from Table 6.1 that the most recently manufactured head (Head B) will require a extremely small grid size due to its level of miniaturisation which in turn, to satisfy the stability requirement for FDTD stated in equation (4.52), enforces a very small time step. Using very small time steps results in a very large number of time iterations of the algorithm. As an example, to obtain the results of a few nanoseconds of head operation will take an average of two months (depending on how small the head is) for the algorithm to come to an end. Due to this difficulty, the parameters of the larger head (Head A) will be used to implement the simulations.

Figure 5.13 represents a scaled diagram of the geometry of the head used in the simulations which corresponds with the experimental data from head A obtained in Chapter 6. The front gap height is 0.5μm which is the smallest dimension within the head and therefore determines the smallest grid size Δx. In this case, the criterion will be to have at least five cells resolution in the front gap region, and thus, the grid size is chosen to be $\Delta x = 0.1\mu$m.

The coil turns are made from a high conductivity material (copper) defined by an electrical conductivity $\sigma = 5.8 \times 10^7 1/\Omega$m and relative permittivity $\epsilon_r = 4.8$. The magnetic material of the thin films is made from a typical NiFe permalloy material

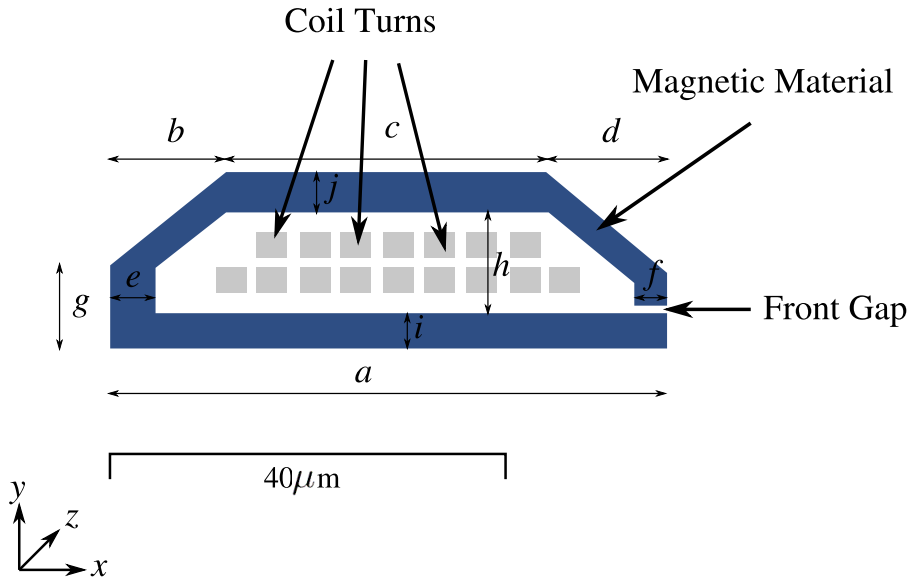

Figure 5.13: Scaled diagram of the head geometry with dimensions: front gap height= 0.5μm, a= 56.7μm, b= 11.5μm, c= 33.3μm, d= 11.9μm, e= 4.6μm, f= 2.7μm, g= 10.2μm, h= 12.4μm, i= 4.6μm, j= 4.6μm. For simulation purposes the axis are taken as shown where the z-axis represents the anisotropy axis.

defined by an electrical conductivity of $\sigma = 5 \times 10^6 1/\Omega$m and, in the case of magnetic linear material, a relative permeability of $\mu_r = 2000$. When considering the case of non-linear material, the parameters of a typical NiFe ferrite are a saturation magnetisation $M_s = 800 \times 10^3$[A/m] (Wang and Taratorin, 1999) and the damping coefficient α. This damping coefficient is highly dependant on the thickness and the proportion of Ni and Fe of the thin film (Wu et al., 2001). For the purpose of this thesis a value of $\alpha = 0.1$ is assumed. The remaining areas of the computational space, including insulating material regions, will be treated as free space.

5.6.2 Implementation and Results

Following section 4.5, the TM_z mode will be used in order to implement the current in the coil turns properly. The computational space where the geometry of Figure 5.13

is to be implemented is a two-dimensional lattice of [590x225] cells with a cell size of $\Delta x = 0.1\mu$m. As before, the cell size is chosen to obtain a resolution of 5 cells in the smallest region of the head, i.e. the front gap. A 0.1μm cell size in combination with stability condition (4.52) leads to a time step for the algorithm of $\Delta t = 0.167$fs. A step function current with an amplitude $A = 15$mA and a rise time $\tau = 20$ps implemented as described in Figure 5.4(b) was used to excite the coil turns represented in Figure 5.13. In order for the simulation to reach the steady state the total simulation time should be at least five times the rise time of the source. Twice that time was chosen to allow the switching of the magnetisation leading to a total simulation time of 2ns. With the time step Δt as above, in order to run 2ns of simulation time the algorithm required 12 million iterations. The computational space was surrounded by a 10 cell thick PML using polynomial grading to absorb outgoing waves. The parameters used to define non-linear materials in the magnetic simulation were $M_s = 8 \times 10^5$A/m, $\sigma = 5 \times 10^6$ 1/Ωm, $K_u = 200\text{J}/m^3$, and $\alpha = 0.1$.

In order to store each sample, the standar FDTD simulation requires 26345603 bytes of free memory while the extended FDTD simulation memory requirement is slightly higher, 153558419 bytes. The computer used for simulations had a 2 Gigabyte of RAM memory, therefore, memory does not represent a limiting factor for the purpose and computer equipment used to carry out the simulations.

Figure 5.14 represents the magnitude of the magnetic fields at three different time instants, $t_1 = 0.1$ns, $t_2 = 0.2$ns and $t_3 = 0.45$ns, of the simulation using the standard FDTD algorithm. Notice the formation of the write field to the right of the head as the simulation progresses. The magnetic field strength resulting from considering the rotation of the magnetisation inside the magnetic material of the thin films is shown in Figure 5.15. Figure 5.15 is analogous to Figure 5.14 using the extended FDTD algorithm. Comparing Figures 5.14 and 5.15 leads to a few observations. It takes more time to develop the write field in the gap region with the extended algorithm as

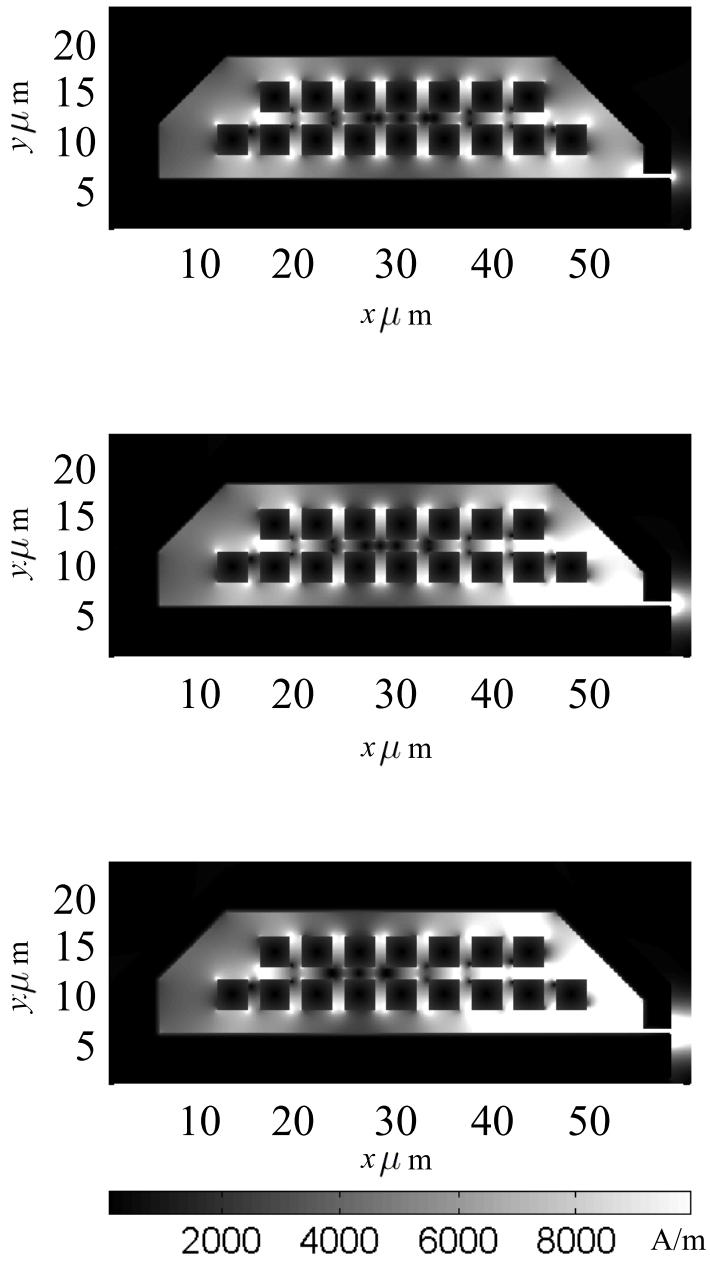

Figure 5.14: Magnetic field magnitude for three time instants ($t_1 = 0.1$ns, $t_2 = 0.2$ns and $t_3 = 0.45$ns) computed using the standard FDTD algorithm (no magnetisation is considered) and a 15mA current step excitation with rise time constant 20ps.

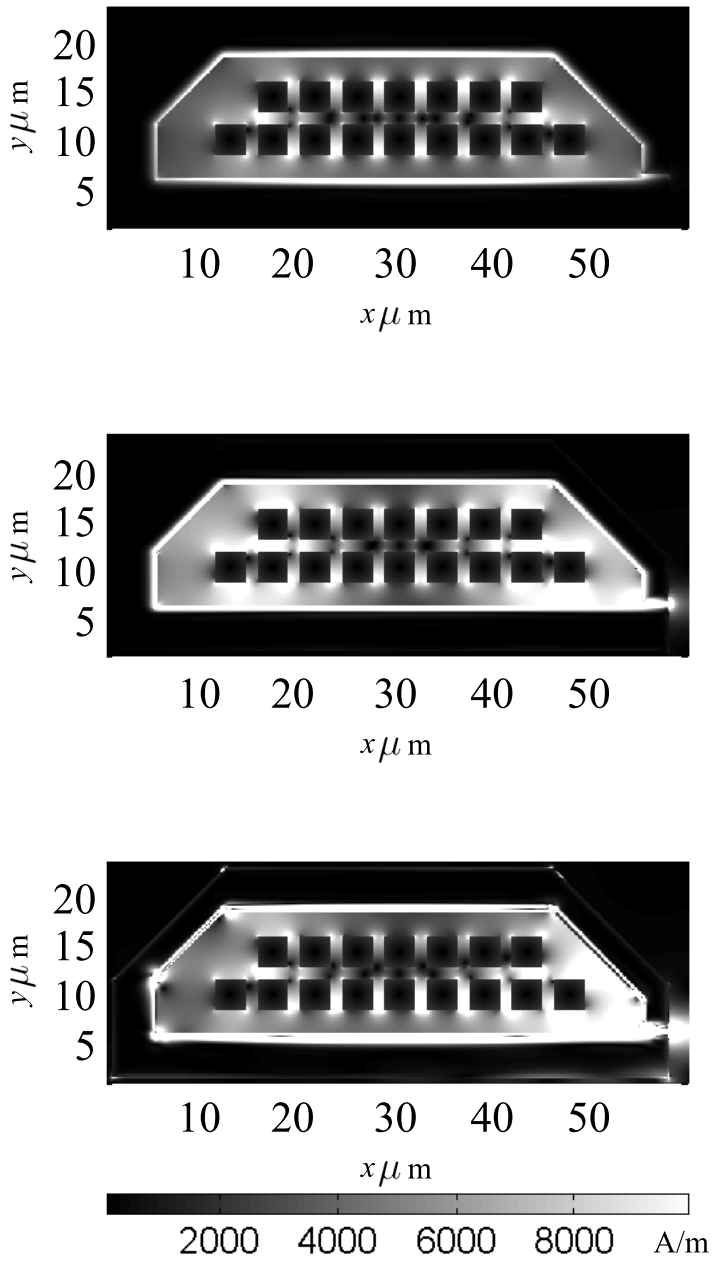

Figure 5.15: Magnetic field magnitude at time $t_1 = 0.1$ns, $t_2 = 0.2$ns and $t_3 = 0.45$ns, computed using the extended FDTD algorithm (i.e. considering magnetisation rotation) and a 15mA current step excitation with rise time constant 20ps.

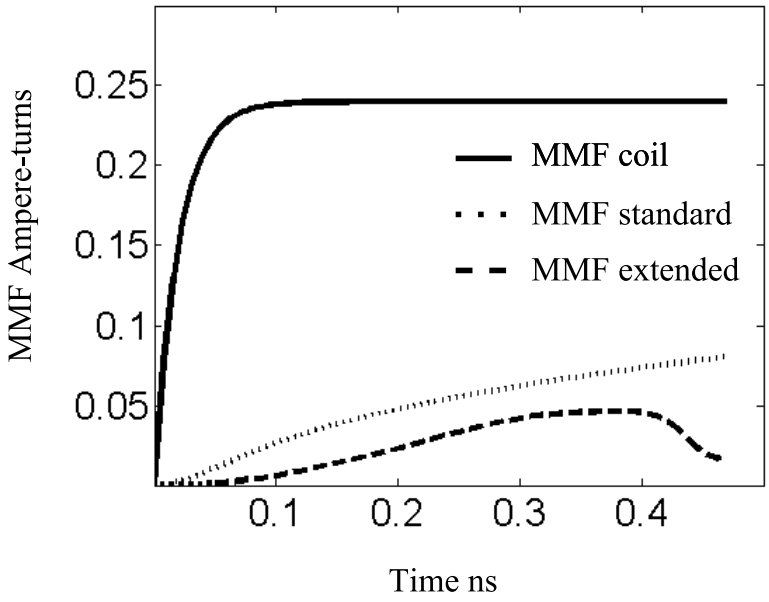

Figure 5.16: Applied mmf (number of coil turns times applied current) and resulting gap mmf (gap field times the gap length) for the standard and the extended FDTD algorithms.

shown Figure 5.16. This is directly related to the time constant τ_r due to magnetisation rotation and reflects the time it takes for the magnetisation to switch. Figure 5.16 indicates that for this particular head geometry more than 0.5ns are required to switch the magnetisation and reach equilibrium, which is in agreement with the experimental measurements described in Chapter 6 where the time constant for rotational magnetisation for this particular head was $\tau_r = 1.42$ns.

The switching of the magnetisation is an energy consuming process and therefore it reduces the efficiency of the head resulting in a smaller write field or write bubble as can be seen in Figure 5.17. Figure 5.17(b) shows that the field concentrates in the head pole corners leading to the feature seen at the top right of the gap, and eventually to an unstability which will be discussed next.

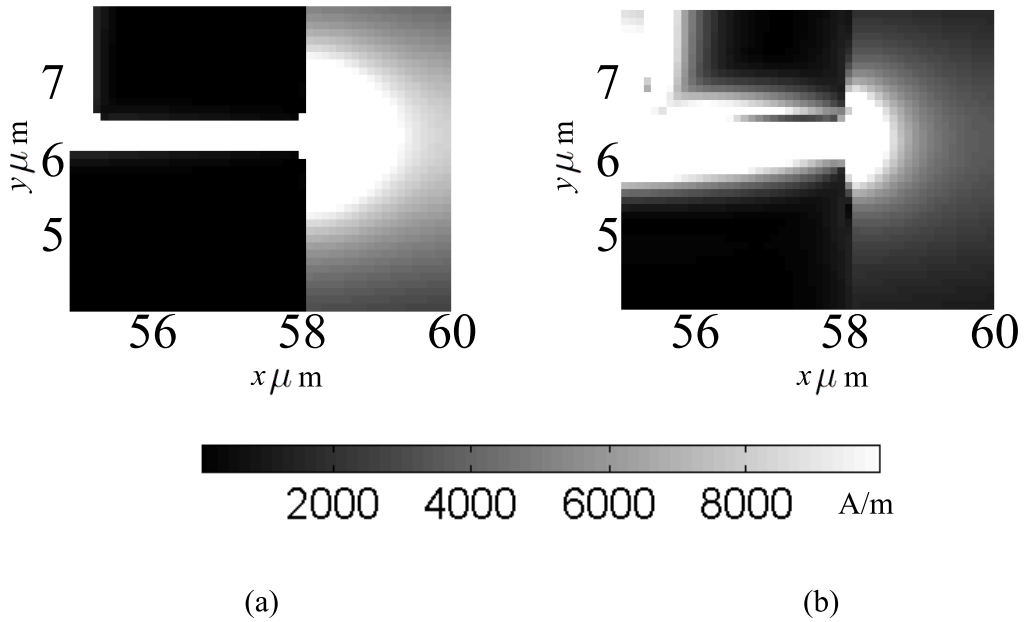

Figure 5.17: Zoomed images of the gap region showing the magnetic field magnitude at time 0.2ns corresponding to (a) the standard FDTD algorithm and (b) the extended FDTD algorithm.

With regard to time stepping and stability, only condition (4.52) has been enforced in the simulation of Figures 5.14 and 5.15. Satisfying the stability limit stated by the extended algorithm in condition (4.109) is not an easy task, particularly at the head corners where the effective field becomes large, thus demanding a smaller time step to stabilise the magnetisation solutions. In order to satisfy (4.109), the maximum effective field acting in the material must be estimated. Once the effective field is estimated, the maximum precession frequency can be calculated as $\omega_0 = \gamma H$ and then the upper limit for the time step is computed as $\Delta t = 2/\omega_0$. However as seen in section 3.3.3, the effective field is formed by the addition of several fields, most of them are very easy to obtain but others, like the demagnetising field, are very complex in nature which makes their estimation very difficult. However, a lower estimate may be obtained and compared with the courant stability limit by assuming that the maximum field in the head is equal to M_s. In this case $\omega_0 = \gamma H = 1.77 \times 10^{11}$rad/s and hence $\Delta t = 2/\omega_0 = 11.3$ps which is within the limits of the courant stability criterion ($\Delta t_{courant} = 0.167$fs).

In particular, the demagnetising field concentrates in the corners of the material with its magnitude being particularly large in comparison to any other part of the material. This can be clearly seen in Figure 5.15 as the effective field concentrates at the inner corners of the magnetic material. This extremely large field gives rise to a very large precession frequency ω_0 which violates the courant stability condition (4.109) or requires a very small time step. The time step in the extended method simulation was fixed and determined by the smallest head feature using courant condition. Due to the previously mentioned increase in the precession frequency originated by the concentration of the fields in some regions of the head, the algorithm became unstable after 0.45ns of simulation time. That is the total simulation time of the experiments shown in this section using the head geometry shown in Figure 5.13.

As discussed in section 3.3.3, the effective field is formed by several field contributions

which make the rotational motion of the magnetisation a complex process. When the dimensions considered are very small, the exchange field contribution, which is proportional to the square of the inverse of the distance between adjacent spins, is larger than the anisotropy contribution and therefore becomes more important. Exchange fields try to align adjacent spins in the same direction, and thus, help to make the system more stable. However, considering the exchange fields contribution did not avoid the increase in the precession frequency indicated above resulting in an unstable solution after 0.45ns of simulation time. This is because the influence of the exchange field was small in the corners since Δx was larger than the exchange length for the head material considered in this work (exchange length= $\sqrt{2A_x/\mu_0 M_s^2} \simeq 5$nm for NiFe)

Figure 5.18 shows the magnetic field distribution near the gap region at time 0.45ns for both the standard and the extended FDTD algorithms. By comparison, it is observed that when using the extended method, the field strength is smaller and the effective field concentrates at the head corners. As explained above, these effects are due to the switching of the magnetisation and the demagnetising fields. The arrow plot of Figure 5.18(b) represents the orientation of the magnetisation. The direction of the magnetic flux density can be visualised by observing the orientation of the magnetisation arrows, it is obvious that there is a flux linking both thin films through the gap resulting in the external radiation of the write field.

Figure 5.19 shows the Karlqvist's head field for the geometry of the simulations, that is a gap height of 0.5μm and a gap field strength of 10×10^4 A/m. A comparison with Figure 5.18 shows that the Karlqvist's head fields near the head poles are not accurately described.

Figure 5.20 is obtained by plotting the magnetic field components H_x and H_y at the head surface and at a distance of 100nm from the head surface in the gap region. Having in mind that the disk surface in a recording system would be parallel to this

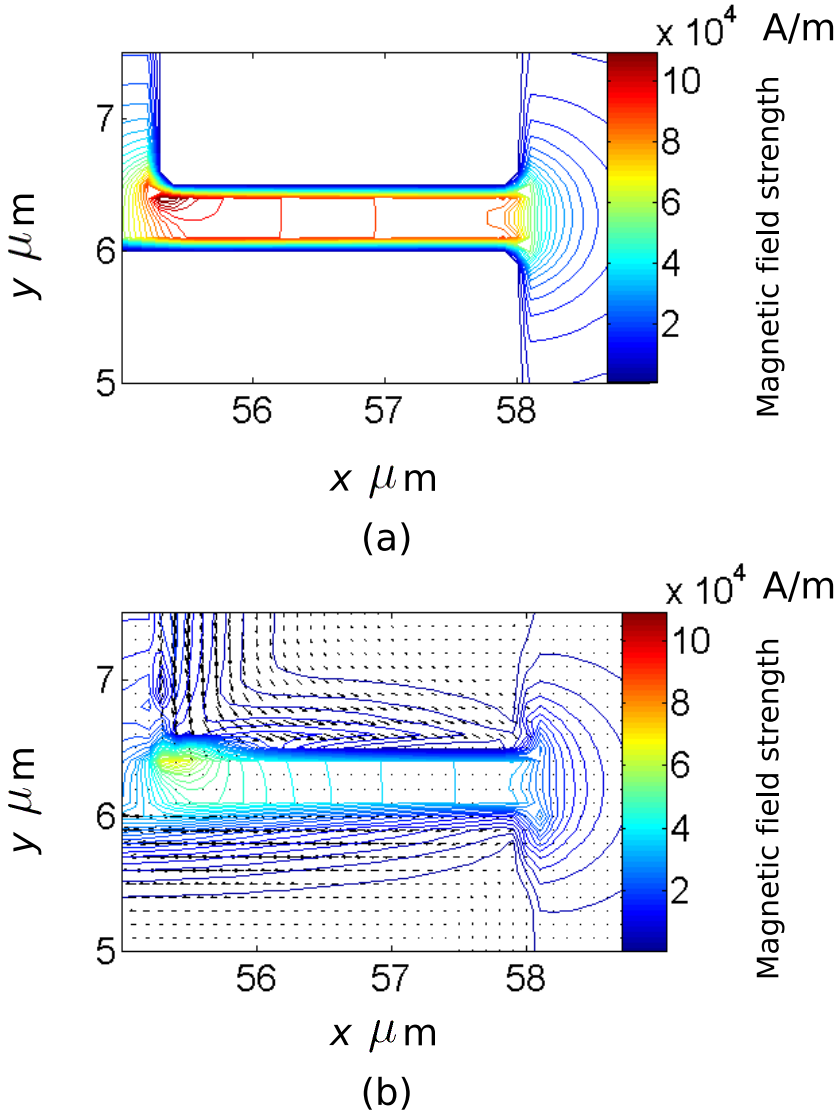

Figure 5.18: Magnetic field distribution of the head geometry near the gap region at simulation time 0.45ns. (a) Contour plot of the field strength for linear material and (b) contour plot of the field strength and arrow plot of the magnetisation for non-linear material.

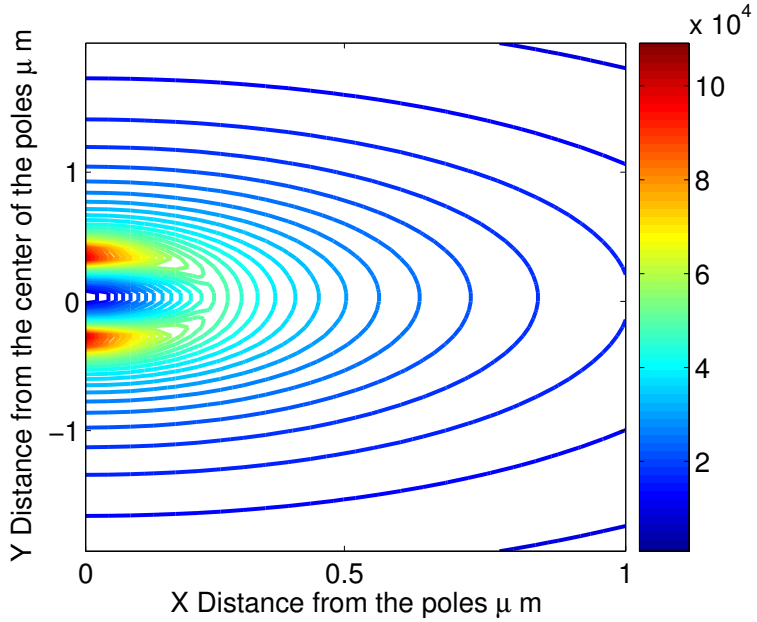

Figure 5.19: Karlqvist's head field for the geometry of the simulations. Gap length 0.5 μm, Gap field strength 10×10^4 A/m.

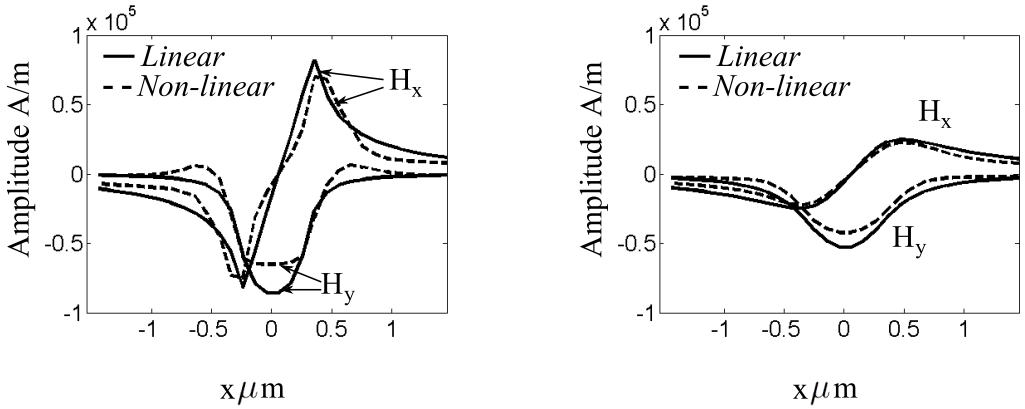

Figure 5.20: Recording gap fields simulating a plane parallel to the disk surface in a recording system. (a) Fields at the pole surface and (b) at 100nm from the head surface.

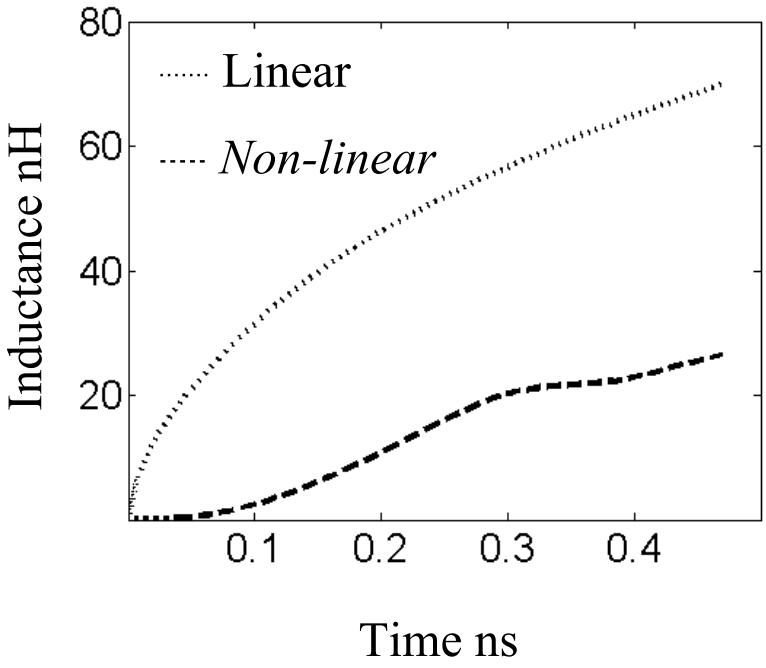

Figure 5.21: Computed inductances with and without the inclusion of the rotational magnetisation using an average thin film width $W = 45\mu$m.

plane, the field magnitude responsible for orientating the magnetisation of the disk in one direction or another will be proportional to the plot in Figure 5.20. In particular, H_y is the main field responsible for the recording process in longitudinal media. Higher field gradients are observed in the pole corner regions with the inclusion of the magnetic details of the core material. This has the implication that shorter transition lengths are recorded in practice than predicted by models that ignore the magnetic detail of the core material.

The inductance of a magnetic circuit is defined as the ratio of the magnetic flux linkage through a closed surface to the current, that is

$$L = \frac{N \oint \mathbf{B} \cdot d\mathbf{S}}{I} \tag{5.29}$$

As the simulations of the head geometry in Figure 5.13 are two-dimensional (x, y), the integral of the magnetic flux density $\mathbf{B}$ through the cross sectional area of the head

(x, z) or (y, z) can not be evaluated. However, working in two dimensions (x and y) means that the magnitude of the fields are the same along the third dimension (z). Then it is possible to give a slightly modified figure of inductance based on the average thin film width W as

$$L = \frac{NW \int \mathbf{B} \cdot d\mathbf{L}}{I} \tag{5.30}$$

Here, W is considered the average thin film width in the z direction. For this particular head experiment W was set to be five times the upper pole width which was measured in Chapter 6 and found to be 9μm, and hence $W = 45\mu$m was used to compute the inductances of the core material. These are shown in Figure 5.21 for the standard and extended FDTD algorithms. The experimental measurements carried out in Chapter 6 yielded an inductance of 74.8nH for this particular head geometry. Although the magnetisation has not been completely switched and therefore the head has not yet reached the steady state the general tendency of both plots in Figure 5.21 does not disagree with the experimental value of inductance due to domain rotation (the orientation of the magnetisation in this model is considered to take place only by domain rotation).

Figure 5.22 represents the configuration used to carry out simulations of the upper pole of head A in TEz mode. These were aimed to study the effects of eddy currents on the switching time due to a field step applied perpendicular to plane of paper, with 20ps time constant and 12×10^3A/m amplitude. The simulation parameters were $\Delta x = 0.5\mu$m, $\Delta t = 0.83333$fs and total simulation time 1ns. The material parameters were the same as in the previous non-linear simulation, $\sigma = 5 \times 10^6 1/\Omega$m, $M_s = 800 \times 10^3$A/m and damping coefficient $\alpha = 0.1$. Demagnetising fields were included as another term in the direction of the applied field into the effective field expression. Considering the head pole as the infinite cylinder represented in Figure

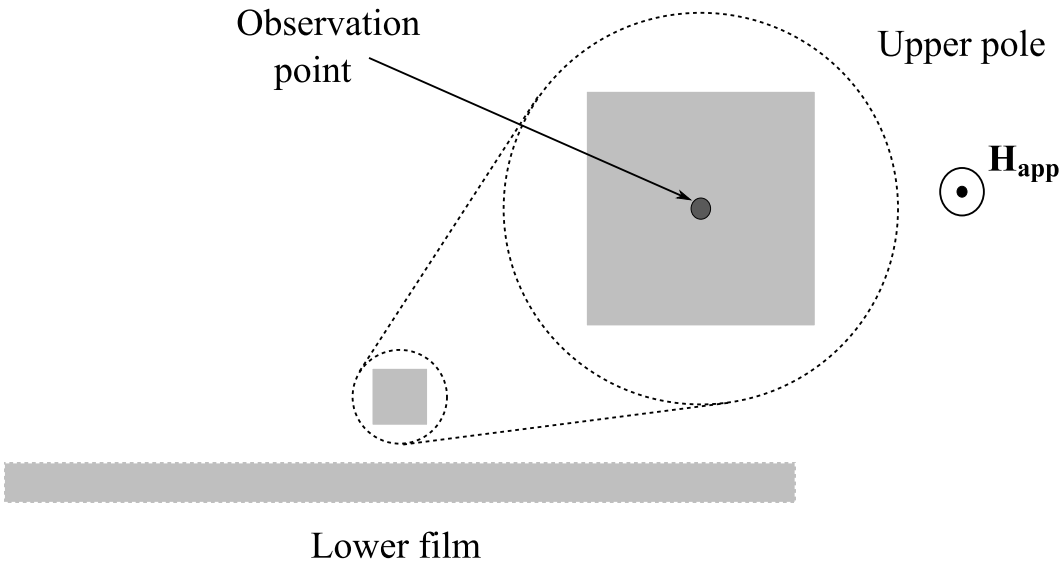

Figure 5.22: Configuration of the upper pole simulation in the TE_z mode. Only the zoomed image of the upper pole is defined in the simulation. The excitation is applied uniformly as indicated by $\mathbf{H_{app}}$.

5.23, the demagnetising energy can be expressed as

$$\mathcal{E}_{demag} = \frac{\mu_0}{2}(N_x M_x^2 + N_y M_y^2 + N_z M_z^2) \tag{5.31}$$

where due to the cylindrical geometry and orientation in the z direction, $N_x = N_y = 1/2$ and $N_z = 0$. Then

$$\mathcal{E}_{demag} = \frac{\mu_0}{2}\left(\frac{M_x^2}{2} + \frac{M_y^2}{2}\right) \tag{5.32}$$

The applied energy can be expressed as

$$\mathcal{E}_h = -\mu_0 \mathbf{M}\mathbf{H_{app}} \tag{5.33}$$

where $\mathbf{H_{app}} = H_z\mathbf{k}$, then

$$\mathcal{E}_h = -\mu_0 M_z H_z \tag{5.34}$$

Now, considering the total free energy as the applied and demagnetising field contributions

$$\mathcal{E}(\mathbf{M}) = \frac{\mu_0}{2}\left(\frac{M_x^2}{2} + \frac{M_y^2}{2}\right) - \mu_0 M_z H_z \tag{5.35}$$

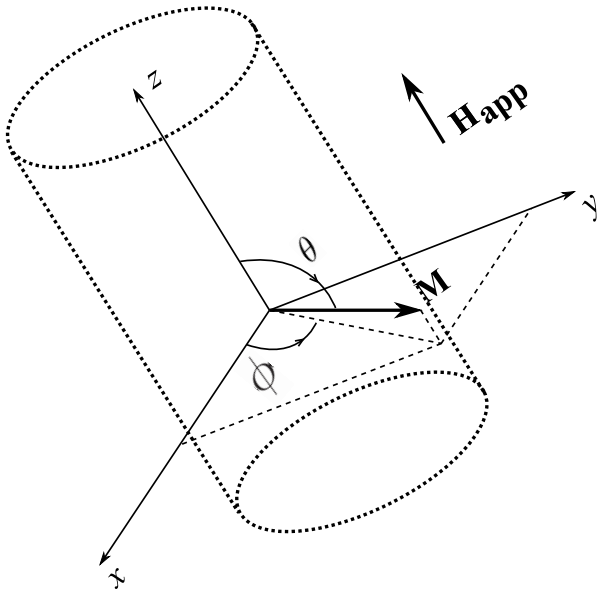

Figure 5.23: Infinite cylinder geometry used to justify the way in which the demagnetising field is included in the simulation of the the upper pole simulation in the TE_z mode.

or by normalising by $\mu_0 M_s$

$$\hat{\mathcal{E}}(\mathbf{m}) = \frac{1}{4}(m_x^2 + m_y^2) - m_z h_z \tag{5.36}$$

Since $m_x^2 + m_y^2 + m_z^2 = 1$, then

$$\hat{\mathcal{E}}(\mathbf{m}) = \frac{1}{4}(1 - m_z^2) - m_z h_z \tag{5.37}$$

which concludes with effective field expression as

$$\mathbf{h_{eff}} = -\frac{\partial \hat{\mathcal{E}}}{\partial \mathbf{m}} = \left(\frac{m_z}{2} + hz\right)\mathbf{k} \tag{5.38}$$

The magnetic fields and the magnetisation were evaluated at the center of the head pole. Figure 5.24(a) shows that eddy currents produce opposing fields to the applied field that increase the time taken to achieve magnetisation equilibrium (minimum energy state), causing a 0.13ns delay in the switching time of the magnetisation and therefore of the head, as shown in Figure 5.24(b). The expanded plot in Figure 5.24(a)

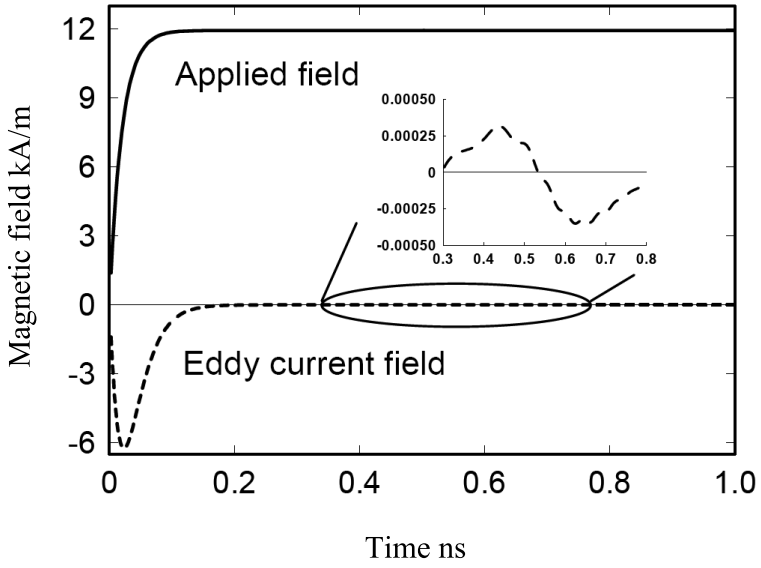

(a)

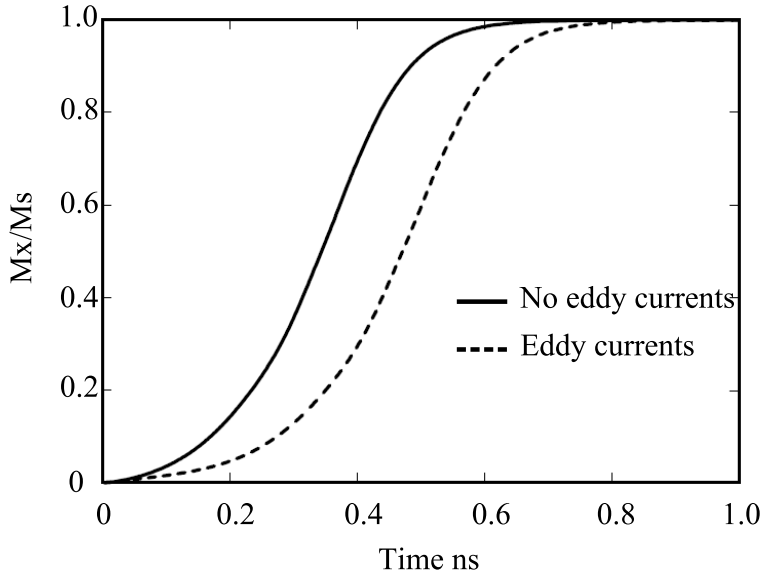

(b)

Figure 5.24: Eddy current effect at the head pole. (a) Applied field and corresponding eddy current field. (b) Out of plane magnetisation versus time showing a 0.13ns delay in switching due to eddy current fields.

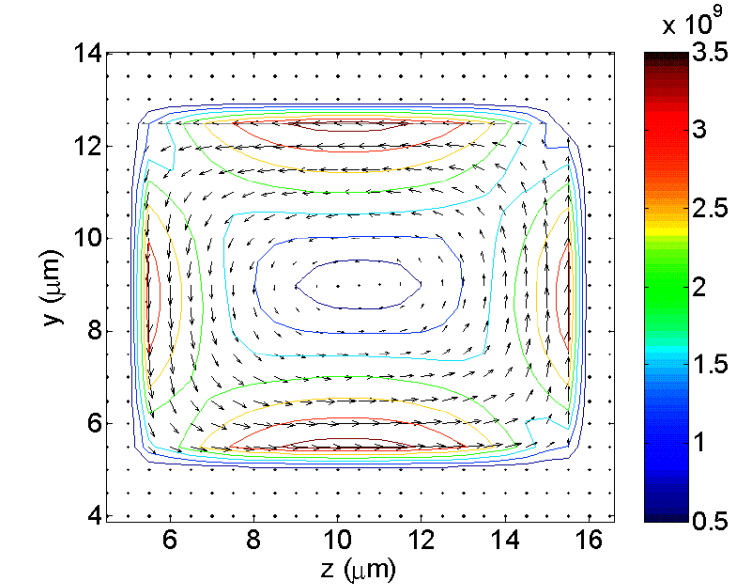

(a)

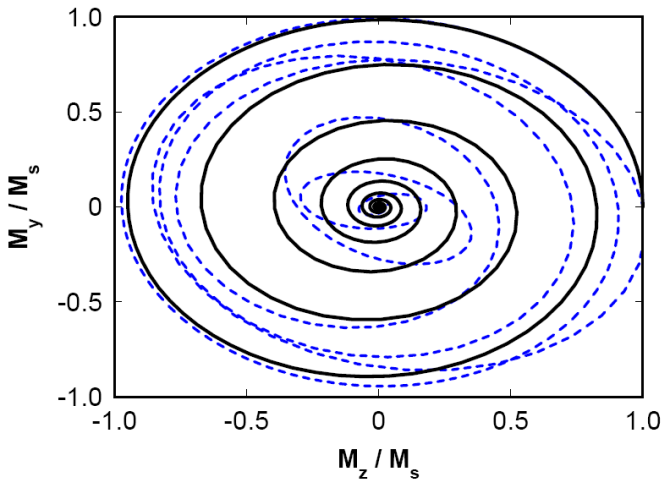

(b)

Figure 5.25: Eddy current effect at the head pole. (a) Contour and arrow plot of the current density (A/m^2) at 0.02ns. (b) Magnetisation precession with (dashed plot) and without (solid plot) eddy current fields.

represents eddy current field due to $\partial M/\partial t$ which is negligible. Figure 5.25(a) shows the current density across the head pole, its distribution agrees with the theory of eddy currents studied in Chapter 2. The eddy current fields introduce a delay in the switching of the magnetisation and also modify its precession as can be seen in Figure 5.25(b).

5.7 Summary

Code has been written in Matlab to fully implement the FDTD algorithm in two dimensions (transverse magnetic TMz, and transverse electric TEz modes). A perfectly matched layer (PML) has been implemented to terminate the simulation space and attenuate outgoing waves with negligible reflections. The correct implementation of current sources has been described. The propagation of electromagnetic waves originated from current sources and its associate phenomena, such as wave reflection, wave penetration, skin depth, etc. have been studied and observed and it is in agreement with theorical computations.

The extended FDTD method with inclusion of the dynamic model of the magnetisation precession has been implemented. To verify the performance of the algorithm, FDTD simulations of a block of material having non-linear properties have been carried out. The precession of the magnetisation has been observed and as predicted by the theory the final magnetisation was aligned with applied field after a period of precession around it.

Two-dimensional TM_z and TE_z simulations of an actual head geometry have been carried out. The TM_z simulation described the cross sectional area of the head and was aimed to study field distributions, field rise times and inductance figures. It was observed a delay in the formation of the write field when the magnetisation is considered compared with the simulation of linear materials. The magnetic field distribution near the gap region showed that the field strength is smaller and the internal field concentrates on the head corners which affects the stability of the extended method. Also, higher recording field gradients are observed in the pole corner regions with the inclusion of the magnetic details of the core material. The rise time of the computed mmf is in agreement with the time constant obtained by experimentation in Chapter 6. Inductance figures have been computed for both linear and non-linear materials,

the results were in agreement with the inductance of the head that was measured in Chapter 6.

The TE_z mode simulation focused on the upper pole of the head and was aimed to study the effect of eddy currents. It was observed that eddy currents produce opposing fields to the applied field that increase the time towards magnetisation equilibrium. A delay of 0.13ns in the switching time of the magnetisation was observed for one of the head structures considered in this work. The eddy current density distribution was plotted. It was observed that eddy currents introduce a delay in the switching time of the magnetisation.

Chapter 6

Thin-Film Heads Measurements

6.1 Introduction

This chapter is intended to study the losses in recording thin-film heads, particularly on those losses with magnetic origin. Considering the performance of the head, a magnetic field excitation **H** originated by the current flowing through the coil generates a magnetic flux ϕ that is proportional to the magnetic flux density **B**. If the head is considered as the simple system represented in Figure 6.1, its response is described by a permeability function μ which contains information on the magnetic losses in the system (Engstrom, 1984).

The equivalent impedance of a magnetic head is typically defined as a pure inductor plus the effects of the coil resistance, capacitance and inductance (see Figure 6.2(a)). The pure inductor is related to the head magnetic material whereas the rest of components are originated in the wires and contacts. An inductor is defined as the circuit or part of a circuit that has the properties of inductance. In magnetic terms, the inductance can be defined as the ratio of the magnetic flux ϕ to the current i.

$$L = \frac{\partial \phi(\mu)}{\partial i} \tag{6.1}$$

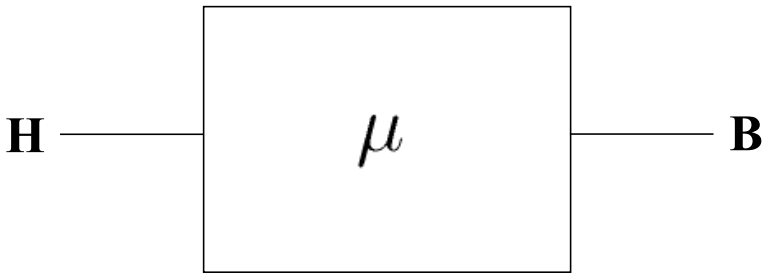

Figure 6.1: System representation of a recording thin-film head. The transfer function of the system is defined by a permeability funcion μ.

Since the inductance is related to the permeability function μ through the magnetic flux ϕ, it allows the quantification of magnetic losses in the system. In electrical terms, the inductance is defined as the imaginary part of the impedance divided by the angular frequency ω

$$L = \frac{Im\{Z\}}{\omega} \tag{6.2}$$

thus it is a measurable parameter. The impedances of actual heads will be measured and from them inductance figures will be obtained to allow quantification of the magnetic losses in the heads.

Magnetic losses are mainly due to domain wall motion and rotational magnetisation. These two phenomena are described by several parameters, e.g. time constants, which are related to the material the head is made of. The problem now lies in deriving an expression that relates the inductance to the parameters that describe the magnetic losses. This expression can then be used to estimate the value of the important parameters that describe the losses from the measured value of the inductance of actual heads.

As mentioned before, this chapter focuses on the quantification of magnetic losses. This chapter also includes the study of the physical geometry and materials of the heads which were used in Chapter 5 to specify the head dimensions and materials for

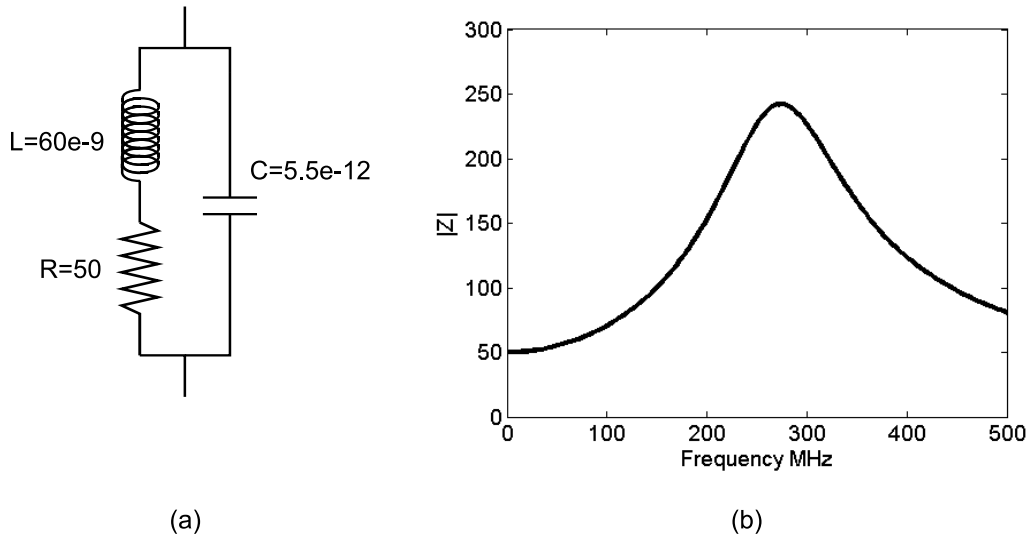

Figure 6.2: Example of equivalent circuit for impedance measurements: (a) equivalent electrical circuit with lumped elements, R=50Ω, L=60nH and C=5.5pF; (b) magnitude of the impedance (Ω) of the equivalent circuit as a function of the frequency (MHz).

the FDTD simulation. Thus, the first part of this chapter presents Scanning Electron Microscope (SEM) analysis of two thin-film commercial heads. These images were used to obtain actual dimensions and material composition of the different parts of the heads. This is followed by the derivation of an expression for the head inductance as a function of the time constants for domain wall motion and rotational magnetisation. Then the experimental impedance measurements are addressed, first with a review of all the equipment needed to perform the measurement followed by the procedure and results of the measurements. The final part of the chapter deals with the estimation of the time constants for rotational magnetisation and domain wall motion using a least squares fit to the measured inductances.

6.2 The Heads

An initial set of 587 heads from 38 different batches dating from 1996 to 2005 was available to make a study of impedance characteristics. These were classed per batch and year of manufacturing. For every batch, a study of the geometry of the contact pads was carried out to select a subset with similar separation between tracks allowing measurement with a single probe, repeated batches from the same manufacturer and year were discarded. The initial set was reduced in this way to 7 batches and 93 heads, the most abundant separation between tracks in the contact pads was roughly 1.5mm. The impedance of one head per batch was measured and stored in a file for later computations. Based on the fact that they all had similar impedance figures and selecting an old and a modern head, the final set was reduced to only two batches. These two were manufactured by Seagate in 1997 and 2005 respectively. A complete study of the geometry and head materials was carried out over the two selected batches. For simplicity, in this text the heads belonging to the batch manufactured in 1997 will be denoted as head A whereas the heads from the 2005 batch will be denoted as head B.

The end view image of the head is defined as seen from the disk surface. The side view of the head is that corresponding to the cross section at the center of symetry of both thin films. The top view of the head is defined as seen from a plane parallel to both films and situated on the same side as the upper film. Figure 6.3 shows diagrams of typical end and side views with comon names of dimensions.

By simple observation with an optical microscope, it is possible to observe the top and end views of a given head. Figure 6.4 shows a top view image of head A where the coil and other metal contacts are clearly visible. However, as the resolution of this kind of optical microscope image does not allow accurate determination of head dimensions, a scanning electron microscope (SEM) was used to accurately estimate the geometry

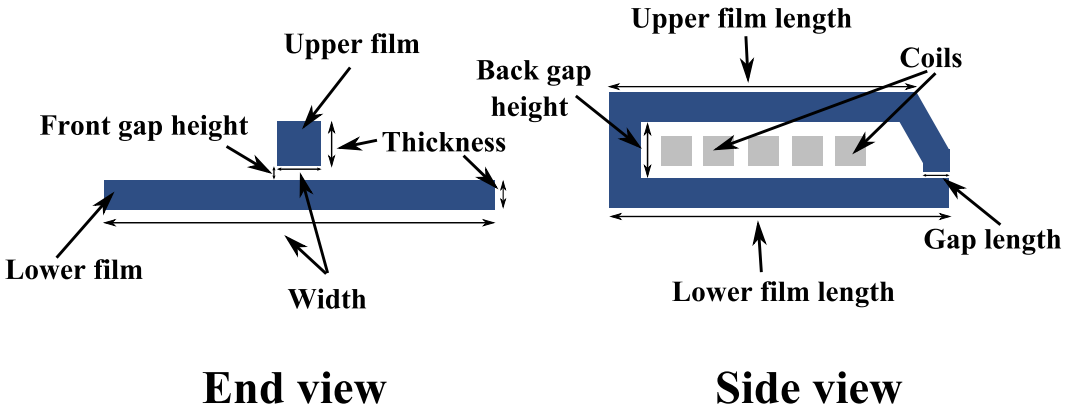

Figure 6.3: Diagram plot of a magnetic head illustrating the names of the most common dimensions.

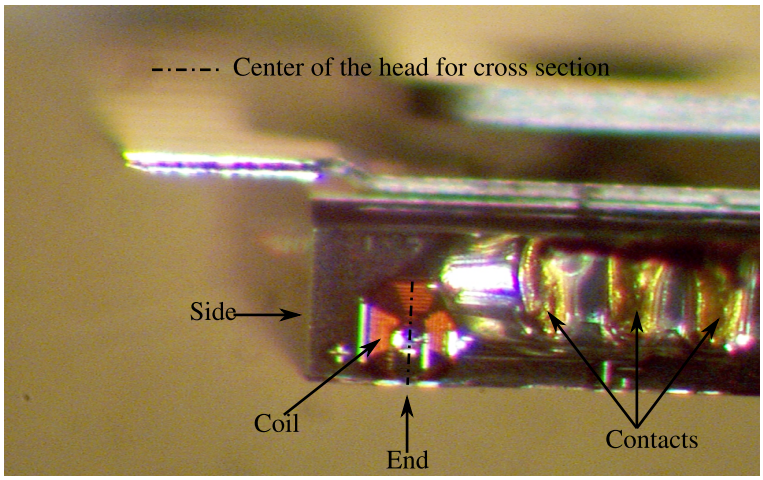

Figure 6.4: Microscopic detail of an actual head (top view). The coil is clearly visible. End and side view for cross section are indicated by arrows.

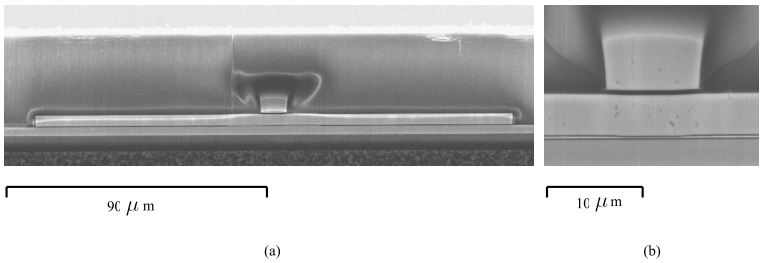

Figure 6.5: End view of head A under an electronic microscope. (a) Difference in thin film width detail and (b) gap region.

of the heads. Without inflicting permanent damage to the head it is only possible to observe the end view of the head using the SEM. Top view images can not be taken because the head is coated with a protective layer that prevented using the SEM to study the poles. Figure 6.5 shows end views with different magnification of head A. Front gap height and lower and upper thin film width and thicknesses can be obtained from this image (see Figure 6.3). These are shown in Table 6.1. In Figure 6.5(a) the difference in width of both upper and lower films is easily observable. Prior to using the sample in the electron microscope, a 5nm gold coating was applied and connected to a ground plane to avoid electrostatic charge.

Lower and upper thin film and gap lengths, back gap height, number of turns, coil cross-sectional area, and some other parameters can be obtained from a cross sectional image of the head (side view). In order to obtain a side view image, half of the head was cut out and therefore the head became unusable. The head sample was placed side down on a 2.5cm resin deposition cylinder, filled and left overnight to dry off. Special care was taken when pouring the resin to avoid any displacement of the sample from its vertical position. The sample was then polished with sand paper until the desired head section was visible. Special care was taken at this stage to stop polishing at or near the middle of the head and not pass through it. The final stage consisted of smoothing the surface by polishing with a fine diamond disk. Figure 6.6 shows an electron microscope image of head A's cross-section with two different magnifications.

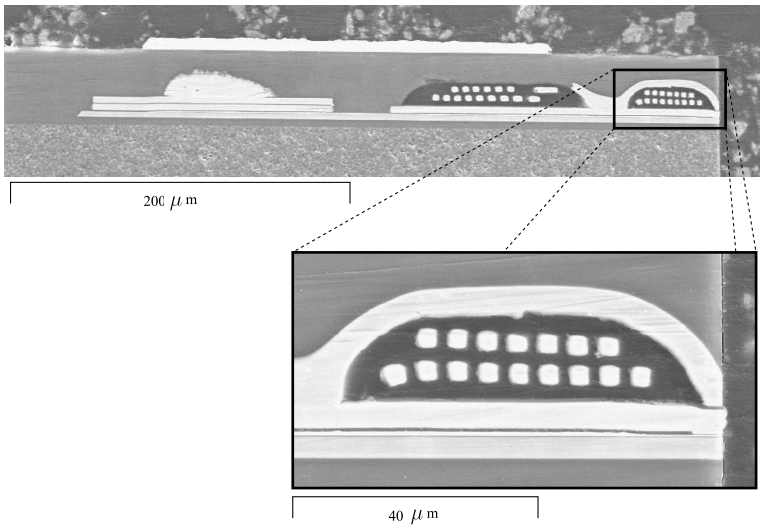

Figure 6.6: Cross-sectional side view of head A. Complete turns of the coil are noticed in the low magnification image. Clearly head A is a 16 turn head.

In the low magnification image it is possible to observe the complete turns and some metallic contacts. Images in Figures 6.5 and 6.6 are scaled therefore they allow the estimation of the actual dimensions of the head.

The same experimental procedure was applied to head B. Figures 6.7 and 6.8 show the end and cross-section images of the head respectively. The technological advances in eight years are noticed in the overall dimensions. A comparison between Figures 6.6 and 6.8 shows that head B is approximately 4 times smaller than head A (see Table 6.1).

INCA software from Oxford Instruments was used to study the material of the head's cross-section. The electronic microscope collects and analyses X-rays emitted from the sample therefore it is possible to display them as an X-ray spectrum. For the purpose of this work, four regions were analysed. These were the coils, the thin films, and the insulation region to the interior and the exterior of the head. The analysis indicated that thin-films are made of NiFe, coil is made of Copper and the insulation layers are

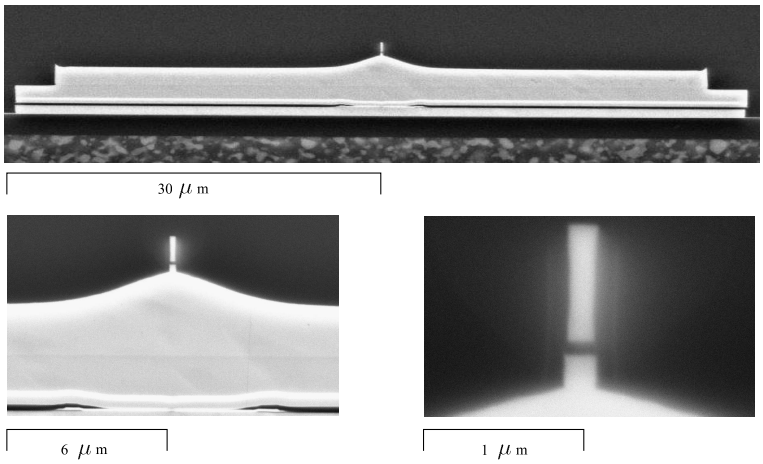

Figure 6.7: SEM images of end view of head B under an electronic microscope with detail of thin film width and gap region.

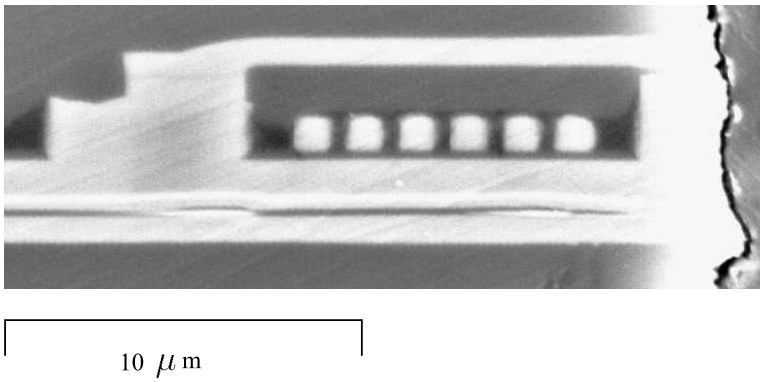

Figure 6.8: Cross-section side view of head B. Clearly head B is a 6 turn head.

Table 6.1: Dimension comparison between the two studied heads. The cross-section of the head represents the x-y plane. Gap height and film thicknesses are taken in the y direction, the overall length is taken in the x direction and the bottom and top film widths are taken in the z direction.

	Head A	Head B
Number of turns	16	6
Front gap height	450nm	100nm
Lower film length	60μm	20μm
Film thickness	4.5μm	1.2μm
Bottom film width	165μm	60μm
Top film width (gap region)	9μm	200nm

made of carbon.

6.3 The Resistance-Reluctance Model

In order to obtain an expression linking the inductance of the head to the time constants of the rotational magnetisation and the domain wall motion the resistance-reluctance model, introduced in Chapter 2, will be used. This model is based on the analogy between electric and magnetic circuits. Figure 6.9(a) shows an electric circuit with a voltage source and a resistive element. The relationship between current and voltage satisfies Ohm's law given by

$$v(t) = i(t)R \tag{6.3}$$

where $v(t)$ represents the electric potential difference, expressed in Volts, $i(t)$ is the electric current, expressed in Amperes, and R the electric resistance, expressed in Ohms.

When the equivalent magnetic circuit of Figure 6.9(b) is considered, Ohm's law becomes

$$\Psi(t) = \phi(t)\mathcal{R} \tag{6.4}$$

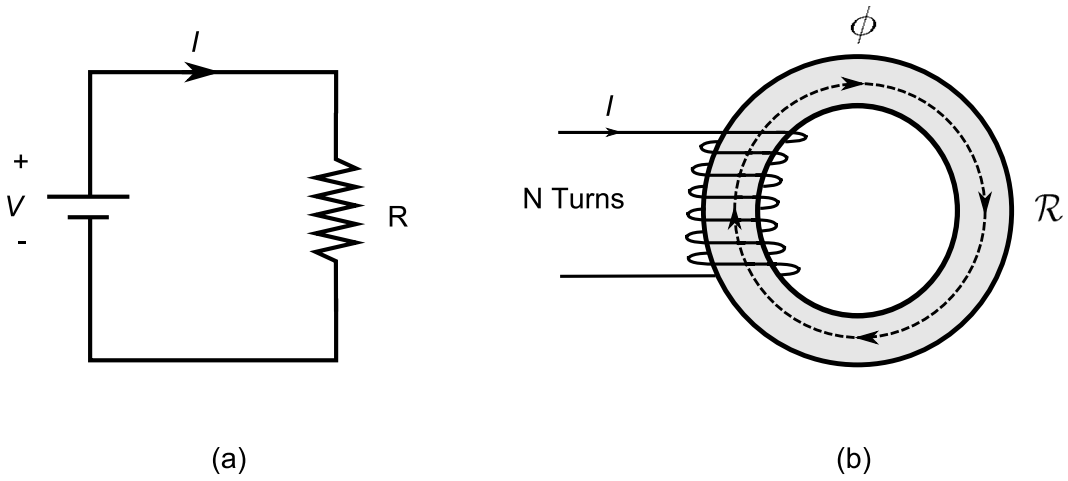

Figure 6.9: Analogy between an electric circuit and a magnetic circuit: (a) representation of an electric circuit with an electric voltage source, current and resistance, and (b) representation of the analogue circuit in the magnetic domain with a magnetic source, magnetic flux and reluctance.

now, Ψ is the magnetic potential difference, expressed in ampere-turns, ϕ is the magnetic flux, expressed in weber, and $\mathcal{R}$ is the reluctance, expressed in Henry^{-1}.

The electric resistance of a given material is defined as

$$R = \frac{l}{\sigma A} \tag{6.5}$$

where l and A represent the closed path length and the area of the material the electric current is flowing in, and σ represents the electrical conductivity of the material.

In the same manner, the magnetic reluctance is defined as

$$\mathcal{R} = \frac{l}{\mu_0 \mu_r A} \tag{6.6}$$

again, l and A represent the closed path length and the area of the material the flux is flowing through, and $\mu = \mu_0 \mu_r$ is the permeability. Equations (6.5) and (6.6) reflect the similarities between the reluctance and resistance of a given material in the electric and magnetic domains.

For linear systems the relation expressed in equation (6.4) can be extended to the frequency domain by taking the Fourier transform

$$\Psi(j\omega) = \Phi(j\omega)Z_m(j\omega) \tag{6.7}$$

in which Z_m is the complex magnetic impedance given by

$$Z_m(j\omega) = \frac{l}{\mu_0\mu_r(j\omega)A} \tag{6.8}$$

Its magnitude $|Z_m|$ is expressed in Henry^{-1}.

The interaction between the electric and magnetic domains in the time domain is from Gauss' and Faraday's laws:

$$\Psi(t) = Ni(t) \tag{6.9}$$

$$v(t) = N\frac{\partial\phi(t)}{\partial t} \tag{6.10}$$

and in the frequency domain by taking the Fourier transform:

$$\Psi(j\omega) = NI(j\omega) \tag{6.11}$$

$$V(j\omega) = j\omega N\Phi(j\omega) \tag{6.12}$$

where N is the number of turns.

The relation between electrical impedance and magnetic impedance can be derived by substituting $\Psi(j\omega)$ and $\Phi(j\omega)$ form equations (6.11) and (6.12) into equation (6.7). Thus

$$Z_e(j\omega) = \frac{j\omega N^2}{Z_m(j\omega)} \tag{6.13}$$

This expression will be used in the following analysis.

6.4 Equivalent Circuit of a Magnetic Impedance

When analysing a circuit containing both electric and magnetic impedances, it is frequently desirable to replace the magnetic impedances by their equivalent circuits in the electric domain. Then, the constraints they impose are accounted for by simple circuit analysis. Before defining an equivalent circuit for the magnetic impedance it is worth studying the magnetic losses which in fact are the origin of any individual circuital component of the equivalent circuit. Magnetic losses can be modeled by the introduction of a complex frequency dependent relative permeability

$$\mu_r(j\omega) = \mu_r'(\omega) + j\mu_r''(\omega) \tag{6.14}$$

Substituting equation (6.8) into (6.13) the electric impedance of a lossy conductor is found to be

$$Z_e(j\omega) = j\omega\mu_0\mu_r(j\omega)N^2\left(\frac{A}{l}\right) \tag{6.15}$$

or expressed in terms of its real and imaginary parts using (6.14)

$$Z_e(j\omega) = j\omega L(\omega) + R(\omega) \tag{6.16}$$

where

$$L(\omega) = \mu_0\mu_r'(\omega)N^2\frac{A}{l} \tag{6.17}$$

$$R(\omega) = \omega\mu_0\mu_r''(\omega)N^2\frac{A}{l} \tag{6.18}$$

Equation (6.16) shows that the electrical equivalent circuit of a lossy dielectric is a series connection of an inductance $L(\omega)$ and a resistance $R(\omega)$.

Equations (6.17) and (6.18) show that the component values of L and R are frequency dependent and therefore can not be determined by simple circuit analysis of frequency independent electrical component values.

In order to avoid this frequency dependence of the circuital components, it is possible to describe the complex permeability in equation (6.14) in terms of the physical relaxation effects of the domain wall movement and of the rotational magnetisation (Blanken and Vlerken, 1991) as

$$\mu_r(j\omega) = \frac{\chi_w}{1 + j\omega\chi_w\tau_w} + \frac{\chi_r}{1 + j\omega\chi_r\tau_r} + 1 \tag{6.19}$$

where χ_w and χ_r are the non-dimensional susceptibilities of the domain wall movement and the rotational magnetisation respectively. The time constants τ_w and τ_r are material properties and are expressed in seconds.

Substituting (6.19) in the general equation for the magnetic impedance (6.8) gives

$$Z_m(j\omega) = \frac{l}{\mu_0 A} \Bigg/ \left(\frac{\chi_w}{1 + j\omega\chi_w\tau_w} + \frac{\chi_r}{1 + j\omega\chi_r\tau_r} + 1 \right) \tag{6.20}$$

dividing numerator and denominator by $l/\mu_0 A$ gives

$$Z_m(j\omega) = 1 \Bigg/ \left(\frac{\chi_w}{\frac{l}{\mu_0 A} + j\omega\chi_w\tau_w\frac{l}{\mu_0 A}} + \frac{\chi_r}{\frac{l}{\mu_0 A} + j\omega\chi_r\tau_r\frac{l}{\mu_0 A}} + \frac{1}{\frac{l}{\mu_0 A}} \right) \tag{6.21}$$

or

$$Z_m(j\omega) = 1 \Bigg/ \left(\frac{1}{\frac{l}{\chi_w\mu_0 A} + j\omega\tau_w\frac{l}{\mu_0 A}} + \frac{1}{\frac{l}{\chi_r\mu_0 A} + j\omega\tau_r\frac{l}{\mu_0 A}} + \frac{1}{\frac{l}{\mu_0 A}} \right) \tag{6.22}$$

by defining the magnetic reluctances $\mathcal{R}$, $\mathcal{R}_w$ and $\mathcal{R}_r$ as

$$\mathcal{R} = \frac{l}{\mu_0 A} \tag{6.23}$$

$$\mathcal{R}_w = \frac{\mathcal{R}}{\chi_w} \tag{6.24}$$

$$\mathcal{R}_r = \frac{\mathcal{R}}{\chi_r} \tag{6.25}$$

and the magnetic inductances $\mathcal{L}_w$ and $\mathcal{L}_r$ as

$$\mathcal{L}_w = \tau_w\mathcal{R} \tag{6.26}$$

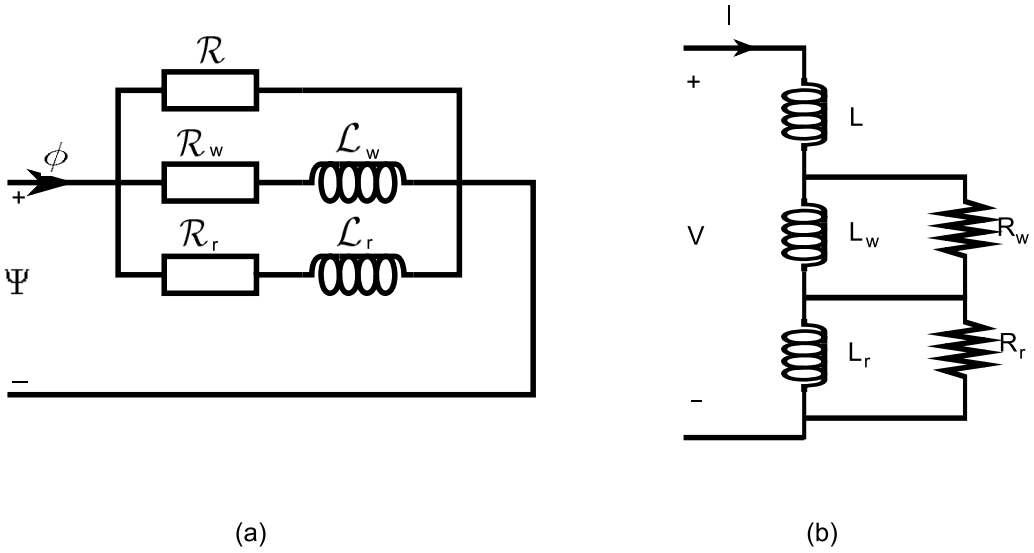

Figure 6.10: Equivalent circuit of a magnetic impedance: (a) in the magnetic domain magnetic reluctances and magnetic inductances are considered; (b) in the electric domain electric resistances and inductances are considered.

$$\mathcal{L}_r = \tau_r \mathcal{R} \tag{6.27}$$

equation (6.22) becomes

$$Z_m(j\omega) = 1 \Big/ \left(\frac{1}{\mathcal{R}_w + j\omega\mathcal{L}_w} + \frac{1}{\mathcal{R}_r + j\omega\mathcal{L}_r} + \frac{1}{\mathcal{R}} \right) \tag{6.28}$$

which can be represented by the reluctance circuit of Figure 6.10(a). $\mathcal{R}$ is the air reluctance of the gap, $\mathcal{R}_w$ and $\mathcal{L}_w$ represent the domain wall contribution and $\mathcal{R}_r$ and $\mathcal{L}_r$ represent the contribution of the rotational magnetisation. The subscript m in the impedance means that the magnetic domain is being considered.

Now, the circuital component values are frequency independent, implying that implementation with simple circuital analysis in the electric domain is possible. The reluctance values are expressed in Henry^{-1} and the magnetic inductance values are expressed in Ω^{-1}. The magnetic losses, implying power dissipation and thermal noise, are modeled by the magnetic inductances $\mathcal{L}_w$ and $\mathcal{L}_r$.

It must be emphasised that the magnetic inductances $\mathcal{L}_w$ and $\mathcal{L}_r$ are dependent on the

material properties τ_w and τ_r only and not on the susceptibilities χ_w and χ_r. A change of the susceptibility χ_r, e.g. caused by a change of the grain size of a polycrystalline ferrite, changes the value of the reluctance $\mathcal{R}_r$, but does not change the time constant τ_r and thus does not change the value of the magnetic inductance $\mathcal{L}_r$ (Johnson and Visser, 1990).

Next, application of equation (6.13) on the magnetic impedance of the circuit in Figure 6.10(a) represented mathematically by (6.28) yields

$$Z_e(j\omega) = j\omega N^2 \left(\frac{1}{\mathcal{R}_w + j\omega\mathcal{L}_w} + \frac{1}{\mathcal{R}_r + j\omega\mathcal{L}_r} + \frac{1}{\mathcal{R}} \right) \tag{6.29}$$

or

$$Z_e(j\omega) = 1 \Bigg/ \left(\frac{1}{\frac{j\omega N^2}{\mathcal{R}_w}} + \frac{1}{\frac{N^2}{\mathcal{L}_w}} \right) + 1 \Bigg/ \left(\frac{1}{\frac{j\omega N^2}{\mathcal{R}_r}} + \frac{1}{\frac{N^2}{\mathcal{L}_r}} \right) + \frac{j\omega N^2}{\mathcal{R}} \tag{6.30}$$

which can be rewritten as

$$Z_e(j\omega) = 1 \Bigg/ \left(\frac{1}{j\omega L_w} + \frac{1}{R_w} \right) + 1 \Bigg/ \left(\frac{1}{j\omega L_r} + \frac{1}{R_r} \right) + j\omega L \tag{6.31}$$

with electrical parameters

$$L = \frac{\mu_0 N^2 A}{l} \tag{6.32}$$

$$L_w = \chi_w L \tag{6.33}$$

$$L_r = \chi_r L \tag{6.34}$$

$$R_w = \frac{L}{\tau_w} \tag{6.35}$$

$$R_r = \frac{L}{\tau_r} \tag{6.36}$$

Figure 6.10(b) shows the equivalent electrical circuit described by equation (6.31), where L is the inductance corresponding to the winding of the coil and the electric resistances and inductances R_w, R_r, L_w and L_r are the contribution of domain wall motion and rotational magnetisation respectively. The magnetic circuits on one hand and their corresponding electrical equivalent form dual circuits (Colin-Cherry, 1948).

6.5 Extension to a Magnetic Head

When a magnetic head is being considered, it is assumed that the current circulating through the coil generates two fluxes, namely the flux through the ferrite core ϕ_{core} and the stray flux ϕ_{stray}. The former flows through a magnetic impedance similar to that of Figure 6.10(a) and the latter flows through a magnetic reluctance connected in parallel. Figure 6.11 shows the magnetic impedance equivalent dual circuits in the magnetic and electric domains for a magnetic head. So far, wire resistance and parasitic capacitance are not accounted for. It is this capacitance that causes the resonance in the impedance figure. Therefore, to complete the head model in the electric domain, the wire resistance must be connected in series and then the parasitic capacitance in parallel to the electrical circuit of Figure 6.10(b) yielding the circuit of Figure 6.12 which is the complete electrical equivalent of a magnetic head, i.e. only the electric domain is being considered and the constraints of the magnetic domain are accounted for by a rearrangement of equivalent impedances. Using this equivalent circuit allows the computation of impedance graphs like the one shown in Figure 6.13.

The physical process involved in an actual head which leads to the resonance can be explained by looking at the simple equivalent circuit of Figure 6.2(a). The impedance of the inductor varies as ωL thus it becomes zero at low frequencies, i.e. equals to a short circuit and therefore only the resistor R is accounted for in the impedance figure. As the frequency increases ωL soon becomes much larger than R and the coil behaves as

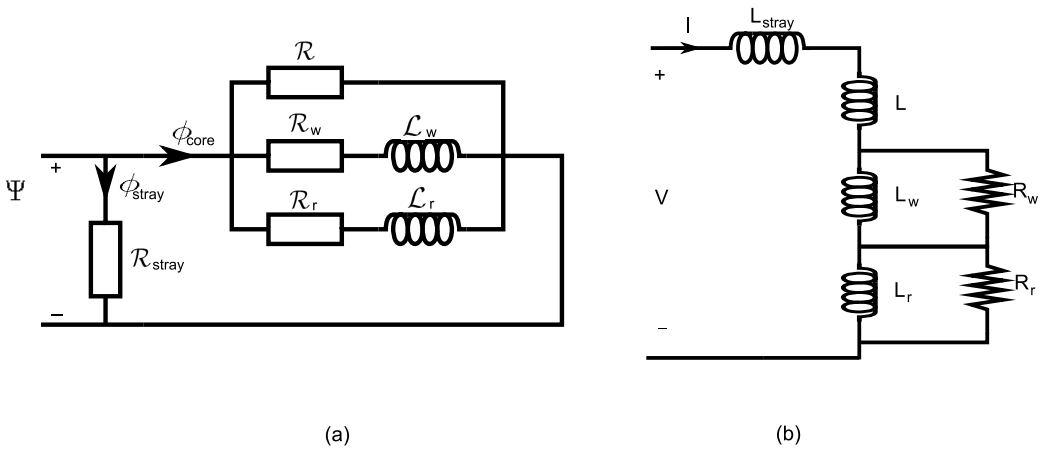

Figure 6.11: Equivalent circuit of the magnetic impedance of a head (a) in the magnetic domain and (b) in the electric domain. The total flux in figure (a) is the contribution of two fluxes, the flux through the ferrite core and the stray flux.

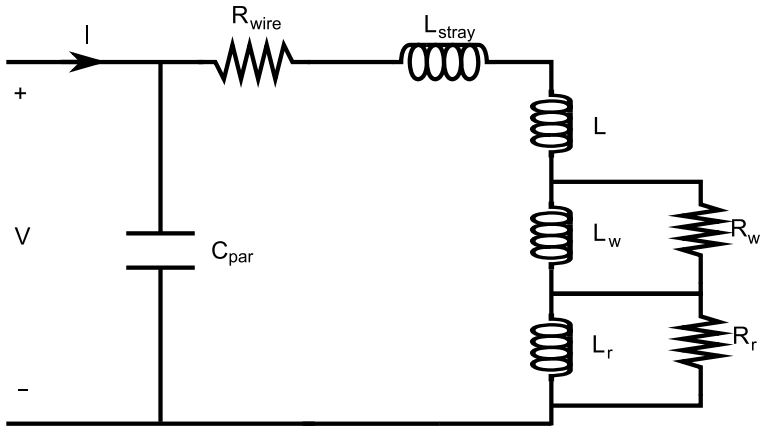

Figure 6.12: Complete equivalent circuit of a magnetic head in the electric domain. Wire resistance and parasitic capacitance have been added to the circuit of Figure 6.11(b) for resonance. Only the electric domain is being considered.

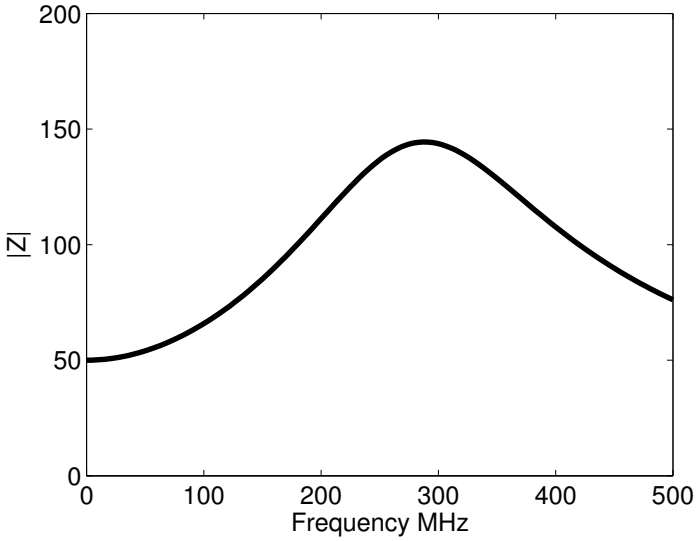

Figure 6.13: Magnitude of the electrical impedance (Ω) as a function of frequency (MHz) of a magnetic head using the equivalent circuit of Figure 6.12 and parameters $R_{wire} = 50\Omega$, $C_{par} = 6$pF, $L_{stray} = 10$nH, $L = 25$nH, $L_w = 6$nH, $R_w = 10\Omega$, $L_r = 7$nH and $R_r = 20\Omega$.

an ideal inductor. As the frequency rises to higher values, the parasitic capacitance of the coil becomes important. The impedance of the capacitor is proportional to $1/\omega C$, which is large for small ω. For small enough frequencies a capacitor is considered as an open circuit and when it is connected in parallel to a load impedance, it draws no current. But at high frequencies, due to the high impedance of the inductor, it is easier for the current to flow through the equivalent capacitor representing the parasitic capacitance between the turns, rather than through the inductor. Thus, the current in the coil jumps from one turn to the other instead of going around and around. Although the current is intended to go around the loop, it takes the easier path, the path of least impedance. This causes the resonance observed in Figure 6.2(b) forcing the magnitude of the impedance to have a maximum value.

The resonance frequency is that at which the impedance of a circuit is purely resistive. When working with circuits involving parallel connections, it is preferable to work

with admittances for simplicity of the equations which reduce to a sum of admittances. As the admittance is the inverse of the impedance, at the resonance frequency, the admittance is also purely resistive. The admittance of the circuit in figure 6.2(a) is

$$Y(j\omega) = \frac{1}{Z(j\omega)} = \frac{1}{R + j\omega L} + j\omega C \tag{6.37}$$

or expressing the series connection of the inductor and the resistor in terms of its real and imaginary parts

$$Y(j\omega) = \frac{R - j\omega L}{R^2 + \omega^2 L^2} + j\omega C \tag{6.38}$$

rearranging terms gives

$$Y(j\omega) = \frac{R}{R^2 + \omega^2 L^2} + j\omega \left(C + \frac{L}{R^2 + \omega^2 L^2} \right) \tag{6.39}$$

The resonance is found at the frequency that satisfies $Im\{Y(j\omega)\} = 0$, that is

$$C + \frac{L}{R^2 + \omega_0^2 L^2} = 0 \tag{6.40}$$

thus

$$\omega_0 = \sqrt{\frac{L - R^2 C}{L^2 C}} \tag{6.41}$$

or

$$f_0 = \frac{\omega_0}{2\pi} = \frac{1}{2\pi} \sqrt{\frac{L - R^2 C}{L^2 C}} \tag{6.42}$$

The magnitude of the admittance is given by

$$|Y(j\omega)| = \frac{R}{R^2 + \omega^2 L^2} + \omega^2 \left(C + \frac{L}{R^2 + \omega^2 L^2} \right)^2 \tag{6.43}$$

At the resonance frequency, the second term in equation (6.43) becomes zero. For all other frequencies this term in greater than zero therefore the admittance reaches its minimum value at the resonance frequency and in turn the impedance gets to its maximum. For the parameter values of Figure 6.2(a) the resonance frequency given by (6.42) is 277.1 MHz which agrees with the frequency at which Figure 6.2(b) shows the maximum value.

6.6 Low Frequency Approximation

As discussed previously, the resonance effect introduced by the coil capacitance becomes important at high frequencies. For all other frequencies, the capacitor can be considered as an open circuit. From equation (6.37), it is possible to consider the capacitor as an open circuit if the following approximation is satisfied

$$j\omega C << j \;\; Im\left\{\frac{1}{R+j\omega L}\right\} \tag{6.44}$$

that is

$$j\omega C << \frac{j\omega L}{R^2+\omega^2 L^2} \tag{6.45}$$

Solving (6.45) for ω gives

$$\omega << \sqrt{\frac{L-CR^2}{CL^2}} \tag{6.46}$$

and applying (6.41)

$$\omega << \omega_0 \tag{6.47}$$

Thus as long as $\omega << \omega_0$ it is possible to dismiss the resonance effect of the parasitic capacitance and simplify the expression for the impedance to a great extent. The circuit in Figure 6.2(a) without the equivalent capacitor of the parasitic capacitance becomes the series connection of the inductor L and the resistor R. Hence the expression of the impedance reduces to a sum, $Z = R + j\omega L$. This approximation applies to all resonant circuits where there is a capacitor in parallel to a load impedance.

The assumption of (6.47) when analysing the circuit of Figure 6.12 allows the measured inductance to be approximated. This can be obtained by considering the impedance of the circuit if the stray capacitance is dismissed

$$Z(j\omega) = R_{wire} + j\omega(L_{stray} + L) + Z_w(\omega) + Z_r(\omega) \tag{6.48}$$

where

$$Z_w(\omega) = 1 \Big/ \left(\frac{1}{R_w} + \frac{1}{j\omega L_w} \right) = \frac{j\omega L_w R_w}{R_w + j\omega L_w} \tag{6.49}$$

and

$$Z_r(\omega) = 1 \Big/ \left(\frac{1}{R_r} + \frac{1}{j\omega L_r} \right) = \frac{j\omega L_r R_r}{R_r + j\omega L_r} \tag{6.50}$$

or in terms of their real and imaginary parts

$$Z_w(\omega) = \frac{\omega^2 R_w L_w^2}{R_w^2 + \omega^2 L_w^2} + j\frac{\omega L_w R_w^2}{R_w^2 + \omega^2 L_w^2} \tag{6.51}$$

and

$$Z_r(\omega) = \frac{\omega^2 R_r L_r^2}{R_r^2 + \omega^2 L_r^2} + j\frac{\omega L_r R_r^2}{R_r^2 + \omega^2 L_r^2} \tag{6.52}$$

To give expressions (6.51) and (6.52) a physical meaning, it is possible to define the time constants of the domain wall motion and the rotational magnetisation as

$$\tau_w = \frac{L_w}{R_w} \tag{6.53}$$

$$\tau_r = \frac{L_r}{R_r} \tag{6.54}$$

then (6.51) and (6.52) become

$$Z_w(\omega) = \frac{\omega^2 L_w \tau_w}{1 + \omega^2 \tau_w^2} + j\frac{\omega L_w}{1 + \omega^2 \tau_w^2} \tag{6.55}$$

$$Z_r(\omega) = \frac{\omega^2 L_r \tau_r}{1 + \omega^2 \tau_r^2} + j\frac{\omega L_r}{1 + \omega^2 \tau_r^2} \tag{6.56}$$

It is observed that both (6.55) and (6.56) have resistive and inductive parts which are frequency dependant thus it is possible to write

$$Z_w = R_{wall}(\omega) + j\omega L_{wall}(\omega) \tag{6.57}$$

$$Z_r = R_{rot\ mag}(\omega) + j\omega L_{rot\ mag}(\omega) \tag{6.58}$$

where $R_{wall}(\omega)$, $R_{rot\ mag}(\omega)$, $L_{wall}(\omega)$ and $L_{rot\ mag}(\omega)$ are

$$R_{wall}(\omega) = \frac{\omega^2 L_w \tau_w}{1 + \omega^2 \tau_w^2} \tag{6.59}$$

$$R_{rot\ mag}(\omega) = \frac{\omega^2 L_r \tau_r}{1 + \omega^2 \tau_r^2} \tag{6.60}$$

$$L_{wall}(\omega) = \frac{L_w}{1 + \omega^2 \tau_w^2} \tag{6.61}$$

$$L_{rot\ mag}(\omega) = \frac{L_r}{1 + \omega^2 \tau_r^2} \tag{6.62}$$

Substituting (6.57) and (6.58) in (6.48) gives

$$\begin{aligned} Z(j\omega) &= R_{wire} + R_{wall}(\omega) + R_{rot\ mag}(\omega) \\ &\quad + j\omega(L_{stray} + L + L_{wall}(\omega) + L_{rot\ mag}(\omega)) \end{aligned} \tag{6.63}$$

being therefore

$$L(\omega) = \sum L_i = L_{stray} + L + L_{wall}(\omega) + L_{rot\ mag}(\omega) \tag{6.64}$$

the inductance of the equivalent circuit. Which is in agreement with (Prabhakar and Filips, 1999)

$$\frac{1}{\omega} Im\{Z(j\omega)\} \equiv L(\omega) \simeq \sum_{i=1}^{N} L_i(\omega) \tag{6.65}$$

where $L_i(\omega)$ represents the inductive contribution of domain wall movement, rotational magnetisation, the stray reluctance and the winding itself.

6.7 Head Saturation

This section shows a way to separate the effects of the rotational magnetisation and domain wall motion from that of the wire itself. It can be done by saturating the head under a strong external field. In this manner rotational magnetisation and domain wall motion are not present.

As seen in section 3.2.1, the magnetisation $\mathbf{M}$ is a field quantity that defines the magnetic flux density $\mathbf{B}$ as

$$\mathbf{B} = \mu_0(\mathbf{H} + \mathbf{M}) \tag{6.66}$$

A relation between the magnetisation $\mathbf{M}$ and the magnetic field strength $\mathbf{H}$ exists in many materials. In diamagnetic and paramagnetic materials, this relation is usually linear.

$$\mathbf{M} = \chi_m \mathbf{H} \tag{6.67}$$

Where χ_m is called the magnetic susceptibility which leads to the relative permeability μ_r that defines the material. However, in ferromagnetic materials there is no one-to-one correspondence between $\mathbf{M}$ and $\mathbf{H}$ but they are still related to one another. This nonlinear relation is described by the hysteresis loop that describes the material. An example of a hysteresis loop for a ferromagnetic material is shown in Figure 6.14. Briefly, when an external field is applied to a ferromagnet, the magnetic dipoles align themselves with the external field generating an increase in the overall magnetisation. Even when the external field is removed, part of the alignment remains. The material has become magnetised. There is a point to the right of the graph where further increases in the magnetic field strength $\mathbf{H}$ will result in no further change in the magnetisation $\mathbf{M}$, this condition is denoted as magnetic saturation. The magnitude of the magnetisation when the material is saturated is called saturation magnetisation M_s. If the magnetic field is then reduced linearly, the magnetisation follows a different curve

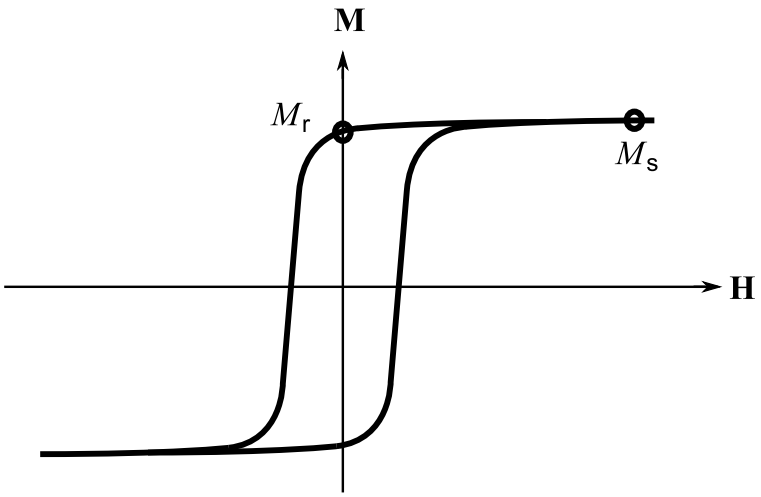

Figure 6.14: Hysteresis loop for a ferromagnetic material. M_s denotes the saturation magnetisation and M_r the remanent magnetisation.

back towards zero magnetic field strength. The magnitude of the magnetisation at this point is denoted remanent magnetisation M_r. In an ideal hysteresis loop M_s and M_r represent the same quantity and the backwards curve is flat.

The saturation condition involves that neither domain wall motion nor rotational magnetisation are present. That is, in terms of relaxation constants

$$\chi_w = 0 \tag{6.68}$$

$$\chi_r = 0 \tag{6.69}$$

Substituting (6.68) and (6.69) in (6.19) results in $\mu_r = 1$ which is equivalent to having a material with the same magnetic properties as free space. When substituted in (6.33) and (6.34) gives

$$L_w = 0 \tag{6.70}$$

$$L_r = 0 \tag{6.71}$$

thus the overall impedance of inductors L_w and L_r can be considered as a short circuit in the equivalent circuit of Figure 6.12. When a current finds a short circuit in parallel

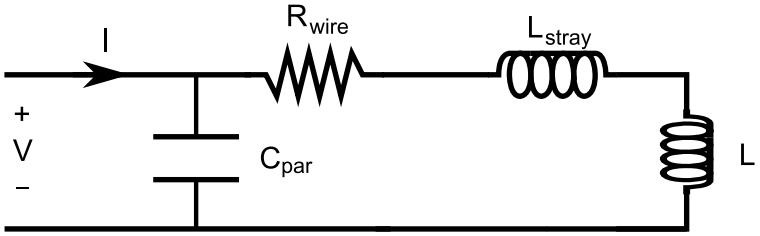

Figure 6.15: Equivalent circuit of a saturated magnetic head in the electric domain. Note that there are no lumped elements related to domain wall motion or rotational magnetisation.

with any load, it flows through the short circuit and the load has no influence in the analysis. Therefore the circuit in Figure 6.12 under saturation conditions reduces to Figure 6.15. Applying the low frequency approximation (6.47) allows to dismiss the stray capacitance and to compute the impedance as

$$Z_{sat}(j\omega) = R_{wire} + j\omega(L_{stray} + L) \tag{6.72}$$

where the subscript *sat* means that the head is saturated. The procedure of saturating the head in order to separate magnetic and electric losses was introduced in section 6.1. By subtracting the saturated impedance in (6.72) from the unsaturated one in (6.63) gives

$$\begin{aligned} Z(j\omega) - Z_{sat}(j\omega) &= R_{wall}(\omega) + R_{rot\ mag}(\omega) \\ &\quad + j\omega(L_{wall}(\omega) + L_{rot\ mag}(\omega)) \end{aligned} \tag{6.73}$$

where the contribution of domain wall motion and rotational magnetisation are isolated from the overall impedance. This allows, for example, by measurement of saturated and unsaturated inductances of the same head the estimation of the relaxation constants χ_w and χ_r.

6.8 Impedance Measurements

The impedance is defined as the total opposition that a device or circuit offers to the flow of an alternating current at a given frequency. It is represented as a complex quantity that consists of a real part or resistance R, and an imaginary part or reactance X:

$$Z = R + jX \tag{6.74}$$

Resistance and reactance determine the magnitude and phase of the impedance through the following relations:

$$|Z| = \sqrt{R^2 + X^2} \tag{6.75}$$

$$\angle Z = tan^{-1}\left(\frac{X}{R}\right) \tag{6.76}$$

A device with a purely resistive impedance exhibits no phase shift between the voltage and current. A component with a finite reactance induces a phase shift between the voltage across it and the current through it. A reactive component is distinguished by the fact that the sinusoidal voltage across the component is in quadrature with the sinusoidal current through the component. This implies that the component alternately absorbs energy from the circuit and then returns energy to the circuit. A pure reactance will not dissipate any power. The reactance can be inductive or capacitive. Inductive reactance takes the form $X_L = \omega L$ whereas capacitive reactance, $X_C = 1/\omega C$. Thus it is possible to define the inductance L and the capacitance C of a device as

$$L = \frac{X_L}{\omega} \tag{6.77}$$

$$C = \frac{1}{X_C \omega} \tag{6.78}$$

The admittance is defined as the inverse of the impedance and its real and imaginary parts are denoted as conductance G and susceptance B respectively. A similar analogy to that in (6.77) and (6.78) applies to susceptance and admittance.

$$Y = \frac{1}{Z} = G + jB \tag{6.79}$$

The Agilent 4396B impedance analyser with a 43961A impedance test kit was used to measure thin-film head impedances (see Figure 6.16(a)). This instrument uses an I-V method to measure the impedance of a DUT (Device Under Test). The I-V method computes the impedance from the measured voltage and current by application of Ohm's law. In consequence, the measurement error does not depend on the impedance of the DUT because the I-V method measures the impedance directly from the ratio of the voltage and current. This way of operation provides constant accuracy which is the major advantage of the I-V method. The Agilent 4396B operates from 100 kHz to 1.8 GHz with 1 mHz resolution and its integrated source provides -60 to +20 dBm of output power with 0.1 dB resolution. The dynamic magnitude and phase accuracy are +/-0.05 dB and +/-0.3 deg so that it can accurately measure gain and group delay flatness.

The measurement set up of the 4396B is shown in Figure 6.17. The instrument has three ports namely RF OUT, R and A port. The source signal is output from RF OUT port. The R port receiver measures a voltage. The A port receiver measures the voltage across the equivalent input impedance of the analyser R_0 to obtain a current and therefore compute the impedance of the DUT. The test signal level actually applied to the DUT depends on the test signal level from the 4396B, the output impedance, the insertion loss of the Impedance Test Kit, and the impedance of the DUT. The simplified equivalent circuit of the impedance analyser is shown in Figure 6.17(b), the output signal is divided by the input impedance R_0 and the impedance of the DUT. It is possible to use the following equation to determine the signal level actually applied to the DUT in volts.

$$V_{DUT} = V_{SET} \frac{Z_{DUT}}{Z_{DUT} + R_0} \tag{6.80}$$

where V_{DUT} is the voltage level that is actually applied to the DUT, V_{SET} is the voltage level set oscillator, Z_{DUT} is the impedance of the DUT, and R_0 is the 50Ω input impedance. The instrument allows to introduce the desirable power level P_{SET}

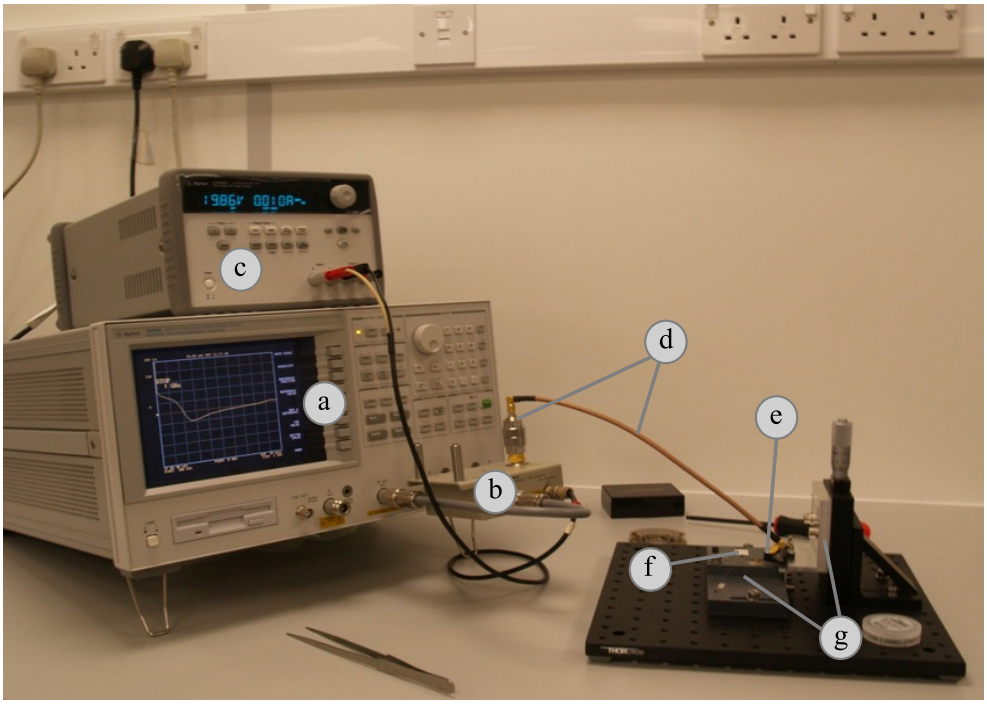

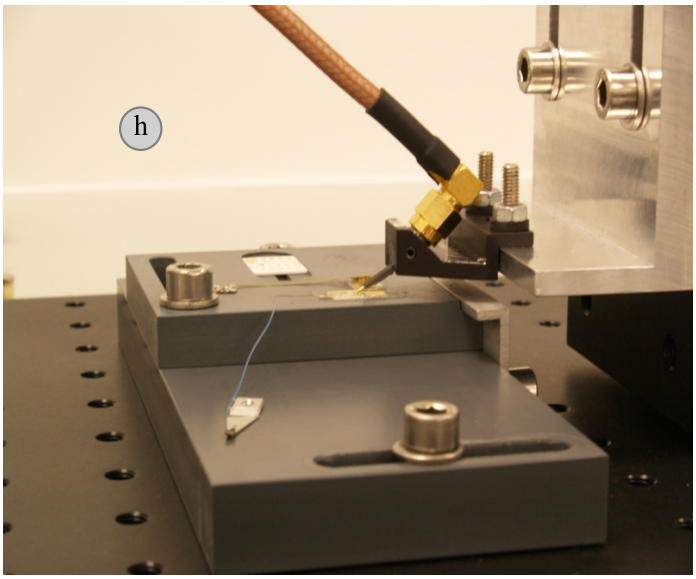

Figure 6.16: Equipment used to measure the head impedances. (a) Impedance analyser (Agilent 4396B), (b) Impedance test kit (Agilent 43961A), (c) DC bias power source (Agilent E364xA), (d) high frequency coaxial cable and connectors, (e) high frequency probe (Picoprobe 40A), (f) calibration substrate (Picoprobe CS17) and (g) positioning station (custom made). On the bottom of the image (h) a zoomed image of the positioning station is shown.

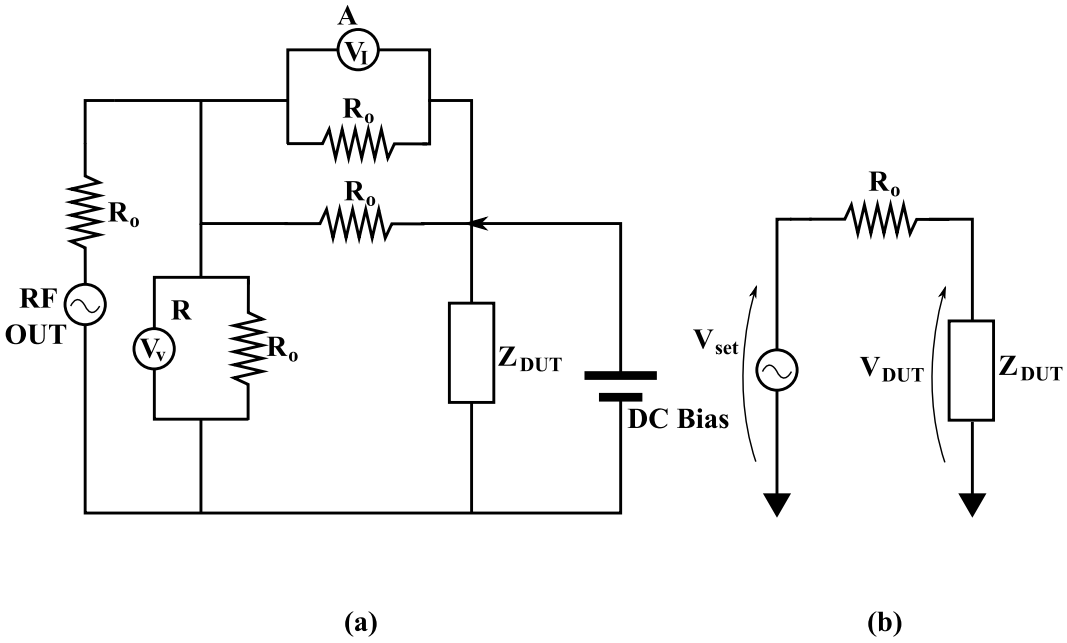

Figure 6.17: Agilent impedance analyser 4396B (a) measurement circuit and (b) test signal level equivalent circuit.

of the RF OUT port in dBm. The output voltage level is defined as the level when the RF OUT port is 50Ω terminated. Therefore

$$V_{SET} = \sqrt{10^{\frac{P_{SET}}{10}} 0.001 R_0} \tag{6.81}$$

The combination of the 4396B impedance analyser and the 43961A test kit allows to measure the impedance of a DUT connected to the measurement port. To connect the instrument to the contact pads of the DUT a test fixture was constructed. The fixture used to carry out the measurements consists of a Picoprobe 40-A-GS-1500-DP high frequency probe with a fixed pitch of 1.5mm between its differential contacts or tips, and connected to the analyser by a high frequency 50Ω coaxial cable. The Model 40A microwave probe provides direct viewing of the probe tips for accurate positioning. The probe with its reliable low resistance contact is one of the key features to providing highly repeatable measurements. It comes with spring loaded tips which ensure a reliable contact to the probing surface. The configuration of the tip footprints is the

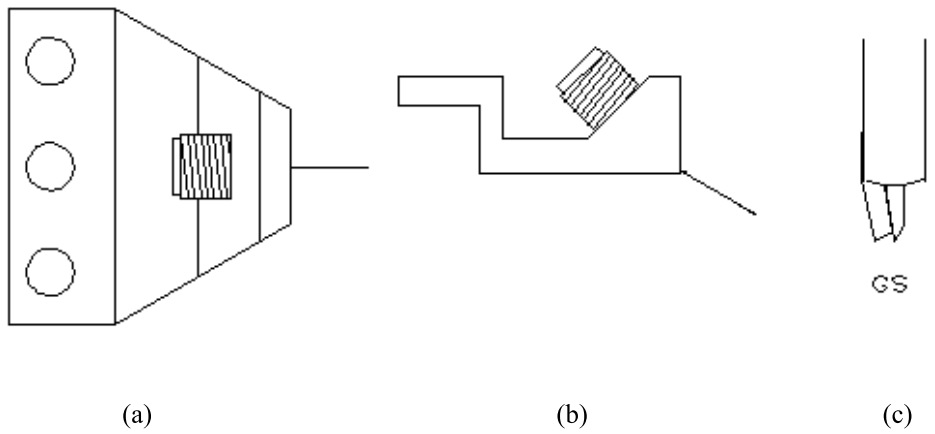

Figure 6.18: Schematic drawing of the Picoprobe 40A microwave probe used for measurement of thin-film head imedances. (a) Top view, (b) side view and (c) detail of the probe tip.

typical ground-signal (GS), as shown in Figure 6.18(b). Connection to the Model 40A is through a female SMA connector. The probe operates from DC to 40GHz, it has 1.6 dB typical insertion loss and the return loss is less than 30dB to 4GHz. Figure 6.16(e) shows an actual image of the 40A probe.

In order to complete the measurement equipment, it was necessary to construct a positioning station that allows the probe to make contact with the DUT. The station used was custom made and allows movement in three dimensions, as shown by Figure 6.19. The main part of the station is a 25mm travel translation stage attached to a 300x300mm breadboard through a right angle bracket, to allow movement in the z direction. The probe is then attached to the positioner through another bracket. The movement in the x and y directions is possible through two PVC slotted boards and a set of screws. The upper board is carved with the dimensions of the calibration substrate to avoid handling and for easy calibration. The contact pads of the heads are attached to the upper board using commercial two side tape. The heads are saturated by applying an external strong magnetic field (3000 - 7000 Oe) from a permanent magnet.

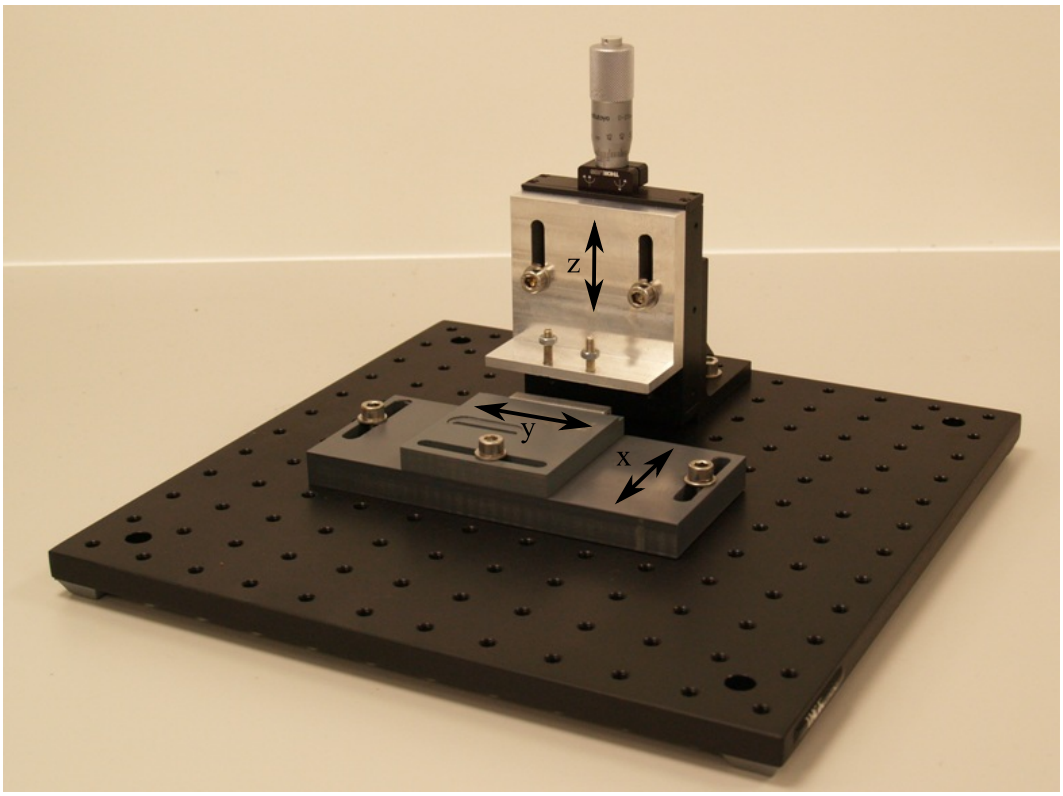

Figure 6.19: Detail of the custom made positioner used for measurement. A 25mm travel translation stage allows movement in the z direction and two custom made PVC boards allow movement in the x and y directions.

Measurement errors in network analysis can be separated into two categories: random and systematic errors. Random errors are non-repeatable measurement variations and are usually unpredictable. Systematic errors on the other hand, are repeatable measurement variations which include mismatch and leakage signals in the test setup, isolation characteristics between the reference and test signal paths, and system frequency response. In most microwave measurements, systematic errors are the most significant source of measurement uncertainty. The process that mathematically compensates for the systematic errors in the measurement system is denoted as calibration. To calibrate an instrument is to define a calibration plane, at which the specific measurement accuracy can be obtained. Standard devices, typically open, short and load, must be connected to the instrument at the calibration plane then the instrument is adjusted mathematically so that it measures within its specified accuracy. Each standard has a precisely known or predictable magnitude and phase response as a function of frequency. The Picoprobe's calibration substrate was used to calibrate the measurement system at the pole tips of the probe. This means that the calibration plane is at the pole tips which are the end point of the measurement system thus no other kind of compensation is needed to improve the accuracy in the measurement. As this calibration kit substrate is not from the same manufacturer as the impedance analyser the compensation parameters were not preprogrammed in the instrument and were programmed and stored in the instrument's memory for further use. The calibration procefure was repeated each time a measurement parameter (e.g. oscillator signal level) was changed.

The impedance analyser displays the information in several ways such as real part of the impedance, imaginary part of the impedance, magnitude of the impedance, phase of the impedance, the corresponding admittance plots, Q factor, inductive reactance, capacitive reactance, reflection coefficient, and many others. As they are all based on mathematical computations there is only need to know and store a couple of measured data that completely define the impedance. Then, only the magnitude and phase of

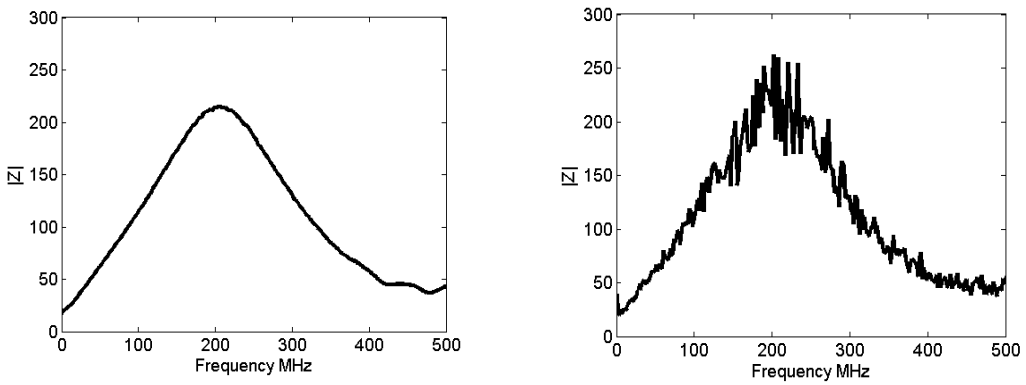

Figure 6.20: Magnitude of the impedance (Ω) of a head with different RF OUT port power levels. (a) $P_{SET} = 0dBm$ and (b) $P_{SET} = -60dBm$. With low power level the measurement becomes noisy.

the impedance were saved to a file for each measurement. If needed, the remaining displayed data can be obtained from the stored impedance by mathematical computation.

Prior to measurement, there were several configuration parameters to set up in the analyser. First, the range of frequencies was set from 100 kHz to 1GHz which is a range large enough that covers sufficient bandwidth to allow the observation of the resonance introduced by the parasitics at high frequencies and the linear behavior of the head at low frequencies. The number of points represents the number of samples uniformly distributed within the frequency range. It was chosen to be 512. The decision was made in consequence of bearing in mind that for some cases only the samples at low frequencies will be considered and the remaining samples will be dismissed. Another important setting is the power level P_{SET} of the RF OUT port. If it is too large, the head may become saturated at the poles. If it is too small, the magnetisation of the head which is initially aligned with its easy direction will not be switched and therefore no magnetisation will contribute to the measurement. Also with a low power level there

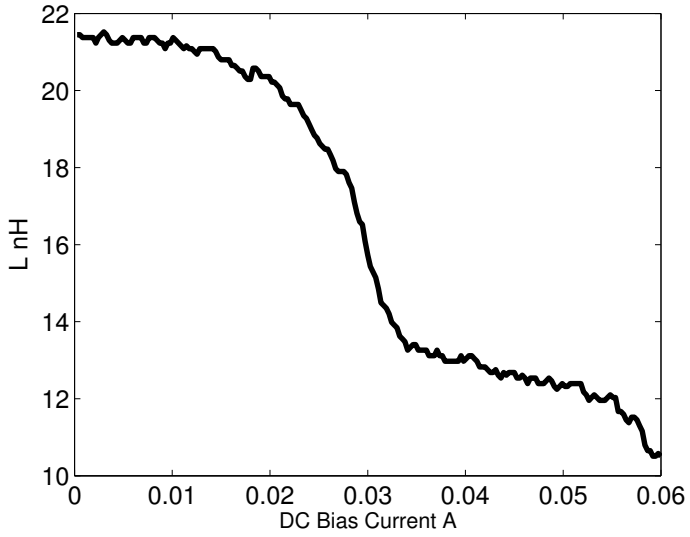

Figure 6.21: Write current dependence of the yoke inductance, (Prabhakar and Filips, 1999).

will not be enough resolution, the measurement becomes noisy as shown in Figure 6.20. In consequence, the power level must be a compromise between three factors namely it has to be high enough to provide sufficient current to switch the magnetisation and to obtain enough resolution and at the same time small enough to avoid saturation. One possible way of studying the effect of the applied signal power and hence current is to measure the head inductance as a function of increasing DC current and at a relatively low frequency. As the current increases and the head becomes saturated, the inductance switches value to indicate head saturation. Figure 6.21 shows a typical inductance vs DC current response of a magnetic thin-film head, (Prabhakar and Filips, 1999). The saturation point of this particular head is 30mA.

With the measurement equipment available it is possible to apply a maximum DC bias current of 20 mA to carry out a similar measurement. For higher currents the equipment may be damaged. The procedure involves measuring the inductance of heads A and B at a fixed frequency of 10MHz and varying DC currents from 0 to

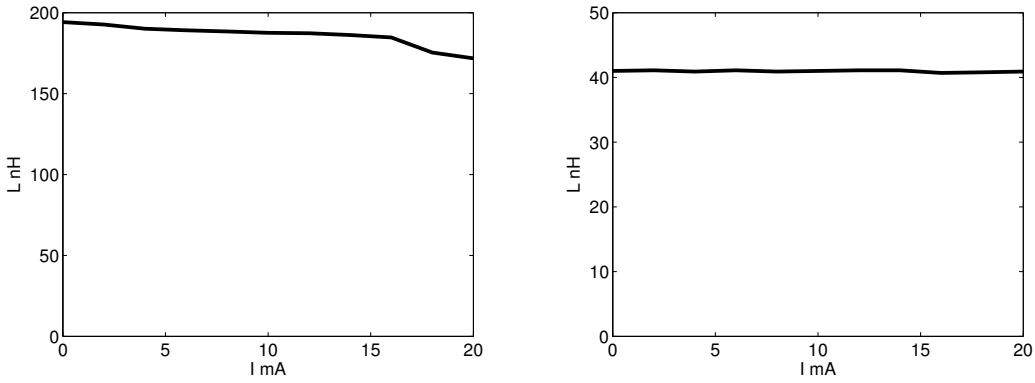

(a) (b)

Figure 6.22: Write current dependence of the heads. (a) Head A, the shift in the inductance values at 16mA indicates saturation. (b) Head B, saturation occurs for currents higher than 20 mA.

20mA. The power level on the analyser was set to -15dBm which from (6.81) equals to an AC voltage signal of approximately 40mV rms. The measured magnitude of the impedance of the heads at 10MHz is roughly 10Ω, this means an applied AC current of 4mA. The 4mA alternating current was added to the DC bias current supplied from the power supply in order to obtain the inductance of the heads as a function of DC current.

The purpose of this measurement is to ensure that the head is not saturated when the impedance measurements are taken. Figures 6.22 (a) and (b) represent the DC current dependence of the head inductances of heads A and B respectively. In Figure 6.22(a), it is observed that the inductance decreases as the current rises to values greater than about 16mA. The shift in the inductance value indicates saturation near this DC current value. On the other hand, Figure 6.22(b) does not show any dependence which indicates that saturation occurs at higher DC bias current levels.

Coming back to the analyser settings, reasonable results were obtained by setting the power level to 0dBm, which using (6.81) corresponds to an rms voltage of 223mV.

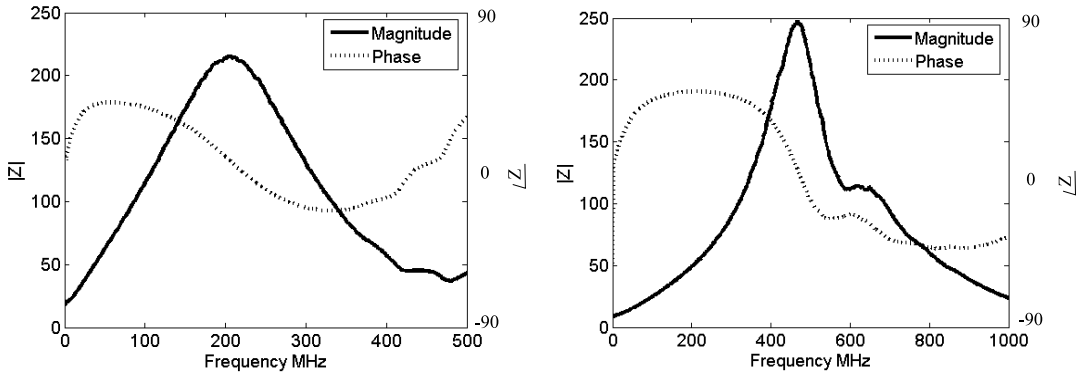

Figure 6.23: Magnitude and Phase of the impedance of the heads. (a) Head A and (b) head B. The magnitude of the impedance is given in Ω and the phase in degrees.

With the smallest value of the magnitude of the impedance being approximately 10Ω, then the current transferred to the head is about 23mA. Figure 6.22(a) indicates that head A may be saturated at low frequencies for that current level, however, at higher frequencies, as the impedance of the head increases and therefore the current supplied is smaller, the head would not be saturated.

In order to obtain accurate and repeatable measurements it is mandatory to follow always the same procedure. That is, first to set up analyser parameters, second, to perform open short and load calibration with the calibration substrate and finally to take the appropriate measurement. For every change in the analyser settings, frequency range or power level, a new calibration must be performed in order to maintain the accuracy of the measurement. After the calibration, the calibration plane is defined at the microwave probe tips and therefore all kind of systematic errors are compensated for.

Measurements of the magnitude and phase of the impedance were taken on heads A and B. Figure 6.23(a) shows the magnitude and phase of the impedance of head A which reaches resonance at approximately 210MHz. The DC magnitude of the impedance is

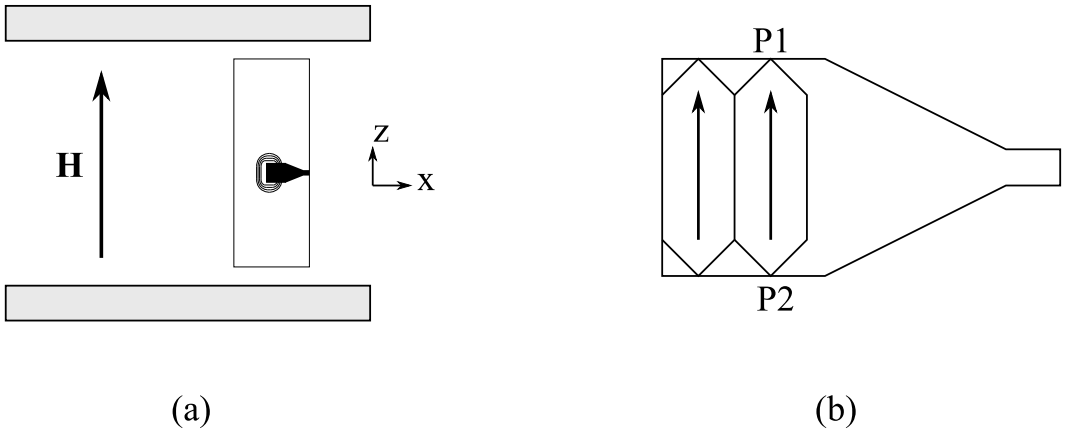

Figure 6.24: Saturation of the heads. Due to magnetic domains it is easier to saturate the heads in the z direction, i.e. direction of easy magnetisation. (a) Position of the head in the correct direction inside the magnet and (b) Poles on a single magnetic domain.

20Ω whereas the magnitude when the head reaches resonance is 200Ω. Figure 6.23(b) shows the magnitude and phase of the impedance of head B. Advances in technology are noticed in a higher resonance point, approximately 500MHz, which in turn gives a larger operating frequency. The smallest magnitude of the impedance is 10Ω and the largest 250Ω at the DC value and resonance point respectively.

Further measurements on the same heads were taken under the effect of an external magnetic field to obtain the impedance of the heads when the magnetisation is saturated and only the effect of the coil is present. In order to saturate the magnetisation, the heads were introduced between the poles of a permanent magnet which generates a strong field greater than 3000Oe in the z direction (see Figure 6.24). It is important to place the head such that the saturation is in the z direction, Figure 6.25(a). This is the easy direction for saturation due to the magnetic domains and therefore the more efficient way to saturate the head. The poles on a single domain are at the points marked as P1 and P2 on Figure 6.24(b). Figures 6.25 (a) and (b) show the magnitude and phase of the saturated heads A and B respectively.

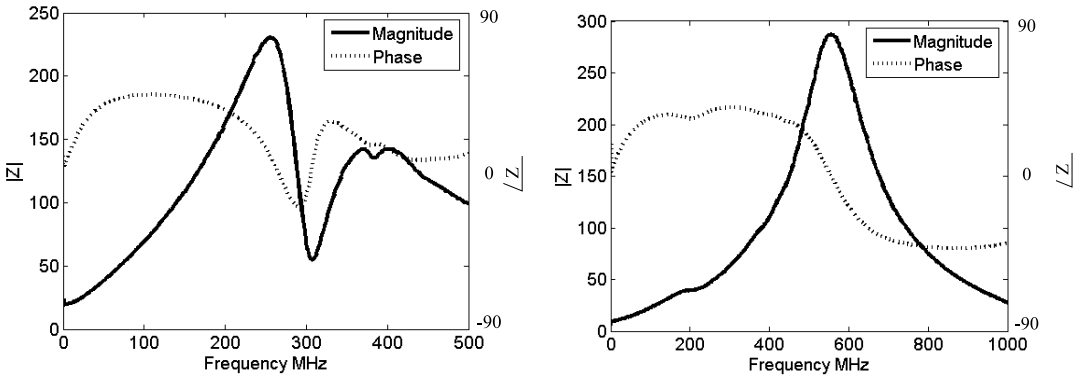

(a) (b)

Figure 6.25: Magnitude and Phase of the impedance of the heads under the effect of an external magnetic field for saturation purposes. (a) Head A and (b) head B. The magnitude of the impedance is given in Ω and the phase in degrees.

6.9 Estimation of Magnetic Time Constants

In this section the magnetic time constants for the rotational magnetisation and domain wall motion will be obtained for heads A and B by fitting of the head core inductance expressions derived through sections 6.3 to 6.7 to the measured core inductances.

Given an actual measurement $y(x)$ and knowing the equation $f(x, a_1, ..., a_n)$ of unknown parameters a_1 to a_n that has to be satisfied by that measurement, the general graph fitting problem consists of finding a set of parameters a_1 to a_n such that

$$y(x) = f(x, a_1, ..., a_n) + S \tag{6.82}$$

where x represents the independent variable, a_1 to a_n are the parameters to be adjusted and S is the error or the difference between the actual and the estimated value. A good fit will minimize the error to a certain value of accuracy. The least squares method, Bevington (1969), estimates the error using the sum square error equation

$$S = \sum_{i=1}^{n} (y_i(x_i) - f(x_i, a_1, ..., a_n))^2 \tag{6.83}$$

and then adjusts the parameters a_1 to a_n to minimize the error. The goodness of the fit is generally expressed in terms of the variance which is a measure that indicates how the actual values are spread around the estimated values.

This work focuses on magnetic losses thus the fitting problem involves inductance figures and parameters related to rotational magnetisation and domain wall motion. The impedance of a magnetic circuit is usually represented by a resistor-inductor series connection $Z = R + j\omega L$. In this manner, the series inductance of a magnetic circuit is by definition the imaginary part of the impedance divided by the angular frequency

$$L = \frac{1}{\omega} Im\{Z\} \tag{6.84}$$

The imaginary part of the impedance is obtained from the measured magnitude and phase of the impedance as

$$Z = |Z|e^{j\angle Z} = Re\{Z\} + jIm\{Z\} \tag{6.85}$$

In Figure 6.26 the inductance of head A for the saturated and unsaturated states are shown. As predicted in (6.72) the inductance of the saturated head has almost constant value whereas the inductance of the unsaturated head computed as (6.64) is frequency dependant. The frequency range has been reduced to a region from DC to the frequency where the inductance of the unsaturated head ceases to be approximately flat, from this point onwards the low frequency approximation (6.47) is no longer valid and resonant effects introduced by the parasitic capacitance become important. Figure 6.26 also shows the difference between the unsaturated and the saturated inductances which from equation (6.73) corresponds to the inductance of the magnetic core material and accounts for the rotational magnetisation and domain wall motion. Equation (6.73) represents the impedance of the core material. The inductance of the core is then

$$L_{core} = L_{wall}(\omega) + L_{rot}(\omega) = \frac{L_w}{1 + \omega^2 \tau_w^2} + \frac{L_r}{1 + \omega^2 \tau_r^2} \tag{6.86}$$

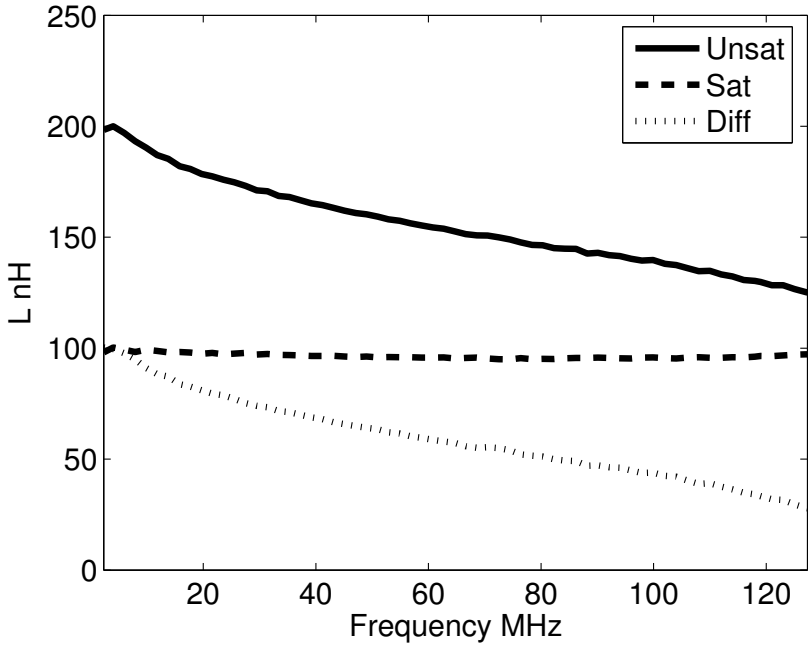

Figure 6.26: Saturated (dashed plot) and unsaturated (continuous plot) inductance of head A. The dotted plot indicates the difference between the two inductances.

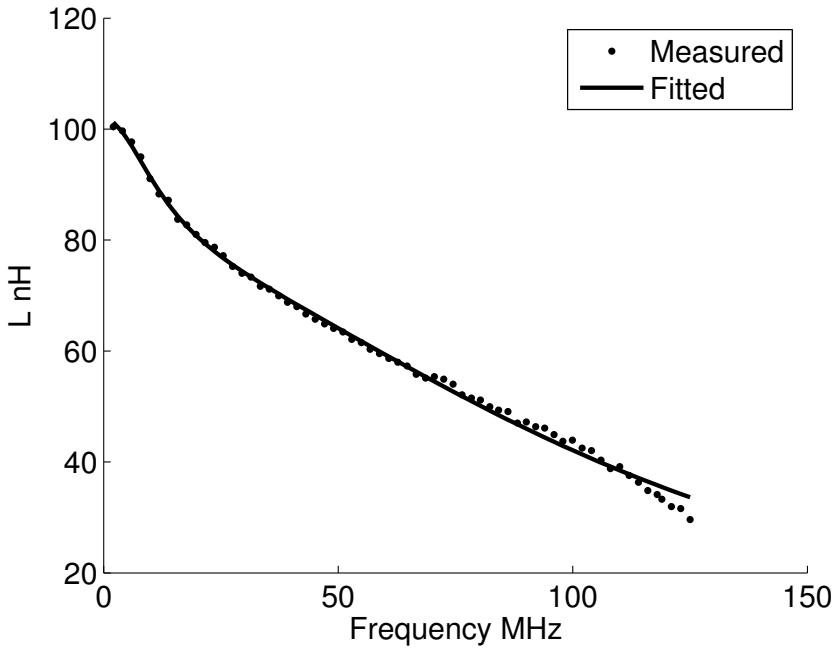

Figure 6.27: Fit of the inductance difference for the material of head A.

Least squares fitting was made over the difference of the unsaturated and the saturated inductances of head A using equation (6.86) for L_w, L_r, τ_w and τ_r. The fitting represented in Figure 6.27 gave the parameters of (6.86) as $L_w = 27.1$nH, $L_r = 74.8$nH, $\tau_w = 12.2$ns and $\tau_r = 1.42$ns. The standard deviation of the fiting was $\sigma = 1.13e - 9$.

The same estimation of parameters was carried out for head B. First the inductance of the saturated head was subtracted from the inductance of the unsaturated head to obtain the inductance of the material as shown in Figure 6.28. Then the parameters of equation (6.86) were adjusted to give the least squares fitting shown in Figure 6.29. These are $L_w = 1.90$nH, $L_r = 3.56$nH, $\tau_w = 4.54$ns and $\tau_r = 0.10$ns. The standard deviation of the fiting was $\sigma = 1.29e - 9$.

The equivalent inductances and time constants due to domain wall and domain rotation are shown in table 6.2. These values were obtained by least square fitting and agree

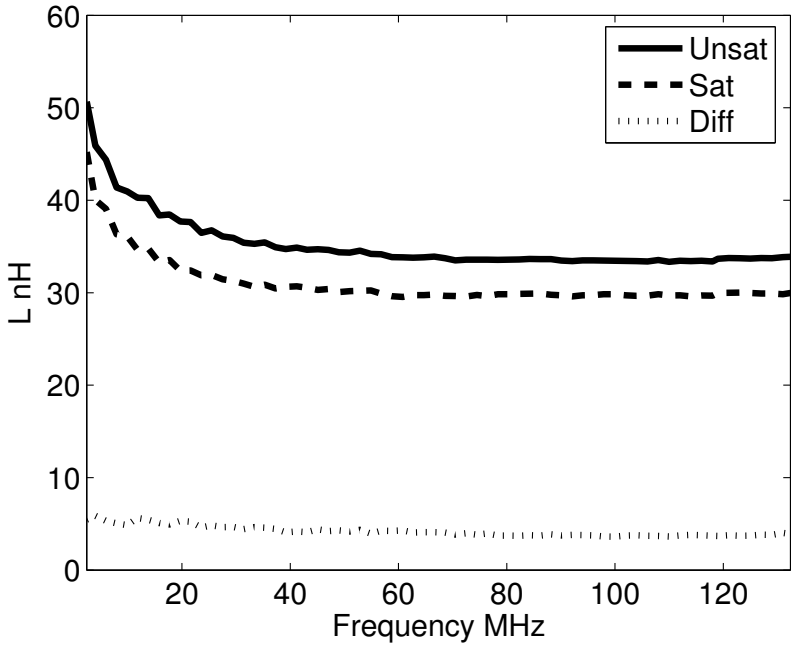

Figure 6.28: Saturated (dashed plot) and unsaturated (continuous plot) inductance of head B. The dotted plot indicates the difference between the two inductances.

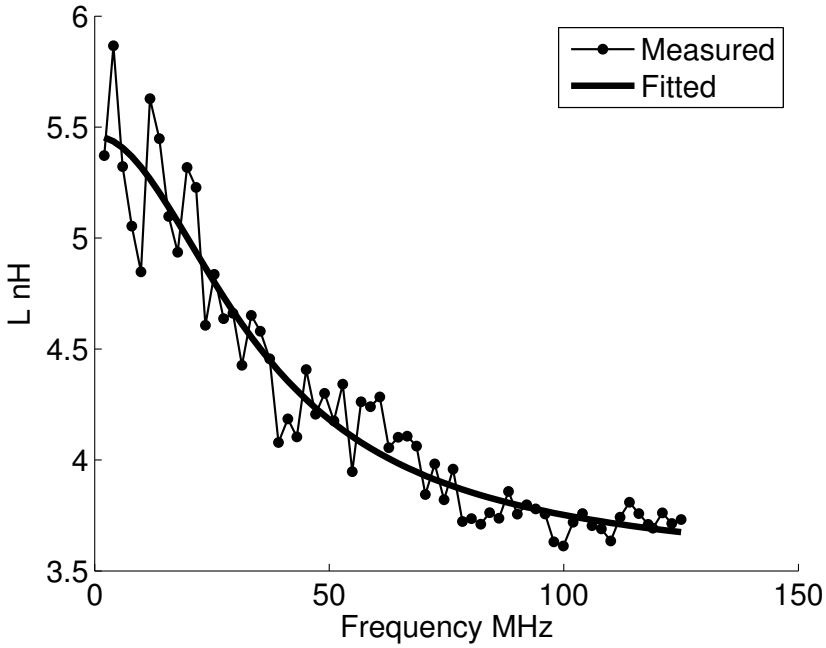

Figure 6.29: Fit of the inductance difference for the material of head B.

with the results of the FDTD simulations carried out in Chapter 5 and with theoretical predictions such as those in Soohoo (1982), Sherrima and Soohoo (1986) and Engstrom (1984).

Table 6.2: Domain wall and rotational magnetisation parameters that give the best least square fitting to the inductance of the head core for the two studied heads.

	Head A	Head B
L_w	27.1nH	1.90nH
L_r	74.8nH	3.56nH
τ_w	12.2ns	4.54ns
τ_r	1.42ns	0.10ns

6.10 Summary

A study of the physical dimensions of two different heads manufactured in an eight year difference period was carried out by polishing off half of the head and then using electron microscope imaging. As initially thought, the advances in technology during an eight year period are reflected in the overall dimensions. Electron microscope analysis of the material showed that the material of the thin films and coils were a NiFe alloy and copper respectively.

A study of the equivalent circuits that best describe the magnetic impedance of a thin-film head was carried out leading to an equivalent circuit model that includes the relaxation effects of the domain wall motion and the rotational magnetisation. Saturation condition was considered in the model with the conclusion that at low frequencies the inductance of the core material can be expressed as the sum of the inductances originated by the domain wall motion and the rotational magnetisation. To focus and study the core impedance, the heads were saturated to reveal the impedance due to the coil only. By substracting the saturated inductance, i.e fixed non magnetic material related parameters, from the unsaturated inductance, i.e. the one that contains all the information of non magnetic material related and magnetic material related parameters, it is possible to isolate such effects as the domain wall motion and the rotational magnetisation.

The magnitude and phase of the impedance were measured and stored for the two studied heads. Resonance was observed at a frequency of 210MHz for head A and at a frequency of 500MHz for head B. The magnitude and phase of the impedance for the same heads were measured under the effect of an external saturating magnetic field of magnitude higher than 3000Oe for saturation purposes. From the measured values of impedance at saturated and unsaturated states of the heads, the inductance of the core material for both heads was evaluated. The relaxation parameters from the equivalent

circuit, equation (6.86), were then adjusted to give the best least squares fit to the inductance computed from the measured data leading to the parameter values shown in Table 6.2 which are in agreement with perviously published work (Soohoo, 1982; Sherrima and Soohoo, 1986; Engstrom, 1984).

Chapter 7

Discussion and conclusion

Recent advances in recording technologies have allowed an increase in area storage densities of hard disk drives in order to meet the ever increasing demands for information storage. Magnetic recording research and development efforts will continue to be aimed toward achieving higher areal density. One of the ways in which this is accomplished is through the minituarisation of the recording heads. The dimensions of magnetic head elements have decreased to the point where the micromagnetic switching mechanisms of domain wall motion and domain rotation and their associated flux propagation and reversal processes have become critical. Further advances in head and media materials and design will be assisted by a better understanding of, and ability to control, domain level phenomena associated with the micromagnetic behaviour of the head materials.

Theoretical and numerical studies tend to separate the micromagnetics from the electromagnetic aspects of the head during switching and hence ignore the lossy nature of recording head material. So far, models of thin-film recording heads can be classed into two categories. Dynamic models of thin-film recording heads that utilise full micromagnetic description of the magnetic material but neglect eddy current effects due to the absence of electromagnetic formulation in the models. On the other hand, static and steady state models are either time independent or limited in the frequency domain to

the fundamental response, and ignore the magnetic detail of the head material. These two approaches have their limitations and therefore the combination of the solution to Maxwell's equations for the electromagnetic fields with models of the magnetic material to accurately simulate the reversal process in magnetic heads is needed.

7.1 Conclusion

This project aimed to develop a numerical simulation approach that simultaneously incorporates the fundamental micromagnetic and electromagnetic details of magnetic materials to study the fast switching process in soft magnetic materials in general, and in thin-film inductive writers in particular. This simulation approach was primarily intended to provide a transient description of the micromagnetic behaviour of lossy magnetic material in the presence of interacting electromagnetic fields in practical structures using a unified approach. The intention was therefore not to produce or develop a pure micromagnetic technique for studying hysteresis and granular material as it is more the domain of pure micromagnetic techniques. Nevertheless, the presented approach can be used to study the hysteresis properties of continuous magnetic material. This project also aimed at establishing an impedance measurement set up to characterise losses in magnetic recording heads, and to allow comparison with the simulations. The simulations and experimental measurements results would help to determine the factors that limit the switching times in magnetic heads and predict the writing performance of magnetic storage systems.

This project successfully met all its original objectives. A numerical technique for simulating the dynamic behaviour of magnetic materials and devices has been developed, and applied to study the subnanosecond switching process in thin-film recording heads. This technique naturally combines the fundamental equation of magnetisation motion with the solution of Maxwell's equations using the Finite- Difference Time-

Domain method, with the unique feature that the micromagnetic (including exchange and anisotropy effects) and electromagnetic (electric and magnetic fields due to charges and currents) descriptions of simulated structures are produced simultaneously. Using this technique will help to design and study complete magnetic devices without ignoring the interaction between the magnetic material and other dielectric and conductive layers in the structure, which is important at high frequencies. Moreover, this feature simplifies the magnetostatic computations which are inherently demanding in numerical micromagnetics, thus extending existing work in micromagnetics to more complex geometries and applications.

Two-dimensional simulations of complete commercial head structures (including the coils) and pole regions were carried out under picosecond excitations and predicted parameters such as gap field distributions, gap field rise times, and core inductances which are important for head designers. Predicted gap field distributions (Figure 5.18) showed an accurate field description near the head poles when compared against simple head models, e.g. Karlqvist. The predicted gap field rise time computed from the mmf in the gap region (Figure 5.16) showed that more than 0.5ns are required to switch the magnetisation and reach equilibrium which is in agreement with the experimental measurements obtained in Chapter 6 where the time constant for rotational magnetisation for this particular head was $\tau_r = 1.42$ns (Table 6.2, head A). It was also observed a smaller write field when the LLG equation is considered compared to the linear model (Figure 5.17) which is in agreement with theoretical predictions as the switching of the magnetisation is a consuming process and therefore it reduces the efficiency of the head (Jones, 1978; Kittel, 1949). The predicted recorded gap field at a plane parallel to the disk surface (Figure 5.20) showed higher field gradients in the pole corner regions with the inclusion of the magnetisation when compared with the linear model which according to the writing theory discussed in Chapter 2 implies that shorter transition lengths are recorded than predicted by other models that ignore the magnetic detail of the core material.

Moreover, the role of eddy currents on magnetisation rotation times was elucidated. It was observed that eddy currents produce opposing fields to the applied field (Figure 5.24(a)) that increase the time taken to achieve magnetisation equilibrium (Park and Won, 2006). The delay in the switching time and therefore in the head due to these opposing fields was found to be 0.13ns (Figure 5.24(b)), this agrees with previous findings such as Takano et al. (2007) where a delay in the head field response due to eddy currents was found. It was also found that these opposing fields modify the precession of the magnetisation if they are taken into account when solving the LLG equation (Figure 5.25(b)). The predicted current density distribution across the head pole was in the form of circulating currents (Figure 5.25(a)) which agrees with the eddy currents and dielectric loss theory discussed in Chapter 2.

A high precision, high bandwidth impedance measurement set up was established to characterise losses in magnetic heads. Fittings of measured core inductances to a proposed equivalent circuit model of the core's relaxation processes revealed the switching times of heads. The measured time constants due to domain rotation and domain wall motion were found to be $\tau_r = 1.42$ns and $\tau_w = 12.2$ns respectively for head A, and $\tau_r = 0.10$ns and $\tau_w = 4.54$ns for head B. These values agree with the existence of fast and slow relaxation processes stated in Engstrom (1984) and Sherrima and Soohoo (1986), and they show an improvement in technology when compared to previously published work, in Soohoo (1982) τ_r and τ_w were found to be 1ns and 170ns respectively. The numerical computations revealed a switching requirement larger than 0.5ns which agrees with the measured value of τ_r for head A.

7.2 Summary of Contributions

An extended FDTD method for modelling of non-linear magnetic materials has been developed by including the solution to the Landau-Lifshitz-Gilbert (LLG) equation in the FDTD formulation. General expression relating field propagation to the rotational magnetisation have been given to allow the implementation of the extended method. So far, FDTD approximations with magnetic description of materials were limited to small signal approximations or with no damping involved and limited to simple magnetic structures.

The solution of the LLG equation describes the precessional motion of the magentisation vectors in a magnetic material under the influence of an effective field. Hence, this formulation allows the inclusion of the anisotropy and exchange fields (which had not been accounted for so far) as effective fields in the model, as well as the electromagnetic fields due to magnetic and/or electric charges and currents are evaluated naturally through the solution of Maxwell's equations. Also, analysis of the stability of the solution of the LLG equation and treatments of boundary conditions have been produced.

Actual commercial head structures have been simulated under picosecond excitations using the developed extended FDTD method. These simulations combine the fundamental equation of magnetisation motion with the solution of Maxwell's equations, with the unique feature that the micromagnetic and electromagnetic descriptions of simulated structures are produced simultaneously, this simplifies the magnetostatic computations which are inherently demanding in numerical micromagnetics. They also consider the effect of exchange and anisotropy fields as part of the effective field that affects the head material.

The outcomes of the work undertaken during the initial stage of this research were presented under the title *Dynamic Simulation of Fast Switching in Magnetic Recroding Heads* at IMST 2006 in Grenoble, France. At the time of submitting this thesis another publication was being produced under the title *Sub-Nanosecond Combined Electromagnetic and Micromagnetic Simulations Using The Finite-Difference Time-Domain Method* with the intention of submitting it to the IEEE Transactions on Magnetics.

7.3 Limitations and Further Work

The main concern or limitation of the extended FDTD technique is related to stability and the time restrictions it imposses. As described in Chapter 4 the numerical dispersion due to the discretisation of Maxwell's equations can lead to numerical instability if certain constraints are not met. These are the bounds impossed by courant stability condition which relates the time and space increments of the FDTD lattice. Thus for very small structures, large simulation times are required.

The time increment in between consecutive iterations is directly related to the spatial resolution of the grid in the FDTD algorithm through equation (4.52). The grid resolution is determined by the most restrictive of two factors: the smallest feature in the simulated structure or the shortest wavelength in the simulated space. In this particular case, where a magnetic head has been simulated, the very small front gap height for the head geometry in Figure 6.3 determined a very small time increment resulting in a large number of iterations. Thus, a small grid resolution results in a very small time increment and therefore large simulation time (CPU time) to obtain the results of a single simulation (TM_z simulation of head A took fifty days overall). Large waiting time requirements have made it impossible to carry out several simulations and other tests over very small head structures.

One possible solution to this limitation is the scaling of the head structure (Mallinson, 1996). When scaling is applied to the spatial increment in the FDTD algorithm, the frequency and hence wavelength in the system must be changed appropriately to maintain the accuracy of the simulation. The normal requirement is that

$$\Delta x = \frac{\lambda}{10} \tag{7.1}$$

for the FDTD algorithm to correctly sample the propagating waves. However, in lossy media this requirement might not be sufficient and if Δx is fixed, then the wavelength and hence frequency of propagating waves must be altered. This normally occurs through modifying the frequency of the source in the FDTD simulation.

To illustrate this, consider the equation for the skin depth, δ, in a lossy medium:

$$\delta = \sqrt{\frac{2}{\omega\mu\sigma}} \tag{7.2}$$

where ω is the maximum or corner frequency. Scaling the spatial increment Δx by a factor of 'r' requires that the frequency of the travelling wave to be altered as:

$$\omega = \frac{2}{(r\delta)^2\mu\sigma} \tag{7.3}$$

to maintain the same scaled skin depth, δ, in the lossy medium.

This frequency can be set through the time constant, T, of the first-order source in the system as: $T = 1/\omega$.

For example, consider the unscaled system with $\mu_r = 3000$, $\sigma = 1 \times 10^7$ 1/Ωm, $T = 20 \times 10^{-12}$s, $\omega = 1/T = 5 \times 10^{10}$rad/s and $\lambda = 2 \times cc/\omega = 0.04$m. In this case, the skin depth is: $\delta = 33$nm. The choice of Δx and hence Δt is being determined by the skin depth δ. For example, $\Delta x = 10$nm and $\Delta t = \Delta x/2cc = 0.0167$fs. For settling time, $T_s \simeq 5T$, then the number of time steps required is $N = T_s/\Delta t = 6 \times 10^6$ time steps.

Now consider the scaled system where Δx is scaled by a factor of $r = 1000$. In this case, $\Delta x = 10\mu$m, $\mu_r = 3000$ and $\sigma = 1 \times 10^7$ 1/Ωm. To maintain the scaled skin

depth in the medium as for the previous examples (i.e. 1000δ), then the frequency of the propagating waves in the medium must now be:

$$\omega = \frac{2}{(r\delta)^2 \mu\sigma} = 49 \times 10^3 rad/s \tag{7.4}$$

Hence the time constant of the source is $T = 1/\omega = 20 \times 10^6$s and $\Delta t = \Delta x/2cc = 16.7$fs.

For a settling time, $T_s \simeq 5T$, then the number of time steps required is $N = T_s/\Delta t = 6000 \times 10^6$ time steps. So although scaling increases Δx and hence Δt, the number of time steps required to maintain the same (scaled) skin depth in lossy media must be increased considerably.

It is certain that a small mistake in the computations propagates over each iteration in time making the error grow bigger with the increasing simulation time. This problem gets worse with a large number of iterations. From the simulation results obtained in Chapter 5, particularly in the TM_z mode simulation of the head cross section, there have been observed stability problems. As discussed in the appropriate section, it is quite difficult to satisfy the stability limit of the extended algorithm or even to establish the conditions under which the algorithm is stable due to the concentration of large amounts of the effective field at the head corners.

It is clear that future research on this matter will have to overcome the stability requirements impossed by equation (4.52) in order to simulate very small material structures. An approach initially reported by (Zheng et al., 1999) provides accurate and numerically stable solutions for values of Δt exceeding the stability limit. As this is a variant of the FDTD method that uses an alternating direction implicit (ADI) time stepping rather than the usual explicit used in Yee's formulation, its implementation requires to start from the beginning including implementation of PML absorbing boundaries, implementation of sources, appropriate modification of space and time synchronism, etc. Thus, it could not be done for the purpose of this research due to the lack of time.

This approach is described in detail in Appendix B and described here as the principal future line of research to continue with the contents of this work.

Moreover, to avoid the complicated interpolations introduced in the FDTD cell to account for the non-staggered nature of the LLG equation, non-taggered methods could be developed, (Hagness and Taflove, 2000; Liu, 1997) . This will significantly reduce the complexity of the implementation of the extended algorithm.

Appendix A

Demagnetising Fields

In a magnetic material, there is no divergence of the induction**B**. The latter can be expressed as

$$\mathbf{B} = \mu_0(\mathbf{H} + \mathbf{M}) \tag{A.1}$$

while the condition of zero divergence is signified by

$$\nabla \cdot \mathbf{B} = 0 \tag{A.2}$$

Combining these two equations gives

$$\nabla \cdot \mathbf{H} = -\nabla \cdot \mathbf{M} \tag{A.3}$$

In magnetic field problems it is usual to express the field in terms of the gradient of a potential ϕ

$$\mathbf{H} = -\nabla\phi \tag{A.4}$$

so that introduction of it into equation (A.3) produces a version of Poissons's equation, namely,

$$\nabla^2\phi = \nabla \cdot \mathbf{M} \tag{A.5}$$

wherein the quantity $-\nabla \cdot \mathbf{M}$ takes on the significance of a magnetic charge density. Solution of Poisson's equation takes the form

$$\phi(r) = -\frac{1}{4\pi}\int_{V'} \frac{\nabla \cdot \mathbf{M}}{|r-r'|} dV' - \frac{1}{4\pi}\int_{A'} \frac{\sigma_m(r')}{|r-r'|} dA' \tag{A.6}$$

where the first term is the potential arising from the volume charges within the magnetic material, with the itegration taking place over all these charges, while the second term is the potential arising from the surface charges $\sigma_m(r')$, with the integation taking place over all the relevant surfaces of the material. The surface charge density can be obtained from

$$\sigma_m(r') = \mathbf{M} \cdot \mathbf{n} \tag{A.7}$$

where $\mathbf{n}$ is the outward normal to the surface.

Following from equation (A.6) the demagnetising field is

$$H_d(r) = -\frac{1}{4\pi}\int_{V'} \frac{\nabla \cdot \mathbf{M}}{|r-r'|^2} dV' + \frac{1}{4\pi}\int_{A'} \frac{\sigma_m(r')}{|r-r'|^2} dA' \tag{A.8}$$

Use of the above equation in any generalised way is extremely difficult. However, certain partirlar cases of interest in this work are now discussed.

First, consider a magnetisation which has only x components varying with the x dimension and giving rise to no surface charges. Then

$$\nabla \cdot \mathbf{M} = \frac{\partial M_x}{\partial x} \tag{A.9}$$

Use of this in equation (A.8) would give rise to a field having, in general, x, y and z components. Considering only the x component yields

$$H_{dx}(x,y,z) = -\frac{1}{4\pi}\int\int\int \frac{\partial M_x}{\partial x'} \frac{(x-x')dx'dy'dz'}{|(x-x')^2+(y-y')^2+(z-z')^2|^{3/2}} \tag{A.10}$$

and when the transverse dimension is so large that the integration over z' may take place from $-\infty$ to $+\infty$, equation (A.10) becomes

$$H_{dx}(x,y) = -\frac{1}{2\pi}\int\int \frac{\partial M_x}{\partial x} \frac{(x-x')dx'dy'}{(x-x')^2+(y-y')^2} \tag{A.11}$$

The second case occurs when there are no volume charges and only y components of the magnetisation. Then $\partial M_y/\partial y = 0$, but there are surface charges of magnitude M_y. The y component of magnetic field is then, using equation (A.8),

$$H_{dy}(x,y,z) = \frac{1}{4\pi}\int\int M_y \frac{(y-y')dx'dz'}{|(x-x')^2+(y-y')^2+(z-z')^2|^{3/2}} \tag{A.12}$$

Again, when the z dimension is infinite, this becomes

$$H_{dy}(x,y) = \frac{1}{2\pi}\int M_y \frac{(y-y')dx'}{(x-x')^2+(y-y')^2} \tag{A.13}$$

Appendix B

Alternating Direction Implicit Algorithm

Numerical stability of the FDTD algorithm requires a bounding of the time step Δt relative to the space increments Δx, and Δy as shown in equation (4.52). This is not an inconvenience when modelling a moderate electrical size problems where a relatively small number of time steps are required for completion of a single simulation. However, there are some application of FDTD modelling in which the stability limit plays an important roll. It is the case of the experiment carried out in this report. The cell size Δ needed to resolve the fine scale geometric detail of the head is fixed, to avoid numerical instability, equation (4.44) fixes the time increment Δt, to a very short value which implies a big number of time steps to complete a single simulation.

To model these kind of structures, a different approach to FDTD must be used in the way that permits accurate and numerically stable operation for values of Δt exceeding the stability limit. Algorithms using an alternating direction implicit (ADI) time stepping rather than the usual explicit used in Yee's are a very good solution to this matter.

The approach presented here was reported by (Zheng et al., 1999) and has numerical

stability for the general three dimensional case. Although the same Yee space lattice as in conventional FDTD is used, the six field vector component are collocated rather than staggered in time. In discussing the numerical formulation of this algorithm, we assume that all of the field components are known everywhere n the lattice at time step n and stored in the computer memory.

Unsimplified System of Time Stepping Equations

To advance a single time step from n to $n+1$, two subiterations are performed, the first from n to $n+\frac{1}{2}$, and the second from $n+\frac{1}{2}$ to $n+1$.

Subiteration 1: Advance the 6 field components from time step n to time step $n+\frac{1}{2}$

$$\begin{aligned} E_x\big|_{i+\frac{1}{2},j,k}^{n+\frac{1}{2}} = E_x\big|_{i+\frac{1}{2},j,k}^{n} &+ \tfrac{\Delta t}{2\epsilon\Delta y}\left(H_z\big|_{i+\frac{1}{2},j+\frac{1}{2},k}^{n+\frac{1}{2}} - H_z\big|_{i+\frac{1}{2},j-\frac{1}{2},k}^{n+\frac{1}{2}}\right) \\ &- \tfrac{\Delta t}{2\epsilon\Delta z}\left(H_y\big|_{i+\frac{1}{2},j,k+\frac{1}{2}}^{n} - H_y\big|_{i+\frac{1}{2},j,k-\frac{1}{2}}^{n}\right) \end{aligned} \tag{B.1a}$$

$$\begin{aligned} E_y\big|_{i,j+\frac{1}{2},k}^{n+\frac{1}{2}} = E_y\big|_{i,j+\frac{1}{2},k}^{n} &+ \tfrac{\Delta t}{2\epsilon\Delta z}\left(H_x\big|_{i,j+\frac{1}{2},k+\frac{1}{2}}^{n+\frac{1}{2}} - H_x\big|_{i,j+\frac{1}{2},k-\frac{1}{2}}^{n+\frac{1}{2}}\right) \\ &- \tfrac{\Delta t}{2\epsilon\Delta x}\left(H_z\big|_{i+\frac{1}{2},j+\frac{1}{2},k}^{n} - H_z\big|_{i-\frac{1}{2},j+\frac{1}{2},k}^{n}\right) \end{aligned} \tag{B.1b}$$

$$\begin{aligned} E_z\big|_{i,j,k+\frac{1}{2}}^{n+\frac{1}{2}} = E_z\big|_{i,j,k+\frac{1}{2}}^{n} &+ \tfrac{\Delta t}{2\epsilon\Delta x}\left(H_y\big|_{i+\frac{1}{2},j,k+\frac{1}{2}}^{n+\frac{1}{2}} - H_y\big|_{i-\frac{1}{2},j,k+\frac{1}{2}}^{n+\frac{1}{2}}\right) \\ &- \tfrac{\Delta t}{2\epsilon\Delta y}\left(H_x\big|_{i,j+\frac{1}{2},k+\frac{1}{2}}^{n} - H_x\big|_{i,j-\frac{1}{2},k+\frac{1}{2}}^{n}\right) \end{aligned} \tag{B.1c}$$

$$\begin{aligned} H_x\big|_{i,j+\frac{1}{2},k+\frac{1}{2}}^{n+\frac{1}{2}} = H_x\big|_{i,j+\frac{1}{2},k+\frac{1}{2}}^{n} &+ \tfrac{\Delta t}{2\mu\Delta z}\left(E_y\big|_{i,j+\frac{1}{2},k+1}^{n+\frac{1}{2}} - E_y\big|_{i,j+\frac{1}{2},k}^{n+\frac{1}{2}}\right) \\ &- \tfrac{\Delta t}{2\mu\Delta y}\left(E_z\big|_{i,j+1,k+\frac{1}{2}}^{n} - E_z\big|_{i,j,k+\frac{1}{2}}^{n}\right) \end{aligned} \tag{B.2a}$$

$$\begin{aligned} H_y\big|_{i+\frac{1}{2},j,k+\frac{1}{2}}^{n+\frac{1}{2}} = H_y\big|_{i+\frac{1}{2},j,k+\frac{1}{2}}^{n} &+ \tfrac{\Delta t}{2\mu\Delta x}\left(E_z\big|_{i+1,j,k+\frac{1}{2}}^{n+\frac{1}{2}} - E_z\big|_{i,j,k+\frac{1}{2}}^{n+\frac{1}{2}}\right) \\ &- \tfrac{\Delta t}{2\mu\Delta z}\left(E_x\big|_{i+\frac{1}{2},j,k+1}^{n} - E_x\big|_{i+\frac{1}{2},j,k}^{n}\right) \end{aligned} \tag{B.2b}$$

$$\begin{aligned} H_z\big|_{i+\frac{1}{2},j+\frac{1}{2},k}^{n+\frac{1}{2}} = H_z\big|_{i+\frac{1}{2},j+\frac{1}{2},k}^{n} &+ \tfrac{\Delta t}{2\mu\Delta y}\left(E_x\big|_{i+\frac{1}{2},j+1,k}^{n+\frac{1}{2}} - E_x\big|_{i+\frac{1}{2},j,k}^{n+\frac{1}{2}}\right) \\ &- \tfrac{\Delta t}{2\mu\Delta x}\left(E_y\big|_{i+1,j+\frac{1}{2},k}^{n} - E_y\big|_{i,j+\frac{1}{2},k}^{n}\right) \end{aligned} \tag{B.2c}$$

In each of the above equations, the first finite difference on the right hand side is set up to be evaluated implicitly from as yet unknown field data at time step $n+\frac{1}{2}$, while the second finite difference on the right hand side is evaluated explicitly from known field data at time step n.

Subiteration 2: Advance the 6 field components from time step $n+\frac{1}{2}$ to $n+1$

$$E_x|^{n+1}_{i+\frac{1}{2},j,k} = E_x|^{n+\frac{1}{2}}_{i+\frac{1}{2},j,k} + \frac{\Delta t}{2\epsilon\Delta y}\left(H_z|^{n+\frac{1}{2}}_{i+\frac{1}{2},j+\frac{1}{2},k} - H_z|^{n+\frac{1}{2}}_{i+\frac{1}{2},j-\frac{1}{2},k}\right) - \frac{\Delta t}{2\epsilon\Delta z}\left(H_y|^{n+1}_{i+\frac{1}{2},j,k+\frac{1}{2}} - H_y|^{n+1}_{i+\frac{1}{2},j,k-\frac{1}{2}}\right) \tag{B.3a}$$

$$E_y|^{n+1}_{i,j+\frac{1}{2},k} = E_y|^{n+\frac{1}{2}}_{i,j+\frac{1}{2},k} + \frac{\Delta t}{2\epsilon\Delta z}\left(H_x|^{n+\frac{1}{2}}_{i,j+\frac{1}{2},k+\frac{1}{2}} - H_x|^{n+\frac{1}{2}}_{i,j+\frac{1}{2},k-\frac{1}{2}}\right) - \frac{\Delta t}{2\epsilon\Delta x}\left(H_z|^{n+1}_{i+\frac{1}{2},j+\frac{1}{2},k} - H_z|^{n+1}_{i-\frac{1}{2},j+\frac{1}{2},k}\right) \tag{B.3b}$$

$$E_z|^{n+1}_{i,j,k+\frac{1}{2}} = E_z|^{n+\frac{1}{2}}_{i,j,k+\frac{1}{2}} + \frac{\Delta t}{2\epsilon\Delta x}\left(H_y|^{n+\frac{1}{2}}_{i+\frac{1}{2},j,k+\frac{1}{2}} - H_y|^{n+\frac{1}{2}}_{i-\frac{1}{2},j,k+\frac{1}{2}}\right) - \frac{\Delta t}{2\epsilon\Delta y}\left(H_x|^{n+1}_{i,j+\frac{1}{2},k+\frac{1}{2}} - H_x|^{n+1}_{i,j-\frac{1}{2},k+\frac{1}{2}}\right) \tag{B.3c}$$

$$H_x|^{n+1}_{i,j+\frac{1}{2},k+\frac{1}{2}} = H_x|^{n+\frac{1}{2}}_{i,j+\frac{1}{2},k+\frac{1}{2}} + \frac{\Delta t}{2\mu\Delta z}\left(E_y|^{n+\frac{1}{2}}_{i,j+\frac{1}{2},k+1} - E_y|^{n+\frac{1}{2}}_{i,j+\frac{1}{2},k}\right) - \frac{\Delta t}{2\mu\Delta y}\left(E_z|^{n+1}_{i,j+1,k+\frac{1}{2}} - E_z|^{n+1}_{i,j,k+\frac{1}{2}}\right) \tag{B.4a}$$

$$H_y|^{n+1}_{i+\frac{1}{2},j,k+\frac{1}{2}} = H_y|^{n+\frac{1}{2}}_{i+\frac{1}{2},j,k+\frac{1}{2}} + \frac{\Delta t}{2\mu\Delta x}\left(E_z|^{n+\frac{1}{2}}_{i+1,j,k+\frac{1}{2}} - E_z|^{n+\frac{1}{2}}_{i,j,k+\frac{1}{2}}\right) - \frac{\Delta t}{2\mu\Delta z}\left(E_x|^{n+1}_{i+\frac{1}{2},j,k+1} - E_x|^{n+1}_{i+\frac{1}{2},j,k}\right) \tag{B.4b}$$

$$H_z|^{n+1}_{i+\frac{1}{2},j+\frac{1}{2},k} = H_z|^{n+\frac{1}{2}}_{i+\frac{1}{2},j+\frac{1}{2},k} + \frac{\Delta t}{2\mu\Delta y}\left(E_x|^{n+\frac{1}{2}}_{i++\frac{1}{2},j+1,k} - E_x|^{n+\frac{1}{2}}_{i+\frac{1}{2},j,k}\right) - \frac{\Delta t}{2\mu\Delta x}\left(E_y|^{n+1}_{i+1,j+\frac{1}{2},k} - E_y|^{n+1}_{i,j+\frac{1}{2},k}\right) \tag{B.4c}$$

In each of the above equations, the second finite difference on the right hand side is set up to be evaluated implicitly from as yet unknown field data at time step $n+1$, while

the first finite difference on the right hand side is evaluated explicitly from known field data at time step $n+\frac{1}{2}$ previously computed using (B.1) and (B.2)

Simplified System of Time Stepping Equations

The system of equations summarised above for each subiteration can be greatly simplified. For subiteraion 1, this is done by substituting the expressions of (B.2) for the H field components evaluated at time step $n+\frac{1}{2}$ into the E field updates of (B.1). Similarly, for subiteration 2, this is done by substituting the expressions of (B.4) for the H field components evaluated at time step $n+1$ into the E field updates of (B.3). This yields the following simplified system of time stepping equations.

Subiteration 1: Advance the 6 field components from time step n to time step $n+\frac{1}{2}$

$$\begin{aligned}\left[1+\tfrac{(\Delta t)^2}{2\mu\epsilon(\Delta y)^2}\right]E_x|^{n+\frac{1}{2}}_{i+\frac{1}{2},j,k} - \left[\tfrac{(\Delta t)^2}{4\mu\epsilon(\Delta y)^2}\right]\left(E_x|^{n+\frac{1}{2}}_{i+\frac{1}{2},j-1,k} + E_x|^{n+\frac{1}{2}}_{i+\frac{1}{2},j+1,k}\right)\\ = E_x|^{n}_{i+\frac{1}{2},j,k} + \tfrac{\Delta t}{2\epsilon\Delta y}\left(H_z|^{n}_{i+\frac{1}{2},j+\frac{1}{2},k} - H_z|^{n}_{i+\frac{1}{2},j-\frac{1}{2},k}\right)\\ -\tfrac{\Delta t}{2\epsilon\Delta z}\left(H_y|^{n}_{i+\frac{1}{2},j,k+\frac{1}{2}} - H_y|^{n}_{i+\frac{1}{2},j,k-\frac{1}{2}}\right)\\ -\left[\tfrac{(\Delta t)^2}{4\mu\epsilon\Delta x\Delta y}\right]\left(E_y|^{n}_{i+1,j+\frac{1}{2},k} - E_y|^{n}_{i,j+\frac{1}{2},k} - E_y|^{n}_{i+1,j-\frac{1}{2},k} + E_y|^{n}_{i,j-\frac{1}{2},k}\right)\end{aligned} \tag{B.5a}$$

$$\begin{aligned}\left[1+\tfrac{(\Delta t)^2}{2\mu\epsilon(\Delta z)^2}\right]E_y|^{n+\frac{1}{2}}_{i,j+\frac{1}{2},k} - \left[\tfrac{(\Delta t)^2}{4\mu\epsilon(\Delta z)^2}\right]\left(E_y|^{n+\frac{1}{2}}_{i,j+\frac{1}{2},k-1} + E_y|^{n+\frac{1}{2}}_{i,j+\frac{1}{2},k+1}\right)\\ = E_y|^{n}_{i,j+\frac{1}{2},k} + \tfrac{\Delta t}{2\epsilon\Delta z}\left(H_x|^{n}_{i,j+\frac{1}{2},k+\frac{1}{2}} - H_x|^{n}_{i,j+\frac{1}{2},k-\frac{1}{2}}\right)\\ -\tfrac{\Delta t}{2\epsilon\Delta x}\left(H_z|^{n}_{i+\frac{1}{2},j+\frac{1}{2},k} - H_z|^{n}_{i-\frac{1}{2},j+\frac{1}{2},k}\right)\\ -\left[\tfrac{(\Delta t)^2}{4\mu\epsilon\Delta y\Delta z}\right]\left(E_z|^{n}_{i,j+1,k+\frac{1}{2}} - E_z|^{n}_{i,j,k+\frac{1}{2}} - E_z|^{n}_{i,j+1,k-\frac{1}{2}} + E_z|^{n}_{i,j,k-\frac{1}{2}}\right)\end{aligned} \tag{B.5b}$$

$$\begin{aligned}\left[1+\tfrac{(\Delta t)^2}{2\mu\epsilon(\Delta x)^2}\right]E_z|^{n+\frac{1}{2}}_{i,j,k+\frac{1}{2}} - \left[\tfrac{(\Delta t)^2}{4\mu\epsilon(\Delta x)^2}\right]\left(E_z|^{n+\frac{1}{2}}_{i-1,j,k+\frac{1}{2}} + E_z|^{n+\frac{1}{2}}_{i+1,j,k+\frac{1}{2}}\right)\\ = E_z|^{n}_{i,j,k+\frac{1}{2}} + \tfrac{\Delta t}{2\epsilon\Delta x}\left(H_y|^{n}_{i+\frac{1}{2},j,k+\frac{1}{2}} - H_y|^{n}_{i-\frac{1}{2},j,k+\frac{1}{2}}\right)\\ -\tfrac{\Delta t}{2\epsilon\Delta y}\left(H_x|^{n}_{i,j+\frac{1}{2},k+\frac{1}{2}} - H_x|^{n}_{i,j-\frac{1}{2},k+\frac{1}{2}}\right)\\ -\left[\tfrac{(\Delta t)^2}{4\mu\epsilon\Delta x\Delta z}\right]\left(E_x|^{n}_{i+\frac{1}{2},j,k+1} - E_x|^{n}_{i+\frac{1}{2},j,k} - E_x|^{n}_{i-\frac{1}{2},j,k+1} + E_x|^{n}_{i-\frac{1}{2},j,k}\right)\end{aligned} \tag{B.5c}$$

$$H_x\big|_{i,j+\frac{1}{2},k+\frac{1}{2}}^{n+\frac{1}{2}} = H_x\big|_{i,j+\frac{1}{2},k+\frac{1}{2}}^{n} + \frac{\Delta t}{2\mu\Delta z}\left(E_y\big|_{i,j+\frac{1}{2},k+1}^{n+\frac{1}{2}} - E_y\big|_{i,j+\frac{1}{2},k}^{n+\frac{1}{2}}\right) - \frac{\Delta t}{2\mu\Delta y}\left(E_z\big|_{i,j+1,k+\frac{1}{2}}^{n} - E_z\big|_{i,j,k+\frac{1}{2}}^{n}\right) \tag{B.6a}$$

$$H_y\big|_{i+\frac{1}{2},j,k+\frac{1}{2}}^{n+\frac{1}{2}} = H_y\big|_{i+\frac{1}{2},j,k+\frac{1}{2}}^{n} + \frac{\Delta t}{2\mu\Delta x}\left(E_z\big|_{i+1,j,k+\frac{1}{2}}^{n+\frac{1}{2}} - E_z\big|_{i,j,k+\frac{1}{2}}^{n+\frac{1}{2}}\right) - \frac{\Delta t}{2\mu\Delta z}\left(E_x\big|_{i+\frac{1}{2},j,k+1}^{n} - E_x\big|_{i+\frac{1}{2},j,k}^{n}\right) \tag{B.6b}$$

$$H_z\big|_{i+\frac{1}{2},j+\frac{1}{2},k}^{n+\frac{1}{2}} = H_z\big|_{i+\frac{1}{2},j+\frac{1}{2},k}^{n} + \frac{\Delta t}{2\mu\Delta y}\left(E_x\big|_{i+\frac{1}{2},j+1,k}^{n+\frac{1}{2}} - E_x\big|_{i+\frac{1}{2},j,k}^{n+\frac{1}{2}}\right) - \frac{\Delta t}{2\mu\Delta x}\left(E_y\big|_{i+1,j+\frac{1}{2},k}^{n} - E_y\big|_{i,j+\frac{1}{2},k}^{n}\right) \tag{B.6c}$$

Equation (B.5a) yields a set of simultaneous equations for $E_x^{n+\frac{1}{2}}$ when written for each j coordinate along a y-directed line through the space lattice. The matrix associated with this system is tridiagonal, and hence, easily solved. This process is repeated for each y-cut through the grid where E_x components are located. Similarly, (B.5b) yields a tridiagonal matrix system for each z-cut through the lattice to obtain $E_y^{n+\frac{1}{2}}$, and (B.5c) yields a tridiagonal matrix system for each x-cut through the lattice to obtain $E_z^{n+\frac{1}{2}}$.

It is also noticed that (B.6a-c) are exactly (B.2a-c), repeated here for convenience. These H-field updating equations are now fully explicit because all of their required E-field component data at time step $n+1/2$ are available upon solving (B.5a-c) in the manner described above.

Subiteration 2: Advance the 6 field components from time step $n+\frac{1}{2}$ to $n+1$

$$\begin{aligned}\left[1+\frac{(\Delta t)^2}{2\mu\epsilon(\Delta z)^2}\right]E_x\big|_{i+\frac{1}{2},j,k}^{n+1} - \left[\frac{(\Delta t)^2}{4\mu\epsilon(\Delta z)^2}\right]\left(E_x\big|_{i+\frac{1}{2},j,k-1}^{n+1} + E_x\big|_{i+\frac{1}{2},j,k+1}^{n+1}\right) \\ = E_x\big|_{i+\frac{1}{2},j,k}^{n+\frac{1}{2}} + \frac{\Delta t}{2\epsilon\Delta y}\left(H_z\big|_{i+\frac{1}{2},j+\frac{1}{2},k}^{n+\frac{1}{2}} - H_z\big|_{i+\frac{1}{2},j-\frac{1}{2},k}^{n+\frac{1}{2}}\right) \\ - \frac{\Delta t}{2\epsilon\Delta z}\left(H_y\big|_{i+\frac{1}{2},j,k+\frac{1}{2}}^{n+\frac{1}{2}} - H_y\big|_{i+\frac{1}{2},j,k-\frac{1}{2}}^{n+\frac{1}{2}}\right) \\ - \left[\frac{(\Delta t)^2}{4\mu\epsilon\Delta x\Delta z}\right]\left(E_z\big|_{i+1,j,k+\frac{1}{2}}^{n+\frac{1}{2}} - E_z\big|_{i,j,k+\frac{1}{2}}^{n+\frac{1}{2}} - E_z\big|_{i+1,j,k-\frac{1}{2}}^{n+\frac{1}{2}} + E_z\big|_{i,j,k-\frac{1}{2}}^{n+\frac{1}{2}}\right)\end{aligned} \tag{B.7a}$$

$$\begin{aligned}\left[1+\tfrac{(\Delta t)^2}{2\mu\epsilon(\Delta x)^2}\right]E_y|^{n+1}_{i,j+\frac{1}{2},k} - \left[\tfrac{(\Delta t)^2}{4\mu\epsilon(\Delta x)^2}\right]\left(E_y|^{n+1}_{i-1,j+\frac{1}{2},k} + E_y|^{n+1}_{i+1,j+\frac{1}{2},k}\right)\\ = E_y|^{n+\frac{1}{2}}_{i,j+\frac{1}{2},k} + \tfrac{\Delta t}{2\epsilon\Delta z}\left(H_x|^{n+\frac{1}{2}}_{i,j+\frac{1}{2},k+\frac{1}{2}} - H_x|^{n+\frac{1}{2}}_{i,j+\frac{1}{2},k-\frac{1}{2}}\right)\\ -\tfrac{\Delta t}{2\epsilon\Delta x}\left(H_z|^{n+\frac{1}{2}}_{i+\frac{1}{2},j+\frac{1}{2},k} - H_z|^{n+\frac{1}{2}}_{i-\frac{1}{2},j+\frac{1}{2},k}\right)\\ -\left[\tfrac{(\Delta t)^2}{4\mu\epsilon\Delta x\Delta y}\right]\left(E_x|^{n+\frac{1}{2}}_{i+\frac{1}{2},j+1,k} - E_x|^{n+\frac{1}{2}}_{i+\frac{1}{2},j,k} - E_x|^{n+\frac{1}{2}}_{i-\frac{1}{2},j+1,k} + E_x|^{n+\frac{1}{2}}_{i-\frac{1}{2},j,k}\right)\end{aligned} \tag{B.7b}$$

$$\begin{aligned}\left[1+\tfrac{(\Delta t)^2}{2\mu\epsilon(\Delta y)^2}\right]E_z|^{n+1}_{i,j,k+\frac{1}{2}} - \left[\tfrac{(\Delta t)^2}{4\mu\epsilon(\Delta y)^2}\right]\left(E_z|^{n+1}_{i,j-1,k+\frac{1}{2}} + E_z|^{n+1}_{i,j+1,k+\frac{1}{2}}\right)\\ = E_z|^{n+\frac{1}{2}}_{i,j,k+\frac{1}{2}} + \tfrac{\Delta t}{2\epsilon\Delta x}\left(H_y|^{n+\frac{1}{2}}_{i+\frac{1}{2},j,k+\frac{1}{2}} - H_y|^{n+\frac{1}{2}}_{i-\frac{1}{2},j,k+\frac{1}{2}}\right)\\ -\tfrac{\Delta t}{2\epsilon\Delta y}\left(H_x|^{n+\frac{1}{2}}_{i,j+\frac{1}{2},k+\frac{1}{2}} - H_x|^{n+\frac{1}{2}}_{i,j-\frac{1}{2},k+\frac{1}{2}}\right)\\ -\left[\tfrac{(\Delta t)^2}{4\mu\epsilon\Delta y\Delta z}\right]\left(E_y|^{n+\frac{1}{2}}_{i,j+\frac{1}{2},k+1} - E_y|^{n+\frac{1}{2}}_{i,j+\frac{1}{2},k} - E_y|^{n+\frac{1}{2}}_{i,j-\frac{1}{2},k+1} + E_y|^{n+\frac{1}{2}}_{i,j-\frac{1}{2},k}\right)\end{aligned} \tag{B.7c}$$

$$\begin{aligned}H_x|^{n+1}_{i,j+\frac{1}{2},k+\frac{1}{2}} = H_x|^{n+\frac{1}{2}}_{i,j+\frac{1}{2},k+\frac{1}{2}} + \tfrac{\Delta t}{2\mu\Delta z}\left(E_y|^{n+\frac{1}{2}}_{i,j+\frac{1}{2},k+1} - E_y|^{n+\frac{1}{2}}_{i,j+\frac{1}{2},k}\right)\\ -\tfrac{\Delta t}{2\mu\Delta y}\left(E_z|^{n+1}_{i,j+1,k+\frac{1}{2}} - E_z|^{n+1}_{i,j,k+\frac{1}{2}}\right)\end{aligned} \tag{B.8a}$$

$$\begin{aligned}H_y|^{n+1}_{i+\frac{1}{2},j,k+\frac{1}{2}} = H_y|^{n+\frac{1}{2}}_{i+\frac{1}{2},j,k+\frac{1}{2}} + \tfrac{\Delta t}{2\mu\Delta x}\left(E_z|^{n+\frac{1}{2}}_{i+1,j,k+\frac{1}{2}} - E_z|^{n+\frac{1}{2}}_{i,j,k+\frac{1}{2}}\right)\\ -\tfrac{\Delta t}{2\mu\Delta z}\left(E_x|^{n+1}_{i+\frac{1}{2},j,k+1} - E_x|^{n+1}_{i+\frac{1}{2},j,k}\right)\end{aligned} \tag{B.8b}$$

$$\begin{aligned}H_z|^{n+1}_{i+\frac{1}{2},j+\frac{1}{2},k} = H_z|^{n+\frac{1}{2}}_{i+\frac{1}{2},j+\frac{1}{2},k} + \tfrac{\Delta t}{2\mu\Delta y}\left(E_x|^{n+\frac{1}{2}}_{i++\frac{1}{2},j+1,k} - E_x|^{n+\frac{1}{2}}_{i+\frac{1}{2},j,k}\right)\\ -\tfrac{\Delta t}{2\mu\Delta x}\left(E_y|^{n+1}_{i+1,j+\frac{1}{2},k} - E_y|^{n+1}_{i,j+\frac{1}{2},k}\right)\end{aligned} \tag{B.8c}$$

Equation (B.7a) yields a tridiagonal matrix system for each z-cut through the lattice to obtain E_x^{n+1}; (B.7b) yields a tridiagonal matrix system for each x-cut through the lattice to obtain E_y^{n+1}; and (B.7c) yields a tridiagonal matrix system for each y-cut through the lattice to obtain E_z^{n+1}. Also (B.8a-c) are exactly (B.4a-c), repeated for convenience. These H-field updating equations are now fully explicit because all of their required E-component data at time step $n+1$ are available upon solving (B.7a-c) in the manner described above. This completes the algorithm.

Too much work has been done on numerical stability for the ADI method, it is worth to mention (Zheng and Chen, 2001) where for the first time unconditional numerical

stability is derived for the full three dimensional case. There has been also publications on the accuracy of the ADI-FDTD method as in (Garcia et al., 2002) where the accuracy of the method is compared with those of the original Crank-Nicolson (from which ADI is derived) and the Yee FDTD schemes.

As with the normal FDTD, when trying to implement the ADI scheme, care must be taken with the implementation of current sources, this is addressed in (Garcia et al., 2004). Also, the way to implement an efficient PML absorber boundary has been published (Wang and Teixeira, 2003).

Bibliography

A. Aharoni. *Introduction to the Theory of Ferromagnetism*. Oxford Science Publications, 2nd edition, 2000.

J. C. Anderson. *Magnetism and Magnetic Materials*. Chapman and Hall LTD, 1968.

T.C. Arnoldussen. A modular transmission line/reluctance head model. *Magnetics, IEEE Transactions on*, 24(6):2482–2484, 1988.

C. H. Back, J. Heidmann, and J. Mc Cord. Time resolvel kerr microscopy: Magnetisation dynamics in thin film write heads. *Magnetics, IEEE Transactions on*, 35: 637–642, 1999.

J.P. Berenger. A perfectly matched layer for the absorption of electromagnetic waves. *Journal of computational physics*, 114:185–200, 1994.

J.P. Berenger. Perfectly matched layer for the fdtd solution of wave structure interaction problems. *Antennas and Propagation, IEEE Transactions on*, 51:110–117, 1996.

J.P. Berenger. Improved pml for the fdtd solution of wave structure interaction problems. *Antennas and Propagation, IEEE Transactions on*, 45:446–473, 1997.

G. Bertotti. *Hysteresis in Magnetism, fot physicists, material scientists, and engineers*. Academic Press, 1998.

P. R. Bevington. *Data Reduction and Error Analysis for the Physical Sciences*. McGraw-Hill Book Company, 1969.

P.G Blanken and J.J.L.M. Van Vlerken. Modeling of electromagnetic systems. *Magnetics, IEEE Transactions on*, 27(6):4509–4515, 1991.

S. Brittenham. Time domain characterization of thin film head/media systems. *Magnetics, IEEE Transactions on*, 24(6):2949–2954, 1988.

S.J.C. Brown, J.C. Mallinson, D.T. Wilton, and H.A. Shute. Calculation of the switching constant of magnetic recording media. *Magnetics, IEEE Transactions on*, 38(1): 271–278, 2002.

W. F. Brown. *Micromagnetics*. Robert E. Krieger publishing company Huntington, New York, 1978.

E. Colin-Cherry. The duality between interlinked electric and magnetic circuits and the formation of transformer equivalent circuits. *Proc. Phys. Soc. London*, 62(part b):101–111, 1948.

B. W. Corb. High frequency response of thin film heads by scanning kerr effect microscopy. *Magnetics, IEEE Transactions on*, 24(6):2838–2840, 1988.

H. Engstrom. Equivalent circuit of a thin film recording head. *Magnetics, IEEE Transactions on*, 20(5):842–844, 1984.

K. Gao and H. N. Bertram. Three dimensional micromagnetic analysis of write head dynamics and field patterns. *Magnetics, IEEE Transactions on*, 37(4):1373–1375, 2001.

S.G. Garcia, T. Lee, and S.C. Hagness. On the accuracy of the adi-fdtd method. *IEEE Antennas and Wireless Propagation Letters*, 1:31–34, 2002.

S.G. Garcia, A.R. Bretones, R.G. Martin, and S.C. Hagness. Accurate implementation of current sources in the adi-fdtd scheme. *IEEE Antennas and Wireless Propagation Letters*, 3:141–144, 2004.

S.D. Gedney. An anisotropic perfectly matched layer absorbing media for the truncation of fdtd lattices. *Antennas and Propagation, IEEE Transactions on*, 44:1630–1639, 1996.

T. L. Gilbert. A lagrangian formulation of the gyromagnetic equation of the magnetic field. *Physical Review*, 100, 1955.

S.C. Hagness and A. Taflove. *Computational Electrodynamics, the finite difference time domain method*. Artech House, 2000.

L. He. Fdtd-advances in sub sampling methods, upml, and higher order boundary conditions. Master's thesis, University of Kentucky, Lexington, KY, 1997.

R. J. Hicken, N. D. Hughes, J. R. Moore, D. S. Schmool, and J. Wu R. Wilks. Magneto-optical studies of magnetism on pico and femtosecond time scales. *Journal of Magnetism and Magnetic Materials*, 242-245(1):559–564, 2002.

W.P. Jayasekara, J.A. Bain, and M.H. Kryder. High frequency initial permeability of nife and fealn. *Magnetics, IEEE Transactions on*, 34(4):1438–1440, 1998.

M. T. Johnson and E. G. Visser. A coherent model for the complex permeability in polycrystalline ferrites. *Magnetics, IEEE Transactions on*, 26(5):1987–1989, 1990.

R. E. Jones. Analysis of the efficiency and inductance of multiturn thin film magnetic recording heads. *Magnetics, IEEE Transactions on*, 14(5):509–511, 1978.

F. Jorgersen. *The complete handbook of magnetic recording*. McGraw-Hill / TAB Books, 4th edition, 1995.

D. S. Katz, E. T. Thiele, and A. Taflove. Validation and extension to three-dimensions of the berenger pml absorbing boundary condition for fdtd meshes. *IEEE Microwave and Guided Wave Letters*, 4:268–270, 1994.

A. Kaya, C.P. Yue, and J.A. Bain. Experimental evidence for gyromagnetic damping in magnetic heads determined by impedance measurements up to 9 ghz. *Magnetics, IEEE Transactions on*, 41(10):2923–2925, 2005.

C. Kittel. Physical theory of ferromagnetic domains. *Reviews of Modern Physics*, 21, 1949.

K.B. Klaassen and R.G. Hirko. Nonlinear, eddy current damped, thin-film write head model. *Magnetics, IEEE Transactions on*, 32(5):3524–3526, 1996.

L. D. Landau and E. M. Lifshitz. Theory of the dispersion of magnetic permeability in ferromagnetic bodies. *Phys. Z. Sowietunion*, 8, 1935.

F. H. Liu, M. D. Schultz, and M. H. Kryder. High frequency dynamic imaging of domains in thin film heads. *Magnetics, IEEE Transactions on*, 26(5):1340–1342, 1990.

F.H. Liu, H. Tong, and L. Milosvlasky. High frequency magnetization response observed at the air-bearing surfaces of thin film heads. *Magnetics, IEEE Transactions on*, 32 (5):3536–3538, 1996.

F.H. Liu, S. Shi, J. Wang, Y. Chen, K. Stoev, L. Leal, R. Saha, H.C. Tong, S. Dey, and M. Nojaba. Magnetic recording at a data rate of one gigabit per second. *Magnetics, IEEE Transactions on*, 37(2):613–618, 2001.

Q. H. Liu. The pseudospectral time-domain (pstd) method: A new algorithm for solution of maxwell's equations. *Proc. IEEE Antennas and Propagation Society Intl. Symp.*, 1:122–125, 1997.

M. Mallary, A. Torabi, S. Batra, A.B. Smith, L. Cappabianca, and W.W. Goller. Frequency response of thin film heads with longitudinal and transverse anisotropy. *Magnetics, IEEE Transactions on*, 26(5):1334–1336, 1990.

J. C. Mallinson. On damped gyromagnetic precession. *Magnetics, IEEE Transactions on*, 23:2003–2004, 1987.

J. C. Mallinson. Scaling in magnetic recording. *Magnetics, IEEE Transactions on*, 32: 599–600, 1996.

J. C. Maxwell. *A Treatise on Electricity and Magnetism*. Clarendon Press, Oxford, 1873.

C. D. Mee and E. D. Daniel. *Magnetic recording handbook*. McGraw-Hill, 1990.

B. K. Middleton, J. J. Miles, and M. M. Aziz. Switching times and transition widths in digital recording theory. *Magnetics, IEEE Transactions on*, 37:1327–1329, 2001.

G. Mur. Absorbing boundary conditions for the finite-difference approximation of the time-domain electromagnetic field equations. *Electromagnetic Compatibility, IEEE Transactions on*, 23:377–382, 1981.

M. Okoniewski and E. Okoniewska. Fdtd analysis of magnetized ferrites: a more efficient algorithm. *Microwave and Guided Wave Letters, IEEE*, 4(6):169–171, 1994.

G. S. Park and H. Won. Eddy current effects on the high density magnetic recording system. *Magnetics, IEEE Transactions on*, 42(4):775–778, April 2006.

A. Paton. Analysis of the efficiency of thin film magnetic recording heads. *J. Appl. Phys.*, 42(13):5868–5870, 1971.

A. Payne, W. Cain, R. Hempstead, and G. McCrea. Measuring core losses in thin film heads. *Magnetics, IEEE Transactions on*, 32(5):3518–3520, 1996.

A. Payne, P. Thayamballi, and P. Macias. Inductance-saturation characteristics in thin film heads. *Magnetics, IEEE Transactions on*, 33(5):2860–2862, 1997.

J. A. Pereda, L. A. Vielva, A. Vegas, and A. Prieto. A treatment of magnetized ferrites using the fdtd method. *Microwave and Guided Wave Letters, IEEE*, 3(5):136–138, 1993.

J. A. Pereda, L. A. Vielva, A. Vegas, and A. Prieto. An extended fdtd method for the treatment of partially magnetized ferrites. *Magnetics, IEEE Transactions on*, 31(3): 1666–1669, 1995.

A. Prabhakar and S. Filips. Flux reversal time in thin film write heads: a nonlinear system theoretic approach. *Journal of Applied Physics*, 85(9):6907–6911, 1999.

A. Reineix, T. Monediere, and F. Jecko. Ferrite analysis using the fdtd method. *Microwave and Optical Technology Letters*, 5, 1992.

M. N. O. Sadiku. *Elements of electromagnetics*. Oxford University Press, 4th edition, 2001.

G. M. Sandler and H. N. Bertram. Micromagnetic simulations with eddy currents of rise time in thin film write heads. *Journal of Applied Physics*, 81:4513–4515, 1997.

F. Sherrima and R. Soohoo. Frequency domain analysis of thin film head response. *Magnetics, IEEE Transactions on*, 22(5):843–844, 1986.

H.A. Shute, D.J. Mapps, and D.T. Wilton. Eddy-current-assisted digital video read/write head. *Magnetics, IEEE Transactions on*, 37(4):3043–3052, 2001.

R. F. Soohoo. Switching dynamics in a thin film recording head. *Magnetics, IEEE Transactions on*, 18:1128–1130, 1982.

J. Sun, F. Collino, P. B. Monk, and L. Wang. An eddy-current and micromagnetism model with applicationsto disk write heads. *International Journal for Numerical Methods in Engineering*, 60(10):1673–1698, 2004.

I. Tagawa, T. Koshikawa, and Y. Sasaki. High performance write head for 10 krpm hdd with high data rate recording up to 45 mb/s. *Magnetics, IEEE Transactions on*, 36(1):177–182, 2000.

H. Takano, K. Itoh, Y. Shiroishi, M. Fuyama, Y. Sugita, and M. Suzuki. High-frequency write characteristics of thin film heads for hdds. *Magnetics, IEEE Transactions on*, 31(6):2651–2656, 1995.

K. Takano. Magnetization dynamics of planar writers. *Magnetics, IEEE Transactions on*, 40(1):257–262, 2004.

K. Takano, X. Zhang, L. Guan, J. Smyth, and M. Dovek. Micromagnetics and eddy current effects in magnetic recording heads. *Magnetics, IEEE Transactions on*, 43 (6):2184–2186, 2007.

X. Tan, J. S. Baras, and P. S. Krishnaprasad. Computational micromagnetics for magnetostrictive actuators. *Technical research report CDCSS series University of Maryland*, 2005.

A.F. Torabi, M.L. Mallary, R. Perry, and G. Kimball. Two dimensional model of eddy currents and saturation in thin film write heads. *Magnetics, IEEE Transactions on*, 34(4):1465–1467, 1998.

E. Della Torre and J.G. Eicke. Eddy currents in micromagnetic calculations. *Magnetics, IEEE Transactions on*, 33(2):1251–1254, 1997.

L. Torres, L. Lopez-Diaz, E. Martinez, and O. Alejos. Micromagnetic dynamic computations including eddy currents. *Magnetics, IEEE Transactions on*, 39(5):2498–2500, 2003.

O. Vacus and N. Vukadinovic. Dynamic susceptibility computations for thin magnetic films. *J. Comput. Appl. Math.*, 176(2):263–281, 2005.

S. Wang and F.L. Teixeira. An efficient pml implementation for the adi-fdtd method. *IEEE Microwave and Wireless Components Letters*, 13:72–74, 2003.

S. X. Wang and A. M. Taratorin. *Magnetic Information Storage*. Academic Press, 1999.

R. M. White, editor. *Introduction to Magnetic Recording*. IEEE Press, 1984.

M. L. Williams and R. L. Comstock. An analytical model for the write process in digital magnetic recording. *17th Anne. AIP Conf. Proc.*, Part I(5), 1971.

R. Wood, M. Williams, and J. Hong. Considerations for high data rate recording with thin-film heads. *Magnetics, IEEE Transactions on*, 26(6):2954–2959, 1990.

J. Wu, N. D. Hughes, J. R. Moore, and R. J. Hicken. Excitation and damping of spin excitations in ferromagnetic thin films. *Journal of Magnetism and Magnetic Materials*, 241:96–109, 2001.

K. Yee. Numerical solution of inital boundary value problems involving maxwell's equations in isotropic media. *Antennas and Propagation, IEEE Transactions on*, 14 (3):302–307, 1966.

N. Yeh. Analysis of thin film head with a generalized transmission line model. *Magnetics, IEEE Transactions on*, 18(1), 1982.

S.W. Yuan, E. Lee, W. Hsiao, H. Santini, H. Lam, G. Sui, T. Lam, Y. Luo, M. Madison, V. Nikitin, B. Webb, Y. Shen, M. Ramasubramanian, J. Jarratt, R. Hsiao, T. Harris, S. Sahami, N. Robertson, D. Freitas, Y. Hsu, M. Williams, A. Taratorin, J. Heidmann, R. Simmons, and J. Smyth. Advanced write heads for high density and high data rate recording. *Magnetics, IEEE Transactions on*, 38(5):1873–1878, 2002.

C.P. Yue and S.S. Wong. Physical modeling of spiral inductors on silicon. *Electron Devices, IEEE Transactions on*, 47(3):560–568, 2000.

Z. Zhang, Y. C. Feng, T. Clinton, G. Badran, N. Yeh, G. Tarnopolsky, E. Girt, M. Munteanu, S. Harkness, H. Richter, T. Nolan, R. Ranjan, S. Hwang, G. Rauch, M. Ghaly, D. Larson, E. Singleton, V. Vas'ko, J. Ho, F. Stageberg, V. Kong, K. Duxstad, and S. Slade. Magnetic recording demonstration over 100 gb/in2. *Magnetics, IEEE Transactions on*, 38(5):1861–1866, 2002.

F. Zheng and Z. Chen. Numerical disperssion analysis of the unconditionally stable 3d adi-fdtd method. *Microwave Theory and Techniques, IEEE Transactions on*, 49: 1006–1009, 2001.

F. Zheng, Z. Chen, and J. Zhang. A finite-difference time-domain method without the courant stability conditions. *IEEE Microwave and Guided Wave Letters*, 9:441–443, 1999.

G. Zheng and K. Chen. Transient analysis of microstrip lines with ferrite substrate by extended fd-td method. *International Journal of Infrared and Millimeter Waves*, 13 (8):1115–1125, 1992.